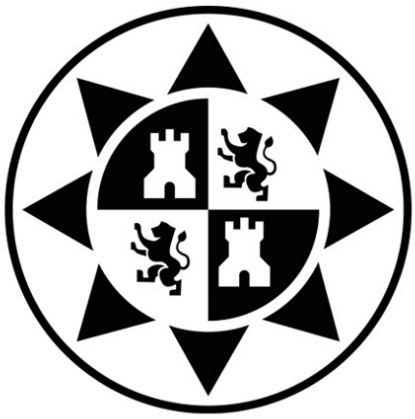

Combustion Modelling of Solid Propellants

Modelado de la combustión de propulsantes sólidos

Carmen López Muñoz

Director: José Ramón García Cascales
Co-director: Francisco Javier Sánchez Velasco

Doctorate Program of Renewable Energies and Energy Efficiency

Department of Thermal and Fluid Engineering, ETSII
Research Group on Modelling of Thermal and Energy Systems
Technical University of Cartagena

July, 2019

Universidad Politécnica de Cartagena

DT-16

CONFORMIDAD DE SOLICITUD DEAUTORIZACIÓN DE DEPÓSITO DE TESIS DOCTORAL POR EL/LA DIRECTOR/A DE LA TESIS

D. JOSÉ RAMÓN GARCÍA CASCALES y FRANCISCO JAVIER SÁNCHEZ VELASCO Directores de la Tesis doctoral COMBUSTION MODELLING OF SOLID PROPELLANTS.

INFORMA:

Que la referida Tesis Doctoral, ha sido realizada por Dª. CARMEN LÓPEZ MUÑOZ, dentro del Programa de Doctorado ENERGÍAS RENOVABLES Y EFICIENCIA ENERGÉTICA, dando nuestra conformidad para que sea presentada ante el Comité de Dirección de la Escuela Internacional de Doctorado para ser autorizado su depósito.

La rama de conocimiento en la que esta tesis ha sido desarrollada es:

- ☐ Ciencias
- ☐ Ciencias Sociales y Jurídicas
- X Ingeniería y Arquitectura

En Cartagena, a 18 de junio de 2019

LOS DIRECTORES DE LA TESIS

JOSE RAMON| GARCIA| CASCALES [redacted]

Fdo.: José Ramón García Cascales

FRANCISCO JAVIER| SANCHEZ| VELASCO [redacted]

Francisco Javier Sánchez Velasco

COMITÉ DE DIRECCIÓN ESCUELA INTERNACIONAL DE DOCTORADO

Universidad Politécnica de Cartagena

DT-17

CONFORMIDAD DE DEPÓSITO DE TESIS DOCTORAL POR LA COMISIÓN ACADÉMICA DEL PROGRAMA

D. Ángel Molina García, Presidente de la Comisión Académica del Programa Energías Renovables y Eficiencia Energética.

INFORMA:

Que la Tesis Doctoral titulada, "COMBUSTION MODELLING OF SOLID PROPELLANTS", ha sido realizada, dentro del mencionado Programa de Doctorado, por Dª. Carmen López Muñoz, bajo la dirección y supervisión de los Dres. José Ramón García Cascales y Francisco Javier Sánchez Velasco.

En reunión de la Comisión Académica, visto que en la misma se acreditan los indicios de calidad correspondientes y la autorización del Director de la misma, se acordó dar la conformidad, con la finalidad de que sea autorizado su depósito por el Comité de Dirección de la Escuela Internacional de Doctorado.

La Rama de conocimiento por la que esta tesis ha sido desarrollada es:

- ☐ Ciencias
- ☐ Ciencias Sociales y Jurídicas
- X Ingeniería y Arquitectura

En Cartagena, a 18 de Junio de 2019

EL PRESIDENTE DE LA COMISIÓN ACADÉMICA

ANGEL| MOLINA| GARCIA [redacted]

Fdo: Ángel Molina García

COMITÉ DE DIRECCIÓN ESCUELA INTERNACIONAL DE DOCTORADO

Abstract

Among all energetic materials, the combustion of granulated, composite AP/HTPB and double-base solid propellants are studied in thesis. The improvement on the design and safety in industrial processes which use solid propellants are of major importance in industry of energetic materials.

Unexpected detonation of granular solid propellants is a key safety issue. Moreover, ignition and subsequent combustion of granular solid propellants are also complex mechanisms of high importance in the manufacturing process of many energetic materials, not only because already mentioned safety issues, but also in due in the design of propulsion systems. Therefore, and in order to properly understand this problem, a model for the characterisation of the detonation process of granular solid propellants under shock tube conditions is developed. To be able to reach this objective, a two-phase model, which considers the conservation equations of mass, momentum and energy and constitutive relations of mass generation, gas-solid particle interaction, interface heat transfer and particle-particle stress is defined. The study performed in this thesis, improve the understanding and modelling of the deflagration-to-denotation (DDT) phenomenon in granular beds of solid propellants. Two different models have been used to calculate pressure, temperature and porosity distributions. The first model considered a modification of the particle momentum governing equation in order to prevent the porosity from reaching values below the minimum value of compaction defined for packed beds of spherical particles. The second model studied does not consider the porosity limiter in the momentum conservation equation but represents the limitation of the porosity directly in the code by preventing the porosity to reach values below a minimum. In addition, the results are obtained by employing several numerical schemes and are compared against those available in the bibliographical sources in order to assess their effectivity to predict the early stages of this transient combustion process. The results show that developed second model accurately represents the physical behaviour of the propellant combustion for all variables of interest becoming a predictive tool for the characterisation of granulated solid propellants.

Modelling the combustion of composite propellants and double-base propellants is a key problem that has focused the interest of several researches in many industrial fields such as chemical engineering, aerospace engineering or safety in industrial processes. Regarding safety, not only gun tubes, but also rocket motors experiment pressure build-up which could increase the chamber pressure, causing the explosion of the rocket motor being of high importance to develop models which could represent accurately the combustion process of these materials. Modelling the combustion of these propellants has been also of high interest for researchers in terms of optimising chemical composition to fulfil industrial requirements, improve propellant design, development and testing activities. The analysis of the burning rate of these materials, which means their decomposition and their subsequent combustion, is one of the main objectives of combustion modelling. Therefore, in this work, a transient multidimensional numerical model to describe the combustion of composite and double-base solid propellants is presented. The kinetics of the model is described by considering firstly, a change of phase of the solid propellant from condensed to gas and secondly, a reduced chemistry scheme which defines simplified chemical reactions to represent the combustion itself. To couple both processes, mass and species conservation, as well as temperature continuity are imposed in the burning surface in which the burning rate will represent a key factor. Moreover, an energy balance is also applied at the burning surface which represents that heat that the gas transfers to the burning surface is invested

firstly, in raising the surface temperature to produce the phase change and secondly, in warming the condensed phase by conduction. The results obtained in the combustion modelling of both, composite and double-base solid propellants, are compared against experimental test and results present in the existing literature. An absolute error between 0.4 mm/s and 1 mm/s is obtained being in the order of magnitude of the experimental error. In addition, the pressure oscillations produced in a rocket motor and the depressurisation suffered in a combustion chamber, as well as at the exit of a barrel, are very interesting technological problems which have not been deeply studied in the literature. Therefore, the results obtained in the numerical modelling of transient combustion of composite and double-base solid propellants are presented in this thesis too. To perform this analysis, a pressure ramp is applied during a short interval of time at the open side of the already defined geometries. The developed tool confirms its robustness for the prediction of composite and double-base propellants combustion behaviour in multidimensional scenarios with transient environmental conditions such as rocket engines and/or base bleed units in ballistics applications.

Resumen

En esta tesis se han estudiado, de entre todos los materiales energéticos, la combustión de propulsantes sólidos de tipo granulado, composite y doble-base. Tanto la mejora del diseño, como de los procesos de seguridad y las instalaciones que usan propulsantes solidos son asuntos de gran importancia en la industria de materiales energéticos.

La detonación inesperada de propulsantes sólidos de tipo granular es clave en materia de seguridad. Además, la ignición y la subsecuente combustión de dicho propulsante es un mecanismo complejo también de gran importancia en los procesos de fabricación de muchos materiales energéticos, no solo por los problemas de seguridad ya mencionados, sino también por el diseño de los sistemas de propulsión. Por lo tanto, en este trabajo se ha desarrollado un modelo para caracterizar el proceso de detonación de propulsantes sólidos granulados bajo condiciones de tubo de choque. Para ser capaz de alcanzar este objetivo, se ha definido un modelo bifásico que considera las ecuaciones de conservación de masa, momento y energía, así como los términos fuente de generación de masa, interacción sólido-gas, calor interfacial y tensión intergranular. El estudio llevado a cabo en esta tesis mejora la comprensión y modelado del fenómeno de deflagración-detonación en propulsantes sólidos. Las distribuciones de presión, temperatura y porosidad se han obtenido mediante dos modelos. El primero considera la modificación de la ecuación de conservación de la cantidad de movimiento de la fase sólida a fin de evitar que la porosidad alcance un valor por debajo del mínimo permitido para partículas esféricas. Por otro lado, el segundo modelo limita la porosidad directamente en el código impidiendo que esta variable alcance valores por debajo del mínimo valor físico en lugar de considerar esta limitación modificando la ecuación de cantidad de movimiento. Además, se han empleado distintos esquemas numéricos en la resolución del modelo a fin de poder comparar los resultados obtenidos entre ellos y con los datos disponibles en la bibliografía. Esto permitirá estudiar su efectividad para predecir las primeras fases de del proceso de combustión. Los resultados obtenidos muestran que el segundo modelo desarrollado representa de forma precisa el comportamiento físico de la combustión del dicho propulsante convirtiéndose por tanto en una herramienta predictiva para la caracterización de la combustión de propulsantes sólidos de tipo granular.

El modelado de la combustión de propulsantes tipo composite y doble-base es un problema clave que ha ocupado el interés de muchos investigadores en diversos ámbitos industriales como la ingeniería química, la ingeniería aeroespacial o la seguridad en procesos industriales. En cuanto a seguridad, los motores cohete pueden experimentar incrementos de presión en la cámara de combustión dando lugar a la explosión del motor cohete. Por tanto, es de gran importancia desarrollar modelos que puedan representar de forma precisa el proceso de combustión de estos materiales. El modelado de la combustión también ha sido de gran interés para investigadores con la idea de optimizar la composición química de los propulsantes para satisfacer requisitos industriales, así como para mejorar el diseño, el desarrollo y las actividades de test del propulsante. El análisis de la velocidad de quemado de estos materiales, que representa su descomposición y su subsecuente combustión, es uno de los objetivos de más interés en el modelado de la combustión. Por lo tanto, en este trabajo se ha presentado un modelo multidimensional transitorio para describir el proceso de combustión de propulsantes sólidos de tipo composite y doble base. La cinética química del modelo considera primero un cambio de fase del propulsante de fase condensada a fase gaseosa y, a continuación, un esquema químico reducido que define reacciones químicas simplificadas para modelar la combustión en sí misma. Con el fin de

acoplar ambos procesos, se han impuesto en la superficie de quemado las condiciones de conservación de masa y especies, así como la continuidad de la temperatura, expresiones en las cuales la velocidad de quemado es determinante. Además, en la superficie de quemado se ha establecido un balance de energía que representa la inversión del calor que el gas transfiere a la superficie de quemado en dos procesos: el primero, en elevar la temperatura de la superficie produciendo el cambio de fase el propulsante y el segundo, en calentar la fase condensada mediante conducción. Los resultados obtenidos en la combustión de ambos propulsantes se comparan con resultados experimentales y obtenidos en la bibliografía. El error absoluto obtenido varía entre 0.4 mm/s y 1 mm/s siendo del orden de magnitud del error experimental. Además, las oscilaciones de presión que se producen en un motor cohete y la despresurización que se sufre en la cámara de combustión y a la salida del barril, son problemas de alto interés tecnológico que no han sido estudiados en profundidad en la literatura. Por tanto, los resultados obtenidos al modelar la combustión transitoria de ambos propulsantes se han presentado también en esta tesis. Para realizar este último análisis, se ha aplicado una rampa de presión durante un corto intervalo de tiempo a la salida de la cámara de combustión de las geometrías previamente utilizadas. Los resultados confirman la robustez de la herramienta desarrollada para la predicción del comportamiento de la combustión de propulsantes de tipo composite y doble-base en escenarios multidimensionales con condiciones ambientales transitorias como es el caso de motores cohete y unidades base-bleed en aplicaciones balísticas.

Acknowledgements

The research of this thesis has been performed due to the financial support of the Spanish Ministry of Economy and Competitiveness and the European Commission throughout the ALMENA project (RTC-2016-5194-8) obeying to the interest of the company Expal Systems S.A.

I would like to thank to Dr. José Ramón García Cascales and Dr. Francisco Javier Sánchez Velasco for giving me the opportunity to be part of this project as well as for their guidance and dedication. To them and to Dr. Ahmed Bentaib I also owe the opportunity to make my pre-doctoral stay in the Institut de Radioprotection et de Sûreté Nucléaire (IRSN) of Paris.

I would like to dedicate a special mention to my college Francisco Nicolás Perez, from whom I had the pleasure to learn a great deal and share many moments during these years.

I am extremely thankful to my family and my beloved ones for supporting and encouraging me as well as for their love and patience. Specially to my parents, for providing me access to education, for relying on me and, above all, for their help beyond what is possible to imagine.

Finally, I would like to thank all my friends. Particularly, I would like to express all my love and gratitude to those whom I can sincerely call family, for listening and understanding me every day without exception.

Contents

List of Figures

List of Tables

Chapter 1

Introduction

1.1 Energetic materials

Energetic materials can be defined as every solid or liquid material which can store energy. These materials are defined on the one hand, by their capacity to start chemical reactions from an energetic stimulation (sensitivity) and on the other hand, their reactivity, which means their capacity to propagate after their ignition. Among these materials are propellants, explosives and pyrotechnics [1].

It is thought that explosives were discovered in China during the seventh century being black powder, a mixture of charcoal, sulphur and potassium nitrate, the first explosive known. Afterwards, nitrocellulose (NC) and nitroglycerine (NG) were developed in Europe leading to the discovering of propellants which are defined as low explosives that can burn slowly and controlled and also provide a large volume of gases which could propel a projectile. A second group of energetic materials, called explosives, such as trinitrotoluene (TNT), cyclotetramethylene tetranitramine (high melting explosive HMX), etc. were also discovered, and due to their powerful but less sensitiveness properties, they are used as filling for bombs, warheads, etc. To conclude, pyrotechnics are formulations based on fuels, oxidisers, binders together with additives and they are used to fulfil military requirements for effects like illumination, incendiary, etc. [2]. Granulated, composite and double-base propellants have been analysed in this thesis and therefore, it is of high interest to have an insight of these ones particularly.

On the one hand, a granulated propellant could be defined as an energetic material composed of granulated energetic grains [3]. The granulated propellants are packed in beds which provides high pressure build-up when they are ignited [4]. The grains of propellant can be done from different kind of explosives such RDX (cyclotrimethylene trinitramine) or HMX (cyclotetramethylene tetranitramine) [5].

On the other hand, heterogeneous propellant could be, composite propellants, composite modified propellants and fuel-rich propellants. The first group are composed by a binder (fuel) and oxidiser. Examples of oxidisers are ammonium nitrate (AN), ammonium perchlorate (AP), ammonium dinitramide (ADN), etc., being the AP the one used most. The oxidiser is retained by the binder, such as castor oil (CO), polypropylene glycol (PPG), hydroxy-terminated polybutadiene (HTPB), etc.

To conclude, homogeneous propellants which are also called colloidal, are characterised because their content of nitrocellulose (NC) and nitroglycerine (NG) as their main ingredient. Additives are also part of this propellant and they are dividid in single, double and triple-base propellants. Single-base propellant only contain nitrocellulose (NC) as explosive ingredients. On the other hand, double-base propellants, as previously mentioned, contain both nitroglycerine and nitrocellulose. Finally, to form triple-base propellants nitroguanidine is added.

Although explosives are seen as a destructive weapon, their major role was and it is to contribute in society to create roads and rails in difficult areas, explore the space, obtain minerals, etc. Among the applications of explosives technology, the more known are the military ones: bombs, grenades,

warheads, etc. These developments are also used for commercial applications such as the High Altitude Fuel, Air Re-generating Composition etc. Another very well known application of explosives are space applications, such as space rockets and Indian satellite launch vehicles which are used in meteorology, weather forecasting, satellite communication, etc.,. Other less known applications are nuclear applications, such as nuclear weapons, agriculture, medical industry (nitroglycerine tablets for example), food industry, civil engineering, automobile industry and oil and gas industry [2].

1.2 Technological context

Among all energetic materials, the combustion of granulated solid propellant, composite AP/HTPB propellant and double-base propellant is studied in thesis. Due to their difference in composition and structure, the properties of each one of them are different, and as a result, their applications vary too.

Granulated propellants are widely used as artillery pieces, black power and pyrotechnic devices [6], such as aerial shell ejection for fireworks [3]. Due to their high mass burning rate, create a short burn time and high pressure in the barrels, being the reason of their usage in gun propulsion. The pressure build-up of granulated propellants in gun tubes has been widely studied due to the detonation phenomenon that can occur at high pressures inside the gun tube [3]. Several authors like Krier and Gokhale [7], study how the flow through a granulated propellant with mobile particles could generate a pressure wave which provokes detonation simulating the combustion inside a closed chamber.

Composite propellants, are extensively used for rockets, missiles and space shuttles. The most of the current operational composite propellants make use of ammonium perchlorate (AP) as an oxidiser. Ammonium perchlorate (oxidiser) together with additives and binders such as carboxy-terminated polybutadiene (CTPB), lactone-terminated polybutadiene (LTPB) or hydroxyl-terminated polybutadiene (HTPB) (among others) have been extensively used for space exploration, meteorological studies and sounding rockets. Simplicity and high reliability and low cost are the main characteristics of using HTPB for composite propellants and therefore, the are used for missiles and launch vehicles. The required thrust to induce a satellite into a predetermined orbit needs propellant to be performed. When the propellant stored in the the solid fuel booster rocket burns, the release of carbon dioxide, nitrogen oxides, hydrochloric acid gases and water vapour in high quantities help push the satellite into space or orbit being AP propellants the ones extensively used as an oxidiser because its decomposition products are all gases already mentioned improving the thrust [2].

The burning of AP composite propellant produces aluminium oxides generating visible smoke. Therefore, if the smoke is required to be removed, aluminium should not be part of AP propellants. However, when AP composite propellants burn in atmospheres with an humidity above 60%, even without aluminium in their composition, the white smoke appears. This behaviour is due to the fact that HCl provokes the formation of relatively large water drops leading to fog or mist [3]. In addition, large amounts of HCl and other chlorine containing compounds released to the atmosphere when burning not only can cause ozone depletion but also acid rain [2]. One solution to remove this smoke AP particles propellant is to replace the propellant by double-base propellant. Double-base propellants, as well as composite propellants, called also low explosives, burn slowly and regularly and therefore, they are less powerful. The formation of large volume of gases in a controllable manner made them suitable of being used for military applications, such antitank missiles, and space exploration.

1.3 Thesis scope

The improvement on the design and safety in industrial processes which use solid propellants are of major importance in industry of energetic materials.

Gun tubes experiment pressure build-up during unstable burning in the chamber leading to high mechanical stresses which act on the grains. Consequently, the chamber suffers an increase of pressure, causing the explosion of the gun tube [3]. Particularly, it is known that unexpected detonation of granular solid propellants is a key safety issue. Moreover, ignition and subsequent combustion of granular solid propellants are complex mechanisms key in manufacturing process of many energetic materials, not only because already mentioned safety issues, but also in due in the design of propulsion systems. The penetration of the hot gases into the voids promote the convective heating of the granules as well as the granule compaction and the rapid pressurisation of the system. In case the ignition is not correctly controlled, the process can generate compressive waves which compact the un-reacting region of the grain bed. Under these conditions, and as it has been already explained, if the strong pressure waves rise, they might rapidly collapse the bed leading to a compressive reaction and a violent explosion. Therefore, and in order to properly understand this problem, a model for the characterisation of the detonation process of granular solid propellants under shock tube conditions has been developed. To be able to reach this objective, a two-phase model, which considers the conservation equations of mass, momentum and energy and constitutive relations for mass generation, gas-solid particle interaction, interface heat transfer and particle-particle stress, has been defined.

Modelling the combustion of composite propellants and double-base propellants is a key problem that has focused the interest of several researches in many industrial fields such as chemical engineering, aerospace engineering or safety in industrial processes. Regarding safety, not only gun tubes, but also rocket motors, experiment pressure build-up which could increase the chamber pressure, causing the explosion of the rocket motor [3]. As a result, it is of high importance to develop models which could represent accurately the combustion process of these materials. Modelling the combustion of composite and double-base propellants has been also of high interest for researchers in terms of optimising chemical composition to fulfil industrial requirements, to improve propellant design as well as for development and testing activities [8]. Analysing the burning rate of these materials, which means their decomposition and their subsequent combustion, is one of the main objectives of combustion modelling [8]. Therefore, a transient multidimensional numerical model to describe the combustion of composite AP/HTPB and double-base solid propellants is presented in this work. The model considers the coupling of both condensed and gas phases by using mass, energy and species conservation, as well as temperature continuity in the burning surface. The kinetics of the model is described a change of phase of the propellant from condensed to gas and afterwards its combustion by a simplified chemistry scheme.

1.4 Thesis objectives and structure

1.4.1 Thesis objectives

The main objective of this thesis is the study of the combustion of granulated, composite and double-base solid propellants. Therefore, several models have been developed to characterise the combustion of these propellants. The research has been performed due to the financial support of the Spanish Ministry of Economy and Competitiveness and the European Commission (European Regional Development Fund (ERDF)/FEDER funds) throughout the ALMENA project (RTC-2016-5194-8) obeying to the interest of the company Expal Systems S.A.

Specifically, the objectives of the thesis could be classified in two depending on the solid propellant. On the one hand, the study of the combustion of granulated solid propellant has as main objective to improve the understanding and modelling of the deflagration-to-denotation (DDT) phenomenon in granular beds of solid propellants. Among all models present in literature, the goal is to develop a tool which provides the characterisation of the process. Due to the amount of source terms and initial conditions used in the bibliography a deep analysis of these variables has to be performed. Moreover, the comparison of the results obtained by employing several numerical schemes against the ones available in the bibliographical sources shall be done in order to assess their effectivity to predict the early stages of this transient combustion process. On the other hand, the goal of the study of composite

and double-base propellants is to characterise their unsteady combustion with the development of a multi-dimensional code which solves the set of differential equations for condensed and gas phases. The combustion of the solid propellant will be performed by considering firstly, a change of phase of the propellant from condensed to gas and secondly, two simplified chemical reactions to represent the combustion itself. To couple both processes, several conditions shall be imposed in the burning surface in which the burning rate will represent a key factor. The results obtained for the combustion of both, composite and double-base propellants, must compared against experimental test and results present in the literature. Finally, the developed tool shall confirm its robustness for the prediction of composite and double propellants combustion behaviour in multidimensional scenarios with transient environmental conditions such as rocket engines and/or base bleed units in ballistics applications.

1.4.2 Thesis structure

The thesis is structured in four main chapters: state of the art, numerical methods, combustion modelling and results and finally, conclusions.

In the chapter dedicated to the state of the art, a literature review of the subject is written for each kind of propellant considered in this work. To begin, a general introduction of the literature is performed for each one. In this introduction the relevant works in literature related, not only to modelling, but also to experimental tests and experimental validation are mentioned. Afterwards, the thesis continues with the description of the models which are found most interesting or are used during the development of the final models applied and programmed to solve the combustion problems of interest.

In addition, there is a chapter dedicated to describe the numerical methods which are used to solve the already mentioned system of equations of the models.

Afterwards, a complete chapter is dedicated to the combustion modelling and the presentation and discussion of the results. The chapter will be divided in three sections, one for each propellant, as it was done in the previous chapter. Each section itself is divided on the one hand, in a subsection to describe the physical model, where system of equations and source terms are explained. On the second hand, the results will be presented and the consequent discussion about them is performed. To close, the conclusions obtained for each propellant are summarised in its specific subsection.

The final chapter is dedicated to explain the main conclusions obtained in this thesis for each one of the propellant analysed, the different test used as well as the conclusion obtained by comparing the results with experimental ones.

Finally, future work, nomenclature, appendixes and bibliography can be found.

Chapter 2

State of the art

Throughout this chapter, a state of the art of the literature related to the combustion of solid propellant will be presented. Firstly, the classical models to characterise transient combustion of solid propellants will be summarised briefly. Afterwards, more specific models used in this theses for the study of granulated high energetic propellants, AP-HTPB composite propellants and double-base propellants will be described.

2.1 Classical models to characterise transient combustion of solid propellants

Throughout this section several classical models of transient combustion used to model solid propellant are presented.

Kuo et al. [9] mentioned that when a propellant is burned rapidly under strong non-steady variations of the pressure, the results can differ significantly from the results obtained on stationary burning. As a result, when considering non-steady conditions, the instant value of the pressure inside the combustion chamber is not enough to determine the burning velocity of a solid propellant. Therefore, the mathematical formulation consists in a set of partial differential equations with non stationary terms for solid and gas phase. According to Kuo et al. [9] the unsteady solid equation of energy has a different approach depending on the author considered however, a general expression can be formulated,

$$\frac{\partial T}{\partial t} + r_b \frac{\partial T}{\partial x} - \alpha_c \frac{\partial^2 T}{\partial x^2} = \frac{\dot{Q}}{\rho_c C_c} + \frac{\dot{Q}_{rad}}{\rho_c C_c} \tag{2.1}$$

where the last term corresponds to radiation heat which is usually neglected in the majority of the studies referred in the revision of Kuo et al. [9]. To solve this equation, initial and boundary conditions depending on the problem will be needed. To set boundary conditions, it will be necessary to understand the physics of the burning process at the interface between solid and gas phase which can be seen in Figures and (Fig. 3 and Fig. 4 from [9]). The boundary conditions at the burning surface are the mass flux, energy and species continuity.

Gas phase system of equations consists, according to Kuo et al. [9] in a set of equations formed by continuity, energy and species mass fraction governing equations which can be written as,

$$\frac{\partial (\alpha \rho_g)}{\partial t} + \overrightarrow{\nabla} \cdot (\alpha \rho_g \overrightarrow{u}_g) = 0 \tag{2.2}$$

$$\rho_g \frac{\partial h}{\partial t} + \rho_g \overrightarrow{u}_g \frac{\partial h}{\partial x} - \frac{\partial p}{\partial t} = \frac{\partial}{\partial x}\left(\lambda_g \frac{\partial T}{\partial x}\right) + \frac{\partial}{\partial x}\left(\rho_g \sum_{i=1}^{N} h_i D_i \frac{\partial Y_i}{\partial x}\right) \tag{2.3}$$

$$\rho_g \frac{\partial Y_i}{\partial t} + \rho_g \overrightarrow{u}_g \frac{\partial Y_i}{\partial x} - \frac{\partial}{\partial x}\left(\rho_g D_i \frac{\partial Y_i}{\partial x}\right) = \dot{\omega}_i \tag{2.4}$$

where i = 1, 2, 3..., N state for N different species.

The system is formed by equations which are coupled between them. In addition, gas phase equations are liked to solid phase equation due to the balance at the interface. Therefore, as happened for solid phase, boundary and initial conditions are needed.

In order to simplify the problem, Kuo et al. [9] described several models which can be classified into two main groups: quasi-steady flame models and unsteady flame models. quasi-steady flame models, which are considered the easiest to be applied, are divided into three different approaches will will be detailed hereafter.

2.1.1 dp/dt approach

In this model (Kuo et al. [9]), the transient term of temperature variation is decomposed as a function of the pressure as,

$$\frac{\partial T}{\partial t} = \frac{\partial T}{\partial p}\frac{dp}{dt} \tag{2.5}$$

The temperature is defined as a pressure series in the following way,

$$T(p,x) = T_0(p,x)|_{p=p_0} + p' \left.\frac{\partial T}{\partial p}\right|_{p=p_0} + \frac{p'^2}{2!}\left.\frac{\partial^2 T}{\partial p^2}\right|_{p=p_0} + ... \tag{2.6}$$

and the burning rate as,

$$r_b(p,x) = r_0 + p'\left(\frac{\partial r_b}{\partial p}\right)_{p=p_0} + \frac{p'^2}{2!}\left(\frac{\partial^2 r_b}{\partial p^2}\right)_{p=p_0} + ... \tag{2.7}$$

By substituting equations (2.5-2.7) into (2.1) the expression obtained is,

$$\left(\frac{\partial T_0}{\partial p}\right)_{p=p_0}\frac{\partial p}{\partial t} + r_b\left(\frac{\partial T_0}{\partial x}\right)_{p=p_0} + r_0\frac{p'}{2}\left(\frac{\partial}{\partial x}\left(\frac{\partial T}{\partial p}\right)\right)_{p=p_0} = \alpha_c \frac{\partial^2}{\partial x^2}\left(T_0 + p'\frac{\partial T}{\partial p}\right)_{p=p_0} \tag{2.8}$$

According to [10], the equation form of the non-steady burning rate can be described as,

$$r = r_0\left[1 + \psi\left(\frac{n}{p}\frac{\alpha}{r_0^2}\right)\frac{dp}{dt}\right] \tag{2.9}$$

where $r_0 = ap^n$ is the steady burning rate expression, n is the exponent of the steady burning rate expression, α is the solid phase thermal diffusivity and ψ is the dynamic burning rate coefficient,

$$\psi = \frac{\left[1 - \frac{(p/p_0)^{n/m}}{m}\right]}{\left[\left(\frac{p}{p_0}\right)^{n/m}\left(2 + \frac{1}{m}\right) - 2H\right]} \tag{2.10}$$

where m is the power of propellant pyrolysis, H is the dimensionless magnitude of surface heat due to propellant decomposition, and p/p_0 is the dimensionless pressure.

The main advantage of these models is the obtainment of a closed solution for the burning rate with the instantaneous pressure, pressurisation rate and propellant properties.

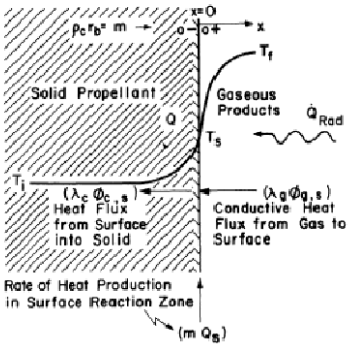

Figure 2.1: One-dimensional temperature profile in burning of solid propellant [9].

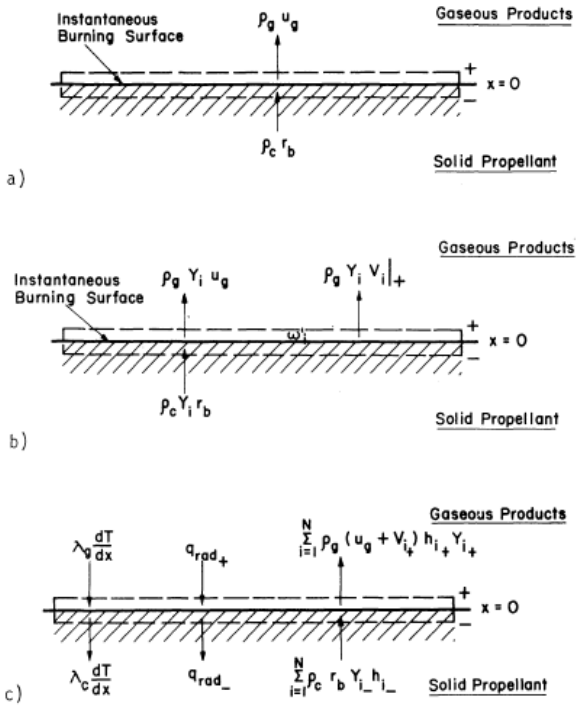

Figure 2.2: Balance of mass, energy and species at interface [9].

2.1.2 Flame description approach

In this case, the solid phase equation is identical to that already described. Regarding the gas phase, the first approximation is to model the gas phase with a quasi-steady stationary approximation so the time derivative terms in the system of equations (2.2)-(2.4) can be deleted (Kuo and Summerfield[9]). Besides that, several assumptions were made such as constant gas density, same value of specific heat and mass diffusivity for all species and validity of Fick's law of diffusion. Moreover, gas phase reactions were assumed to be represented as one step reactions. Under all these conditions, the following is expression is obtained for the gas energy governing equation [9],

$$\lambda_g \frac{\partial T}{\partial x}\bigg|_{x=0} = Q_f \int_0^\infty e\left[\frac{\rho_c r_b C_g x}{\lambda_g}\right] \rho_g \dot{\varepsilon} dx \tag{2.11}$$

where $\dot{\varepsilon}$ is the generation product species and Q_f is the heat generation term.

The definition of the generation product species as a value uniformly distributed in the reaction zone is done by Krier et al. [11] as,

$$\rho_g \dot{\varepsilon} = \overline{\omega} \qquad for \qquad x_i < x \leq x_f \tag{2.12}$$

In this work, Krier et al. [11] presented the KTSS (Krier, T'ien, Sirignano, Summerfield), in which equation (2.11) can be expressed as,

$$\lambda_g \frac{\partial T}{\partial x}\bigg|_{x=0} = -\frac{\lambda_g \overline{\omega} Q_f}{\rho_c r_b C_g} e^{-\frac{\rho_c r_b C_g}{\lambda_g}(x_f - x_i)} \tag{2.13}$$

where $\overline{\omega}$ is the average value of the dimensionless frequency and x_i is initial coordinate and x_f is flame coordinate.

According to Krier et al. [11], since in the propellant pyrolysis the temperature is the main parameter of the sublimation process, the pyrolysis law can be written as,

$$r = b\left(T_s - T_\infty\right)^m \tag{2.14}$$

where T_s is the surface temperature, T_∞ is the temperature far from the burning surface and m and b are the exponent and the burning rate constant respectively in the pyrolysis law.

2.1.3 Zeldovich approach

Flame description approach, as explained by Kuo and Summerfield [9] needs from the knowledge of spatial distribution of the heat release. To solve this problem Zeldovich developed a method by considering steady-state data of burning rate, surface temperature, pressure and propellant temperature in order to get the following expression for the gas phase energy balance

$$\dot{m} h_{c,s}(T_s) = \dot{m} h_{g,f}(T_f, p) + \lambda_c \phi_{c,s} \tag{2.15}$$

where $\dot{m}$ is the mass burning rate in the gas phase, and $\phi_{c,s}$ is the temperature gradient in the solid phase. The energy balance is represented in Figure (2.3).

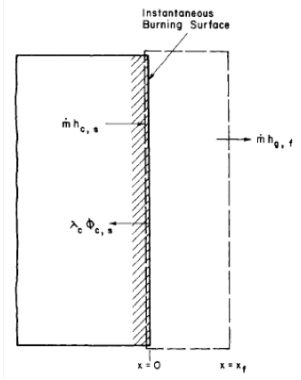

Figure 2.3: Balance of mass, energy and species at interface [9].

2.2 Multidimensional models to characterise combustion of granulated propellants

The theoretical modelling of this problem has focused the interests of many researches in the last decades and different approaches can be found in the literature.

Some of the first researchers on facing the theoretical modelling of this kind of problem were Kuo et al. [12] who developed in their work a fixed-bed model, usually referred as KVS (Kuo, Vichenevetsky, Summerfield) model, to describe the transient problem of flame propagation in a packed fixed-bed of granular propellants. In this case they used a combination of explicit finite difference scheme and the method of characteristics to numerically solve the problems. Koo and Kuo [13] compared the model predictions with experimental firing tests with satisfactory results.

On the other hand, Markatos [14] proposed a different approach based on the previous work of Spalding [15]. In this case, the description of the problem considers the governing equations on the basis that mass, momentum and energy fluxes are balanced over control volumes occupied by space-sharing interspersed continua. According to that concept, distinct phases are present within the same space, their shares of space being measured by their "volume fractions". The approach was used to simulate the accelerating flame front for beds of granulated solid propellants fixed in a rigid enclosure with satisfactory results [14].

Another type of approach is that developed by Gough [16] and adopted by Oton-Martinez et al. [17] among many others which is based on the formal averaging of the solid propellant and the surrounding gas in the spatial domain considered. This approach relies on the conservation equations of the solid and gas phases. In this case, the phases are considered to be a homogeneous continuum. This means that, both, the gas and the propellant grains, are defined to have a uniform value of density and porosity within each fundamental volume cell. Thus, the heterogeneous flow composed of two interacting continua can be described by appropriately defined averages of flow properties.

Regarding the experimental data to feed numerical models, Sandusky [18] provided constitutive relations of compaction obtained from quasi-static compaction experiments with bed diameters approaching that of gun breeches were performed on five cannon propellants. The granular materials tested were single-base, double-base, triple-base propellant as well as nitramine-composite propellant. They found that the dominant compaction mechanism was plastic deformation with the virtual absence of fracture. Kooker et al. [19] experimentally studied the convective ignition process of granular solid propellant bed with the help of an previously built apparatus that apparatus that transform a confined bed to a planar hot gas ignition wave. The investigation examined convective ignition behaviour of five different granular solid propellants with the same flow conditions: single-base, double-base, triple-base and nitramine composites.

To mathematically model the problem of combustion of granulated propellant, four different models may be found in the existing literature: statistics, continuous, average models and finally two-phase fluid dynamics. The first kind of models are not considered in this thesis. The second and the third kind, which are used in some of the works from Krier and Gough, will be detailed at the beginning of the following section. Finally, the fourth ones, used by Kuo, Butler and Powers among others, will be also reviewed. Due to the amount of expressions found in literature, a brief summary will be done. This summary will be useful in Chapter 4 where a sensitivity analysis is presented in order to determine which source terms are more suitable to be used.

Finally, the same summary will be done for the initiation condition due to the variety of them among the literature. The results of this sensitivity analysis will be presented in Chapter 4 too.

2.2.1 Model comparison

2.2.1.1 Kuo et al., 1973

This model [12] is used to characterise an adiabatic combustion chamber in which convective combustion of a granulated an spherical propellant is performed. One-dimensional flux and null velocity

of the propellant are assumed.

The system of partial differential equations is formed by mass, momentum and energy conservation equations for gas phase. To these three equations, ideal gas law and several source terms are added in order to solve the system.

$$\frac{\partial(\alpha\rho_g)}{\partial t} + \frac{\partial}{\partial x}(\alpha\rho_g u_g) = \Gamma_c \tag{2.16}$$

$$\frac{\partial(\alpha\rho_g u_g)}{\partial t} + \frac{\partial}{\partial x}\left(\alpha\rho_g u_g^2\right) = \alpha\frac{\partial p_g}{\partial x} + \frac{\partial}{\partial x}\left(\frac{4}{3}\mu\alpha\frac{\partial u_g}{\partial x}\right) - F_D\frac{3(1-\alpha)}{r_p} - \frac{P_w\tau_w}{A} \tag{2.17}$$

$$\frac{\partial(\alpha\rho_g E_g)}{\partial t} + \frac{\partial}{\partial x}(\alpha\rho_g E_g u_g) = - \frac{\partial}{\partial x}(p_g\alpha u_g) + \frac{\partial}{\partial x}\left(k\alpha\frac{\partial T}{\partial x}\right) - \frac{2q_t}{r_t} + \frac{3(1-\alpha)}{r_p}\left[\rho_p\dot{r}h_f - h_c(T_g - T_p)\right] \tag{2.18}$$

where P_w is wetted perimeter and τ_w is the shear stress on the tube wall, which will be neglected. The mass transfer Γ_c is defined as,

$$\Gamma_c = \frac{3(1-\alpha)}{r_p}\dot{r}\rho_p \tag{2.19}$$

where $\dot{r}$is the combustion law,

$$\dot{r} = ap_g^n \tag{2.20}$$

The drag force F_D for a non-fluidized bed of spheres as,

$$F_D = \frac{\rho_g u_g |u_g|}{6\alpha}\left\{\frac{150(1-\alpha)}{Re_p} + 1.75\right\} \tag{2.21}$$

where Re_p is the Reynolds number based on particle diameter. Finally, the heat transfer correlation h_c is expressed as,

$$h_c = 0.65\frac{k_g}{r_p}\left(\frac{\alpha\rho_g |u_g| r_p}{\mu_g}\right)^{0.7} Pr^{0.33} \tag{2.22}$$

To solve the problem, Kuo et al. [12] assumed neglected the heat loss to the tube wall, the friction force between the gas and the tube wall, the work of viscous stress from the velocity gradient, dissipative heat, molecular heat conduction from gas to gas, imperfection of gas equation of state, dependence of the temperature from the specific heat, dynamic burning effect and erosive burning effect.

2.2.1.2 Kuo and Summerfield, 1974

The model of Kuo and Summerfield [20] is very similar to Kuo et al. [12], being the main difference is the the mathematical formulation of the equation system being,

$$\frac{\partial(\alpha\rho_g)}{\partial t} + \frac{\partial}{\partial x}(\alpha\rho_g u_g) = \Gamma_c \tag{2.23}$$

$$\frac{\partial(\alpha\rho_g u_g)}{\partial t} + \frac{\partial}{\partial x}\left(\alpha\rho_g u_g^2\right) = \alpha\frac{\partial p_g}{\partial x} + \frac{\partial}{\partial x}(\alpha\tau_{xx}) - F_D A_s \tag{2.24}$$

$$\frac{\partial\left(\alpha\rho_g E_g\right)}{\partial t}+\frac{\partial}{\partial x}\left(\alpha\rho_g E_g u_g\right)= \\ -\frac{\partial}{\partial x}\left(p_g\alpha u_g\right)+\frac{\partial}{\partial x}\left(\alpha\tau_{xx}u_g\right)+\frac{\partial}{\partial x}\left(k\alpha\frac{\partial T}{\partial x}\right)+A_s\left[\rho_p\dot{r}h_f-h_c\left(T_g-T_{ps}\right)\right] \quad (2.25)$$

where τ_{xx} is the shear stress in the normal direction. The mass transfer Γ_c is defined as,

$$\Gamma_c = A_s\dot{r}\rho_p \quad (2.26)$$

where

$$A_s = \frac{3(1-\alpha)}{r_p} \quad (2.27)$$

and the combustion law is that of equation (2.20). The remaining source terms are considered the same as in Kuo et al. [12].

2.2.1.3 van Tassel and Krier, 1975

This model [21] is based in the previously cited work from Kuo et al. [12]. The technological need of provide results to simulate the combustion of mobile propellants brought the development of this model in which two species, solid and gas are considered,

$$\frac{\partial\left(\alpha\rho_g\right)}{\partial t}+\frac{\partial}{\partial x}\left(\alpha\rho_g u_g\right)=\Gamma_g \quad (2.28)$$

$$\alpha\rho_g\left[\frac{\partial u_g}{\partial t}+u_g\frac{\partial u_g}{\partial x}\right]=-\frac{\partial\left(\alpha p_g\right)}{\partial x}+\frac{\partial}{\partial x}\left(\alpha\rho_g\left(u_g-u_m\right)^2\right)-\Gamma_g\left(u_g-u_m\right)+F_D \quad (2.29)$$

$$\alpha\rho_g\left[\frac{\partial E_g}{\partial t}+u_g\frac{\partial E_g}{\partial x}\right]=\frac{\partial}{\partial x}\left(u_g\left(-\alpha p_g+\alpha\rho_g\left(u_g-u_m\right)^2\right)\right)+\Gamma_g\left(E^g_{chem}-E_g\right) \\ +\frac{\partial}{\partial x}\left(\alpha\rho_g E_g\left(u_g-u_m\right)\right)-\frac{\partial}{\partial x}\left[E_g\left(u_g-u_m\right)\left(-\alpha p_g+\alpha\rho_g\left(u_g-u_m\right)^2\right)\right] \\ +\alpha\frac{Nuk_g}{d_p^2}\left(T_g-T_p\right) \quad (2.30)$$

$$\frac{\partial\left(\left(1-\alpha\right)\rho_p\right)}{\partial t}+\frac{\partial}{\partial x}\left(\left(1-\alpha\right)\rho_g u_p\right)=\Gamma_p \quad (2.31)$$

$$\left(1-\alpha\right)\rho_p\left[\frac{\partial u_p}{\partial t}+u_p\frac{\partial u_p}{\partial x}\right]=\frac{\partial}{\partial x}\left(\left(1-\alpha\right)\rho_p\left(u_p-u_m\right)^2\right)-\Gamma_p\left(u_p-u_m\right)-F_D \quad (2.32)$$

$$\left(1-\alpha\right)\rho_p\left[\frac{\partial E_p}{\partial t}+u_p\frac{\partial E_p}{\partial x}\right]=\frac{\partial}{\partial x}\left(u_p\left(\left(1-\alpha\right)\rho_p\left(u_p-u_m\right)^2\right)\right)+\Gamma_p\left(E^p_{chem}-E_p\right) \\ +\frac{\partial}{\partial x}\left(\left(1-\alpha\right)\rho_p E_p\left(u_p-u_m\right)\right)-\frac{\partial}{\partial x}\left[\left(u_p-u_m\right)\left(\left(1-\alpha\right)\rho_p\left(u_g-u_m\right)^2\right)\right] \\ +\left(1-\alpha\right)\frac{Nuk_g}{d_p^2}\left(T_g-T_p\right) \quad (2.33)$$

where the density and the average velocity are described as,

$$\rho_p\left(1-\alpha\right)u_p+\alpha\rho_g u_g=\rho_m u_m \quad (2.34)$$

$$\rho_p (1-\alpha) + \alpha\rho_g = \rho_m \tag{2.35}$$

and the mass transfer,

$$\Gamma_p = -\Gamma_g \tag{2.36}$$

The total energy is written as,

$$E_g = c_{v_g}(T_g - T_0) + 1/2u_g^2 \tag{2.37}$$

$$E_p = c_{v_p}(T_p - T_0) + 1/2u_p^2 \tag{2.38}$$

where c_v is the specific heat of gas and solid depending on the subscript.

This model assumed that the particles are spheres and there is no mass and heat loss through the tube walls. The burning law has the following form,

$$\dot{r} = b + ap_g^n \tag{2.39}$$

In order to close the equations heat transfer and drag force are needed. Van Tassel and Krier presented in their work a summary of several friction coefficient and Nusselt number correlations. The gas is assumed to be ideal therefore, pressure may be determined by means of,

$$p_g = \rho_g R_g T_g \tag{2.40}$$

This model is afterwards modified by Krier et al. [22] to analyse the flame-spreading and combustion of small solid propellant grains. The problem could be described as the combustion of solid propellant in a cylindrical chamber with the initiator in the end.

2.2.1.4 Kuo et al., 1976

This is a theoretical model [23] which describes the physical phenomenon of two-phase combustion. The system of equation is done, as the previous one for gas and particle phases as,

$$\frac{\partial(\alpha\rho_g)}{\partial t} + \frac{1}{A}\frac{\partial}{\partial x}(A\alpha\rho_g u_g) = A_s\rho_p\dot{r} \tag{2.41}$$

$$\frac{\partial(\alpha\rho_g u_g)}{\partial t} + \frac{1}{A}\frac{\partial}{\partial x}\left(A\alpha\rho_g u_g^2\right) + \frac{g}{A}\frac{\partial(\alpha p_g A)}{\partial x} - \frac{g}{A}\frac{\partial}{\partial x}(A\alpha\tau_{xx}) = - gF_D A_s + A_s\dot{r}\rho_p u_p + \frac{gp_g}{A}\frac{\partial A}{\partial x} \tag{2.42}$$

$$\frac{\partial(\alpha\rho_g E_g)}{\partial t} + \frac{1}{A}\frac{\partial}{\partial x}(A\alpha\rho_g E_g u_g) + \frac{1}{AJ}\frac{\partial}{\partial x}(Ap_g\alpha u_g) = +\frac{1}{A}\frac{\partial}{\partial x}(\alpha\tau_{xx}u_g A) - \frac{1}{A}\frac{\partial}{\partial x}(qA\alpha) + A_s\rho_p\dot{r}\left[h_{chem} + \frac{U_p^2}{2gJ}\right] - A_s h_t(T - T_{ps}) - \frac{A_s u_p F_D}{J} - \frac{p_g}{AJ}\frac{\partial(\alpha A)}{\partial t} - \dot{Q}_w \tag{2.43}$$

$$\frac{\partial((1-\alpha)\rho_p)}{\partial t} + \frac{1}{A}\frac{\partial}{\partial x}((1-\alpha)\rho_g u_p A) = -A_s\rho_p\dot{r} \tag{2.44}$$

$$\frac{\partial\left(\left(1-\alpha\right)\rho_p u_p\right)}{\partial t}+\frac{1}{A}\frac{\partial}{\partial x}\left(A\left(1-\alpha\right)\rho_p u_p^2\right)-\frac{g}{A}\frac{\partial}{\partial x}\left(A\left(1-\alpha\right)\tau_{xx}\right)= \\ -A_s\dot{r}\rho_p u_p+gF_D A_s-g\frac{\tau_{wp}P_{wp}}{Q} \quad (2.45)$$

where A_s is the specific surface of the granular propellant, A is the cross section of the cylindrical combustion chamber, J is the heat to work conversion factor, $h_t$is the total heat transfer coefficient, h_{chem} is the enthalpy of the propellant gas at flame temperature, q is the rate of conduction heat transfer per unit area T_{ps} is the particle surface temperature, $\dot{Q}_w$ is the rate of heat loss to the chamber wall, τ_{wp} is the shear stress between the camber wall and particle phase and P_{wp} is the wetted perimeter between the chamber wall and the particle phase.

For the particle energy governing equation, instead of using the same formulation as for the gas phase, they use the heat transfer equation as,

$$\left(\frac{DT_p}{Dt}\right)_p=\frac{\alpha_p}{r}\frac{\partial^2\left(rT_p\right)}{\partial r^2} \quad (2.46)$$

To solve this system of equation the solid is assumed to be incompressible and the gas is modelled by the equation of Noble-Abel as,

$$p_g=\frac{\rho_g(\gamma_g-1)e_g}{1-\rho_g\eta_g} \quad (2.47)$$

A very interesting difference respect the previous models is the usage of the expression of Lenoir and Robbillard [24] as,

$$\dot{r}=ap_g^n+K_e h_c e^{\left(-\frac{\beta\dot{r}\rho_p}{\rho_g\left|u_g-u_p\right|}\right)} \quad (2.48)$$

where h_c is the heat transfer coefficient, K_e is the erosive burning constant and β is the erosive burning exponent.

To solve the equation system (2.41)-(2.46) heat transfer and drag force expressions are needed and defined as,

$$F_D=\frac{\mu_g\left(u_g-u_p\right)\left(1-\alpha\right)}{12gr_p\alpha}f_{pg} \quad (2.49)$$

where the friction coefficient is calculated as,

$$f_{pg}=\left\{276.23+5.05\left(\frac{Re_p}{1-\alpha}\right)^{0.87}\right\} \\ 1<\frac{Re_p}{1-\alpha}<24000 \quad (2.50)$$

and,

$$h_c=\frac{k_g}{r_p}0.65\left(\frac{\alpha\rho_g\left|u_g-u_p\right|r_p}{\mu_g}\right)^{0.7}Pr^{1/3} \quad (2.51)$$

valid for Reynolds up to 50000 and porosity around 0.37.

2.2.1.5 Beckstead et al., 1977

The mathematical formulation of this model [4] is a system of partial differential equations which characterise the behaviour of a mixture including the effects produced by the combustion of the granulated propellant and the increase of gas pressure. The model is able to reproduce the main variable distributions.

The number of differential equations depends on the spatial dimension considered while modelling. Considering one-dimensional flux, the system could be written as,

$$\frac{\partial(\alpha\rho_g)}{\partial t} + \frac{\partial}{\partial x}(\alpha\rho_g u_g) = \Gamma_g \tag{2.52}$$

$$\frac{\partial(\alpha\rho_g u_g)}{\partial t} + \frac{\partial}{\partial x}\left(\alpha\left(\rho_g u_g^2 + p_g\right)\right) = p_g\frac{\partial\alpha}{\partial x} + \Gamma_g(u_g - u_p) - F_D \tag{2.53}$$

$$\frac{\partial(\alpha\rho_g E_g)}{\partial t} + \frac{\partial}{\partial x}(\alpha u_g(\rho_g E_g + p_g)) = \Gamma_g(E^g_{chem} - E_g) - \dot{Q} \tag{2.54}$$

$$\frac{\partial((1-\alpha)\rho_p)}{\partial t} + \frac{\partial}{\partial x}((1-\alpha)\rho_g u_p) = \Gamma_p \tag{2.55}$$

$$\frac{\partial((1-\alpha)\rho_p u_p)}{\partial t} + \frac{\partial}{\partial x}\left((1-\alpha)\rho_p u_p^2\right) = +F_D \tag{2.56}$$

$$\frac{\partial((1-\alpha)\rho_p E_p)}{\partial t} + \frac{\partial}{\partial x}((1-\alpha)u_p\rho_p E_p) = \Gamma_p(E^p_{chem} - E_p) + \dot{Q} \tag{2.57}$$

where the mass transfer of gas and solid phases is,

$$\Gamma_p = -\Gamma_g \tag{2.58}$$

and it is calculated as equation (2.19). The solid is assumed to be incompressible and the gas is model by the equation of Noble-Abel (equation (2.47)). Burning rate expression used by the authors is the already mentioned equation (2.20). heat transfer and drag force are calculated as,

$$h_c = \frac{k_g}{d_p}Nu \tag{2.59}$$

$$F_D = \frac{\mu_g(u_g - u_p)}{d_p^2}f_{fg} \tag{2.60}$$

where the Nusselt number and the friction coefficient are defined with Denton [25] and Ergun [26] correlations respectively as,

$$Nu = 0.58Re_p^{0.7}Pr^{0.33} \tag{2.61}$$

$$f_{pg} = \frac{(1-\alpha)^2}{\alpha^2}\left\{150 + 1.75\frac{Re_p}{1-\alpha}\right\} \tag{2.62}$$

Finally, to solve the problem, Beckstead et al. [4] considered that the control volume has a small portion already initiated, which means that it has high pressure and temperature.

2.2.1.6 Krier and Gokhale, 1978

Krier and Gokhale [7] based its study in the development of a model which solves the problem of a closed chamber in which part of the propellant is ignited. The problem is considered one-dimensional and the system of equation is formed by 6 partial differential equations similar to that of van Tassel and Krier [21],

$$\frac{\partial(\alpha\rho_g)}{\partial t} + \frac{\partial}{\partial x}(\alpha\rho_g u_g) = \Gamma_g \tag{2.63}$$

$$\alpha\rho_g\left[\frac{\partial u_g}{\partial t} + u_g\frac{\partial u_g}{\partial x}\right] = -\frac{\partial(\alpha p_g)}{\partial x} + \frac{\partial}{\partial x}\left(\alpha\rho_g(u_g - u_m)^2\right) - \Gamma_g(u_g - u_m) - F_D \tag{2.64}$$

$$\alpha\rho_g\left[\frac{\partial e_g}{\partial t}+u_g\frac{\partial e_g}{\partial x}\right]=-\frac{\partial}{\partial x}\left(u_g\alpha p_g\right)+\Gamma_g\left(e_g-e^g_{chem}\right)+\frac{\partial}{\partial x}\left(\alpha\rho_g e_g\left(u_g-u_m\right)\right)-\frac{3(1-\alpha)}{r_p c_v}h\left(e_g-\gamma e_p\right) \quad (2.65)$$

$$\frac{\partial\left(\left(1-\alpha\right)\rho_p\right)}{\partial t}+\frac{\partial}{\partial x}\left(\left(1-\alpha\right)\rho_g u_p\right)=\Gamma_p \quad (2.66)$$

$$\left(1-\alpha\right)\rho_p\left[\frac{\partial u_p}{\partial t}+u_p\frac{\partial u_p}{\partial x}\right]=-\frac{\partial\left(\left(1-\alpha\right)\tau_p\right)}{\partial x}+\frac{\partial}{\partial x}\left(\left(1-\alpha\right)\rho_p\left(u_p-u_m\right)^2\right)+\Gamma\left(u_p-u_m\right)+F_D \quad (2.67)$$

$$\left(1-\alpha\right)\rho_p\left[\frac{\partial e_p}{\partial t}+u_p\frac{\partial e_p}{\partial x}\right]=\frac{\partial}{\partial x}\left(u_m\left(1-\alpha\right)\tau_p\right)-\Gamma_g\left(e^p_{chem}-e_p\right)+\frac{\partial}{\partial x}\left(\left(1-\alpha\right)\rho_p e_p\left(u_p-u_m\right)\right)+\frac{3(1-\alpha)}{r_p C_{v_g}}h\left(e_g-\gamma e_p\right) \quad (2.68)$$

where the mass transfer Γ_g has the expression of equation (2.19), γ is the relation of specific heats, and $e_g=C_{v_g}T_g$.

In this case, the relation used for the burning rate is similar to (2.39) and can be written as,

$$\dot{r}=\left(a+bT_p\right)p_g^n \quad (2.69)$$

where a, b and $n$are assumed constants. Gas pressure is obtained with the gas phase state equation where simple Noble-Abel (2.47) is used.

The term related to the particle stress is introduced in this model and defined as,

$$\tau_p=p_g+p_s \quad (2.70)$$

where p_s is defined by the following empirical equation,

$$\left(1-\alpha\right)\frac{\partial p_s}{\partial x}=mB'(1-\alpha)^m\frac{\partial(1-\alpha)}{\partial x} \quad (2.71)$$

where m and B are empirical coefficients.

The expressions used in this case for the heat transfer and drag force are the same ones used by Beckstead et al. [4].

2.2.1.7 Gough, 1979

This model [16] considered both gas and particle phases and is mathematically expressed as a system of partial differential equations. The model is capable of reproduce the distribution of the main variables of interest along the control volume.

$$\frac{\partial\left(\alpha\rho_g\right)}{\partial t}+\overrightarrow{\nabla}\cdot\left(\alpha\rho_g\overrightarrow{u}_g\right)=\Gamma_c+\Gamma_{ign} \quad (2.72)$$

$$\frac{\partial\left(\alpha\rho_g\overrightarrow{u}_g\right)}{\partial t}+\overrightarrow{\nabla}\cdot\left(\alpha\rho_g\overrightarrow{u}_g\otimes\overrightarrow{u}_g+\alpha p\overrightarrow{I}\right)+p_g\overrightarrow{\nabla}\left(1-\alpha\right)=\Gamma_{ign}\overrightarrow{u}_{ign}+\Gamma_c\overrightarrow{u}_p-\overrightarrow{F}_D \quad (2.73)$$

$$\frac{\partial\left(\alpha\rho_g E_g\right)}{\partial t}+\overrightarrow{\nabla}\cdot\left(\alpha\rho_g\overrightarrow{u}_g\left(E_g+\frac{p}{\rho_g}\right)\right)+p_g\overrightarrow{\nabla}\left[\left(1-\alpha\right)\overrightarrow{u}_p\right]= \Gamma_c\left(Q_{ex}+\frac{p_g}{\rho_p}+\frac{\left|\overrightarrow{u}_p\right|^2}{2}\right)-\overrightarrow{u}_p\overrightarrow{F}_D-Q_{ign}\Gamma_{ign} \quad (2.74)$$

$$\frac{\partial\left(\left(1-\alpha\right)\rho_p\right)}{\partial t}+\overrightarrow{\nabla}\cdot\left(\left(1-\alpha\right)\rho_p\overrightarrow{u}_p\right)=-\Gamma_c \quad (2.75)$$

$$\frac{\partial\left(\left(1-\alpha\right)\rho_p\overrightarrow{u}_p\right)}{\partial t}+\overrightarrow{\nabla}\cdot\left(\left(1-\alpha\right)\rho_p\overrightarrow{u}_p\otimes\overrightarrow{u}_p+\left(1-\alpha\right)p_p\overrightarrow{I}\right)-p_g\overrightarrow{\nabla}\left(1-\alpha\right)=-\Gamma_c\overrightarrow{u}_p+\overrightarrow{F}_D \quad (2.76)$$

$$\frac{\partial H_s}{\partial t}+\overrightarrow{u}_p\cdot\overrightarrow{\nabla}\cdot\left(H_s\right)=\kappa\dot{q}_t \quad (2.77)$$

$$\frac{\partial d_q}{\partial t}+\overrightarrow{u}_p\cdot\overrightarrow{\nabla}\cdot\left(d_q\right)=\dot{r} \quad (2.78)$$

where κ is the thermal diffusivity of the solid phase, $\dot{q}_t$ is the interfacial heat flux, Q_{ex} is the combustion heat, Γ_{ign} , Q_{ign}, $\overrightarrow{u}_{ign}$, mass transfer, heat and velocity of ignition respectively, d_p is the average distance of all propellant grains which is burned due to combustion and h_s is specific enthalphy of the propellant grains and it is defined as,

$$h_s=c_{v,p}T_p \quad (2.79)$$

being $c_{v,p}$ is the specific heat at constant volume for the solid phase.

Energy for gas and solid phase follow equations (2.37) and (2.38). Equations (2.20) and (2.47) are used for the evaluation of the burning rate and the characterisation of the thermodynamic state of the gas phase.

2.2.1.8 Krier and Kezerle, 1979

In this model, Krier and Kezerle [27] modify the work done by Kier and Gokhale [7] and consider the problem as separated two-phase flow. The problem represents the combustion of a propellant inside a close chamber initiated in one end.

In order to solve the system of equations, the following assumptions are made: incompressible solid, gas obeys gas Noble-Abel state equation with constant co-volume, heat transfer due to radiation and conduction are dismissed, constant specific heats and viscosity and conductivity dependence of temperature.

The system of partial differential equations was written as,

$$\frac{\partial\left(\alpha\rho_g\right)}{\partial t}+\frac{\partial}{\partial x}\left(\alpha\rho_g u_g\right)=\Gamma_g \quad (2.80)$$

$$\alpha\rho_g\left[\frac{\partial u_g}{\partial t}+u_g\frac{\partial u_g}{\partial x}\right]=-\frac{\partial\left(\alpha p_g\right)}{\partial x}-\Gamma_g\left(u_g-u_p\right)-F_D \quad (2.81)$$

$$\alpha\rho_g\left[\frac{\partial E_g}{\partial t}+u_g\frac{\partial E_g}{\partial x}\right]=-\frac{\partial}{\partial x}\left(u_g\alpha p_g\right)-\Gamma_g\left(E_g-E_g^{chem}\right)+\Gamma_g\left(\frac{u_g^2}{2}+\frac{u_p^2}{2}-u_g u_p\right)+F_D\left(u_g-u_p\right)-\Phi \quad (2.82)$$

$$\frac{\partial\left(\left(1-\alpha\right)\rho_p\right)}{\partial t}+\frac{\partial}{\partial x}\left(\left(1-\alpha\right)\rho_g u_p\right)=-\Gamma_g \quad (2.83)$$

$$(1-\alpha)\,\rho_p\left[\frac{\partial u_p}{\partial t}+u_p\frac{\partial u_p}{\partial x}\right]=-\frac{\partial\left((1-\alpha)\,\tau_p\right)}{\partial x}+F_D \tag{2.84}$$

$$(1-\alpha)\,\rho_p\left[\frac{\partial E_p}{\partial t}+u_p\frac{\partial E_p}{\partial x}\right]=u_p\,(1-\alpha)\,\frac{\partial \tau_p}{\partial x}+\Gamma_g\left(E_p+E_p^{chem}\right)+\Phi \tag{2.85}$$

where $E_g = C_{v_g}T_g$ and $E_p = C_{v_p}T_p$. τ_p is defined as the resistance that the solid does to avoid compaction and it has the following form,

$$\tau_p=\frac{K}{(1-\alpha)}\left(\frac{1}{(1-\alpha_c)}-\frac{1}{(1-\alpha)}\right) \tag{2.86}$$

where K is the bulk modulus for the propellant.

Φ is the interface heat transfer defined as,

$$\Phi=\frac{6(1-\alpha)}{d_p}h_c(T_g-T_p) \tag{2.87}$$

where $h_c=\frac{k_g}{d_p}Nu$ is the heat transfer coefficient and Nusselt is calculated according to Denton [25] equation (2.61).

Drag force F_D is calculated as,

$$F_D=\frac{\mu_g\,(u_g-u_p)}{d_p^2}\frac{(1-\alpha)^2}{\alpha^2}f_{fg} \tag{2.88}$$

where f_{fg} is the friction coefficient calculated with Ergun [26] expression (2.62) and Reynolds number is calculated as,

$$Re_p=\frac{d_p\alpha\rho_g\,|u_g-u_p|}{\mu_g} \tag{2.89}$$

To finalise with the source terms used by Krier and Kezerle mass transfer expression needs to be detailed. In this case, equation (2.19) is used and the burning rate is defined as,

$$\dot{r}=b\left(\frac{T_p}{T_{p0}}\right)^m\left(\frac{p_g}{p_0}\right)^n \tag{2.90}$$

where m, n and b are assumed known constants and T_{p0} and p_0 are initial temperature of the solid phase and pressure respectively.

2.2.1.9 Hoffman and Krier, 1980-1981

The model used by Hoffman and Krier in their works from 1980 and 1981 [28, 29] is very similar to that of Krier and Kezerle [27] but with some differences that will be explained afterwards. The system is formed by a set of partial differential equations, three for the gas phase and another 3 for the solid phase as,

$$\frac{\partial\,(\alpha\rho_g)}{\partial t}+\frac{\partial}{\partial x}\,(\alpha\rho_g u_g)=\Gamma \tag{2.91}$$

$$\frac{\partial\,(\alpha\rho_g u_g)}{\partial t}+\frac{\partial}{\partial x}\left(\alpha\rho_g u_g^2\right)=-\alpha\frac{\partial p_g}{\partial x}+\Gamma u_p-F_D \tag{2.92}$$

$$\frac{\partial\,(\alpha\rho_g E_g)}{\partial t}+\frac{\partial}{\partial x}\,(\alpha u_g\,(\rho_g E_g+p_g))=\Gamma\left(E_g^{chem}+\frac{u_p^2}{2}\right)-F_D u_p-\dot{Q} \tag{2.93}$$

$$\frac{\partial\,((1-\alpha)\,\rho_p)}{\partial t}+\frac{\partial}{\partial x}\,((1-\alpha)\,\rho_p u_p)=-\Gamma \tag{2.94}$$

$$\frac{\partial\left(\left(1-\alpha\right)\rho_p u_p\right)}{\partial t}+\frac{\partial}{\partial x}\left(\left(1-\alpha\right)\rho_p u_p^2\right)=-\left(1-\alpha\right)\frac{\partial p_p}{\partial x}-\Gamma u_p+F_D \tag{2.95}$$

$$\frac{\partial\left(\left(1-\alpha\right)\rho_p E_p\right)}{\partial t}+\frac{\partial}{\partial x}\left(\left(1-\alpha\right)u_p\left(\rho_p E_p+p_p\right)\right)=\Gamma\left(E_p^{chem}-\frac{u_p^2}{2}\right)+F_D u_p+\dot{Q} \tag{2.96}$$

where gas and solid energies are defined with equations (2.37) and (2.38). Noble-Abel equation of state for gas is assumed and p_p is defined as the particle-particle stress as,

$$p_p=\begin{cases}\frac{K}{(1-\alpha)}\left(\frac{1}{(1-\alpha_c)}-\frac{1}{(1-\alpha)}\right) & \alpha\leq\alpha_c\\ 0 & \alpha>\alpha_c\end{cases} \tag{2.97}$$

where α_c is the critical porosity above which the particles do not touch and K is the particle stress proportionality constant. This expression is similar to the one from Krier and Kezerle [27] but considering zero the value of particle stress in case of having porosity values under the critical one.

Remaining source terms are mass transfer, drag and convective heat transfer. Mass transfer has the same expression detailed for previous authors (2.19) but burning rate is defined as,

$$\dot{r}=\left(\frac{T_p}{T_{p0}}\right)^m\left(bp_g\right)^n \tag{2.98}$$

Drag force is calculated as equation where the friction coefficient has the expression defined by Kuo and Nydegger [30] written as,

$$f_{pg}=\left\{276+5.05\left(\frac{Re_p}{1-\alpha}\right)^{0.87}\right\} \tag{2.99}$$

valid for Reynolds up to 1500. Reynolds is defined with equation (2.89). Gas viscosity is defined in this case as,

$$\mu_g=\mu_{g,0}(T_g/T_{g,0}) \tag{2.100}$$

Finally, heat transfer is calculated as in equation (2.87) where Nusselt is calculated as,

$$Nu=0.65Re_p^{0.65}Pr^{0.33} \tag{2.101}$$

One interesting aspect of the work provided by Hoffman and Krier [28], which is not considered by other authors, is the problem of reaching a porosity under the minimum physical values. In their work, Hoffman and Krier [28] remarked that the set of equations (2.91) - (2.96) does not prevent compaction below the minimum porosity that for spheric particles is calculated to $\alpha_{min}=0.2595$ (see Annex of their work). The approach used to solve this issue consisted in introducing a function which depends on the porosity in the momentum equation of the solid phase as follows,

$$\frac{\partial\left(\left(1-\alpha\right)\rho_p\overrightarrow{u}_p\right)}{\partial t}+\frac{\partial}{\partial x}\left(\left(1-\alpha\right)\rho_p u_p^2\right)=-\Gamma u_p+\left(1-f\left(\alpha\right)\right)\left[F_D-\left(1-\alpha\right)\frac{\partial p_g}{\partial x}\right] \tag{2.102}$$

where $f\left(\alpha\right)$ is defined as:

$$f\left(\alpha\right)=\begin{cases}0 & \alpha>\alpha_c\\ \left(\frac{\alpha_c-\alpha}{\alpha_c-\alpha_{min}}\right)^l & \alpha_{min}\leq\alpha\leq\alpha_c\\ 1 & \alpha<\alpha_{min}\end{cases} \tag{2.103}$$

2.2.1.10 Gokhale and Krier, 1982

In their work, Gokhale and Krier [31] presented a model to describe a two-phase flow trough a gas-solid mixture. They presented the set of equations for two cases: one considering the theory of mixtures and other considering the separated flow theory. In addition they presented a formulation for propellant which contain particle of different sizes particles which will not be considered in this work.

The mixture formulation is an hybrid between the work done by Krier and Gokhale [7] in 1978 and the one from Hoffman and Krier [28] from 1980 and can be written as,

$$\frac{\partial\left(\alpha\rho_g\right)}{\partial t}+\frac{\partial}{\partial x}\left(\alpha\rho_g u_g\right)=\Gamma \tag{2.104}$$

$$\frac{\partial\left(\alpha\rho_g u_g\right)}{\partial t}+\frac{\partial}{\partial x}\left(\alpha\rho_g u_g^2\right)=-\frac{\partial\left(\alpha p_g\right)}{\partial x}+\Gamma u_m-F_D+\frac{\partial}{\partial x}\left(\alpha\rho_g\left(u_g-u_m\right)^2\right) \tag{2.105}$$

$$\frac{\partial\left(\alpha\rho_g E_g\right)}{\partial t}+\frac{\partial}{\partial x}\left(\rho_g E_g\alpha u_g\right)=-\frac{\partial}{\partial x}\left(u_m\alpha p_g\right)+\frac{\partial}{\partial x}\left(\alpha\rho_g E_g\left(u_g-u_m\right)\right)+\Gamma E_g^{chem}-F_D u_m-\dot{Q} \tag{2.106}$$

$$\frac{\partial\left(\left(1-\alpha\right)\rho_p\right)}{\partial t}+\frac{\partial}{\partial x}\left(\left(1-\alpha\right)\rho_g u_p\right)=-\Gamma \tag{2.107}$$

$$\frac{\partial\left(\left(1-\alpha\right)\rho_p u_p\right)}{\partial t}+\frac{\partial}{\partial x}\left(\left(1-\alpha\right)\rho_p u_p^2\right)= -\frac{\partial\left(\tau_p\left(1-\alpha\right)\right)}{\partial x}-\Gamma u_m+F_D+\frac{\partial}{\partial x}\left(\left(1-\alpha\right)\rho_p\left(u_p-u_m\right)^2\right) \tag{2.108}$$

$$\frac{\partial\left(\left(1-\alpha\right)\rho_p E_p\right)}{\partial t}+\frac{\partial}{\partial x}\left(\left(1-\alpha\right)u_p\rho_p E_p\right)= -\frac{\partial}{\partial x}\left(u_m\left(1-\alpha\right)\tau_p\right)+\frac{\partial}{\partial x}\left(\left(1-\alpha\right)\rho_p E_p\left(u_p-u_m\right)\right)+\Gamma E_p^{chem}+F_D u_m+\dot{Q} \tag{2.109}$$

where the definition of the average velocity, u_m , is that introduced in equation (2.34).

On the other hand, the theory of the separated flow is represented by the system of partial differential equations (2.91)-(2.109) already used by Hoffman and Krier [28].

Regarding the source terms, Denton [25] equation (2.61) is used for the expression of the Nusselt number and Ergun [26] and Kuo and Nydegger [30] expressions for friction coefficients are used depending on the Reynolds number. In addition, as in the work done by Hoffman and Krier [28], not only Noble-Abel equation of state of gases but also same expression for the particle-particle stressed and mass transfer and are used.

2.2.1.11 Butler and Krier, 1986

The model of Butler and Krier [32] is developed for a packed bed of high energy granulated propellant. The governing equations are based in the ones from Hoffman and Krier [28]. The system is composed by six equations, three for gas and another 3 for solid phase expressed in one-dimensional form as,

$$\frac{\partial\left(\alpha\rho_g\right)}{\partial t}+\frac{\partial}{\partial x}\left(\alpha\rho_g u_g\right)=\Gamma \tag{2.110}$$

$$\frac{\partial\left(\alpha\rho_g u_g\right)}{\partial t}+\frac{\partial}{\partial x}\left(\alpha\rho_g u_g^2+\alpha p_g\right)=\Gamma u_p-F_D \tag{2.111}$$

$$\frac{\partial\left(\alpha\rho_g E_g\right)}{\partial t}+\frac{\partial}{\partial x}\left(\alpha u_g\left(\rho_g E_g+p_g\right)\right)=\Gamma\left(E^{chem}+\frac{u_p^2}{2}\right)-F_D u_p-\dot{Q} \tag{2.112}$$

$$\frac{\partial\left(\left(1-\alpha\right)\rho_p\right)}{\partial t}+\frac{\partial}{\partial x}\left(\left(1-\alpha\right)\rho_p u_p\right)=-\Gamma \tag{2.113}$$

$$\frac{\partial\left(\left(1-\alpha\right)\rho_p u_p\right)}{\partial t}+\frac{\partial}{\partial x}\left(\left(1-\alpha\right)\rho_p u_p^2+\left(1-\alpha\right)p_p\right)=F_D-\Gamma u_p \tag{2.114}$$

$$\frac{\partial\left(\left(1-\alpha\right)\rho_p E_p\right)}{\partial t}+\frac{\partial}{\partial x}\left(\left(1-\alpha\right)u_p\left(\rho_p E_p+p_p\right)\right)=\Gamma\left(-\frac{u_p^2}{2}\right)+F_D u_p+\dot{Q} \tag{2.115}$$

where E^{chem} is defined as,

$$E^{chem}=E_g^{chem}+E_p^{chem} \tag{2.116}$$

Mass transfer source term is expressed with equation (2.19) where the burning rate is given by equation (2.20). Noble-Abel equation of state is used too.

The expression used for the drag force and, as consequence, the friction coefficient are equations (2.88) and (2.99). The heat transfer $\dot{Q}$ is calculated with equation (2.87) and its Nusselt number calculated by means of,

$$Nu=0.65Re_p^{0.65}Pr^{0.33} \tag{2.117}$$

Finally p_p is called the solid phase stressed and it is expressed as a function of the gas pressure and equilibrated stress,

$$p_p=p_g+p^e \tag{2.118}$$

The equilibrated stress is function of the porosity and it has the following expression depending of the phase of compaction $\phi=1/(1-\alpha)$,

$$p^e=\begin{cases}\frac{4G'(\phi_0-\phi)}{3\phi(\phi-1)} & elastic\ phase\ (\phi_0\geq\phi>\phi_1)\\ \frac{2}{3}Y\left\{1-\frac{2G'}{Y\phi}(\phi_0-\phi)+ln\left[\frac{2G'(\phi_0-\phi)}{Y(\phi-1)}\right]\right\} & elastic-plastic\ phase\ (\phi_1\geq\phi>\phi_2)\\ \frac{2}{3}Yln\left(\frac{\phi}{(\phi-1)}\right) & plastic\ phase\ (\phi_2\geq\phi>1.0)\end{cases} \tag{2.119}$$

where $Y$and G' are the yield strength and the shear modulus respectively and their values are found in Table 1 of their work and $\phi_1$and ϕ_2 have the following form,

$$\phi_1=\frac{2G'\phi_0+Y}{2G'+Y} \tag{2.120}$$

$$\phi_2=\frac{2G'\phi_0}{2G'+Y} \tag{2.121}$$

and $\phi_0=(1-\alpha_0)$ where α_0 correspond to initial porosity.

2.2.1.12 Powers dissertation, 1988

In his dissertation, Powers [33] developed a model to predict the behaviour of combustion waves in a mixture of gas and reactive solid particles. The model considers a two phase flow and it is a modification of the model of Butler and Krier [32] and Baer and Nunziato [34]. The main difference with those is the inclusion of a expression which consider the radius evolution of the particle (equation (2.128)). In order to close the system, a dynamic compaction equation is considered. This equation states that the solid volume fraction changes due to the combustion and due to the difference between solid pressure and the sum of the gas pressure and inter granular stress (equation (2.129)). Therefore, the system of partial differential equations can be written as,

$$\frac{\partial(\alpha\rho_g)}{\partial t}+\frac{\partial}{\partial x}(\alpha\rho_g u_g)=\Gamma \tag{2.122}$$

$$\frac{\partial(\alpha\rho_g u_g)}{\partial t}+\frac{\partial}{\partial x}\left(\alpha\rho_g u_g^2+\alpha p_g\right)=\Gamma u_p-F_D \tag{2.123}$$

$$\frac{\partial(\alpha\rho_g E_g)}{\partial t}+\frac{\partial}{\partial x}(\alpha u_g(\rho_g E_g+p_g))=\Gamma E_p-F_D u_p-\dot{Q} \tag{2.124}$$

$$\frac{\partial((1-\alpha)\rho_p)}{\partial t}+\frac{\partial}{\partial x}((1-\alpha)\rho_p u_p)=-\Gamma \tag{2.125}$$

$$\frac{\partial((1-\alpha)\rho_p u_p)}{\partial t}+\frac{\partial}{\partial x}\left((1-\alpha)\rho_p u_p^2+(1-\alpha)p_p\right)=F_D-\Gamma u_p \tag{2.126}$$

$$\frac{\partial((1-\alpha)\rho_p E_p)}{\partial t}+\frac{\partial}{\partial x}((1-\alpha)u_p(\rho_p E_p+p_p))=-\Gamma E_p+F_D u_p+\dot{Q} \tag{2.127}$$

$$\frac{\partial\left[(1-\alpha)/r^3\right]}{\partial t}+\frac{\partial}{\partial x}\left[(1-\alpha)u_p/r^3\right]=0 \tag{2.128}$$

$$\frac{\partial(1-\alpha)}{\partial t}+u_p\frac{\partial}{\partial x}(1-\alpha)=\frac{(1-\alpha)\alpha}{\mu_c}\left[p_p-p_g-\frac{p_{p0}-p_{g0}}{1-\alpha_0}(1-\alpha)\right]-\frac{3(1-\alpha)\dot{r}}{r} \tag{2.129}$$

where μ_c is the compaction viscosity and r is the solid particle radius. Mass transfer source term is expressed as equation (2.19) where the burning rate is equation (2.20) and Noble-Abel state equation is used for gas phase. Particle stress has the following expression,

$$p_p=(\gamma_p-1)c_{v_p}\rho_p T_p-\frac{\rho_{p0}\sigma}{\gamma_p} \tag{2.130}$$

where γ_p is the Tait equation parameter, the subscript '0' indicates undisturbed conditions and σ is the non-ideal solid parameter.

Mass transfer, drag force and heat transfer expressions are needed to solve the system of equations being,

$$\Gamma=\frac{3(1-\alpha)}{r}ap_g^m\rho_p \tag{2.131}$$

$$F_D=\frac{(1-\alpha)\alpha}{r}(u_g-u_p)\beta \tag{2.132}$$

$$\dot{Q}=\frac{(1-\alpha)\alpha}{r^{1/3}}(T_g-T_p)h \tag{2.133}$$

where a and m are burning constant and burn index respectively. β and h coefficients are defined as positive constants values. Note that in this model, the particle radius does not have a constant

value as it varies while the propellant is burning. In this model, Powers defines the gas and particle total energies with the following expressions,

$$E_g = c_{v_g} T_g + \frac{u_g^2}{2} \tag{2.134}$$

$$E_p = c_{v_p} T_p + \frac{u_p^2}{2} + \frac{\rho_{p0}\sigma}{\gamma_p} + q \tag{2.135}$$

where q is the heat of reaction.

2.2.1.13 Powers et al., 1990

The model presented by Powers et al. [35, 36] is very similar to the previous one from Powers [33] but including some terms in momentum equations of gas and solid as,

$$\frac{\partial(\alpha\rho_g)}{\partial t} + \frac{\partial}{\partial x}(\alpha\rho_g u_g) = \Gamma \tag{2.136}$$

$$\frac{\partial(\alpha\rho_g u_g)}{\partial t} + \frac{\partial}{\partial x}\left(\alpha\rho_g u_g^2 + \alpha p_g\right) = \Gamma u_p - F_D + \delta_a p_g \frac{\partial\alpha}{\partial x} \tag{2.137}$$

$$\frac{\partial(\alpha\rho_g E_g)}{\partial t} + \frac{\partial}{\partial x}(\alpha u_g(\rho_g E_g + p_g)) = \Gamma E_p - F_D u_p - \dot{Q} + \delta_a u_p p_g \frac{\partial\alpha}{\partial x} \tag{2.138}$$

$$\frac{\partial((1-\alpha)\rho_p)}{\partial t} + \frac{\partial}{\partial x}((1-\alpha)\rho_p u_p) = -\Gamma \tag{2.139}$$

$$\frac{\partial((1-\alpha)\rho_p u_p)}{\partial t} + \frac{\partial}{\partial x}\left((1-\alpha)\rho_p u_p^2 + (1-\alpha)p_p\right) = F_D - \Gamma u_p - \delta_a p_g \frac{\partial\alpha}{\partial x} \tag{2.140}$$

$$\begin{aligned}\frac{\partial((1-\alpha)\rho_p E_p)}{\partial t} + \frac{\partial}{\partial x}((1-\alpha)u_p(\rho_p E_p + p_p)) = \\ -\Gamma E_p + F_D u_p + \dot{Q} - \delta_a u_p p_g \frac{\partial\alpha}{\partial x} - \delta_b(p_p - f_p)\left[p_p - f_p - (p_g - f_g)\right]\frac{(1-\alpha)\alpha}{\mu_c}\end{aligned} \tag{2.141}$$

$$\frac{\partial(1-\alpha)}{\partial t} + u_p \frac{\partial}{\partial x}(1-\alpha) = \frac{(1-\alpha)\alpha}{\mu_c}\left[p_p - f_p - (p_g - f_g)\right] - \frac{3(1-\alpha)\dot{r}}{r} \tag{2.142}$$

$$(1-\delta_c)\left[\frac{\partial n}{\partial t} + \frac{\partial}{\partial x}[n u_p]\right] = (1-\delta_c)F(p_g, \rho_g, p_p, \rho_p, (1-\alpha)) \tag{2.143}$$

where $n = \frac{3(1-\alpha)}{4\pi r^3}$, δ parameter is used to determine if the formulation corresponds to the model of Baer Nunziato [34] or the one from Powers, Stewart and Krier [37]and f_g and f_p are the stress of gas and solid being,

$$f_g = 0 \tag{2.144}$$

$$f_p = \frac{p_{p0} - p_{g0}}{1-\alpha_0}(1-\alpha) \tag{2.145}$$

respectively.

Solid pressure has the same expression as equation (2.130) and gas pressure is modelled by using Noble-Abel equation.

Drag force and heat transfer are defined as,

$$F_D = B(u_g - u_p) \tag{2.146}$$

$$\dot{Q} = C(T_g - T_p) \tag{2.147}$$

where B and C are strictly positives function of the flow variables defined as,

$$B = \frac{(1-\alpha)\alpha}{r}\beta \tag{2.148}$$

$$C = \frac{(1-\alpha)\alpha}{r^{1/3}}h \tag{2.149}$$

Mass transfer was written as,

$$\Gamma = \frac{3(1-\alpha)}{r}ap_g^m\rho_p H(T_p - T_{ign}) \tag{2.150}$$

where $H(T_p - T_{ign})$ is a step function included in the combustion model to prevent combustion until an ignition temperature is reached. Same expressions of gas and solid energy than the ones used by Powers in his dissertation [33] are used in this model.

2.2.2 Summary of convective heat transfer and friction coefficients

When describing the main models used in the literature to simulate the process of combustion of granulated propellants, different correlations of heat transfer and friction coefficient have appeared. In order to know, which one of the coefficients suits better with the model used, in subsection 4.1.3 of Chapter 4, the results of a sensitivity analysis are presented. Therefore, and in order to be able to have a clear reference afterwards, a summary of the expressions found in literature is written throughout this subsection.

Interface convective heat has this expression as general form,

$$\dot{Q} = (1-\alpha)\frac{S_p}{V_p}h_c(T_g - T_p) \tag{2.151}$$

In case of having spherical particles, the diameter of the particles can be defined as,

$$d_p = 6\frac{V_p}{S_p} \tag{2.152}$$

and therefore, the interface convective heat can be written as,

$$\dot{Q} = \frac{6(1-\alpha)}{d_p}h_c(T_g - T_p) \tag{2.153}$$

The convective heat transfer coefficient depends on the Nusselt number in the following manner,

$$h_c = \frac{k_g}{d_p}Nu \tag{2.154}$$

where the Prandtl number can be defined as,

$$Pr = \frac{c_{pg}\mu_g}{k_g} \tag{2.155}$$

and gas conductivity as,

$$k_g = \frac{15R_u}{4M_g}\mu_g\left(\frac{4M_g c_{vg}}{15R_u} + \frac{3}{5}\right) \tag{2.156}$$

The difference between the convective heat transfer expressions found in the literature comes from the definition that each author did of the Nusselt number. In this review, three expression will be considered and analysed calling them Nusselt 1, Nusselt 2 and Nusselt 3 to simplify the reference afterwards. Nusselt 1 is the expression proposed by Gelperin and Einstein [38] for fluidised beds that appeared in the work by van Tassel and Krier [21] and Krier et al. [22] as,

$$Nu = \left(2 + 0.4 Re_p^{2/3} Pr^{1/3}\right) \tag{2.157}$$

The second one (called hereafter Nusselt 2) was used by many authors in the existing literature, among them, Beckstead et al. [4], Krier and Gokhale [7], Krier and Kezerle [27] and Gokhale and Krier [31],

$$Nu = 0.58 Re_p^{0.7} Pr^{0.33} \tag{2.158}$$

To conclude, the last correlation, called from now on Nusselt 3, that used by Hoffman and Krier [28, 29], Butler et al. [39] and Butler and Krier [32],

$$Nu = 0.65 Re_p^{0.65} Pr^{0.33} \tag{2.159}$$

On the other hand, the expression of the drag force considered in the bibliography is the following,

$$F_D = \frac{\mu_g \left(u_g - u_p\right)}{d_p^2} \frac{\left(1-\alpha\right)^2}{\alpha^2} f_{fg} \tag{2.160}$$

where f_{fg} is the friction coefficient. Depending on the author, the expression of the friction coefficient changes its form.

Beckstead et al. [4], Krier and Gokhale [7] and Gough [16] used the following form of the friction coefficient which will be called hereafter "Friction 1",

$$f_{pg} = \left\{150 + 1.75 \frac{Re_p}{1-\alpha}\right\} \tag{2.161}$$

According to Gokhale and Krier [31] this correlation is only valid when Reynolds number has a value below 1500. Therefore, they proposed an alternative expression valid for values of Reynolds number up to 15000 which has been also used by Hoffman and Krier [28, 29] and will be called from now on "Friction 2".

$$f_{pg} = \left\{276 + 5.05 \left(\frac{Re_p}{1-\alpha}\right)^{0.87}\right\} \tag{2.162}$$

To conclude, Butler et al. [39] presented in his work an expression, called hereafter "Friction 3", developed by Wilcox, Jones and Krier [40] which provide them good results for high Reynolds numbers,

$$\begin{gathered} f_{pg} = \left\{150 + 3.89 \left(\frac{Re_p}{1-\alpha}\right)^{0.88}\right\} \\ 10^3 < Re_p < 2 \cdot 10^5 \end{gathered} \tag{2.163}$$

2.2.3 Initiation conditions

After a review of the bibliography, it has been observed that the authors consider that the propellant is already initiated. Each author, consider their own initiation conditions to simulate the combustion process. The ones which have been identified have been summarised in Table 2.1). The influence of the initiation conditions to the final results will be studied through a sensitivity analysis in in subsection 2.2.3 of Chapter 4. The main features of each initiation condition is detailed in the paragraph below.

Beckstead et al. [4] proposed a slope initiation in which the 10% of the tube is considered initiated region. From this length , the temperature and pressure decrease until reaching 1 bar and 295K conditions. Krier and Gokhale [7] however, assumed that the ignited region was 15% of the total length. Krier and Kezerle [27] proposed to have 10% of the domain with high values of pressure and gas temperature and 3% of the domain with particle temperature 100K above the ignition temperature. Hoffman and Krier [28] studied two initiation conditions. On the first hand, one similar to the one of Krier and Kezerle [27] but changing the ignition temperature. On the other hand, they assume an exponential distribution of the gas pressure and a linear distribution of gas and particle temperature during 9% of the domain. Finally, the first initiation of Hoffman and Krier [28] has been reproduced considering the control volume at 1 bar pressure.

The values of pressure, gas and particle temperature for all initiation can be seen in Figure 2.4. To be able to refer to each initiation type easily, each one of them has been named as Test and a number.

Author	$p_g(Pa)$	$T_g(K)$	$T_p(K)$	$T_{ign}(K)$
Beckstead et al. [4]– Test 1	$9.28 \cdot 10^5$	1865	1865	303
Krier and Gokhale [7]– Test 2	10^7	3277.78	$T_{ign} + 100$	310.8
Krier and Kezerle [27] – Test 3	10^7	3277.78	$T_{ign} + 100$	314.0
Hoffman and Krier [28] – Test 4	10^7	3277.78	$T_{ign} + 100$	302.78
Hoffman and Krier [28] – Test 5	10^7	3277.78	$T_{ign} + 100$	302.78
Test 6	10^5	3277.78	$T_{ign} + 100$	302.78

Table 2.1: Pressure, gas and particle temperature and ignition temperature data for the considered initiation.

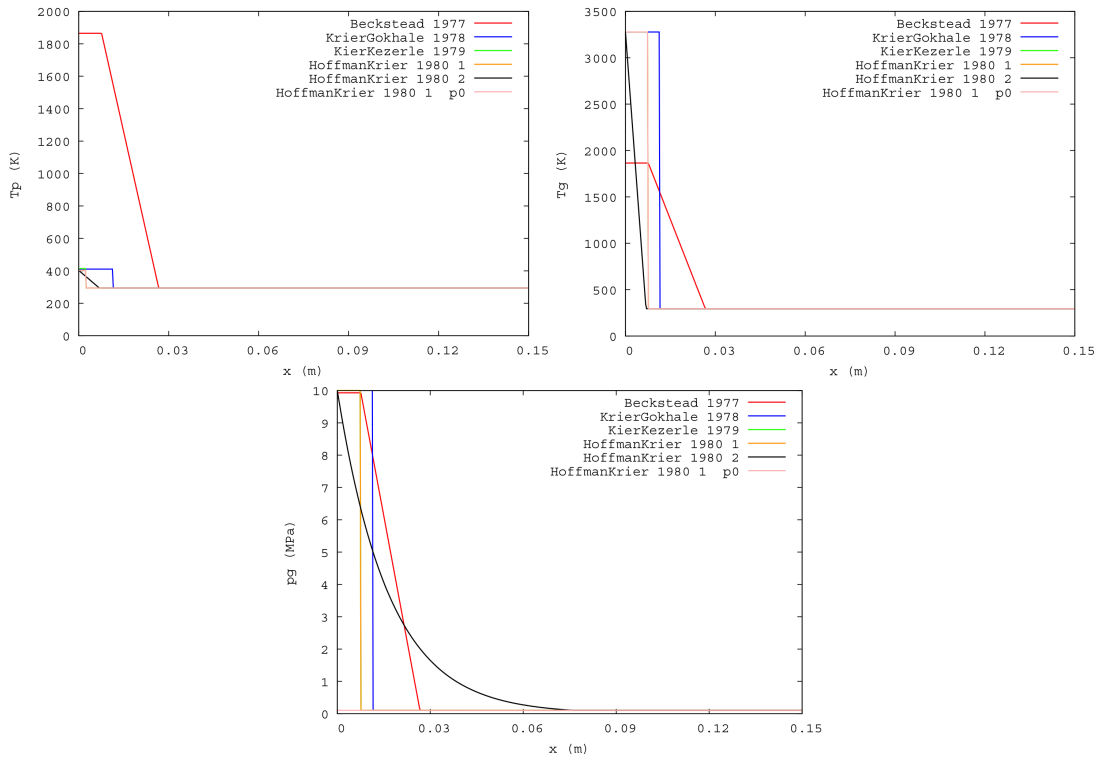

Figure 2.4: Initial conditions initiation of pressure, particle temperature and gas temperature.

2.3 Models to characterise composite propellants combustion

Composite solid propellants are heterogeneous mixtures of crystalline oxidiser and polymer fuel binder with some other additives. Modelling the combustion of composite propellants is a key problem that has focused the interest of several researches in many industrial fields such as chemical engineering, aerospace engineering or safety in industrial processes.

Kuo and Summerfield [9] made a review of some classical models used to characterise the combustion of this type of materials. Among those models, BDP (Beckstead, Derr, Price) model [41] was developed to describe the combustion of ammonium perchlorate (AP)-based composite propellants. It defines three separate flame zones: i) a primary flame consisting in the reactions of of binder and oxidiser decomposition products, ii) a premixed oxidiser flame and iii) a final diffusion flame involving the products of the other two flames. This one-dimensional (1D) model considers simple global chemical kinetics for the reactions of the gas phase whereas the surface decomposition of the propellant ingredients is described by simple Arrhenius expressions. In general terms, the calculated burning rate, surface temperature and temperature sensitivity obtained with this model provides a fair agreement with experimental data. The PEM (petite ensemble model), similar to BDP, is another example of a classical combustion model for composite propellants which considers the existence of different small flames associated with the distribution of particles sizes of AP [9].

In contrast to these classical models, there are currently available other complex models based on detailed chemical kinetics for the combustion of AP-based propellants. For example, in the case of AP composite propellants mixed with hydroxyl-terminated polybutadiene (HTPB) as inert binder, it is noteworthy the detailed combustion mechanism proposed by Jeppson and Beckstead [42]. In that work, the authors presented a full kinetic mechanism based on 72 reactions and 44 species for the gas phase and a semi-global mechanism consisting of 8 steps for condensed phase decomposition. The model accurately describes burn rate versus pressure data for low to moderate pressure ranges.

In addition to the classic and the complex combustion models, there are several alternatives in the literature based on simplified combustion mechanisms with reduced chemistry kinetics. Among them, the works of Guirao and Williams [43], Knott and Brewster [44], Cai et al. [45], Ye et al. [46] and Cao et al. [47] stand out. The work done by Vo et al. [48] needs also to be remarked since they model the problem of combustion of a solid propellant in which the burning surface is moving which will be the case of the present work since the sublimation of solid will lead to a change of the cells from solid to gas phase changing as a results the domains of each two of them.

The model of Guirao and Williams [43] assumes a one-step, second-order gas-phase reaction deduced from a 14-step gas-phase mechanism. A Lewis number of unity is considered in the gas phase. Their calculations suggest that 70% of AP is decomposed at the surface by condensed- phase reactions and the remaining 30% vaporises into ammonia and perchloric acid.

Knott and Brewster [44] developed a two-dimensional model, able to capture the flame structure proposed by BDP and limited to steady state conditions, to describe the combustion of an AP sandwich with two layers HTPB binder assuming a two-steps global reaction. The model considers energy and species balance as governing equations for both gas and condensed phase. Energy and species conservation and temperature continuity are considered at the interface surface to couple both phases.

Cai et al. [45, 49] developed a 2D model for the combustion of AP/HTPB in sandwich configuration for rocket motor environments. The model uses a two-step global chemical reaction mechanism similar to the one adopted by Knott and Brewster [44] taking into account the governing equations for both gas and condensed phases. The model was used to examine erosive burning under cross-flow laminar conditions and to analyse the flame regime in terms of the Damköhler number (Da) in a rocket motor chamber.

The model proposed by Cao et al. [47] and Ye et al. [46] considers energy conservation equation for condensed phase and mass, momentum, energy and species governing equations for gas phase which is treated as ideal gas being viscous terms included in momentum conservation equation.

Regarding the validation of combustion dynamics of AP propellants with experimental results,

special attention may be drawn to the work of Moriñigo et al. [50] in which the combustion dynamics of HTPB with oxygen in a wind tunnel is studied by comparing qualitatively the experimental data obtained with numerical simulations performed with LES (Large Eddy Simulation). In that study, they propose a reduced chemical model with 2 steps and another model with 6 steps. In addition, Kohga [51] provides experimental results of burning AP/HTPB composite propellant with and without the use of additives for low and high pressures and AP content from 20% to 80% and his results are afterwards used by Cao et al. [47]. Ramakrishna et al. [52] modelled the behaviour of sandwich propellant combustion and validate their results against the experimental ones provided by by Price [53] and Price et al. [54]. Experimental results in gas temperature for AP/HTPB are obtained by Fitzgerald and Brewster [55] who made images the combustion of AP/HTPB propellant by using infrared and ultraviolet emission simultaneously.

Finally, it is worth remarking that, in case of AP/HTPB propellants, several authors as Miccio [56] and Favale and Miccio [57] have pointed out that it is mandatory to consider the two-dimensional (2D) and/or the three-dimensional (3D) aspects of the problem due the involvement of diffusion flames. This remark was also done by other authors such Knott and Brewster [58] which also develop a two-dimensional model for the combustion of heterogeneous propellants. In addition, Zhou et al. [59] used the model developed on previous works from Jackson and Buckmaster [60] to model the combustion of particles of AP embedded in a binder as done by Favale and Miccio [57]. Therefore, it seems of major importance to develop multidimensional models to study the burning of this type of propellants, especially in the case of transient combustion.

To end this subsection, a detailed review of the models used from the literature to develop the one established in this work is performed afterwards.

2.3.1 Model comparison

2.3.1.1 Knott and Brewster, 2002

Knott and Brewster [44] presented a steady-state model of the burning of a composite propellant which intends to simplify as much as possible the combustion kinetics. The geometry used for the study is a region of fuel embedded in two layers of oxidiser as a sandwich. This sandwich is in contact with the gas phase along a surface called burning surface (see Figure 2.5).

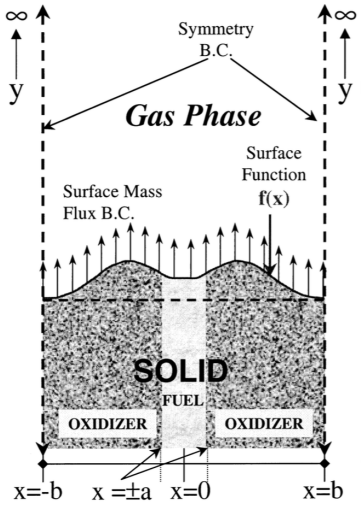

Figure 2.5: Combustion model Knott and Brewster [44].

The model is defined with a set of equations for both phases coupled with the conditions at

the boundary. Assuming ideal gas behaviour and constant thermophysical properties, the partial differential system of equations for the gas phase can be written as,

$$\dot{m}'' \frac{\partial Y_{i,g}}{\partial y} = \rho_g D_g \nabla^2 Y_{i,g} + \Phi_{Y_i,g} \tag{2.164}$$

$$\dot{m}'' c_{p,g} \frac{\partial T_g}{\partial y} = k_g \nabla^2 T_g + \Phi_{T,g} \tag{2.165}$$

being equations (2.164) and (2.165) species and energy equations respectively where, i stands for the i-gas species, $\dot{m}''$ is the mass flux, k_g is the thermal conductivity of the gas, D_g is gas diffusivity, $\Phi_{Y_i,g}$ is the sum of source terms corresponding to species generation or consumption and $\Phi_{T,g}$ is the source term related to the heat of reaction being both depending of Arrhenius reaction kinetics. Zero gradient boundary conditions are assumed for temperature and species variables in x direction and fixed in y direction.

Solid propellant is modelled with an equation for energy and an equation for species such as,

$$\dot{m}'' c_{p,c} \frac{\partial T_c}{\partial y} = k_c \nabla^2 T_c + \Phi_{T,c} \tag{2.166}$$

$$\dot{m}'' \frac{\partial Y_c}{\partial y} = \Phi_{Y_c} \tag{2.167}$$

where Y_c is the mass fraction of the condensed phase, k_c is the thermal conductivity of the condensed phase, Φ_{Y_c} is the sum of source terms corresponding to species generation or consumption of the condensed phase and $\Phi_{T,c}$ is the source term related to the energy release in the condensed phase. Zero gradient boundary conditions are assumed for temperature in x direction and fixed to initial temperature in y direction. For condensed phase concentration the boundaries assumed for the wall are considered value equal to 0 and 1 in y direction.

To couple both systems, boundary conditions at the burning surface need to be established guarantying mass and energy conservation as temperature continuity,

$$\left[(k\nabla T)\cdot\hat{n}\right]_{s,g} = \left[(k\nabla T)\cdot\hat{n}\right]_{s,c} \tag{2.168}$$

$$T_g|_s = T_c|_s \tag{2.169}$$

$$\rho V \cdot \hat{n}\,(Y_i|_s - Y_{i,0}) = (\rho D_g \nabla Y_{i,g})\cdot\hat{n} \tag{2.170}$$

The chemical mechanism defined by Knott a Brewster is defined by two processes: firstly, the propellant changes its phase from condensed to gas at the burning surface and secondly, a two-step chemical reaction process which is responsible of the combustion of the propellant. On the one hand, in R1, the oxidiser is decomposed in molecular oxygen and a first group of reaction products. On the other hand, in R2, binder, molecular oxygen and the group of products of R1 react to obtain carbon dioxide and water. The mechanism can be written as,

$$NH_4ClO_4 \longrightarrow 1.25O_2 + \underbrace{1.5H_2O + HCl + 0.5N_2}_{P_1}\ (R1) \tag{2.171}$$

$$HC + 1.25O_2 + P_1 \longrightarrow CO_2 + 0.5H_2O + P_1\ (R2) \tag{2.172}$$

Once these two reactions are defined, the reaction rates are defined by the authors as,

$$R_1 = A_1 p^2 Y_{AP} e^{\left(-\frac{E_1}{R_u T_g}\right)} \tag{2.173}$$

$$R_2 = A_2 p^2 Y_{HTPB} Y_{O_2} e^{\left(-\frac{E_2}{R_u T_g}\right)} \tag{2.174}$$

where A is the reaction rate coefficient and E is the activation energy of reactions 1 and 2. And the burning rate of the condensed phase is define as,

$$R_{solid} = \rho_c B e^{\frac{-E_c}{RT}} \tag{2.175}$$

where E_c is the activation energy of the solid and B is the burning coefficient.

2.3.1.2 Cai et al., 2008

Cai et al. [49] considered the combustion of composite propellant as a two physicochemical processes: the first one is the decomposition of the condensed phase into gas phase and the second one is the reaction of the propellant in gas phase. For these authors, the propellant in condensed phase melt when it reach a determined temperature called melting temperature which for AP is defined around 830 K.

The geometry consist in a cylindrical chamber containing AP/HTPB and a exhaust nozzle. The AP/HTPB is placed in sandwich configuration with an AP layer in between two of HTPB as for Knott and Brewster [44] (see Figure 2.6) .

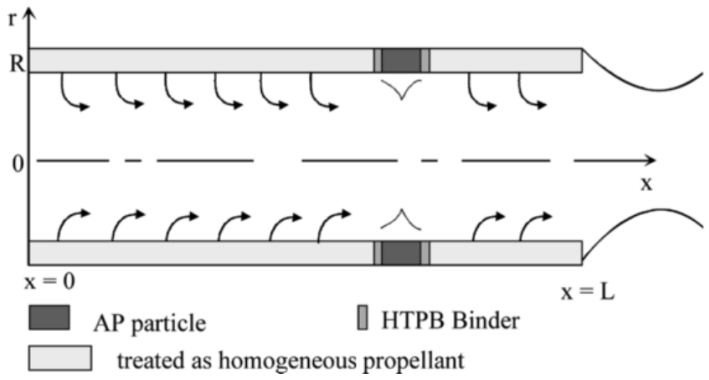

Figure 2.6: Combustion model Cai et al. [49].

The model is defined as a system of differential equations for the gas and the condensed phase being,

$$\frac{\partial \boldsymbol{Q}}{\partial t} + \frac{\partial}{\partial x}(\boldsymbol{E} - \boldsymbol{E}_v) + \frac{\partial}{\partial y}(\boldsymbol{F} - \boldsymbol{F}_v) = \boldsymbol{S} \tag{2.176}$$

where x e y are the axial and radial coordinates, the vector Q is defined as,

$$\boldsymbol{Q} = y^{\delta} \left[\rho, \rho u, \rho v, \rho e, \rho Y_i\right]^T \tag{2.177}$$

being $\delta = [1, 0]$ depending if the problem is considered axisymmetric or two-dimensional, $\boldsymbol{S}$ the source terms, $\boldsymbol{E}$ and $\boldsymbol{F}$ are the flux vectors and $\boldsymbol{E}_v$ and$\boldsymbol{F}_v$ the diffusive flux vectors.

According to the authors, when treating the combustion of AP/HTPB propellant, several facts need to be considered, firstly the mass loading of AP is much higher than HTPB, secondly the AP is more reactive than HTPB and can provide exothermic reaction without the presence of HTPB and the last one, the size of AP particles have a decisive role in the burning behaviour. Therefore, in the combustion of the composite propellant, the authors considered AP degradation as the controlling factor and HTPB burning is collaborating only in the degradation into gas products in the sublimation process. As a result, only the AP will be considered in the chemical kinetics,

$$AP \longrightarrow Products\ (R1) \tag{2.178}$$

being the reaction rate defined as,

$$\dot{\omega}_{AP} = Ap^n Y_{AP} e^{\left(-\frac{E_{AP}}{R_u T_g}\right)} \tag{2.179}$$

where A is the pre-exponential factor and E_{AP} is the activation energy.

To model the behaviour of the condensed phase mass, energy and species conservation equations were used,

$$\dot{m}_{AP} = \rho_{AP} r_b \tag{2.180}$$

$$\dot{m}_{HTPB} = \rho_{HTPB} r_b \tag{2.181}$$

$$\overline{\rho}_{AP} C_{AP} \frac{\partial T}{\partial t} + \dot{m}_{AP} \overline{\rho}_{AP} \bar{C}_{AP} \frac{\partial T}{\partial y} = \frac{\partial}{\partial y}\left(\overline{\lambda}_{AP} \frac{\partial T}{\partial y}\right) + Q_{AP} \dot{\omega}_{AP} \tag{2.182}$$

$$\dot{m}_{HTPB}\left[C_{HTPB}(T_s - T_i) + Q_{HTPB}\right] = \left(\lambda_{HTPB} \frac{\partial T}{\partial y}\right) + Q_{AP \longrightarrow HTPB} \tag{2.183}$$

$$\overline{\rho}_{AP} \frac{\partial Y_{AP}}{\partial t} + \dot{m}_{AP} \frac{\partial Y_{AP}}{\partial y} = \dot{\omega}_{AP} \tag{2.184}$$

where $Q_{AP \longrightarrow HTPB}$ is the energy of AP decomposition provided to support HTPB pyrolysis, $\overline{\rho}_{AP}$, $\bar{C}_{AP}$, and $\overline{\lambda}_{AP}$ state for averaged density, specific heat and thermal conductivity. r_b is the propellant burning rate defined with the expression developed by Cai [61], which was an approach itself from the works of Lengelle [62] and Ibiricu and Williams [63],

$$r_b^2 = \alpha_{AP}\left(\frac{Ap^n e^{-\beta}}{\beta}\right) \frac{1}{\frac{\lambda_g}{\dot{m}_{AP} C_{AP} T_s}\left(\frac{\partial T}{\partial y}\right) + \frac{Q_{AP}}{1 C_{AP} T_s}} \frac{Q_{AP}}{Q_s(T_s)} \tag{2.185}$$

where the heat of change of phase is defined as,

$$Q_s(T_s) = C_{AP} T_s + \Delta h^0_{f,AP} - C_{Ox} T_s - \Delta h^0_{f,Ox} \tag{2.186}$$

and $\beta = \frac{-E_{AP}}{R_u T_s}$ and h^0_f is the heat of formation of species.

2.3.1.3 Ye et al., 2013

Ye et al. [46] developed a two-dimensional model for the combustion of AP/HTPB in sandwich configuration as in Figure 2.7. In order to solve the system of equations several assumptions were made by the authors, AP and HTPB are treated as two separated ingredients, condensed phase only reacts at the surface and only the conduction effect is considered in the condensed phase, the gas is considered ideal and Lewis number is equal to the unity, specific heat of gases is constant and thermal conductivity varies with temperature, to model sublimation of the solid Arrhenius expression is used and finally the coupling is done at the burning surface which is considered to be a plane. Once these assumptions were made, the model was written as,

$$\frac{\partial \rho_g}{\partial t} + \overrightarrow{\nabla} \cdot \left(\rho_g \overrightarrow{u}_g\right) = 0 \tag{2.187}$$

$$\rho_g \frac{\partial\left(q_i\right)}{\partial t} + \rho_g\left(\overrightarrow{q} \cdot \nabla\right) q_i = \frac{\partial p}{\partial x_i} + \frac{\partial}{\partial x_j}\left(\mu \frac{\partial q_i}{\partial x_j}\right) + \frac{\partial}{\partial x_j}\left(\mu \frac{\partial q_i}{\partial x_i}\right) - \frac{2}{3} \frac{\partial}{\partial x_i}\left(\mu \frac{\partial q_k}{\partial x_k}\right) \tag{2.188}$$

$$\rho_g \frac{\partial (T_g)}{\partial t} + \rho_g (\overrightarrow{q} \cdot \nabla) T = \nabla \left(\left(\frac{\lambda_g}{c_g} \right) \nabla T \right) + \Phi_T \tag{2.189}$$

$$\rho_g \frac{\partial (Y_i)}{\partial t} + \rho_g (\overrightarrow{q} \cdot \nabla) Y_i = \nabla (\rho_g D \nabla Y_i) + \Phi_{Y_i} \qquad i = 1, 2, ..., n-1 \tag{2.190}$$

$$\rho_c c_c \frac{\partial (T_c)}{\partial t} + \dot{m} \frac{\partial (T)}{\partial y} = \nabla (\lambda_c \nabla T) \tag{2.191}$$

where c could state for AP or HTPB, $\overrightarrow{q} = (q_1, q_2)$ is the velocity vector and Φ_T and Φ_C are the energy and species source respectively. Gas phase is considered to be ideal.

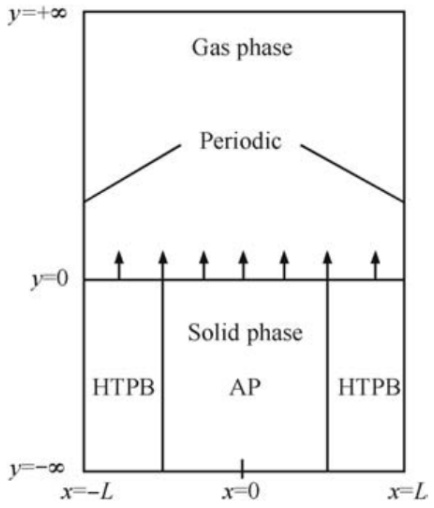

Figure 2.7: Combustion model Ye et al. [46].

The reaction mechanism is very similar to that of Knott and Brewster [44] being,

$$\underbrace{NH_4ClO_4}_{X} \longrightarrow \underbrace{1.25O_2 + 1.5H_2O + HCl + 0.5N_2}_{Z} \, (R1) \tag{2.192}$$

$$\underbrace{HC}_{Y} + \underbrace{1.25O_2 + 1.5H_2O + HCl + 0.5N_2}_{Z} \longrightarrow \underbrace{CO_2 + 2H_2O + HCl + 0.5N_2}_{Final\ products} \, (R2) \tag{2.193}$$

where the reaction rates could be written as,

$$R_1 = D_1 p^{n_1} X e^{\left(-\frac{E_1}{Ru T_g}\right)} \tag{2.194}$$

$$R_2 = D_2 p^{n_2} Z Y e^{\left(-\frac{E_2}{Ru T_g}\right)} \tag{2.195}$$

where D_1 and D_2 are the reaction rate pre-exponential factors, and n is the pressure constant.

The gas and the solid phase, as seen in the previous model needs coupling which will be done in the burning surface as,

$$T|_{y=0^+} = T|_{y=0^-} \tag{2.196}$$

$$\lambda_g \overrightarrow{\nabla} T\Big|_{y=0^+} = \lambda_c \overrightarrow{\nabla} T\Big|_{y=0^-} - \dot{m} Q_s \tag{2.197}$$

$$\dot{m} = \rho_g \left(u_g + r_b\right) = \rho_c r_b \tag{2.198}$$

$$\dot{m} Y_{s,0} = \dot{m} Y_i|_{y=0^+} + D \left.\frac{\partial}{\partial y} Y_i\right|_{y=0^+} \tag{2.199}$$

where, D is the diffusivity, Q_s is he surface heat release and the burning rate is defined as,

$$r_b = A_b e^{\frac{-E_b}{R_u T_s}} \tag{2.200}$$

where b can be binder or oxidiser depending on the zone considered.

2.3.1.4 Cao et al., 2015

The model of Cao et al.[47] is very similar to that of Ye et al. [46] not only in the reaction mechanism but also in the mathematical equation model. In this case, the authors considered a region in which the propellant changes its phase from solid to gas instead of considering a flat surface like it was the case from Ye et al. [46]. The geometry used by the authors could be seen in Figure 2.8. Due to this addition, Cao et al. considered an additional source term to describe region 2.

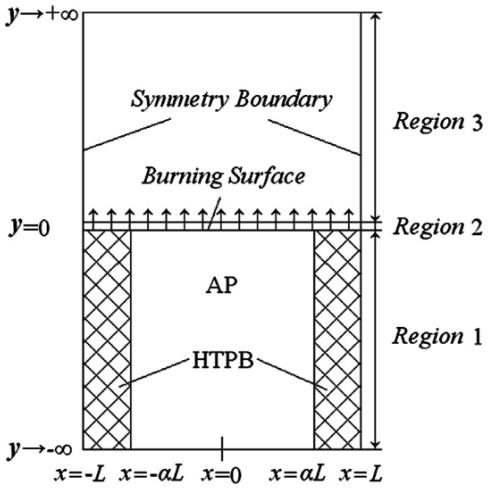

Figure 2.8: Combustion model Cao et al. [47].

The system of governing equations can be written as,

$$\frac{\partial \rho_g}{\partial t} + \overrightarrow{\nabla} \cdot \left(\rho_g \overrightarrow{u}_g\right) = S_m \tag{2.201}$$

$$\frac{\partial \left(\rho_g \overrightarrow{u}_g\right)}{\partial t} + \overrightarrow{\nabla} \cdot \left(\rho_g \overrightarrow{u}_g \overrightarrow{u}_g\right) = -\nabla p + \frac{\mu}{3} \nabla \left(\nabla \cdot \overrightarrow{u}_g\right) + \mu \Delta \overrightarrow{u}_g + S_{\overrightarrow{u}_g} \tag{2.202}$$

$$\frac{\partial \left(\rho_g T_g\right)}{\partial t} + \overrightarrow{\nabla} \cdot \left(\rho_g \overrightarrow{u}_g T_g\right) = \nabla \left(\frac{\lambda_g}{c_p} \nabla \cdot T_g\right) + \left(Q_{g1} R_1 + Q_{g2} R_2\right) / c_p \tag{2.203}$$

$$\frac{\partial \left(\rho_g Y_i\right)}{\partial t} + \overrightarrow{\nabla} \cdot \left(\rho_g \overrightarrow{u}_g Y_i\right) = \nabla \left(\frac{\lambda_g}{c_p} \nabla \cdot Y_i\right) \Phi_{Y_i} \qquad i = 1, 2, ..., n-1 \tag{2.204}$$

$$\rho_c c \frac{\partial (T_c)}{\partial t} = \nabla (\lambda_c \nabla \cdot T_c) \tag{2.205}$$

where Q_g is the heat of reaction of R1 or R2 depending on the subscript, subscript c stands for condensed phase which could be AP and HTPB depending on the zone considered, S_m is the mass source term, $S_{\overrightarrow{u}_g}$ is the momentum source term which can be defined as,

$$S_m = \frac{\dot{m} A_{cell}}{V_{cell}} = \frac{\rho_c \dot{r} A_{cell}}{V_{cell}} \tag{2.206}$$

$$S_{\overrightarrow{u}_g} = S_m \overrightarrow{u}_g \tag{2.207}$$

Energy, species and mass conservation as well as temperature continuity are established as boundary conditions in the burning surface as follows,

$$T_g = T_c \tag{2.208}$$

$$\dot{m} = \rho_g (|\overrightarrow{u}_g| + \dot{r}) = \rho_c \dot{r} \tag{2.209}$$

$$\dot{m}\, Y_i|_{0^+} - \frac{\lambda_c}{c_p} \left.\frac{\partial Y_i}{\partial y}\right|_{0^+} = \dot{m}\, Y_i|_0 \tag{2.210}$$

$$\lambda_g \left.\frac{\partial T_g}{\partial y}\right|_{0^+} = \lambda_c \left.\frac{\partial T_c}{\partial y}\right|_{0^+} = \rho_c \dot{r} Q_c \tag{2.211}$$

where Q_c is the heat release of phase change. As for the the far field boundaries considered are the same as in other works from previous authors.

The chemical kinetics of the combustion process is exactly the same defined by Ye et al. [46] in equations (2.192) and (2.193) and the reaction rates of R1 and R2 as equations (2.194) and (2.195).

The burning rate, however will be calculated as the product of the burning rates calculated for each propellant, AP or HTPB being,

$$\dot{r} = \dot{r}_{AP}^{1-\alpha} \dot{r}_{HTPB}^{\alpha} \tag{2.212}$$

where $\dot{r}_{AP}$ and $\dot{r}_{HTPB}$ are the burning rates of AP or HTPB respectively which are calculated with equation (2.200).

2.4 Models to characterise double-base propellants combustion

Double-base propellants are homogeneous propellants formed by NC (nitrocellulose) and NG (nitroglycerine). In the existing literature, both detailed and simplified chemical kinetic models can be found to represent their combustion.

On the one hand, among the simplified models found in literature, Lengelle [64] and Bizot and Beckstead [65] used similar models with three reactions for the condensed phase and 4 for the gas phase. This model was improved by Roh et al. [66]. Hsieh and Yang [67] developed a model applied to solve reacting flows and validated it by applying it to several problems such as one-dimensional nozzle flows, two-dimensional channel flows, rocket motor internal flows and acoustic waves in porous chambers. Brewster et al. [68] compared the combustion of two models, one considering high activation energy and another one with low activation energy. Both models are compared with experimental data to estimate the sensitivity of the temperature and pressure exponent with pressure variation.

On the other hand, several models are considered in literature to model the combustion of double-base propellants with detailed chemistry and/or turbulence. Among them, Apte et al. [69] used LED Smagorinsky to model the problem and not only to analyse the vorticity inside the chamber of the

rocket motor but also to study the effect that the turbulence has in the flame structure. The model of equations is based in that of Roh et al. [70, 66]. Wu et al. [71] developed an aerothermochemical or erosive model to reproduce erosive combustion. In their work the authors are focused on detailing the combustion modelling considering the chemical kinetics and the diffusive effects of the gaseous phase. Tseng and Yang [72] studied the combustion of homogeneous double-base propellant developing a model and solving it using $k-\epsilon$ turbulence. In their results they observed that the turbulence seemed not to have a relevant effect in chemistry combustion but in friction forces. Closing, Arkhipov et al. [73] presented several methods to describe the results of experimental studies of erosive combustion of solid propellants under transonic and supersonic flux.

Regarding experimental test, it is relevant to highlight the test performed by several authors such Robbins and Keys [74] who made a review of experimental results for propellants which contained 12% or 13% of NC quantifying the effect that this mass fraction, as well as the habitual additives, have in the burning rate. In addition, Long et al. [75, 76] made an experimental study about the combustion of several double-base propellants containing nitrogen heterocyclic nitroamines (RDX, TNAD, HMX and DNP). The experimental apparatus consists in a chimney strand burner with several observation windows. Aoki and Kubuta [77] also used a chimney-type strand burner with four transparent widows to analyse the burning rate of twelve different kinds of propellant previously prepared with different compositions. Finally, Markov et al. [78] studied the combustion of a double-base propellant in a semi-closed volume. They also presented a short theoretical model in order to interpret and define several experiments performed in steady and non-steady conditions.

Finally, the work done by the authors from literature which have been used to develop the model to represent combustion of double-base propellant in this thesis will be described n the following subsection. The final model itself will be afterwards explained in detail in subsection 4.3.3.1 from Chapter 4.

2.4.1 Model comparison

2.4.1.1 Wu et al.,1983

Wu et al. [71] presented an aerothermochemical model of erosive burning of double-base propellants which considers heat, mass and momentum transfer in the boundary layer. To be able to perform the model, they consider 5 different reaction zones: preheat zone, foam zone, fizz zone, dark zone and luminous zone. In the first two zones, the surface or subsurface reactions are taking place. However, in the remaining three the gas reaction happens. To illustrate this process they use Figure 2.9.

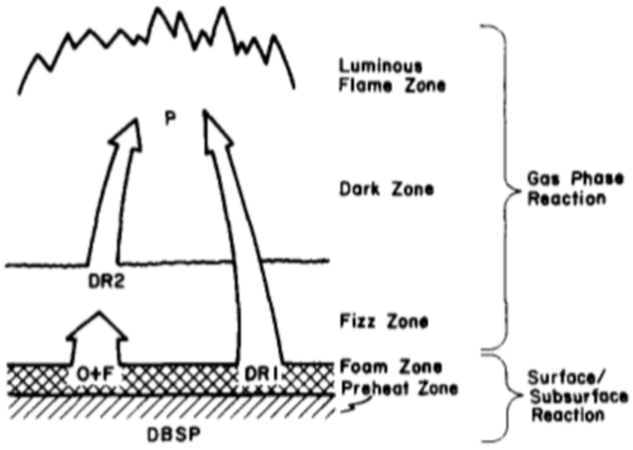

Figure 2.9: Modelling of double-base propellant combustion Wu et al. [71].

In this model, Wu et al. [71] considered NO_2 as oxidiser (O) and CH_2O as fuel (F). In addition, they consider as a result of the surface sublimation, another group of species that they called delayed species (DR1). Both, fuel and oxidiser, once they are in gas form, they form a second group of delayed species called DR2. Both delayed species contribute in the formation of the final products.

To model the rate of production of gas from the solid phase they used a simple Arrhenius expression of the form,

$$r_b = A_s e^{-\frac{E_{a,s}}{R_u T_s}} \tag{2.213}$$

Once the fuel, oxidiser and first group of reaction species are in gas phase, the chemical process is described by the authors as,

$$c_f F + c_O O \longrightarrow c_{DR2} DR2 \; (R1) \tag{2.214}$$

$$c_{DR1} DR1 \longrightarrow c_P P \; (R2) \tag{2.215}$$

$$c_{DR2} DR2 \longrightarrow c_P P \; (R3) \tag{2.216}$$

The reaction rate determined for the reactions described below,

$$\overline{\dot{\omega}}_{F,ch} = -A_{fz} \overline{\rho}_g^2 \frac{\widetilde{Y}_F \widetilde{Y}_O}{W_O} e^{\left(-\frac{E_{a,fz}}{R_u \widetilde{T}}\right)} \tag{2.217}$$

$$\overline{\dot{\omega}}_{DR1,ch} = -A_{DR1} \overline{\rho}_g^2 \frac{\widetilde{Y}_{DR1}^2}{W_{DR1}} e^{\left(-\frac{E_{a,DR1}}{R_u \widetilde{T}}\right)} \tag{2.218}$$

$$\overline{\dot{\omega}}_{DR2,ch} = -A_{DR2} \overline{\rho}_g^2 \frac{\widetilde{Y}_{DR2}^2}{W_{DR2}} e^{\left(-\frac{E_{a,DR2}}{R_u \widetilde{T}}\right)} - \left(1 + \frac{v_O W_O}{v_F W_F}\right) \dot{\omega}_{F,ch} \tag{2.219}$$

where $\dot{\omega}$ is the reaction rate, A is the pre-exponential factor, v is the stoichiometric coefficient, $W$is the molecular weight, Y is the mass fraction and E_a is the activation energy.

Afterwards the authors proceed to write the set of conservation equations for which assume: averaged flow properties are steady, there are no body forces present, radiation heat transfer is neglected, Lewis number equal to unity and validity of Fick's law of diffusion. Once all assumptions are made, the set of differential equation is written as,

$$\frac{\partial}{\partial x}\left(r^m \overline{\rho}\widetilde{u}\right) + \frac{\partial}{\partial r}\left(r^m \overline{\rho}\widetilde{v}\right) = 0 \tag{2.220}$$

$$\overline{\rho}\widetilde{u}\frac{\partial \widetilde{u}}{\partial x} + \overline{\rho}\widetilde{v}\frac{\partial \widetilde{v}}{\partial r} = \frac{1}{r^m}\frac{\partial}{\partial r}\left[r^m \mu_{eff}\frac{\partial \widetilde{u}}{\partial r}\right] - \frac{d\overline{p}}{dx} \tag{2.221}$$

$$\overline{\rho}\widetilde{u}\frac{\partial \widetilde{Y}_i}{\partial x} + \overline{\rho}\widetilde{v}\frac{\partial \widetilde{Y}_i}{\partial r} = \frac{1}{r^m}\frac{\partial}{\partial r}\left[r^m \left(\frac{\mu}{Sc}\right)_{eff}\frac{\partial \widetilde{Y}_i}{\partial r}\right] + \overline{\dot{\omega}}_i \tag{2.222}$$

$$\overline{\rho}\widetilde{u}\frac{\partial \widetilde{H}}{\partial x} + \overline{\rho}\widetilde{v}\frac{\partial \widetilde{H}}{\partial r} = \frac{1}{r^m}\frac{\partial}{\partial r}\left\{r^m\left[\left(\frac{\mu}{Sc}\right)_{eff}\frac{\partial \widetilde{H}}{\partial r} + \left\{\mu_{eff} - \left(\frac{\mu}{Pr}\right)_{eff}\right\}\frac{\partial \widetilde{u}^2/2}{\partial r}\right]\right\} \tag{2.223}$$

$$\overline{\rho}\widetilde{u}\frac{\partial k}{\partial x} + \overline{\rho}\widetilde{v}\frac{\partial k}{\partial r} = \frac{1}{r^m}\frac{\partial}{\partial r}\left[r^m\left(\mu + \frac{\mu_t}{C_1}\right)\frac{\partial k}{\partial r}\right] + \mu_t\left(\frac{\partial \widetilde{u}}{\partial r}\right)^2 - \overline{\rho}\epsilon \tag{2.224}$$

$$\overline{\rho}\widetilde{u}\frac{\partial \epsilon}{\partial x} + \overline{\rho}\widetilde{v}\frac{\partial \epsilon}{\partial r} = \frac{1}{r^m}\frac{\partial}{\partial r}\left[r^m\left(\mu + \frac{\mu_t}{C_2}\right)\frac{\partial \epsilon}{\partial r}\right] + C_3\mu_t\left(\frac{\partial \widetilde{u}}{\partial r}\right)^2\frac{\epsilon}{k} - -C_4\overline{\rho}\frac{\epsilon^2}{k} \tag{2.225}$$

where u, $\widetilde{u}$, and u'' represent the instantaneous, the mass weighted mean and the fluctuating velocities as,

$$\widetilde{u} \equiv \overline{\rho u}/\overline{\rho} \quad and \quad u \equiv \widetilde{u} + u'' \tag{2.226}$$

and p, $\widetilde{p}$, p' represent the instantaneous, the time mean and the fluctuating pressures as,

$$p \equiv \overline{p} + p' \tag{2.227}$$

Pressure follows ideal gas equation,

$$\overline{p} = \overline{\rho} R_u \widetilde{T}/W \tag{2.228}$$

The exponent of r, m is set to 0 for planar flows and for 1 for axisymmetric flows.
Turbulent viscosity is expressed as a function of k and ϵ as,

$$\mu_t = c_\mu \overline{\rho} \frac{k^2}{\epsilon} \tag{2.229}$$

As explained for AP/HTPB, to solve the problem, boundary conditions need to be applied in the boundary solid-gas interface which are written by the authors as,

$$\left(\overline{\rho}\widetilde{v}\widetilde{Y_i}\right)_g - \rho_s r_b Y_{i,s} - \left(\overline{\rho} D \frac{\partial \widetilde{Y_i}}{\partial r}\right) = 0 \tag{2.230}$$

$$\lambda \left.\frac{\partial T}{\partial r}\right|_g = \lambda_s \left.\frac{\partial T_c}{\partial r}\right|_s = \rho_c r_b \left[\left(c_p - c_c\right)\left(T_s - T_{s,ref}\right) + Q_{c,ref}\right] \tag{2.231}$$

where $Q_{c,ref}$ is the heat release at a certain temperature $T_{s,ref}$, c_p is the mass averaged specific heat of gas species, c_c is the heat capacity of solid propellant and D is the diffusion term.

The authors use the k-epsilon turbulence model to solve the equation system and discuss the results accordingly.

2.4.1.2 Bizot and Beckstead, 1988

Bizot and Beckstead [65] present a model which uses a set of differential equations to calculate the burning rate of double-base solid propellants being the differential equations defined for both gas and condensed phases.

The set of equations for the condensed phase is formed by the three concentrations equations of the species appearing in the three reactions which, according to the authors, take place in the condensed phase, and another equation of energy conservation being defined the system as,

$$\rho_{p\infty} R_b \frac{dY_p}{dx} = -\rho_{p\infty} B_c e^{-\frac{E_c}{RT}} \tag{2.232}$$

$$\rho_{p\infty} R_b \frac{dY_{NO_2}}{dx} = -\rho_{p\infty} Y_{NO_2} B_c e^{-\frac{E_c}{RT}} - B_{NO_2,c} Y_{NO_2} \frac{PM}{RT} e^{-\frac{E_{g,NO_2}}{RT}} \tag{2.233}$$

$$\rho_{p\infty} R_b \frac{dY_{aldx}}{dx} = -\rho_{p\infty} Y_{aldx} B_c e^{-\frac{E_c}{RT}} - B_{aldx,c} Y_{aldx}^2 \left(\frac{PM}{RT}\right)^2 e^{-\frac{E_{g,aldx}}{RT}} \tag{2.234}$$

$$\rho_{p\infty} R_b C_p \frac{dT}{dx} - \lambda_p \frac{d^2T}{dx^2} = Q_d \rho_{p\infty} Y_{aldx} B_c e^{-\frac{E_c}{RT}} + Q_{r,NO_2} B_{NO_2,c} Y_{NO_2} \frac{PM}{RT} e^{-\frac{E_{g,NO_2}}{RT}} + Q_{r,aldx} B_{aldx,c} Y_{aldx}^2 \left(\frac{PM}{RT}\right)^2 e^{-\frac{E_{g,aldx}}{RT}} \tag{2.235}$$

where aldx is related to complex aldehyde reaction, B is the pre-exponential factor, E is the activation energy, Q_r is the heat release, $Q_d$is the heat of endothermic degradation, $\rho_{p\infty}$ is the density of the propellant, C_p is the specific heat capacity of propellant assumed constant, P is the pressure and M is the average gas molar mass.

On the one hand, the reactions of the condensed phase are defined as,

$$Propellant \longrightarrow RCHO + NO_2 \tag{2.236}$$

$$NO_2 \longrightarrow NO + - - - \tag{2.237}$$

$$RCHO \longrightarrow CH_2O, CO, CO_2, H_2O \tag{2.238}$$

On the other hand, the reactions of the gas phase are,

$$NO_2 \longrightarrow NO + - - - \tag{2.239}$$

$$aldehyde \longrightarrow CO, CO_2, H_2O \tag{2.240}$$

$$NO + C \longrightarrow CO, CO_2, N_2 \tag{2.241}$$

$$NO + CO \longrightarrow CO, CO_2, N_2 \tag{2.242}$$

being the first three present in the primary flame and the last one in the secondary flame.

The system of equations for the gas phase is defined with an energy equation and four species equations as,

$$\begin{aligned}\dot{m}C_g\frac{dT}{dx} - \lambda_g\frac{d^2T}{dx^2} = Q_{r,NO_2}A_{g,NO_2}Y_{NO_2}\frac{PM}{RT}e^{-\frac{E_{g,NO_2}}{RT}} + \\ + Q_{r,ald}A_{g,ald}Y_{ald}^2\left(\frac{PM}{RT}\right)^2 e^{-\frac{E_{g,ald}}{RT}} + Q_{r,carb}A_{g,carb}S_{carb}\eta Y_{NO}\rho_{carb}PMe^{-\frac{E_{g,carb}}{RT}} + \\ Q_{r,NO}A_{g,NO}Y_{NO}^2\left(\frac{PM}{RT}\right)^2 e^{-\frac{E_{g,NO}}{RT}}\end{aligned} \tag{2.243}$$

$$\dot{m}\frac{dY_{NO_2}}{dx} = -A_{g,NO_2}Y_{NO_2}\frac{PM}{RT}e^{-\frac{E_{g,NO_2}}{RT}} \tag{2.244}$$

$$\dot{m}\frac{dY_{ald}}{dx} = -A_{g,ald}Y_{ald}^2\left(\frac{PM}{RT}\right)^2 e^{-\frac{E_{g,ald}}{RT}} \tag{2.245}$$

$$\begin{aligned}\dot{m}\frac{dY_{NO}}{dx} = \frac{M_{NO}}{M_{NO_2}}A_{g,NO_2}Y_{NO_2}\frac{PM}{RT}e^{-\frac{E_{g,NO_2}}{RT}} \\ - A_{g,NO}Y_{NO}^2\left(\frac{PM}{RT}\right)^2 e^{-\frac{E_{g,NO}}{RT}} - A_{g,carb}S_{carb}\eta Y_{NO}\rho_{carb}PMe^{-\frac{E_{g,carb}}{RT}}\end{aligned} \tag{2.246}$$

$$\dot{m}\frac{d\rho_{carb}}{dx} = \frac{M_{carb}}{M_{NO}}\rho_{p\infty}A_{g,carb}S_{carb}\eta Y_{NO}\rho_{carb}PMe^{-\frac{E_{g,carb}}{RT}} \tag{2.247}$$

where η is the NO/carbon heterogeneous reaction efficiency, *carb* stands for carbon and S_{carb} is the carbon specific surface.

2.4.1.3 Tseng and Yang, 1994

Tseng and Yang [72] developed a model to analyse the combustion of double-base solid propellants in rocket motors and study two aspects: how the flow conditions affect to the burning and how the motor internal flow is established by the propellant burning.

The authors divide the control volume in several regions: preheated and superficial degradation which are under the propellant surface, primary flame, dark and secondary flame, being these last three zones in the gas phase (see Figure 2.10).

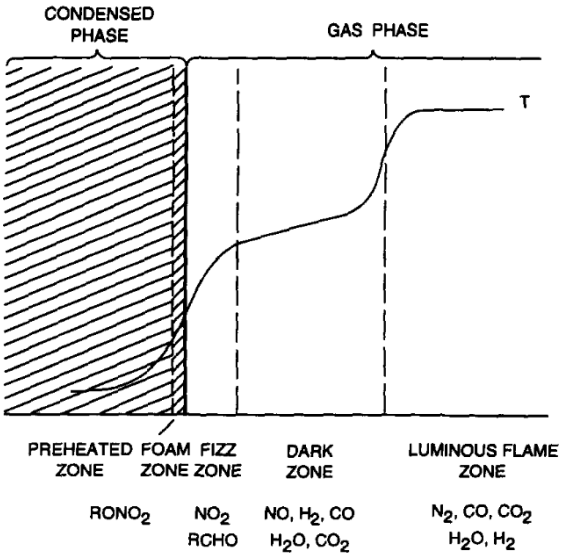

Figure 2.10: Combustion wave structure. Tseng and Yang [72].

According to the authors, and as it was also explained by Wu et al. [71] the propellant remains stable in the preheated zone until the surface reaches the temperature of melting, which means that the temperature is sufficiently high to start the solid degradation.

The problem analysed is a two-dimensional combustion chamber loaded with a double-base propellant grain and connected to an exhaust nozzle like the one depicted in Figure 2.11.

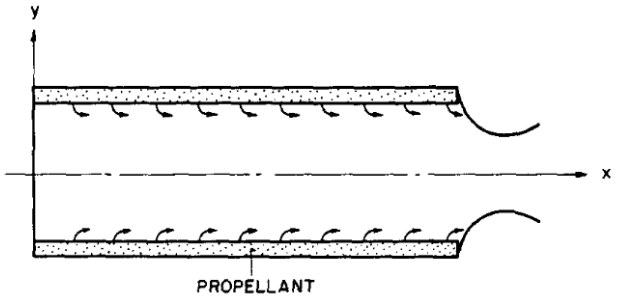

Figure 2.11: Schematic Diagram of solid-propellant rocket motor. Tseng and Yang [72].

To model it, a set of partial differential equation is defined in vector form as,

$$\frac{\partial \boldsymbol{Q}}{\partial t} + \frac{\partial}{\partial x}(\boldsymbol{E} - \boldsymbol{E}_v) + \frac{\partial}{\partial y}(\boldsymbol{F} - \boldsymbol{F}_v) = \boldsymbol{S} \tag{2.248}$$

where x and y are the axial and radial coordinates, the vector Q is defined as,

$$\boldsymbol{Q} = [\rho, \rho u, \rho v, \rho e, \rho Y_i] \tag{2.249}$$

$$\boldsymbol{E} = \left[\rho u, \rho u^2 + p, \rho uv, u(\rho e + p), \rho u Y_i\right] \tag{2.250}$$

$$\boldsymbol{F} = \left[\rho v, \rho uv, \rho v^2 + p, v(\rho e + p), \rho v Y_i\right] \tag{2.251}$$

$$\boldsymbol{E}_v = \begin{bmatrix} 0 \\ \tau_{xx} \\ \tau_{xy} \\ u\tau_{xx} + v\tau_{xy} - q_x \\ -\rho \hat{u}_i Y_i \end{bmatrix} \tag{2.252}$$

$$\boldsymbol{F}_v = \begin{bmatrix} 0 \\ \tau_{xy} \\ \tau_{yy} \\ u\tau_{xy} + v\tau_{yy} - q_y \\ -\rho \hat{v}_i Y_i \end{bmatrix} \tag{2.253}$$

$$\boldsymbol{S} = \begin{bmatrix} 0 \\ 0 \\ 0 \\ 0 \\ \dot{\omega}_i \end{bmatrix} \tag{2.254}$$

where the subscript i stands for ith-speciess, τ_{xy}, τ_{xx}, τ_{yy} are the shear and normal stresses and $\dot{\omega}$ stands for the reaction rate.

The model developed by these authors, as it was done by Wu et al. [71], considers that the degradation of the solid phase will give fuel (CH_2O), oxidiser (NO_2) and a first group of delayed reaction species. Once this three components are in gas phase, fuel and oxidiser react to produce the second group of delayed species an both of them produce the final products. These products are observed in R1, R2 and R3 defined by Wu et al. [71] which correspond to equations (2.214), (2.215) and (2.216). Rate of production of the species is given by equations (2.217), (2.218) and (2.219).

In order to be able to couple both phases, and as it was also defined by other authors in the existing literature, boundary conditions are needed at the burning surface . These conditions are mass, species and energy balances,

$$(\rho v)_g = \rho_c r_b \tag{2.255}$$

$$(\rho v Y_i)_g - \left(\rho D \frac{\partial Y_i}{\partial y}\right)_g = -\rho_s r_b Y_{i,s} \tag{2.256}$$

$$-\lambda_g \left(\frac{\partial T}{\partial y}\right)_g + \left[\rho \sum_{i=1}^{N} Y_i h_i \left(v + \hat{v}_i\right)\right]_g = -\lambda_s \left(\frac{\partial T}{\partial y}\right)_s - \rho_c r_b \left[C_s \left(T_s - T_{ref}\right) + \sum_{i=1}^{N} Y_i h^0_{f,i}\right] \tag{2.257}$$

being $h^0_{f,i}$ the specific enthalpy of specie and r_b is the burning rate.

According to the authors, the condensed phase turns into gas at the interface according to the following burning rate formula,

$$r_b^2 = \frac{\beta \alpha_p A_c e^{-\beta}}{1 - \frac{T_0}{T_s} - \frac{Q_s}{2 c_s T_s}} \tag{2.258}$$

where α_p is the thermal diffusivity of the condensed phase, Q_s is the heat release, $\beta = \frac{E_{a,c}}{R_u T_s}$ and T_s is the burning surface.

2.4.1.4 Roh et al., 1998

Roh et al. [66] take as reference a previous work on the gas phase combustion of a double-base propellant in a rocket motor [70]. In 1998, the authors extended the analysis of the gas phase done in [70] by adding the equations of condensed phase and coupling both phases in the burning surface.

The model was formed by a set of differential equations as follows,

$$\frac{\partial \boldsymbol{Q}}{\partial t} + \frac{\partial}{\partial x}(\boldsymbol{E} - \boldsymbol{E}_v) + \frac{\partial}{\partial y}(\boldsymbol{F} - \boldsymbol{F}_v) = \boldsymbol{S} \tag{2.259}$$

where

$$\boldsymbol{Q} = [\rho, \rho u, \rho v, \rho e, \rho Y_i]^T \tag{2.260}$$

$$\boldsymbol{E} = \left[\rho u, \rho u^2 + p, \rho uv, u(\rho e + p), \rho u Y_i\right]^T \tag{2.261}$$

$$\boldsymbol{F} = \left[\rho v, \rho uv, \rho v^2 + p, v(\rho e + p), \rho v Y_i\right]^T \tag{2.262}$$

$$\boldsymbol{E}_v = \begin{bmatrix} 0 \\ \tau_{xx} \\ \tau_{xy} \\ u\tau_{xx} + v\tau_{xy} - q_{e_x} \\ -q_{i_x} \end{bmatrix}^T \tag{2.263}$$

$$\boldsymbol{F}_v = \begin{bmatrix} 0 \\ \tau_{xy} \\ \tau_{yy} \\ u\tau_{xy} + v\tau_{yy} - q_{e_y} \\ -q_{i_y} \end{bmatrix}^T \tag{2.264}$$

$$\boldsymbol{S} = \begin{bmatrix} 0 \\ 0 \\ 0 \\ 0 \\ \dot{\omega}_i \end{bmatrix} \tag{2.265}$$

where subscript i stands for ith-species which varies from 1 to N-1, τrepresent the viscous stress and q_{ex} and q_{ey} are the thermal diffusion term which stands for the contribution of heat conduction and mass diffusion processes. The species diffusion terms (q_i) are approximated by Fick's Law.

As mentioned, the kinetic mechanism for the condensed phase is described in [70] so,

$$double{-}base\ propellant \rightarrow 2.49NO_2 + 2.36CH_2O + 1.26(CHO)_2 + 0.17CO + minor\ residuals \tag{2.266}$$

$$NO_2 + 0.56CH_2O + 0.16(CHO)_2 \rightarrow NO + 0.38CO + 0.5CO_2 + 0.5H_2O + 0.22H_2 \tag{2.267}$$

The reaction rate of each reaction is defined as,

$$\dot{\omega}_c = -\rho_c B_c e^{-\frac{E_c}{RT}} \tag{2.268}$$

$$\dot{\omega}_{NO_2} = Y_{NO_{2_0}}\dot{\omega}_c - \rho_g Y_{NO_2} p^{0.39} B_{NO_2} e^{-\frac{E_{NO_2}}{RT}} \tag{2.269}$$

In addition to the system of equations of the gas phase, several equations are considered for the condensed phase phase being, mass, energy and species concentration,

$$\dot{m} = \rho_c r_b \tag{2.270}$$

$$\rho_c C_c \frac{\partial T}{\partial t} + \dot{m} C_c \frac{\partial T}{\partial y} = \lambda_c \frac{\partial^2 T}{\partial y^2} + \dot{q}_c \tag{2.271}$$

$$\rho_c \frac{\partial Y_i}{\partial t} + \dot{m} \frac{\partial Y_i}{\partial y} = \dot{\omega}_i \tag{2.272}$$

where $\dot{q}_c$ is the net effect of the endothermic decomposition and the exothermic reaction in the condensed phase.

The coupling between both phases is done by applying mass, energy and species balance at the interface so,

$$(\rho v)_g = \rho_c r_b \tag{2.273}$$

$$\left[\rho\left(v + \hat{v}_i\right) Y_i\right]_g = -\rho_s r_b Y_{i,s} \tag{2.274}$$

$$-\lambda_g \left(\frac{\partial T}{\partial y}\right)_g + \left[\rho \sum_{i=1}^{N} Y_i h_i \left(v + \hat{v}_i\right)\right]_g = -\lambda_c \left(\frac{\partial T}{\partial y}\right)_s - \rho_c r_b \left[C_c\left(T_s - \overline{T}_s\right) + \sum_{i=1}^{N} Y_i h_{f,i}^0\right] \tag{2.275}$$

The degradation of the solid is defined with an expression similar to that by Tseng and Yang [72].

$$r_b^2 = \frac{\left(\alpha_c A_c e^{-\beta}\right)/\beta}{\frac{\left\{(\lambda_g/\dot{m})\left(\frac{\partial T}{\partial y}\right)_g + \left[\overline{Q}_c + (C_c - C_p)(T_s - T_{ref})\right]\cdot 0.5\right\}}{C_s T_s}} \tag{2.276}$$

where $\overline{Q}_c$ is the subsurface heat release, $\beta = \frac{E_c}{RT}$ and $\overline{T}_s$ is the surface temperature under steady-state conditions.

Chapter 3

Numerical methods

The aim of numerical methods is to to solve the PDEs by replacing the continuous problem of Fluid Dynamics represented by the PDEs (Partial Differential Equations) by a finite set of discrete values. In order to do that, the domain of the PDEs must be discretised in a finite set of points of volumes either by a mesh or a grid. In the Finite Difference approach, the discrete values are point values defined at grid points however, in the Finite Volume approach, the discrete values are average values over finite volumes.

The multi-dimensional Euler equations used in this work for modelling and describing the physical problem of combustion of propellants can be written with the following general conservative form,

$$\frac{\partial \boldsymbol{U}}{\partial t} + \nabla \cdot \mathcal{H} = \boldsymbol{S}(\boldsymbol{U}) \tag{3.1}$$

where $\boldsymbol{U}$ is the conserved variables vector, $\mathcal{H} = (\boldsymbol{F}, \boldsymbol{G}, \boldsymbol{H})$ is the tensor of fluxes and $\boldsymbol{S}$ is the source terms which may or not include non conservative terms and can be defined as,

$$\boldsymbol{U} = \begin{bmatrix} q_1 \\ q_2 \\ \dots \\ q_m \end{bmatrix}, \boldsymbol{F} = \begin{bmatrix} f_1 \\ f_2 \\ \dots \\ f_m \end{bmatrix}, \boldsymbol{G} = \begin{bmatrix} g \\ g_2 \\ \dots \\ g_m \end{bmatrix}, \boldsymbol{H} = \begin{bmatrix} h_1 \\ h_2 \\ \dots \\ h_m \end{bmatrix}, \boldsymbol{S} = \begin{bmatrix} s_1 \\ s_2 \\ \dots \\ s_m \end{bmatrix} \tag{3.2}$$

The integration of the homogeneous part of the equation system (3.1) in a control volume Ω yields,

$$\frac{\partial}{\partial t} \int\int\int_{\Omega} \boldsymbol{U} d\Omega + \int\int_{A} \mathcal{H} \hat{n} dA = 0 \tag{3.3}$$

where A is the boundary of the volume Ω and $\hat{n}$ is the normal vector to the surface A depicted in Figure 3.1.

Considering the first integral as a time rate of change of the averaging of the conserved variables $\boldsymbol{U}$ and the boundary A formed by N surfaces so that $A = \sum_{s=1}^{N} A_s$equation 3.3 can be written as,

$$\frac{\partial \boldsymbol{U}}{\partial t} + \frac{1}{|\Omega|} \sum_{s=1}^{N} \int\int_{A_s} \mathcal{H} \hat{n} dA = 0 \tag{3.4}$$

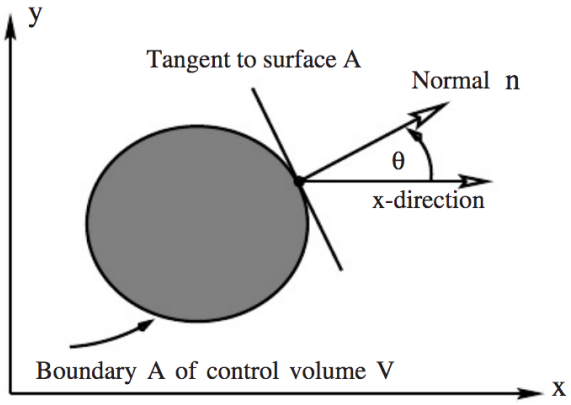

Figure 3.1: Control volume in x-y plane [79].

The time derivative of the conserved variables is defined as $\frac{\boldsymbol{U}_j^{n+1}-\boldsymbol{U}_j^n}{\triangle t}$. Therefore, making use of the Rotational property $\mathcal{H}\hat{n} = \overline{T_s}^{-1}\boldsymbol{F}\left(\overline{T_s}\boldsymbol{U}\right)$ and considering that the surface integral of the flux is approached by $\int\int_{A_s}\boldsymbol{F}\hat{n}dA \approx \overline{T_s}^{-1}F\left(\overline{T_s}\boldsymbol{U}\right)A_s$, a finite volume scheme for multiple dimensions in unstructured grids is obtained,

$$\boldsymbol{U}_j^{n+1} = \boldsymbol{U}_j^n - \frac{\triangle t}{|\Omega|}\sum_{s=1}^{N}\overline{T_s}^{-1}\boldsymbol{F}\left(\overline{T_s}\boldsymbol{U}_j^n\right)A_s \tag{3.5}$$

where $\overline{T_s}$ is the rotation matrix, $\overline{T_s}^{-1}$ its inverse and A_s is the area of the s^{th} surface bounding volume Ω . Considering the source terms, the system results,

$$\overline{\boldsymbol{U}}_j^{n+1} = \boldsymbol{U}_j^n - \frac{\triangle t}{|\Omega|}\sum_{s=1}^{N}\overline{T_s}^{-1}\boldsymbol{F}\left(\overline{T_s}\boldsymbol{U}_j^n\right)A_s + \triangle t\boldsymbol{S}(\boldsymbol{U}_j^n) \tag{3.6}$$

where $\triangle t$ is the time step which is calculated with the following expression,

$$\triangle t = CFL\cdot\left(\frac{\triangle x_j}{\lambda}\right) \tag{3.7}$$

such that,

$$0 < CFL \leq 1 \tag{3.8}$$

CFL stands for the Courant-Friedichs-Lewy coefficient or the Courant number coefficient which and it is a dimensionless quantity. condition of convergence to solve partial differential equations.

The discretisation of the domain in cells is represented in Figure 3.2.

In order to evaluate the fluxes, several approximations such as the first-order upwind method of Godunov, Lax-Friedrichs scheme and Lax-Wendroff scheme can be found in the existing literature.

These methods, require the solution of the Riemann problem which can be highly demanding. Therefore, approximate Riemann solvers are used in this work. Approximate and non-iterative solutions can be used to provide the information for numerical purposes. These information can be extracted in two ways: one is to find an approximation of the numerical flux employed in the numerical method and the other is to find an approximation to a state and then evaluate the numerical flux in this state. The approximate Riemann solvers do not need an iteration process since they approximate the solution for the state required to evaluate the flux.

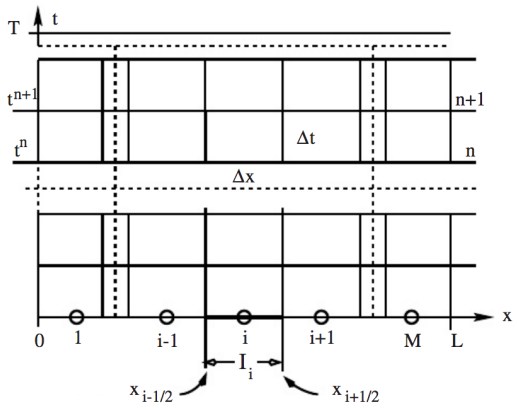

Figure 3.2: Discretisation of domain $[0, L]$ into M finite volumes I_i (computing cells) [79].

Among the numerical schemes found in literature, Rusanov and MacCormack numerical schemes have been chosen in this thesis to solve the problem of propellant combustion. Throughout this chapter, not only these two, but also Lax-Wendroff scheme, used by the authors already mentioned in the literature review, will be presented.

3.1 Rusanov numerical scheme

Rusanov scheme [80] is particular case of HLL (Harten Lax and van Leer) Riemann solver [79]. The structure of the approximate solution of the HLL Riemann problem can be seen in Figure 3.3 which consists of three constant states separated by two waves. In this approach, an approximation for the intercell numerical flux is obtained directly.

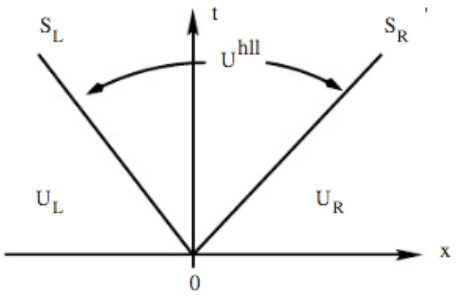

Figure 3.3: Approximate HLL Riemann Solver [79].

The approximation consist in finding, for each interface between two cells, the approximate numerical flow that will be an average value of the numerical flows computed for each cell in the previous step time, corrected with a factor. This factor is proportional to the difference of conservative variables of each cell in the previous step time and a positive speed value S^+, so the numerical flux at each interface is computed as,

$$\boldsymbol{F}^n_{j+1/2} = \frac{1}{2}\left(\boldsymbol{F}\left(\overline{T_s}\boldsymbol{U}^n_L\right) + \boldsymbol{F}\left(\overline{T_s}\boldsymbol{U}^n_R\right) - S^+\left(\boldsymbol{U}^n_R - \boldsymbol{U}^n_L\right)\right) \tag{3.9}$$

where R and L stand for right and left respectively, $\boldsymbol{F}^n_{j+1/2}$ is the flux in the interface, $\boldsymbol{F}\left(\overline{T_s}\boldsymbol{U}^n_L\right)$ and $\boldsymbol{F}\left(\overline{T_s}\boldsymbol{U}^n_R\right)$ are the convective fluxes evaluated in the previous time step in the left and right cells

respectively and S^+ is a positive value of speed calculated by means of the wave speeds S_L and S_R being,

$$S_L = min\left\{u_L - c_L, u_R - c_R\right\},\ S_R = max\left\{u_L + c_L, u_R + c_R\right\} \tag{3.10}$$

and therefore,

$$S^+ = max\left\{\left|u_L - c_L\right|, \left|u_R - c_R\right|, \left|u_L + c_L\right|, \left|u_R + c_R\right|\right\} \tag{3.11}$$

3.2 MacCormack and MacCormack-TVD numerical scheme

MacCormack numerical method of second order in both time and space which is presented to solve Navier-Stokes equations developed by Robert MacCormack [81]. According to according to Lee and Kim [82], the scheme can be written as a variation of two steps Lax-Wendroff scheme [83], one predictor and one corrector.

Considering the one dimensional problem,

$$\frac{\partial \boldsymbol{U}}{\partial t} + \frac{\partial \boldsymbol{F}}{\partial x} = \boldsymbol{S}(\boldsymbol{U}) \tag{3.12}$$

the MacCormack method can be defined in two steps with the following expressions,

$$\overline{\boldsymbol{U}}_j^p = \boldsymbol{U}_j^n - \frac{\triangle t}{\triangle x}\left(\boldsymbol{F}_{j+1}^n - \boldsymbol{F}_j^n\right) + \triangle t \boldsymbol{S}(\boldsymbol{U}_j^n) \tag{3.13}$$

$$\overline{\boldsymbol{U}}_j^c = \boldsymbol{U}_j^n - \frac{\triangle t}{\triangle x}\left(\boldsymbol{F}_j^p - \boldsymbol{F}_{j-1}^p\right) + \triangle t \boldsymbol{S}(\boldsymbol{U}_j^p) \tag{3.14}$$

$$\boldsymbol{U}_j^{n+1} = \frac{1}{2}\left(\overline{\boldsymbol{U}}_j^p + \overline{\boldsymbol{U}}_j^c\right) \tag{3.15}$$

According to Liang et al. [84] the use of a total variation diminishing (TVD) of the MacCormack scheme will reproduce all flow regimes in an accurate way. Considering the previous equation system (3.1), the scheme can be written as,

$$\overline{\boldsymbol{U}}_j^p = \boldsymbol{U}_j^n - \frac{\triangle t}{\triangle x}\left(\boldsymbol{F}_j^n - \boldsymbol{F}_{j-1}^n\right) + \triangle t \boldsymbol{S}(\boldsymbol{U}_j^n) \tag{3.16}$$

$$\overline{\boldsymbol{U}}_j^c = \boldsymbol{U}_j^n - \frac{\triangle t}{\triangle x}\left(\boldsymbol{F}_{j+1}^p - \boldsymbol{F}_j^p\right) + \triangle t \boldsymbol{S}(\boldsymbol{U}_j^p) \tag{3.17}$$

$$\boldsymbol{U}_j^{n+1} = \frac{1}{2}\left(\overline{\boldsymbol{U}}_j^p + \overline{\boldsymbol{U}}_j^c\right) + [G(r_j^+) + G(r_{j+1}^-)]\Delta \boldsymbol{U}_{j+1/2}^n - [G(r_{j-1}^+) + G(r_j^-)]\Delta \boldsymbol{U}_{j-1/2}^n \tag{3.18}$$

where $G(x)$ is a function defined as,

$$G(x) = 0.5C[1 - \varphi(x)] \tag{3.19}$$

with $\varphi(x)$ a flow limiting function such as,

$$\varphi(x) = max(0, min(2x, 1)) \tag{3.20}$$

and C a variable defined as,

$$C = \begin{cases} CFL \cdot (1 - CFL) & CFL \leq 0.5 \\ 0.25 & CFL > 0.5 \end{cases} \tag{3.21}$$

where CFL is the Courant-Friedrichs–Lewy factor.
Vectors $\triangle \boldsymbol{U}^n_{j+1/2}$ and $\triangle \boldsymbol{U}^n_{j-1/2}$ are defined as:

$$\triangle \boldsymbol{U}^n_{j+1/2} = \boldsymbol{U}^n_{j+1} - \boldsymbol{U}^n_j \tag{3.22}$$

$$\triangle \boldsymbol{U}^n_{j-1/2} = \boldsymbol{U}^n_j - \boldsymbol{U}^n_{j-1} \tag{3.23}$$

The values of r^+_j and r^-_j depend on the definition of equations (3.22) and (3.23),

$$r^+_j = \frac{\triangle \boldsymbol{U}^n_{j-1/2} \cdot \triangle \boldsymbol{U}^n_{j+1/2}}{\triangle \boldsymbol{U}^n_{j+1/2} \cdot \triangle \boldsymbol{U}^n_{j+1/2}} \tag{3.24}$$

$$r^-_j = \frac{\triangle \boldsymbol{U}^n_{j-1/2} \cdot \triangle \boldsymbol{U}^n_{j+1/2}}{\triangle \boldsymbol{U}^n_{j-1/2} \cdot \triangle \boldsymbol{U}^n_{j-1/2}} \tag{3.25}$$

According to Liang et al. [84] , the use of this scheme will prevent numerical oscillation close to the sharp gradient regions.

3.3 Lax-Wendroff scheme

Considering the Initial Boundary Value Problem (IBVP) in one dimension,

$$\left.\begin{array}{c} PDE:\ u_t + \lambda u_x = 0 \\ IC:\ u(x,0) = u_0(x) \\ BC:\ u(0,t) = u_l(t),\ u(L,t) = u_r(t) \end{array}\right\} \tag{3.26}$$

where l stands for left and r for right.
The method express de solution at $u^{n+1}_i = u(x_i, t_{n+1})$ as a Taylor series in time,

$$u^{n+1}_i = u^n_i + \triangle t \frac{\partial u^n_i}{\partial t} + \frac{1}{2}\triangle t^2 \frac{\partial^2 u^n_i}{\partial t^2} + \mathcal{O}\left(\triangle t^3\right) \tag{3.27}$$

By means of the Cauchy-Kowalewski procedure, the time derivatives can be replaced by space derivatives,

$$\left.\begin{array}{l} \frac{\partial q(x,t)}{\partial t} = -\lambda \frac{\partial q(x,t)}{\partial x} \\ \frac{\partial q^2(x,t)}{\partial t^2} = -\lambda^2 \frac{\partial q^2(x,t)}{\partial x^2} \\ \frac{\partial q^k(x,t)}{\partial t^k} = (-\lambda)^k \frac{\partial q^k(x,t)}{\partial x^k} \end{array}\right\} \tag{3.28}$$

Therefore, equation (3.27) can be written,

$$u^{n+1}_i = u^n_i + \triangle t \lambda \frac{\partial u^n_i}{\partial x} + \frac{1}{2}\triangle t^2 \lambda^2 \frac{\partial^2 u^n_i}{\partial x^2} + \mathcal{O}\left(\triangle t^3\right) \tag{3.29}$$

If the derivatives are approximated by central finite differences (see Figure 3.4)

$$\frac{\partial u^n_i}{\partial x} = \frac{u^n_{i+1} - u^n_{i-1}}{2\Delta x},\ \frac{\partial^2 u^n_i}{\partial x^2} = \frac{u^n_{i+1} - 2u^n_i + u^n_{i-1}}{\Delta x^2} \tag{3.30}$$

then the Lax-Wendroff scheme,

$$u^{n+1}_i = \frac{1}{2}c\left(1+c\right)u^n_{i-1} + \left(1+c^2\right)u^n_i - \frac{1}{2}c\left(1-c\right)u^n_{i+1} \tag{3.31}$$

where $c = \frac{\lambda \triangle t}{\triangle x}$ is the Courant number, or the CFL number and λ is the characteristic speed.

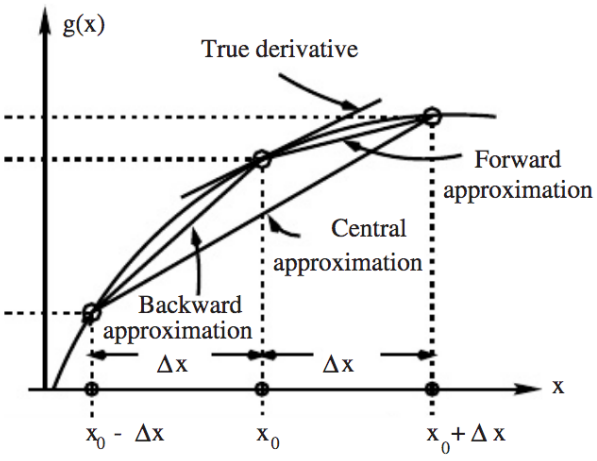

Figure 3.4: Finite differences approximation to the first derivative of a function $g(x)$ [79].

The conventional finite difference method of Lax-Wendroff can also be written in conservative form.

Considering the one-dimensional homogeneous problem,

$$\frac{\partial \boldsymbol{U}}{\partial t} + \frac{\partial \boldsymbol{F}}{\partial x} = 0 \tag{3.32}$$

A conservative numerical method to solve the previous equation is the scheme in finite volumes,

$$\boldsymbol{U}_j^{n+1} = \boldsymbol{U}_j^n - \frac{\triangle t}{\triangle x}\left(\boldsymbol{F}_{j+1/2} - \boldsymbol{F}_{j-1/2}\right) \tag{3.33}$$

where $\boldsymbol{F}_{j+1/2}$ is the numerical flux which for the two-step version of the Lax-Wendroff method is written as,

$$\boldsymbol{F}_{j+1/2} = \boldsymbol{F}(\boldsymbol{U}_{j+1/2}^{n+1/2}) \tag{3.34}$$

being $\boldsymbol{U}_{j+1/2}^{n+1/2}$ defined with the following expression,

$$\boldsymbol{U}_{j+1/2}^{n+1/2} = \frac{1}{2}\left(\boldsymbol{U}_j^n + \boldsymbol{U}_{j+1}^n\right) + \frac{1}{2}\frac{\triangle t}{\triangle x}\left(\boldsymbol{F}_j^n - \boldsymbol{F}_{j+1}^n\right) \tag{3.35}$$

Chapter 4

Combustion modelling and results

4.1 Combustion of granulated propellants

In this subsection a two-phase model which considers a set of equations of continuity, momentum and energy for the solid and the gas phase to describe the transient behaviour of this combustion process is presented. Firstly, the physical model and the constitutive relations considered to close the model are described. Afterwards, the numerical schemes used for the integration of the model are presented. Finally, the results provided by the code are compared with data available in the literature.

4.1.1 Physical model

4.1.1.1 Governing equations

From all models found in literature to solve the problem of combustion of granulated propellants, the one which is found more suitable is the one proposed by Hoffman and Krier [28]. The considerations described by Gidaspow [85] are included in this model. Gidaspow [85] insists on including the time derivative of the porosity into the energy equation in order to satisfy the inequality of Clausius-Duhem. Another key aspect is the definition of a pressure into the solid which is the addition of gas pressure and inter-granular stress. In that way, the differential equation system considered in this document can be expressed as:

$$\frac{\partial\left(\alpha\rho_g\right)}{\partial t}+\overrightarrow{\nabla}\cdot\left(\alpha\rho_g\overrightarrow{u}_g\right)=\dot{\Gamma} \tag{4.1}$$

$$\frac{\partial\left(\alpha\rho_g\overrightarrow{u}_g\right)}{\partial t}+\overrightarrow{\nabla}\cdot\left(\alpha\rho_g\overrightarrow{u}_g\otimes\overrightarrow{u}_g+\alpha p_g\overrightarrow{I}\right)=p_g\frac{\partial\alpha}{\partial x}+\dot{\Gamma}\overrightarrow{u}_p-\overrightarrow{F}_D \tag{4.2}$$

$$\frac{\partial\left(\alpha\rho_g E_g\right)}{\partial t}+\overrightarrow{\nabla}\cdot\left(\alpha\rho_g\overrightarrow{u}_g\left(E_g+\frac{p_g}{\rho_g}\right)\right)=-p_g\frac{\partial\alpha}{\partial t}+\dot{\Gamma}\left(E^g_{chem}+\frac{|\overrightarrow{u}_p|^2}{2}\right)-\overrightarrow{u}_p\overrightarrow{F}_D-\dot{Q} \tag{4.3}$$

$$\frac{\partial\left(\left(1-\alpha\right)\rho_p\right)}{\partial t}+\overrightarrow{\nabla}\cdot\left(\left(1-\alpha\right)\rho_p\overrightarrow{u}_p\right)=-\dot{\Gamma} \tag{4.4}$$

$$\frac{\partial\left(\left(1-\alpha\right)\rho_p\overrightarrow{u}_p\right)}{\partial t}+\overrightarrow{\nabla}\cdot\left(\left(1-\alpha\right)\rho_p\overrightarrow{u}_p\otimes\overrightarrow{u}_p+\left(1-\alpha\right)p_p\overrightarrow{I}\right)=-p_p\frac{\partial\alpha}{\partial x}-\dot{\Gamma}\overrightarrow{u}_p+\overrightarrow{F}_D \tag{4.5}$$

$$\frac{\partial\left(\left(1-\alpha\right)\rho_p E_p\right)}{\partial t}+\overrightarrow{\nabla}\cdot\left(\left(1-\alpha\right)\rho_p\overrightarrow{u}_p\left(E_p+\frac{p_p}{\rho_p}\right)\right)= p_g\frac{\partial\alpha}{\partial t}+\dot{\Gamma}\left(E^p_{chem}+\frac{|\overrightarrow{u}_p|^2}{2}\right)+\overrightarrow{u}_p\overrightarrow{F}_D+\dot{Q} \tag{4.6}$$

$$p_p = p_g + \tau_p \tag{4.7}$$

where the chemical energy of the gas phase is defined as,

$$E^g_{chem} = E_{chem} - E^p_{chem} \tag{4.8}$$

4.1.1.2 Particle momentum conservation equation modification

According to Hoffman and Krier [28], inter-granular stress formulation does not prevent particles compaction below minimum compaction. To consider that limitation, they proposed a modification of the momentum equation of the particle, so the particles cannot accelerate once reached that porosity value. If that limitation is imposed, the equation (4.5) can be rewritten to:

$$\frac{\partial\left(\left(1-\alpha\right)\rho_p\overrightarrow{u}_p\right)}{\partial t} + \overrightarrow{\nabla}\cdot\left(\left(1-\alpha\right)\rho_p\overrightarrow{u}_p\otimes\overrightarrow{u}_p + \left(1-\alpha\right)p_p\overrightarrow{I}\left(1-f\left(\alpha\right)\right)\right) = - p_p\frac{\partial\left(\alpha\left(1-f\left(\alpha\right)\right)\right)}{\partial x} - \dot{\Gamma}\overrightarrow{u}_p + \left(1-f\left(\alpha\right)\right)\overrightarrow{F}_D \tag{4.9}$$

where $f\left(\alpha\right)$ is defined as:

$$f\left(\alpha\right) = \begin{cases} 0 & \alpha > \alpha_c \\ \left(\frac{\alpha_c-\alpha}{\alpha_c-\alpha_{min}}\right)^l & \alpha_{min} \leq \alpha \leq \alpha_c \\ 1 & \alpha < \alpha_{min} \end{cases} \tag{4.10}$$

where l is a constant value that considers the properties of the particles framework, α_{min} and α_c are the minimum and critical porosity respectively.

Therefore, the equation system could be finally written as,

$$\frac{\partial\left(\alpha\rho_g\right)}{\partial t} + \overrightarrow{\nabla}\cdot\left(\alpha\rho_g\overrightarrow{u}_g\right) = \dot{\Gamma} \tag{4.11}$$

$$\frac{\partial\left(\alpha\rho_g\overrightarrow{u}_g\right)}{\partial t} + \overrightarrow{\nabla}\cdot\left(\alpha\rho_g\overrightarrow{u}_g\otimes\overrightarrow{u}_g + \alpha p_g\overrightarrow{I}\right) = p_g\frac{\partial\alpha}{\partial x} + \dot{\Gamma}\overrightarrow{u}_p - \overrightarrow{F}_D \tag{4.12}$$

$$\frac{\partial\left(\alpha\rho_g E_g\right)}{\partial t} + \overrightarrow{\nabla}\cdot\left(\alpha\rho_g\overrightarrow{u}_g\left(E_g + \frac{p_g}{\rho_g}\right)\right) = -p_g\frac{\partial\alpha}{\partial t} + \dot{\Gamma}\left(E^g_{chem} + \frac{\left|\overrightarrow{u}_p\right|^2}{2}\right) - \overrightarrow{u}_p\overrightarrow{F}_D - \dot{Q} \tag{4.13}$$

$$\frac{\partial\left(\left(1-\alpha\right)\rho_p\right)}{\partial t} + \overrightarrow{\nabla}\cdot\left(\left(1-\alpha\right)\rho_p\overrightarrow{u}_p\right) = -\dot{\Gamma} \tag{4.14}$$

$$\frac{\partial\left(\left(1-\alpha\right)\rho_p\overrightarrow{u}_p\right)}{\partial t} + \overrightarrow{\nabla}\cdot\left(\left(1-\alpha\right)\rho_p\overrightarrow{u}_p\otimes\overrightarrow{u}_p + \left(1-\alpha\right)p_p\overrightarrow{I}\left(1-f\left(\alpha\right)\right)\right) = - p_p\frac{\partial\left(\alpha\left(1-f\left(\alpha\right)\right)\right)}{\partial x} - \dot{\Gamma}\overrightarrow{u}_p + \left(1-f\left(\alpha\right)\right)\overrightarrow{F}_D \tag{4.15}$$

$$\frac{\partial\left(\left(1-\alpha\right)\rho_p E_p\right)}{\partial t} + \overrightarrow{\nabla}\cdot\left(\left(1-\alpha\right)\rho_p\overrightarrow{u}_p\left(E_p + \frac{p_p}{\rho_p}\right)\right) = p_g\frac{\partial\alpha}{\partial t} + \dot{\Gamma}\left(E^p_{chem} + \frac{\left|\overrightarrow{u}_p\right|^2}{2}\right) + \overrightarrow{u}_p\overrightarrow{F}_D + \dot{Q} \tag{4.16}$$

$$p_p = p_g + \tau_p \tag{4.17}$$

4.1.1.3 Source terms

In Chapter 2, a deep analysis of the expressions found in literature was performed. In this subsection, a summarised list of the expressions used to close the model chosen to represent the combustion of granulated propellants is done.

The first expression to be considered is the viscosity, which will be a variable used in several parameters afterwards. The formula chosen is the one provided by Hoffman and Krier [28],

$$\mu_g = \mu_{g,0}(T_g/T_{g,0})^{0.65} \tag{4.18}$$

where $\mu_{g,0}$ is the value of viscosity at 2000K and $T_{g,0}$ is 2000 K [27].

The following subsection, presents a sensitivity analysis about the expressions found in literature for drag coefficient and heat transfer coefficient and a final decision of which one is more suitable for the model developed. In order to summarise all source terms used to close the model, the two expressions finally decided will be briefly written in the following lines. The expression used finally for the drag force is,

$$F_D = \frac{\mu_g(u_g - u_p)}{d_p^2} f_{pg} \tag{4.19}$$

where f_{pg} is the drag coefficient. Butler et al. [39] present in their study an expression developed by Wilcox, Jones and Krier [40]. The use of that expression provided good result at high Reynolds numbers.

$$\begin{gathered} f_{pg} = \frac{(1-\alpha)^2}{\alpha^2} 150 + 3.89 \left(\frac{Re_p}{(1-\alpha)}\right)^{0.88} \\ 10^3 < Re_p < 2 \cdot 10^5 \end{gathered} \tag{4.20}$$

As for the interfacial heat transfer coefficient, the heat expression form is,

$$\dot{Q} = (1-\alpha)\frac{S_p}{V_p} h_c (T_g - T_p) \tag{4.21}$$

In the case of spherical particles, $S_p/V_p = 6/d_p$, and therefore the heat is defined as:

$$\dot{Q} = \frac{6(1-\alpha)}{d_p} h_c (T_g - T_p) \tag{4.22}$$

The convective heat coefficient depends of the Nusselt number (Nu) with the following expression,

$$h_c = \frac{k_g}{d_p} Nu \tag{4.23}$$

where $Pr = (c_{p,g}\mu_g)/k_g$ is the Prandtl number and k_g is the gas conductivity defined as,

$$k_g = \frac{15}{4}\frac{R_u}{M_g}\mu_g\left(\frac{4}{15}\frac{c_{v,g}M_g}{R_u} + \frac{3}{5}\right) \tag{4.24}$$

The correlation of the Nusselt number proposed by Hoffman and Krier [28], Butler et al. [39] and Butler and Krier [32] has the following form:

$$Nu = 0.65 Re_p^{0.7} Pr^{0.33} \tag{4.25}$$

The gas mass generation equation assuming that particles are spheres is related to the combustion velocity and has the following form,

$$\dot{\Gamma} = \frac{6(1-\alpha)}{d_p} \dot{r} \rho_p \tag{4.26}$$

where the combustion law is given by:

$$\dot{r} = a p_g^n \tag{4.27}$$

where a and n are vales that depend on the propellant.
As for the gas equation of state, the equation of Noble-Abel is considered.

$$p_g = \frac{\rho_g(\gamma_g - 1)e_g}{1 - \rho_g \eta_g} \tag{4.28}$$

In this model, the solid is considered incompressible. However, as presented in equation 4.17 in the model there is a solid pressure defined as the addition of gas pressure and the intergranular stress (τ_p), defined as the resistance of the particles to be compacted under a limit porosity that is the critical porosity. In this study, the authors consider the expressions proposed by Krier and Kezerle [27], Hoffman and Krier [28] and Gokhale and Krier [31].

$$\tau_p = \begin{cases} \frac{K}{(1-\alpha)}\left(\frac{1}{(1-\alpha_c)} - \frac{1}{(1-\alpha)}\right) & \alpha \leq \alpha_c \\ 0 & \alpha > \alpha_c \end{cases} \tag{4.29}$$

where K is the bulk modulus and α_c is the critical porosity under which appears the intergranular stress.

4.1.2 Numerical method

4.1.2.1 Numerical method proposed to solve equation system

The system of equations (4.11)-(4.17) can be written in vector form as:

$$\frac{\partial \boldsymbol{U}}{\partial t} + \nabla \cdot \mathcal{H} = \boldsymbol{S}(\boldsymbol{U}) \tag{4.30}$$

where $(\boldsymbol{U})$ is the conserved variables vector, $(\mathcal{H})$ is the flux tensor and $(\boldsymbol{S})$ the source terms which are written below,

$$\boldsymbol{U} = \begin{pmatrix} \alpha\rho_g \\ \alpha\rho_g \overrightarrow{u}_g \\ \alpha\rho_g E_g \\ (1-\alpha)\rho_p \\ (1-\alpha)\rho_p \overrightarrow{u}_p \\ (1-\alpha)\rho_p E_p \end{pmatrix}, \tag{4.31}$$

$$\mathcal{H} = \begin{pmatrix} \alpha\rho_g \overrightarrow{u}_g \\ \alpha\rho_g \overrightarrow{u}_g \otimes \overrightarrow{u}_g + \alpha p_g \overrightarrow{I} \\ \alpha\rho_g \overrightarrow{u}_g \left(E_g + \frac{p_g}{\rho_g}\right) \\ (1-\alpha)\rho_p \overrightarrow{u}_p \\ (1-\alpha)\rho_p \overrightarrow{u}_p \otimes \overrightarrow{u}_p + (1-\alpha) p_p \overrightarrow{I}\,(1 - f(\alpha)) \\ (1-\alpha)\rho_p \overrightarrow{u}_p \left(E_p + \frac{p_p}{\rho_p}\right) \end{pmatrix}, \tag{4.32}$$

$$\boldsymbol{S}(\boldsymbol{U}) = \begin{pmatrix} \dot{\Gamma} \\ p_g \frac{\partial \alpha}{\partial x} + \dot{\Gamma}\overrightarrow{u}_p - \overrightarrow{F}_D \\ -p_g \frac{\partial \alpha}{\partial t} + \dot{\Gamma}\left(E^g_{chem} + \frac{|\overrightarrow{u}_p|^2}{2}\right) - \overrightarrow{u}_p \overrightarrow{F}_D - \dot{Q} \\ -\dot{\Gamma} \\ -(1 - f(\alpha)) p_p \frac{\partial \alpha}{\partial x} - \dot{\Gamma}\overrightarrow{u}_p + (1 - f(\alpha))\overrightarrow{F}_D \\ p_g \frac{\partial \alpha}{\partial t} + \dot{\Gamma}\left(E^p_{chem} + \frac{|\overrightarrow{u}_p|^2}{2}\right) + \overrightarrow{u}_p \overrightarrow{F}_D + \dot{Q} \end{pmatrix} \tag{4.33}$$

To solve the system of equation (4.30), Rusanov and MacCormack schemes detailed in chapter 3 are used.

4.1.2.2 Time integration

The time step to solve the equation system of previous subsection is calculated as,

$$\triangle t = CFL{\cdot}min\left[min\left(\frac{\triangle x_j}{|\overrightarrow{u}_g| + c_g}\right), min\left(\frac{\triangle x_j}{|\overrightarrow{u}_p| + c_p}\right)\right] \tag{4.34}$$

where the speed of sound of the gas phase, c_g ,is calculated as,

$$c_g = \sqrt{\frac{\gamma_g p_g}{\rho_g\left(1 - \eta\rho_g\right)}} \tag{4.35}$$

and the one of the solid phase,

$$c_p = \sqrt{\frac{K_0}{\rho_p}} \tag{4.36}$$

where K_0 is the initial bulk modulus which value has been taken from Hoffman and Krier [28] and ρ_p is the density of the propellant. Both values are detailed in Table 4.1.

4.1.3 Sensitivity analysis

Due to the amount of different initiation conditions as well as expressions for the source terms found in the literature, a sensitivity analysis in order to chose the most suitable one for the calculation is necessary. Therefore, the Nusselt number, which directly determines the convective heat transfer coefficient, the friction coefficient and the influence of the initiation conditions are studied throughout this section.

To perform this analysis, a closed and insulated tube of 0.15 m length ignited in the left side has been chosen. Therefore, there is not transfer of mass and heat through the walls of the tube being the boundary conditions zero gradient for all variables despite velocity which is assumed to be zero at the right and left walls.

The necessary input data for the calculation is obtained from the existing bibliography and it is written in Table 4.1. The initial distributions of pressure and temperature depend on the initiation test considered. For the sensitivity analysis of heat transfer coefficient and friction coefficient, pressure and temperature distribution corresponding to Test 1 are used. The code has been run using Rusanov and MacCormack-TVD numerical schemes and their results have been compared.

4.1.3.1 Heat transfer coefficient effect

The values obtained for each expression of the Nusselt number have been depicted against Reynolds number as shown in Figure (4.1). As it can be observed, the values adopted by the Nusselt number proposed by Gokhale and Krier [31] and Krier and Kezerle [27] (Nusselt 2) are similar to those of Hoffman and Krier [28] and those from Butler et al. [32] (Nusselt 3). However, the results obtained with Nusselt 1 present higher differences compared with the other two. This behaviour is the same regardless the value of porosity used.

Distributions of pressure, porosity and gas speed has been obtained for every Nusselt number fixing the correlation of friction coefficients used for all cases. The results are depicted in Figures from 4.2 to 4.4. As can be seen in Figure 4.2, for coefficient Friction 1, the results obtained by using Nusselt 2 and Nusselt 3 expressions are very similar appearing slight differences after $60\,\mu s$. The distributions of the variables obtained with Nusselt 1 at $20\,\mu s$ are the same as the ones obtained with Nusselt 2 and 3 but differences start to appear in $40\,\mu s$ and are very visible at $60\,\mu s$. Being the results obtained with Rusanov and MacCormack-TVD numerical schemes alike.

The behaviour of the variables obtained when using coefficient Friction 2 and 3 (Figures 4.3 and 4.4) is exactly the same that the one with Friction 1.

Parameter	Value	Units
α_c	0.4	
α_{min}	0.2595	
ρ_p	1580.52	kg/m^3
c_{vg}	1776.96	J/kgK
γ_g	1.25	
c_{vp}	1269.27	J/kgK
K	$48.8 \cdot 10^6$	Pa
K_0	$1.38 \cdot 10^9$	Pa
E_{chem}	$5.49 \cdot 10^6$	J/kg
E^p_{chem}	$0.22 \cdot 10^6$	J/kg
η	$1.08 \cdot 10^{-3}$	
$\mu_{g,0}$	$4.45 \cdot 10^{-5}$	Ns/m^2
α_0	0.4	
$u_{g0} = u_{p0}$	0	(m/s)

Table 4.1: Input data.

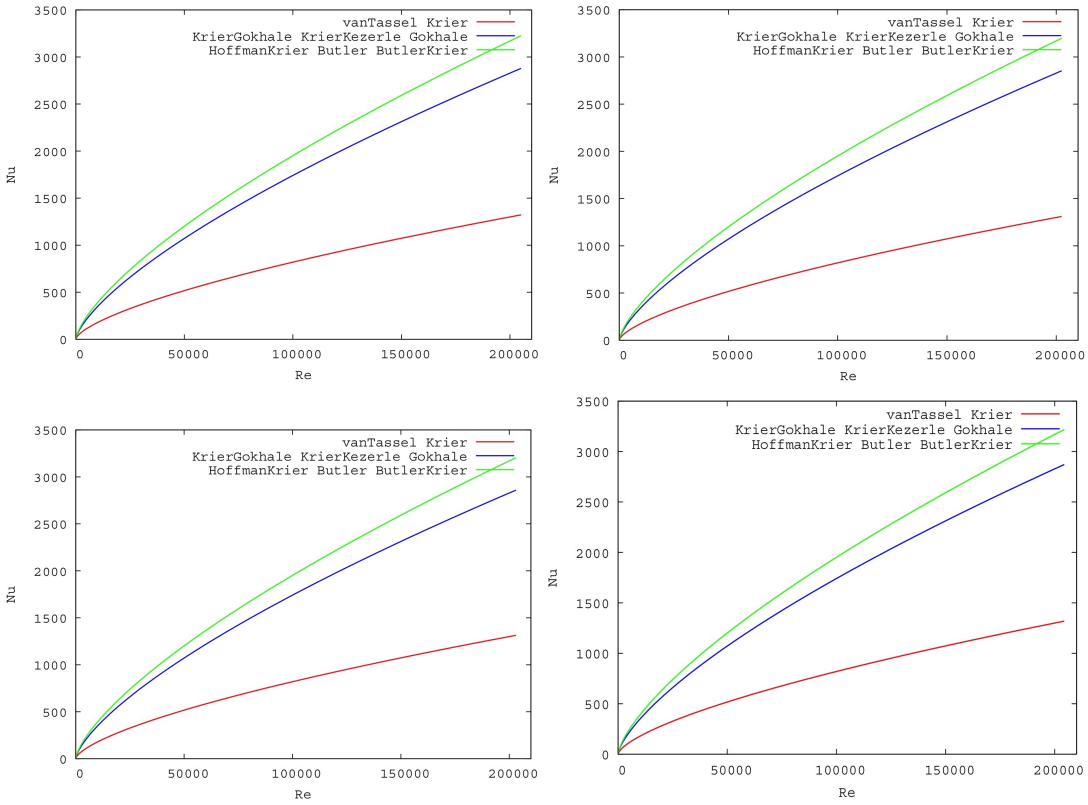

Figure 4.1: Influence of Reynolds number in the Nusselt number for several values of porosity 0.6 (above-left), 0.5 (above-right), 0.4 (below-left) and 0.3 (below-right).

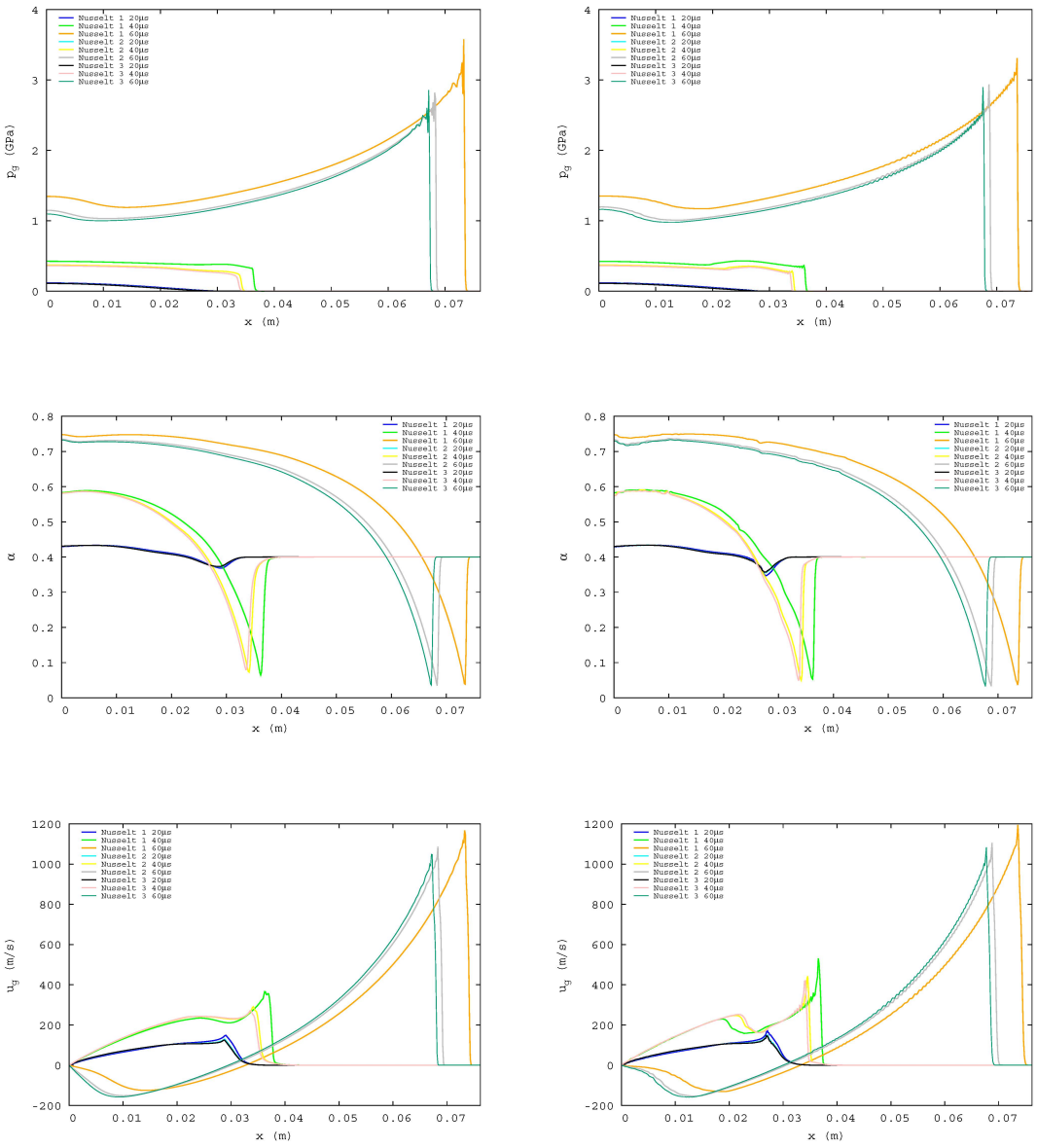

Figure 4.2: Distributions of pressure, porosity and gas velocity for Rusanov (left) and MacCormack-TVD (right) with Friction 1.

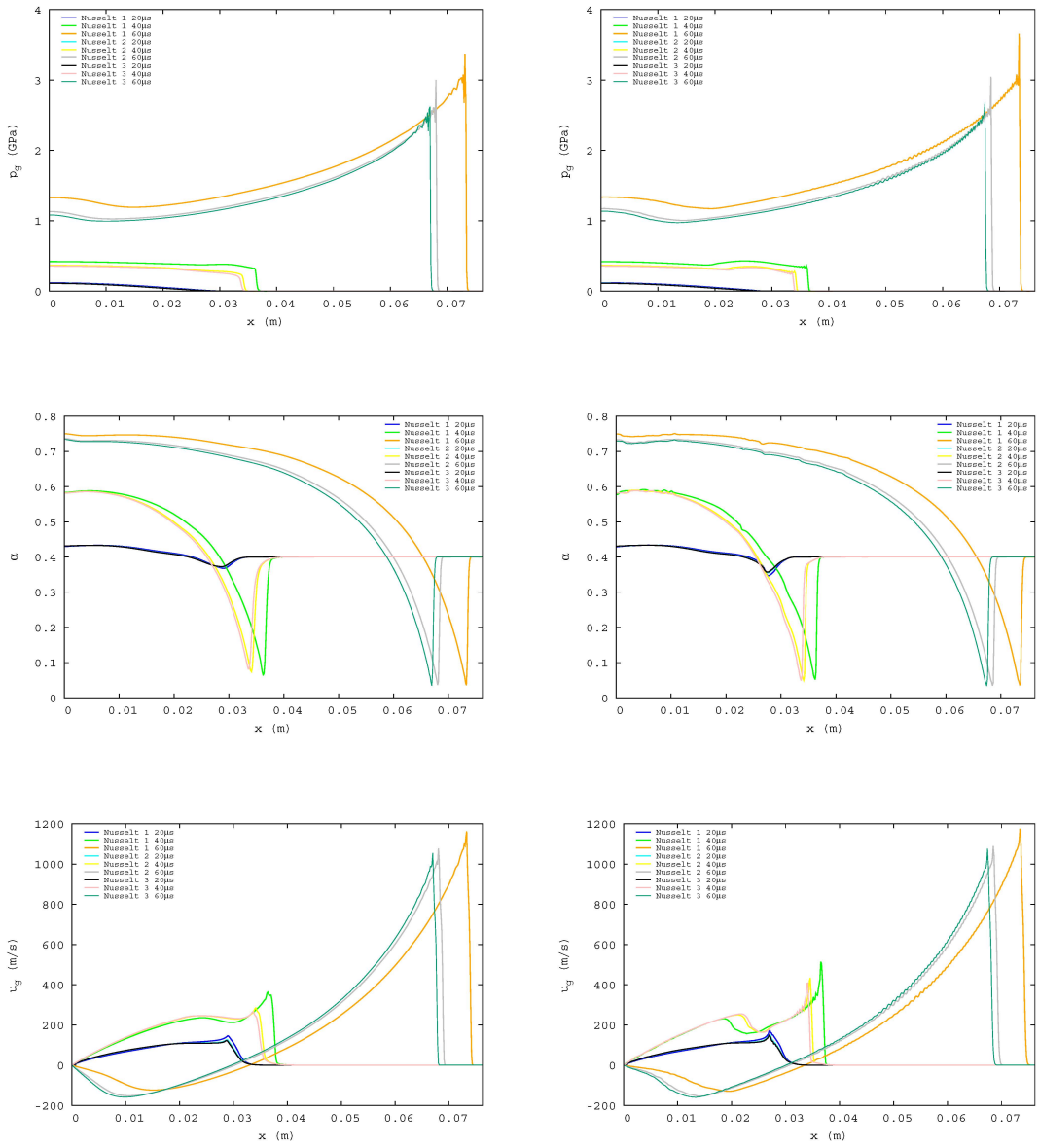

Figure 4.3: Distributions of pressure, porosity and gas velocity for Rusanov (left) and MacCormack-TVD (right) with Friction 2.

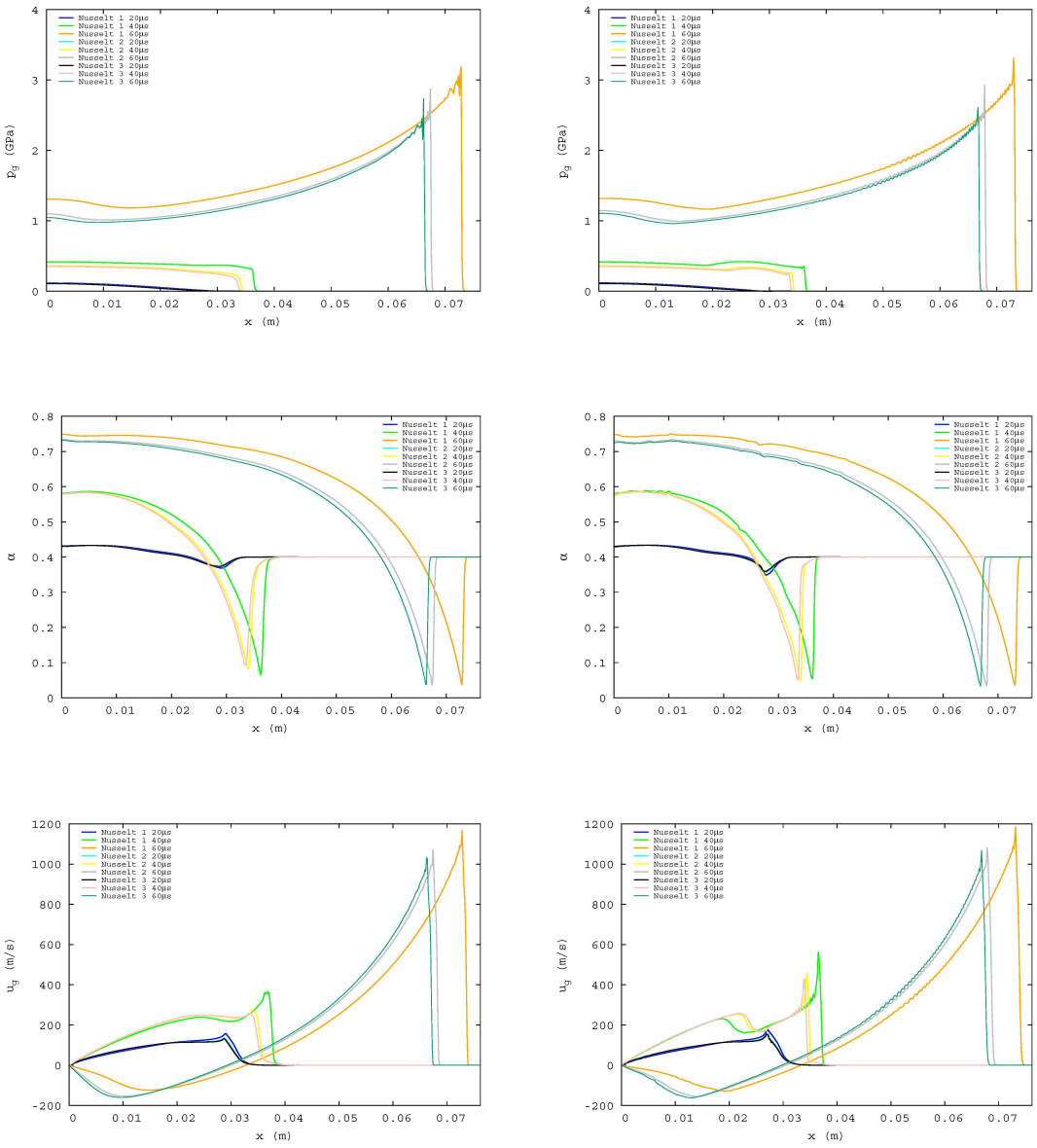

Figure 4.4: Distributions of pressure, porosity and gas velocity for Rusanov (left) and MacCormack-TVD (right) with Friction 3.

4.1.3.2 Friction coefficient effect

Distributions of pressure, porosity and gas speed has been obtained for each expression of the friction coefficient while fixing the correlation of Nusselt number are depicted in Figures 4.6, Figure 4.7 and Figure 4.8. The results obtained when using the several coefficients are similar only appearing slight differences after $60\,\mu s$. No significant mismatches between Rusanov and MacCormack-TVD schemes are present despite of the peak of gas velocity distribution at $40\,\mu s$.

As has been done for the Nusselt number, the different friction coefficients depending on the Reynolds are depicted in Figure (4.5). The values adopted with the expression proposed by Gokhale and Krier [31] and Hoffman and Krier [28] (Friction 2) and those from Butler et al. [39] (Friction 3) are very similar. However, the results obtained with Friction 1 differ from the other two. This behaviour is the same regardless the value of porosity used.

Since Butler et al. [39] claimed a better behaviour of their correlations of the coefficient of friction and Nusselt number (Friction 3 and Nusselt 3) for a wider range of Reynolds numbers, and since there is no significant differences in between the results when using one or other coefficient, these expressions will be the ones used hereafter.

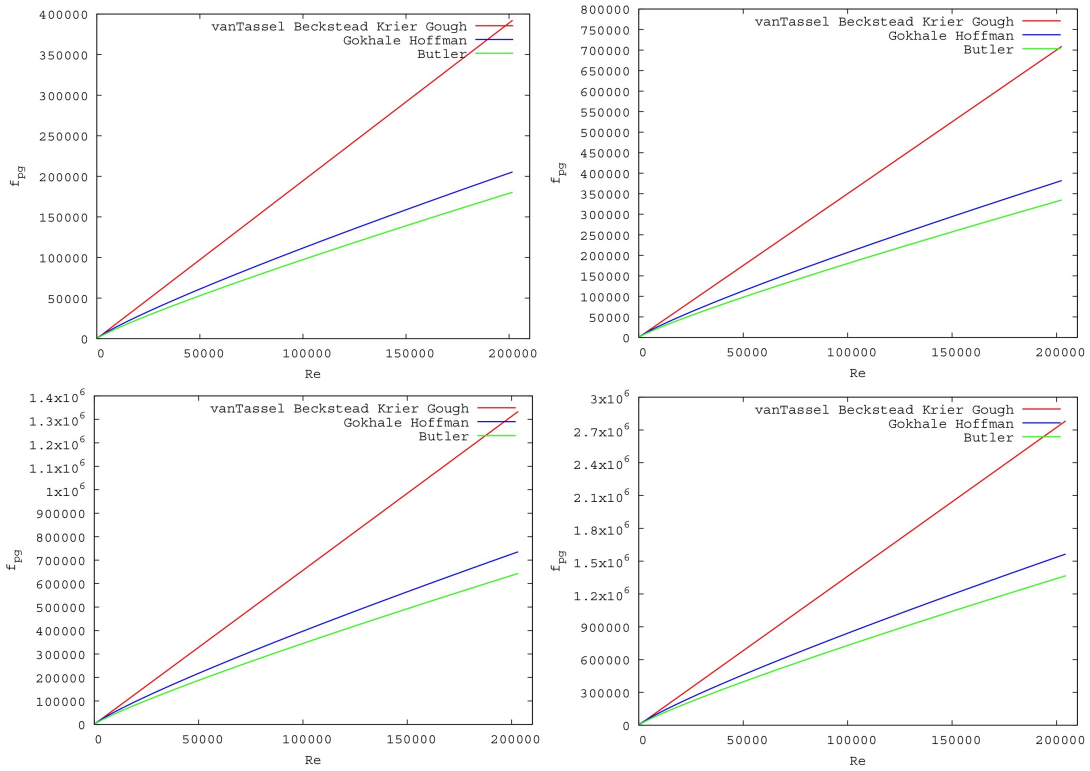

Figure 4.5: Influence of Reynolds number in the friction coefficient for several values of porosity 0.6 (above-left), 0.5 (above-right), 0.4 (below-left) and 0.3 (below-right).

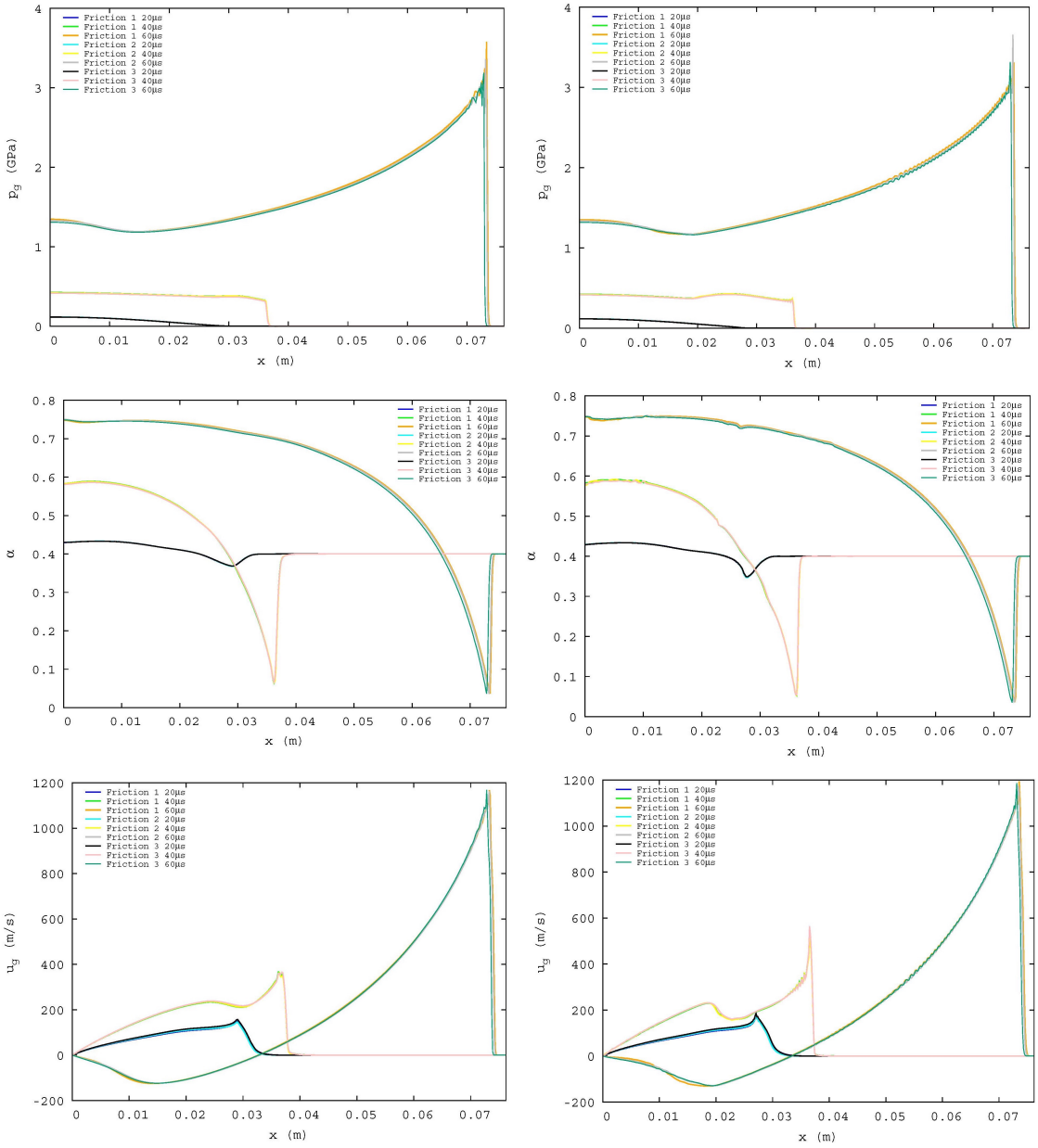

Figure 4.6: Distributions of pressure obtained with Rusanov (above) and MacCormack-TVD (below) numerical schemes for Nusselt 1.

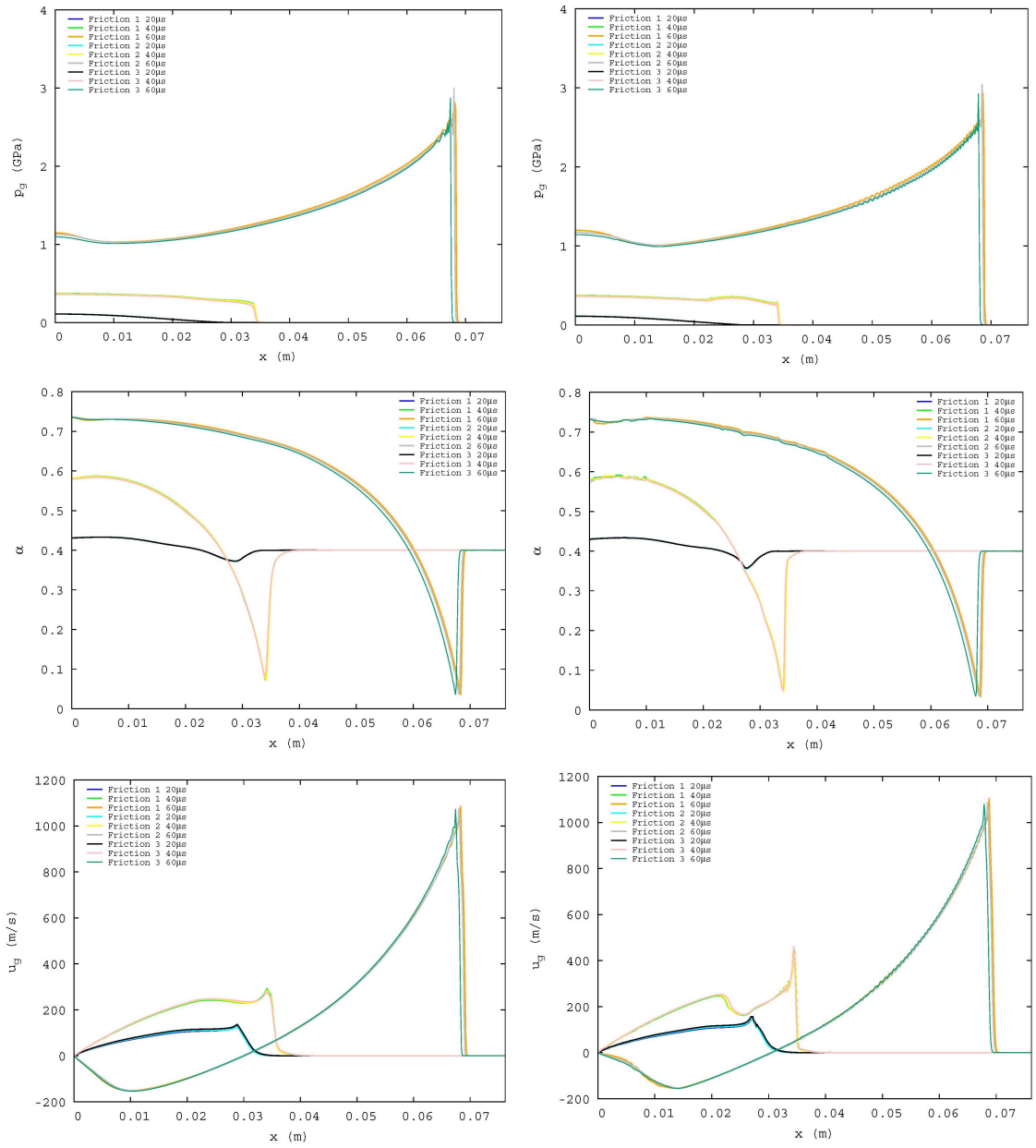

Figure 4.7: Distributions of pressure obtained with Rusanov (above) and MacCormack-TVD (below) numerical schemes for Nusselt 2.

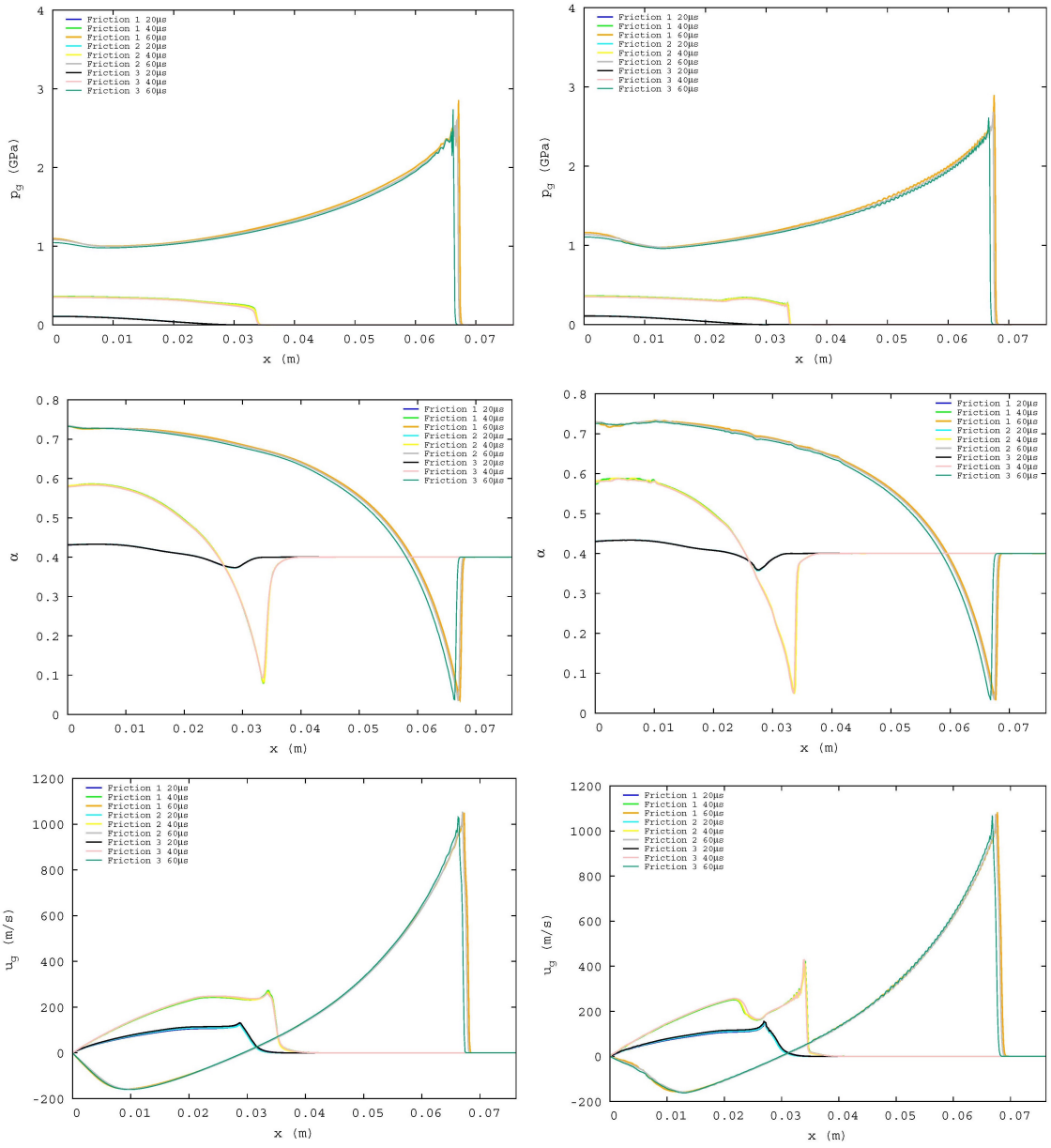

Figure 4.8: Distributions of pressure obtained with Rusanov (above) and MacCormack-TVD (below) numerical schemes for Nusselt 3

4.1.3.3 Initiation effect

The influence of the initiation in the final solution is studied by solving the equation system (4.1)-(4.7) for the initiation tests described in section 2.2.3. Pressure, porosity, gas and particle temperatures and gas velocity can be seen in Figures 4.9 to4.13. Pressure distribution results at $20\,\mu s$ are very similar, not only between both Rusanov and MacCormack-TVD schemes, but for all initiation tests. The differences start to appear slightly after $40\,\mu s$ and are very visible after $60\,\mu s$ not only in magnitude but also in the location of the peak value since the results after $60\,\mu s$ reach their maximum in differ-

ent x-coordinates depending on the initiation test used. However, Rusanov and MacCormack-TVD numerical schemes provide very similar results regardless the initiation test used. MacCormack-TVD presents oscillatory results for all test despite Test 1 which behaves smoothly. It can be concluded that Test 1 is the one which presents less oscillations in all significant variables and similar results independently the numerical scheme used. However, high values of pressure and temperature are obtained. As visible in the results, the initiation influences enormously in the results of the simulation. Due to the difficulty to identify the initiation parameters from bibliography, the results from Hoffman and Krier [28] at 20 μs are used as initial conditions in order to validate the developed code.

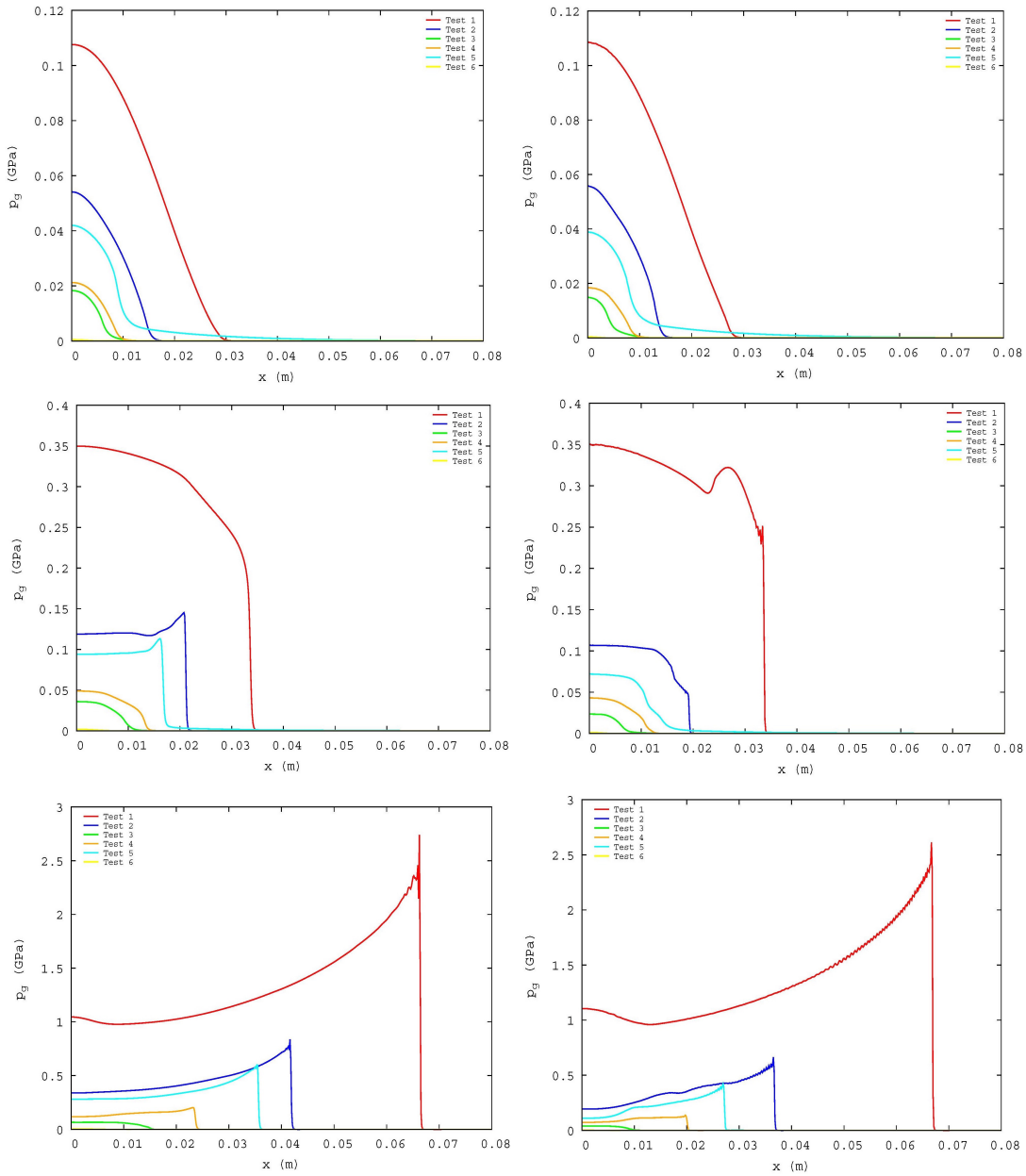

Figure 4.9: Pressure distribution obtained with Rusanov (left) and MacCormack TVD (right) for 20 μs, 40 μs and 60 μs

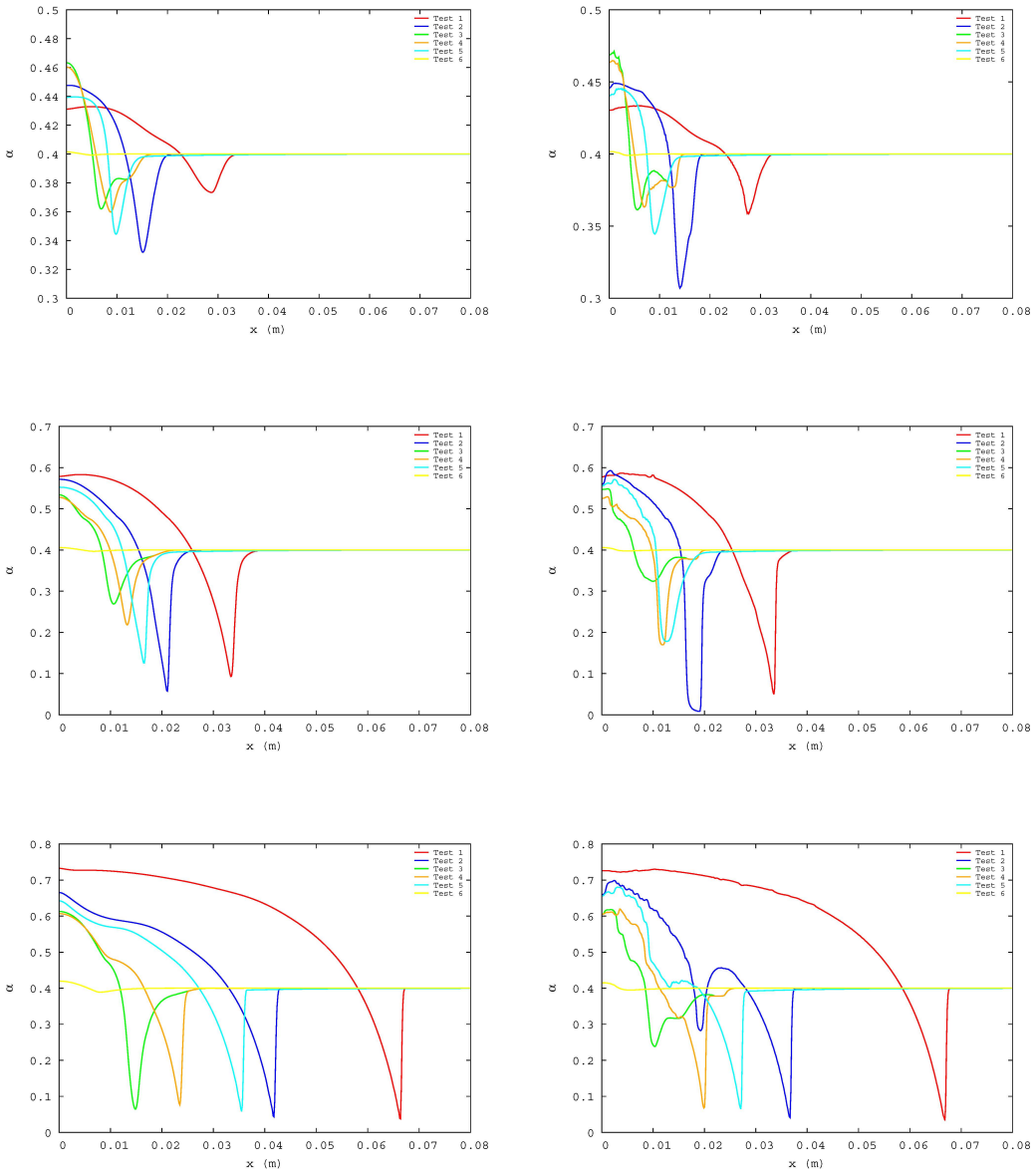

Figure 4.10: Porosity distribution obtained with Rusanov (left) and MacCormack TVD (right) for 20 μs, 40 μs and 60 μs

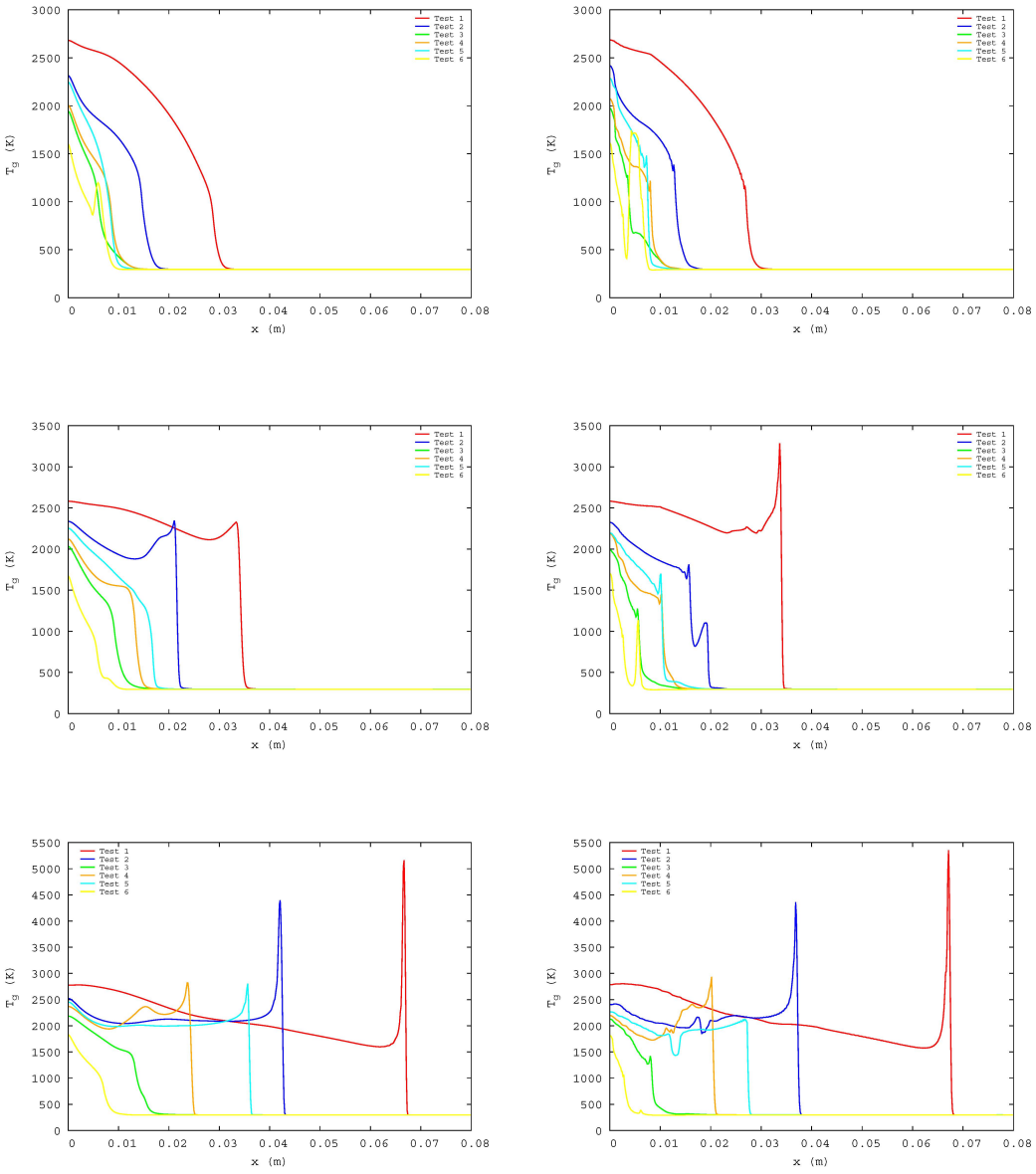

Figure 4.11: Gas temperature distribution obtained with Rusanov (left) and MacCormack TVD (right) for 20 μs, 40 μs and 60 μs.

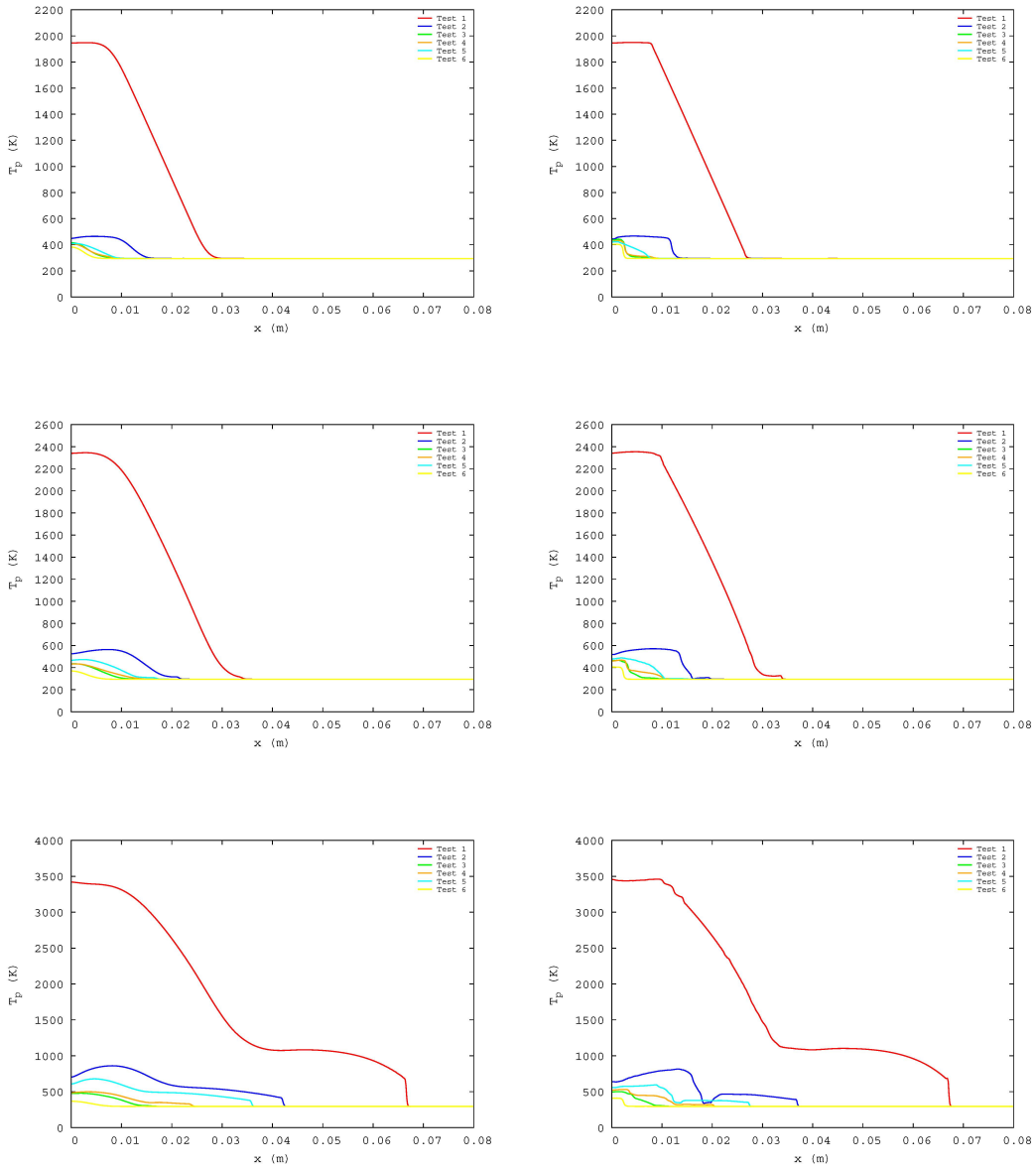

Figure 4.12: Particle temperature distribution obtained with Rusanov (left) and MacCormack TVD (right) for 20 μs, 40 μs and 60 μs.

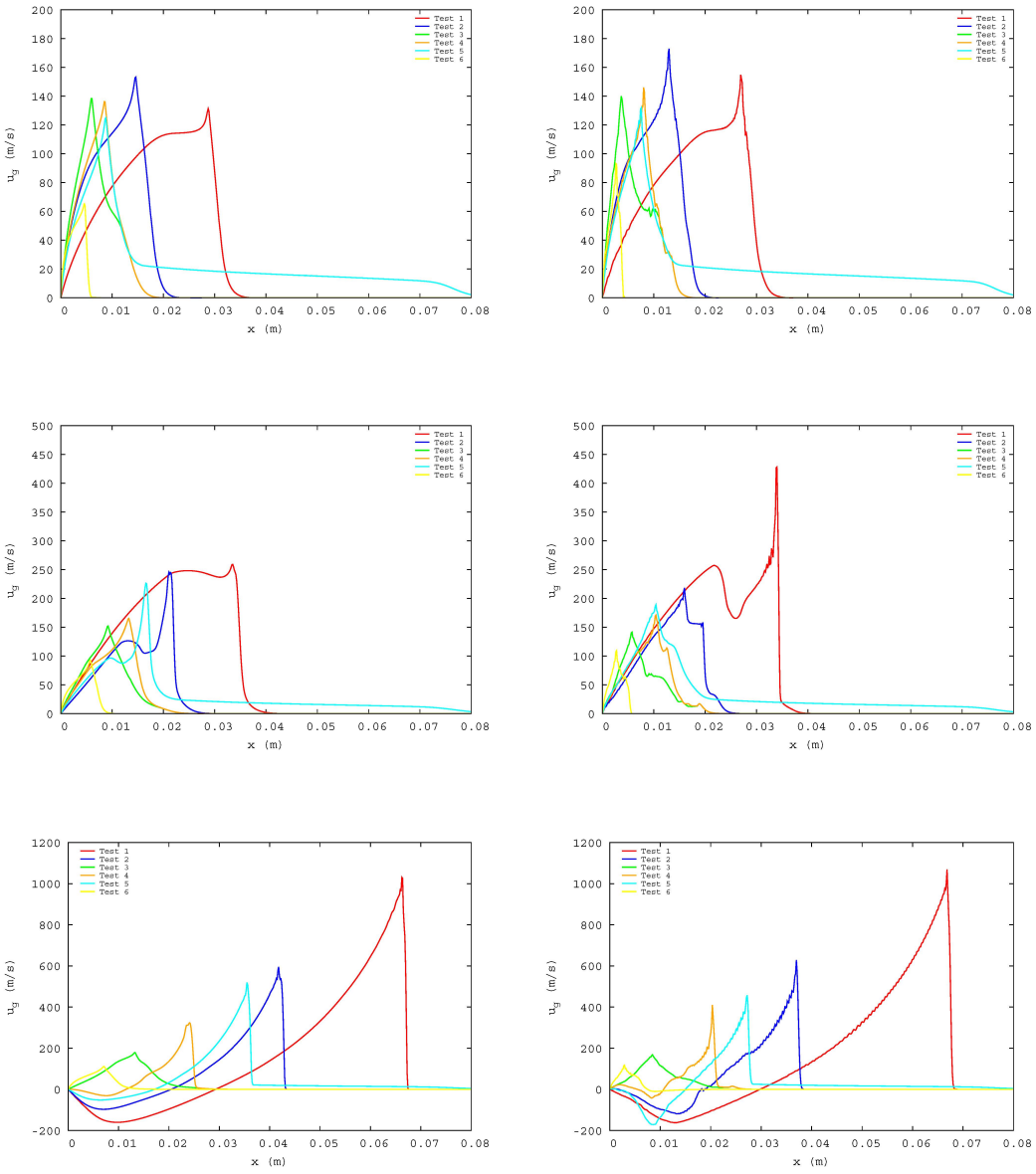

Figure 4.13: Gas velocity distribution obtained with Rusanov (left) and MacCormack TVD (right) for 20 μs, 40 μs and 60 μs.

4.1.4 Results

In this section, the results obtained once the source terms and the initiation has been defined will be presented. Firstly, Hoffman and Krier [28] equation system with their modification to the momentum conservation equation detailed in Section 4.1.1.2 is applied. As will be seen, the system of equations (4.14)- (4.17) provides a solution with a flame front similar to that obtained by Hoffman and Krier [28]. However, the values obtained for the temperature of the particle do not match the results obtained by the authors in the article. Afterwards, the results obtained when limiting directly the porosity in the equation system (4.4) - (4.7), will provide a displacement of the peak values of pressure and pressure when time is equal to 60 μs compared those obtained by Hoffman and Krier [28] in their work.

4.1.4.1 Momentum conservation equation modification

Once the modification of the momentum conservation equation of the particle is performed, the system to be considered is formed by the equations (4.14) - (4.17) and the solutions are plotted in Figures 4.14, 4.15, 4.16 and 4.17. The results obtained with Rusanov and MacCormack agree well at 40 μs and present slight but not relevant differences at 60 μs for porosity, pressure and gas temperature. The frame front distributions obtained with both numerical schemes are also very similar to the one provided by Hoffman and Krier [28] in their work. The code has been run with 250 cells and $f = 0.2$ for the solution with Rusanov scheme and 100 cell and $f = 0.11$ for MacCormack-TVD.

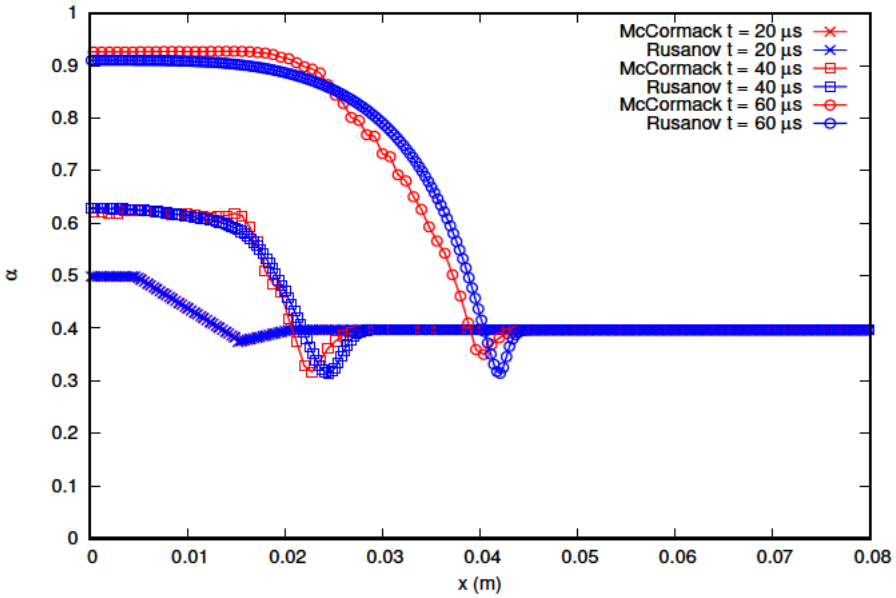

Figure 4.14: Porosity distribution for 20, 40 and 60 μs.

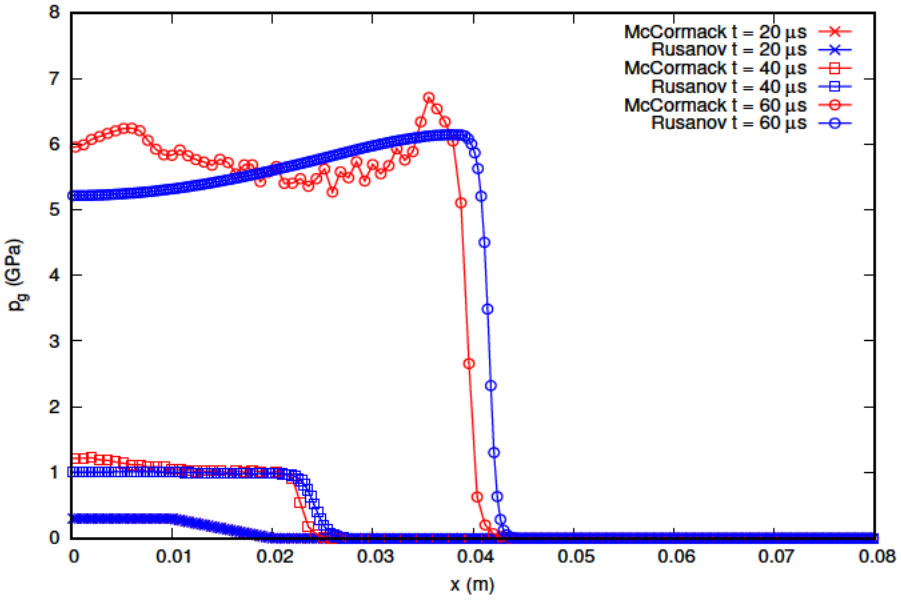

Figure 4.15: Pressure distribution for 20, 40 and 60 μs.

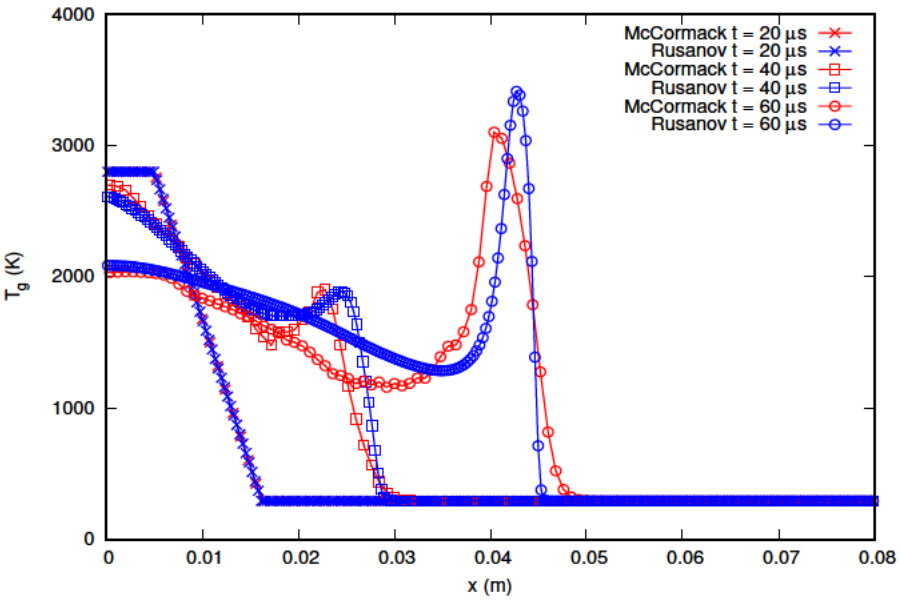

Figure 4.16: Gas temperature distribution for 20, 40 and 60 μs.

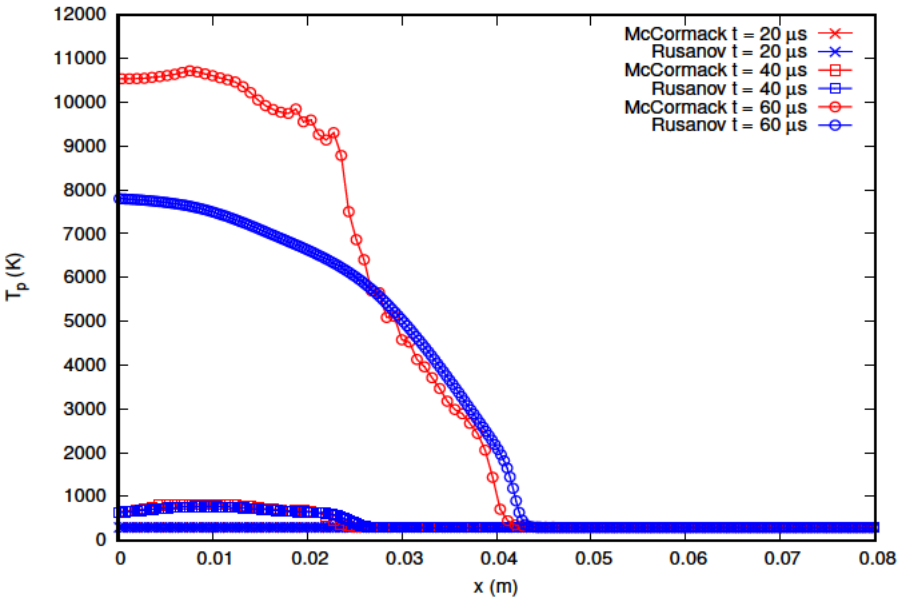

Figure 4.17: Particle temperature distribution for 20, 40 and 60 μs.

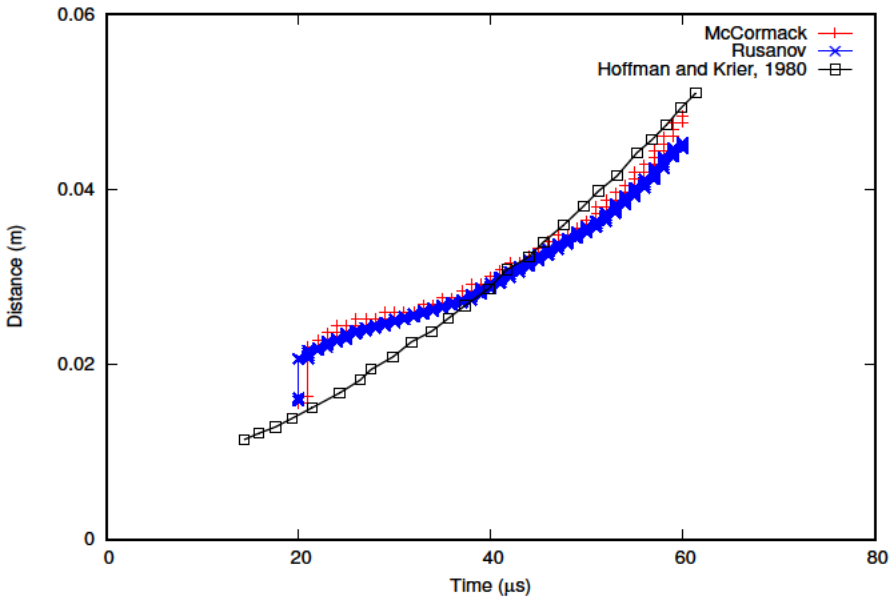

Figure 4.18: Flame front propagation.

However, the particle temperature shows high discrepancies between both numerical schemes. In addition, the magnitude of the variable does not seem to adjust properly to physical conditions since the gas temperature does not get over 4000 K. In order to reduce particle temperature, the partial derivative of alpha with time in equation 4.16 is deleted, resulting an equation system as,

$$\frac{\partial(\alpha\rho_g)}{\partial t} + \vec{\nabla}\cdot(\alpha\rho_g\vec{u}_g) = \dot{\Gamma} \tag{4.37}$$

$$\frac{\partial(\alpha\rho_g\vec{u}_g)}{\partial t} + \vec{\nabla}\cdot\left(\alpha\rho_g\vec{u}_g\otimes\vec{u}_g + \alpha p\vec{I}\right) = p_g\frac{\partial\alpha}{\partial x} + \dot{\Gamma}\vec{u}_p - \vec{F}_D \tag{4.38}$$

$$\frac{\partial(\alpha\rho_g E_g)}{\partial t} + \vec{\nabla}\cdot\left(\alpha\rho_g\vec{u}_g\left(E_g + \frac{p}{\rho_g}\right)\right) = -p_g\frac{\partial\alpha}{\partial t} + \dot{\Gamma}\left(E^g_{chem} + \frac{|\vec{u}_p|^2}{2}\right) - \vec{u}_p\vec{F}_D - \dot{Q} \tag{4.39}$$

$$\frac{\partial((1-\alpha)\rho_p)}{\partial t} + \vec{\nabla}\cdot((1-\alpha)\rho_p\vec{u}_p) = -\dot{\Gamma} \tag{4.40}$$

$$\frac{\partial((1-\alpha)\rho_p\vec{u}_p)}{\partial t} + \vec{\nabla}\cdot\left((1-\alpha)\rho_p\vec{u}_p\otimes\vec{u}_p + (1-\alpha)p\vec{I}\,(1-f(\alpha))\right) = - p_p\frac{\partial(\alpha(1-f(\alpha)))}{\partial x} - \dot{\Gamma}\vec{u}_p + (1-f(\alpha))\vec{F}_D \tag{4.41}$$

$$\frac{\partial((1-\alpha)\rho_p E_p)}{\partial t} + \vec{\nabla}\cdot\left((1-\alpha)\rho_p\vec{u}_p\left(E_p + \frac{p}{\rho_p}\right)\right) = + \dot{\Gamma}\left(E^p_{chem} + \frac{|\vec{u}_p|^2}{2}\right) + \vec{u}_p\vec{F}_D + \dot{Q} \tag{4.42}$$

$$p_p = p_g + \tau_p \tag{4.43}$$

The results obtained are detailed in Figures 4.19, 4.20, 4.21, 4.22 and 4.23. The number of cells and parameter f chosen for calculation are the same as before.

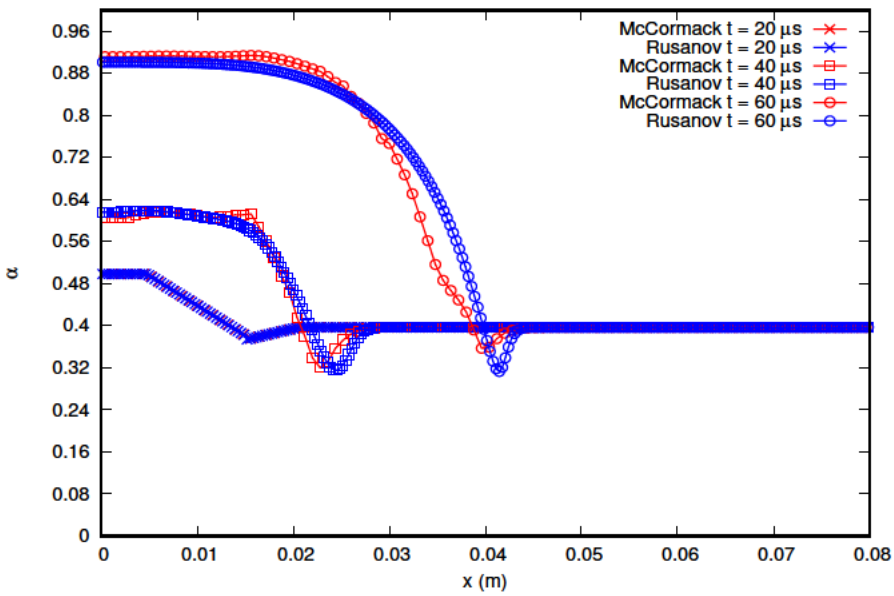

Figure 4.19: Porosity distribution for 20, 40 and 60 μs.

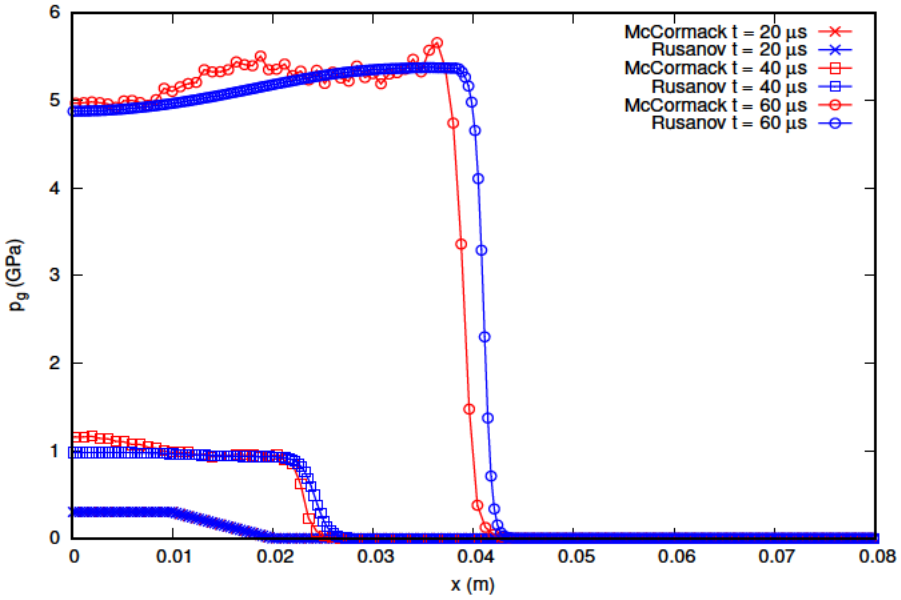

Figure 4.20: Pressure distribution for 20, 40 and 60 μs.

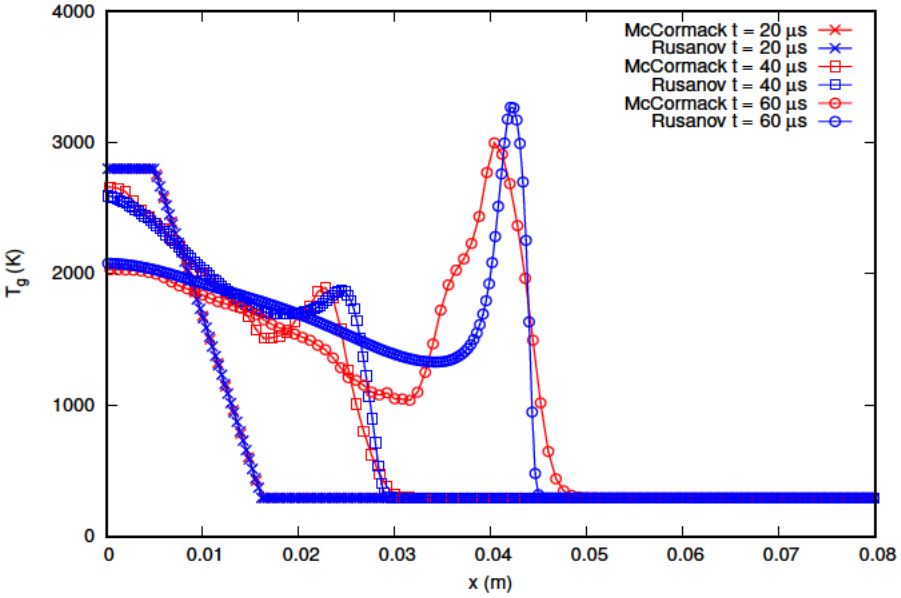

Figure 4.21: Gas temperature distribution for 20, 40 and 60 μs.

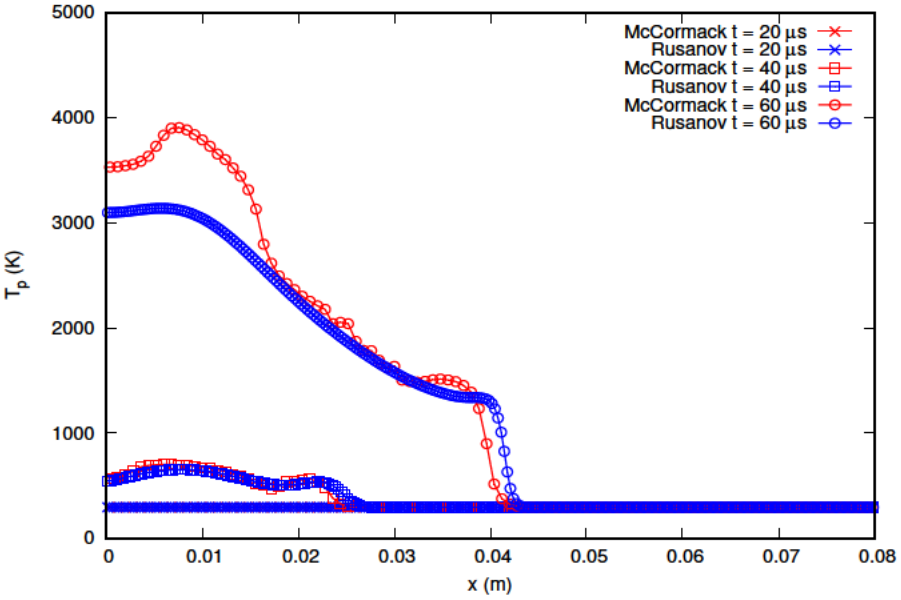

Figure 4.22: Particle temperature distribution for 20, 40 and 60 μs.

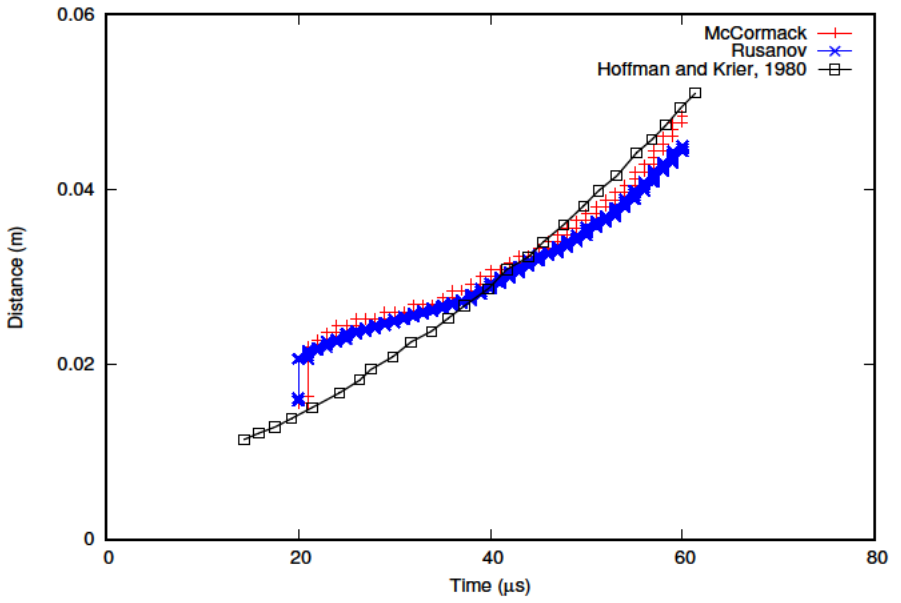

Figure 4.23: Flame front propagation.

Figures 4.19, 4.20 and 4.21 show similar results to those obtained before deleting the temporal partial derivative in the particle energy equation. However, in Figure 4.22 can be appreciated how the temperature of the solid phase decrease up to 3000 K. Flame front distribution obtained with this modification is similar to the previous one. As before, the code has been run with 250 cells and $f = 0.2$ for the solution with Rusanov scheme and 100 cell and $f = 0.11$ for MacCormack-TVD.

4.1.4.2 Porosity direct limiter

As seen in subsection 4.1.3, the equation system (4.1)-(4.7) provides a solution in which the porosity reaches values under the minimum physical value. To avoid this phenomenon, the porosity is limited during the calculation obtaining the results of Figure 4.24 for the distribution of the porosity, and Figures 4.25, 4.26 and 4.27, for pressure and gas and particle temperatures respectively. The results obtained are qualitatively similar to those obtained by Hoffman and Krier [28] with a good agreement between Rusanov and MacCormack numerical schemes. In addition, the distribution of particle temperature reaches physical values. However, the x-locations of the peak of pressure and temperatures at 60 μs show a displacement compared with those presented by Hoffman and Krier [28] in their work. This phenomenon can be appreciated in the results the flame front propagation of Figure 4.28. The figure shows a good agreement of both numerical schemes with the result of the bibliography up to 50 μs increasing the difference between the calculation and the results from literature from this time on. To run the code 100 cells and CFL of 0.1 has been chosen for MacCormack-TVD resolution and 200 cells and CFL of 0.5 for Rusanov.

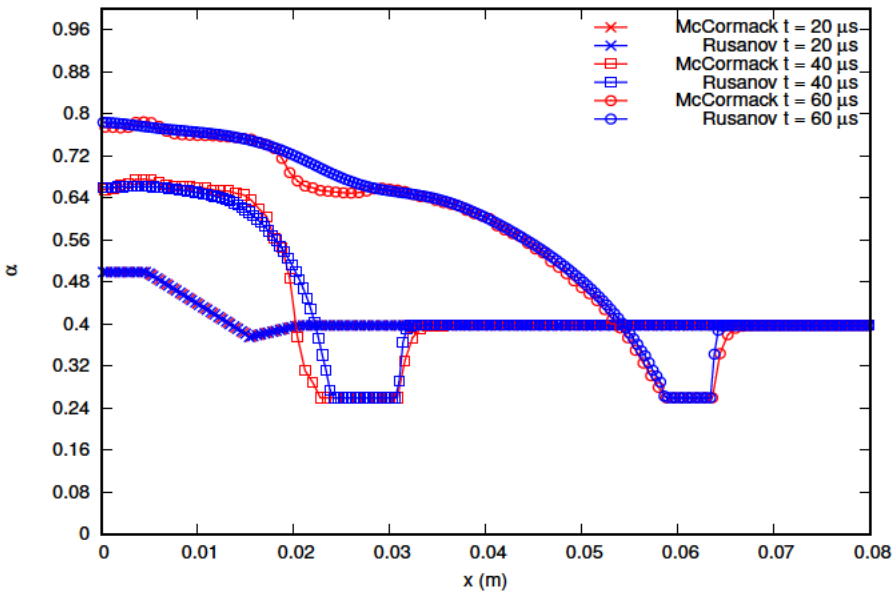

Figure 4.24: Porosity distribution for 20, 40 and 60 μs.

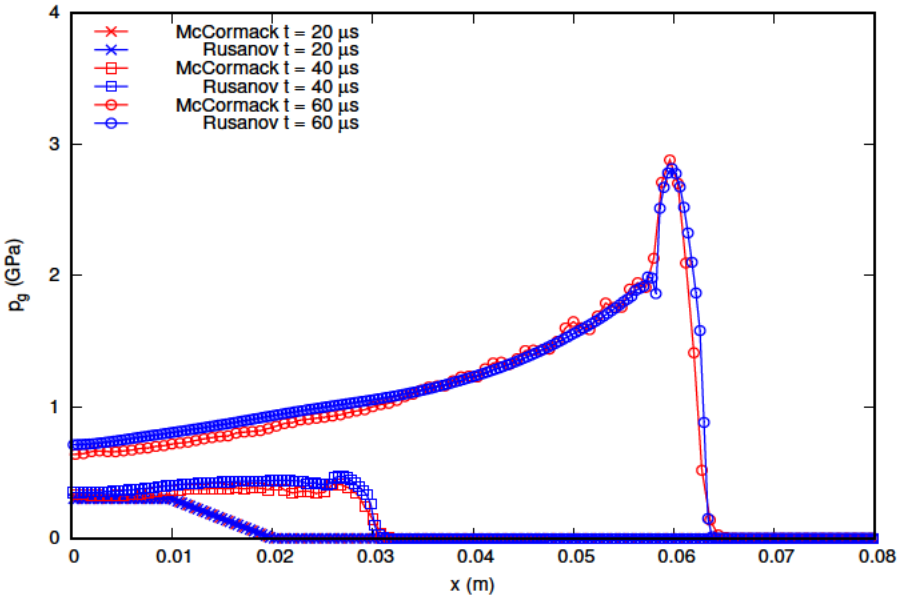

Figure 4.25: Pressure distribution for 20, 40 and 60 μs.

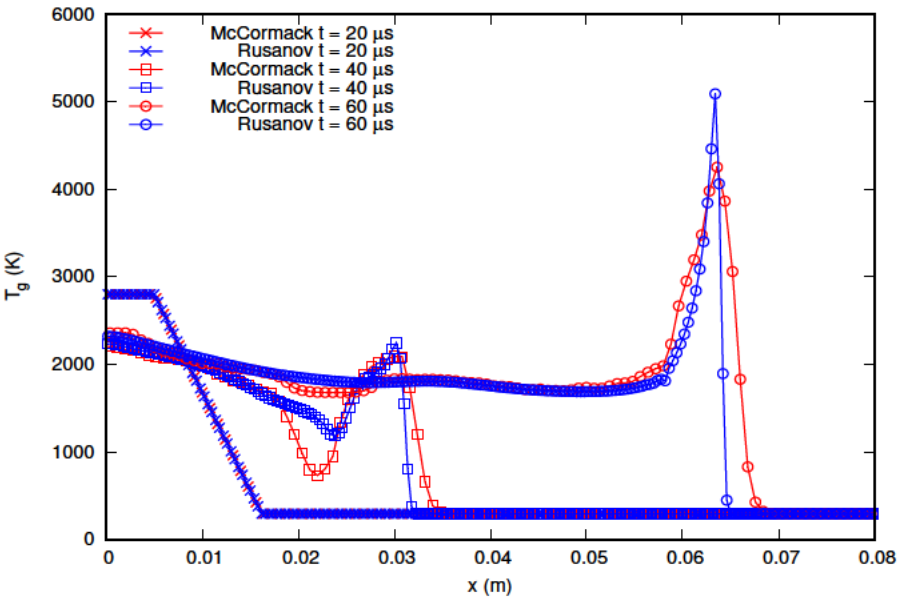

Figure 4.26: Gas temperature distribution for 20, 40 and 60 μs.

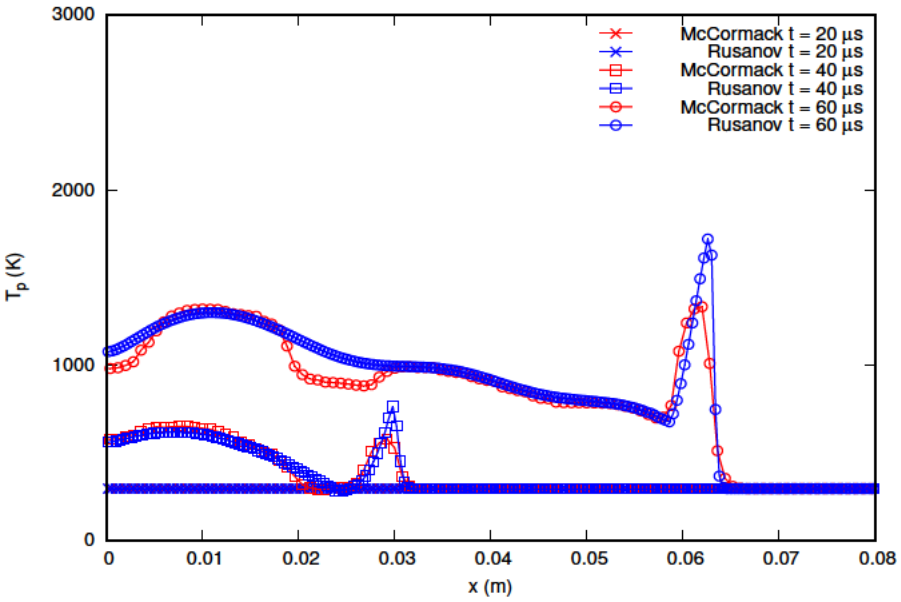

Figure 4.27: Particle temperature distribution for 20, 40 and 60 μs.

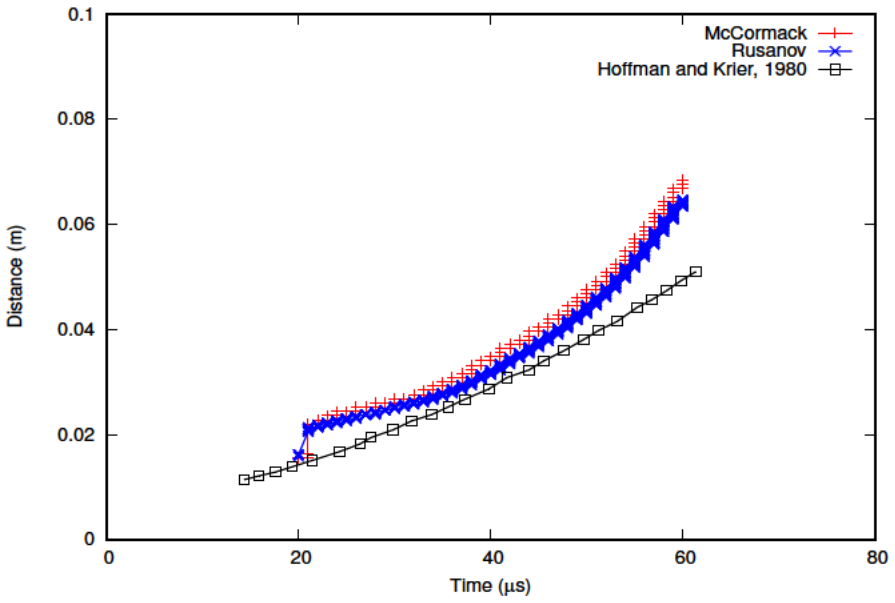

Figure 4.28: Flame front propagation.

4.1.5 Conclusions

A code to study the modelling of granular propellants combustion has been developed in C++. To solve the system of differential equations for both, gas and solid phase, Rusanov and MacCormack-TVD numerical schemes have been used. In addition, first-order Euler method has been used to solve the source terms.

Due to the amount of different expression found in literature to evaluate the source terms, there is a necessity of determining which one is the most suitable for the model developed in this work. Therefore, a sensitivity analysis is performed to determine the effect that Nusselt number, friction coefficient and initiation conditions have in the results. Rusanov and MacCormack numerical schemes, detailed in Chapter 3, have been used to solve the system of equations. The sensitivity analysis determines on the one hand, which expression of Nusselt number and friction coefficient is the one which provides more similar results for the numerical schemes used. On the other hand, it is used to determine how the application of the different initiation conditions found in literature affect to the variables distributions. As a conclusion, due to the capacity of reproducing very similar results between both numerical schemes and the good behaviour at a wide range of Reynolds number, the Nusselt number and friction coefficient presented by Butler et al. [39] in their work will be adopted afterwards for calculation.

As happened with the closure laws, although all authors consider a small zone of the control volume already initiated, each one applies different values of pressure and temperature as initial conditions of the test. High differences in the results can be obtained depending on the initial values assumed for the variables. Therefore, and in order to validate the model with literature values, the distributions of pressure, porosity and gas and particle temperatures provided by Hoffman and Krier [28] at 20 μs, are used as initial conditions for the calculations performed in subsection 4.1.4.

Afterwards, and once initial conditions and source terms are defined, two different models have been used to calculate pressure, temperature and porosity distributions. The first model studied is defined by the system of differential equations (4.14) - (4.17) in which the modification of the particle momentum governing equation done by Hoffman and Krier [28] is considered. According to the authors, this modification prevents the porosity from reaching values below the minimum value of compaction that packed beds of spherical particles can reach. However, when this model is applied, the temperature of the particle phase increases and reaches values up to 8000K. In order to reduce the particle temperature, a modification of this equation system has been done and the partial time derivative of the porosity in the particle momentum equation is deleted leading to the system (4.40) - (4.43). This modification reduces slightly the maximum value of particle temperature but the results obtained are not matching quantitatively the ones found in the literature. The second model studied does not consider the porosity limiter from Hoffman and Krier [28] performing the limitation of the porosity directly in the code by preventing the porosity to reach values below the minimum one. The magnitude of the values obtained for the main variables of interest when applying this model (equations (4.4) - (4.7)) are similar to those found in literature. Moreover, the results obtained using Rusanov scheme agree well with those resulting of applying MacCormack-TVD numerical scheme. However, the distributions of the variables are displaced in x-direction respect those from literature. This behaviour can be seen by observing the x-coordinate position of the peak values obtained for pressure, temperature and porosity variables. These differences could be due on the one hand, to the initial values of the parameters chosen as initial conditions which highly determine the x-location of the peak values for all variables and on the other hand, to the lack of all necessary input data in a single work from bibliography making necessary to collect the values from different works increasing the difficulty of reproducing the tests available in the bibliography.

Finally, it can be concluded that, despite the difference in the x-location peak values, the last model considered represents accurately the physical behaviour of the propellant combustion for all variables of interest becoming a predictive tool for the characterisation of the early stages of the detonation process of granular solid propellants.

4.2 Combustion of composite AP/HTPB propellant

In this section a model for the characterisation of unsteady combustion of AP/HTPB composite propellants is proposed. The model describes a change of phase of the propellant from condensed to gas phase and afterwards its combustion by a simplified chemistry scheme. After presenting the model, the finite volume approximation used to solve the system of equations is described. Finally, the code is validated with two tests: the burning of a strand composed by AP particles uniformly distributed within HTPB comparing the numerical text with experimental data and the burning of a strand composed by AP oxidiser and HTPB binder in sandwich configuration.

4.2.1 Physical model

The combustion of AP/HTPB propellant is modelled by considering a solid phase zone (hereafter cited as condensed phase) and a gas phase zone. Both zones were assumed to be insulated excepting the contact surface between gas and condensed phases which is called burning surface.

The gas phase will be formed initially by air but, when the condensed phase located at the burning surface reaches the melting temperature (T_{melt}), AP (NH_4ClO_4) and HTPB (HC) will change their phase from solid to gaseous form appearing these two chemical compounds in the gas zone too. Afterwards, the chemical reaction will take place and combustion products will be part of the gaseous mixture too.

The process of combustion of AP and HTPB in their gaseous form is described by a two-step reaction mechanism as done by Knott and Brewster [44] chemical kinetic scheme,

$$NH_4ClO_4 \longrightarrow 1.25O_2 + \underbrace{1.5H_2O + HCl + 0.5N_2}_{P_1} \ (R1) \tag{4.44}$$

$$HC + 1.25O_2 + P_1 \longrightarrow CO_2 + 0.5H_2O + P_1 \ (R2) \tag{4.45}$$

4.2.1.1 Governing equations

The mathematical model applied to reproduce the combustion problem considers mass, momentum, energy and species mass fraction governing equations for the gas phase and energy equation for the solid phase as in the following equation system,

$$\frac{\partial \rho_g}{\partial t} + \overrightarrow{\nabla} \cdot (\rho_g \overrightarrow{u}_g) = 0 \tag{4.46}$$

$$\frac{\partial (\rho_g \overrightarrow{u}_g)}{\partial t} + \overrightarrow{\nabla} \cdot \left(\rho_g \overrightarrow{u}_g \otimes \overrightarrow{u}_g + p \overrightarrow{I} \right) = 0 \tag{4.47}$$

$$\frac{\partial (\rho_g E_g)}{\partial t} + \overrightarrow{\nabla} \cdot \left(\rho_g \overrightarrow{u}_g \left(E_g + \frac{p}{\rho_g} \right) \right) = k_g \nabla^2 T_g + \sum_{j=1}^{N} Q_{g,j} R_j \tag{4.48}$$

$$\frac{\partial (\rho_g Y_i)}{\partial t} + \overrightarrow{\nabla} \cdot (\rho_g \overrightarrow{u}_g Y_i) = \frac{k_g}{\gamma_g c_{vg}} \nabla^2 Y_i + \phi_i \qquad i = 1, 2, ..., n-1 \tag{4.49}$$

$$\frac{\partial (\rho_c E_c)}{\partial t} = k_c \nabla^2 T_c \tag{4.50}$$

where the subscripts i stands for the ith-species from 1 to n-1 and j stands for reaction number from 1 to N. The specific heat at constant volume for a mixture of gases is defined as,

$$c_{vg} = \sum_{i=0}^{n} Y_i c_{vg,i} \tag{4.51}$$

4.2.1.2 Burning surface coupling

The coupling of the phases needs the following boundary conditions to be established:

1. Gas and solid temperature must be the same and equal to the surface temperature (T_s),

$$T_g = T_c = T_s \tag{4.52}$$

2. Energy balance at the burning surface is required,

$$k_g \nabla T_g|_s = k_c \nabla T_c|_s + \rho_c \dot{r} \left(Q_c - c_c \left(T_s - T_0\right)\right) \tag{4.53}$$

3. The continuity of mass must be ensured. When the temperature of the surface is higher than the melting temperature (T_{melt}), the solid changes phase to gas. Otherwise the velocity in the burning surface must be zero. Therefore, the following relationship is set,

$$u_g = \begin{cases} \frac{\rho_c \dot{r}}{\rho_g}, & T_s > T_{melt} \\ 0, & T_s < T_{melt} \end{cases} \tag{4.54}$$

4. Finally, species conservation must be ensured too.

$$\rho_c \dot{r}\ Y_i|_s = \rho_c \dot{r}\ Y_{c,i}|_{0^-} + \frac{k_g}{\gamma_g c_{vg}}\ \nabla Y_i|_{0^+} \tag{4.55}$$

where $\dot{r}$ is the burning rate and i stands for the specie from 1 to n-1. Among all expressions found in the literature to define the burning rate of solid propellants (see 2.3), that defined by Cai et al. [49], which considers the burning rate as a function of the pressure, is employed in this case. Therefore, the burning rates expressions of AP and HTPB which result after applying the formula are,

$$\frac{Q_{g,1}}{2c_{AP}T_s}\dot{r}_{AP}^2 + \frac{k_g\left(T_g - T_s\right)}{d\rho_{AP}c_{AP}T_s}\dot{r}_{AP} = \frac{\alpha_{AP}}{\rho_{AP}}\left(\frac{D_1 p^{n_1} e^{\left(-\frac{E_1}{RuT_g}\right)}}{\frac{E_1}{RuT_g}}\right)\frac{Q_{g,1}}{Q_{c,AP}} \tag{4.56}$$

$$\frac{Q_{g,2}}{2c_{HTPB}T_s}\dot{r}_{HTPB}^2 + \frac{k_g\left(T_g - T_s\right)}{d\rho_{HTPB}c_{HTPB}T_s}\dot{r}_{HTPB} = \frac{\alpha_{HTPB}}{\rho_{HTPB}}\left(\frac{D_2 p^{n_2} e^{\left(-\frac{E_2}{R_u T_g}\right)}}{\frac{E_2}{R_u T_g}}\right)\frac{Q_{g,2}}{Q_{c,HTPB}} \tag{4.57}$$

When the propellant is heterogeneous, each cell will move at a different velocity,$\dot{r}_{AP}$ or $\dot{r}_{HTPB}$ depending on the content of the cell. However, when the propellant is distributed uniformly, the burning rate is defined as an average value between both burning rates being function of the mass fraction of each specie present in the propellant. Therefore, in case of having and homogeneous AP/HTPB propellant, the burning rate can be defined as,

$$\dot{r} = \alpha\dot{r}_{AP} + (1-\alpha)\dot{r}_{HTPB} \tag{4.58}$$

where α is the mass fraction of AP in the propellant.

4.2.1.3 Source terms

To solve the system of equations (4.46)-(4.50), to consider the state equation of gases and the reaction rates of AP and HTPB will be needed.

The gases are assumed to behave like an ideal gas whose equation of state is,

$$p = \rho_g R_g T_g \tag{4.59}$$

being R_g the specific constant of gases which for a mixture of gases is as calculated as,

$$R_g = R_u \sum_{i=0}^{n} Y_i / M_{g,i} \tag{4.60}$$

The production rates of AP and HTPB combustion reactions (4.44) and (4.45) are described with an Arrhenius expression as a function of the mass fraction of the main reactive, the pressure and the temperature of the gas mixture as,

$$R_1 = D_1 p^{n_1} Y_{AP} e^{\left(-\frac{E_1}{R u T_g}\right)} \tag{4.61}$$

$$R_2 = D_2 p^{n_2} Y_{HTPB} Y_{O_2} e^{\left(-\frac{E_2}{R u T_g}\right)} \tag{4.62}$$

where D_1, and D_2 are the pre-exponential factors of the reaction rate, and n_1 and n_2 are the pressure exponents and E_1 and E_2 are the activation energies. All this parameters will be considered input data and will be taken from literature.

4.2.2 Numerical method applied

In this subsection, it will be detailed how the Rusanov numerical method explained in section 3.1 is applied to solve the system of governing equation which represent the gas phase. In addition, the solution to the condensed phase energy equation and how to calculate the time integration will be described.

4.2.2.1 Numerical method proposed to solve gas phase equation system

The system of equations for gas phase can be written in vector form as,

$$\frac{\partial \boldsymbol{U}}{\partial t} + \nabla \cdot \boldsymbol{F} = \boldsymbol{S}_1(\boldsymbol{U}) + \boldsymbol{S}_2(\boldsymbol{U}) \tag{4.63}$$

where $(\boldsymbol{U})$ is the conserved variables vector, $(\boldsymbol{F})$ is the flux tensor and $(\boldsymbol{S})$ the source terms which are split into two: $\boldsymbol{S}_1(\boldsymbol{U})$ with the diffusive terms and $\boldsymbol{S}_2(\boldsymbol{U})$ with the combustion terms,

$$\boldsymbol{U} = \begin{pmatrix} \rho_g \\ \rho_g \overrightarrow{u}_g \\ \rho_g E_g \\ \rho_g Y_i \end{pmatrix}, \tag{4.64}$$

$$\boldsymbol{F} = \begin{pmatrix} \rho_g \overrightarrow{u}_g \\ \rho_g \overrightarrow{u}_g \otimes \overrightarrow{u}_g + p \overrightarrow{I} \\ \rho_g \overrightarrow{u}_g \left(E_g + \frac{p}{\rho_g}\right) \\ \rho_g \overrightarrow{u}_g Y_i \end{pmatrix}, \tag{4.65}$$

$$\boldsymbol{S}_1(\boldsymbol{U}) = \begin{pmatrix} 0 \\ 0 \\ k_g \nabla^2 T_g \\ \frac{k_g}{\gamma_g c_{v\,g}} \nabla^2 Y_i \end{pmatrix} \tag{4.66}$$

$$\boldsymbol{S}_2(\boldsymbol{U}) = \begin{pmatrix} 0 \\ 0 \\ \sum_{j=1}^{N} Q_{g,j} R_j \\ \phi_i \end{pmatrix} \tag{4.67}$$

The system of equations (4.63) is solved in two steps as follows:

1. Firstly, the complete equation system without the combustion source terms is set,

$$\frac{\partial \boldsymbol{U}}{\partial t} + \nabla \cdot \boldsymbol{F} = \boldsymbol{S}_1(\boldsymbol{U}) \tag{4.68}$$

   The solution is obtained by adopting a finite volume approach,

$$\overline{\boldsymbol{U}}_j^{n+1} = \boldsymbol{U}_j^n - \frac{\triangle t}{|\Omega|} \sum_{s=1}^{N} \overline{T_s}^{-1} F\left(\overline{T_s}\boldsymbol{U}\right) A_s + \triangle t \boldsymbol{S}_1(\boldsymbol{U}_j^n) \tag{4.69}$$

   where the numerical flux is computed by solving approximately the Riemann problem at each interface and the source terms have been evaluated at t_n leaving the scheme explicit. The fluxes are calculated using Rusanov numerical scheme.

2. Next, the ODE

$$\frac{\partial \boldsymbol{U}}{\partial t} = \boldsymbol{S}_2(\boldsymbol{U}) \tag{4.70}$$

   which considers, as mentioned before, the source terms associated to the combustion process, is solved by using a first-order Euler method,

$$\boldsymbol{U}_j^{n+1} = \overline{\boldsymbol{U}}_j^{n+1} + \triangle t_{chem} \overline{\boldsymbol{S}}_{2,j}^{n+1} \tag{4.71}$$

4.2.2.2 Time integration

On the one hand, the time step considered to solve equation (4.69), called hereafter numerical time step, is calculated as,

$$\triangle t = CFL \cdot min\left[min\left(\frac{\triangle x_j}{|\overrightarrow{u}_g| + c_g}\right)\right] \tag{4.72}$$

where the speed of sound c_g is calculated as,

$$c_g = \sqrt{\gamma_g R_g T_g} \tag{4.73}$$

On the other hand, to solve equation (4.71), the time step is obtained using the procedure detailed in García-Cascales et al. [17]. The calculation consists in defining small steps associated to chemical reaction until their cumulative sum is equal to the numerical time step step calculated in equation (4.72). The process can be defined as the following:

1. A value of chemical time step is imposed ($\triangle t_{chem,0}$). This value must be very small and smaller than numerical time step.

2. Reaction rates R_1 and R_2, for AP and HTPB respectively, are calculated with the primitive values obtained from equation system 4.69.

3. With these reaction rates, a value of time step associated to the ith-speciess consumed in jth-reaction is calculated as follows,

$$\triangle t_{chem,i,j} = \frac{\rho_g Y_i}{\left| R_j coef_{i,j} \frac{M_{g,i}}{M_{g,j}} \right|} \tag{4.74}$$

where i stands for the ith-speciess and j for reaction and $coef_{i,j}$ was defined as,

$$coef_{i,j} = coef_{i-p,j} - coef_{i-r,j} \tag{4.75}$$

being $coef_{i-p,j}$ the stoichiometric coefficient of the ith-species in jth-reaction as product, and $coef_{i-r,j}$ the stoichiometric coefficient of the ith-species in jth-reaction as reactive. There will be as many $\triangle t_{chem,i,j}$ as consumed species in jth-reactions. From all those $\triangle t_{chem,i,j}$ the smallest one is chosen ($\triangle t_{chem}$).

4. The chemical time ($\triangle t_{chem}$) is compared with that imposed initially ($\triangle t_{chem,0}$) . In case of being smaller, the calculated $\triangle t_{chem}$ is used to solve equation (4.71). In opposite case, the initial chemical time step ($\triangle t_{chem,0}$) will be used to solve the equation.

5. Equation (4.71) is solved and primitive variables are updated.

6. Remaining time is calculated in first iteration as the difference between total numerical time step step and the calculated chemical time step,

$$\triangle t_{remaining} = \triangle t - \triangle t_{chem} \tag{4.76}$$

in following iterations the remaining time will be calculated as,

$$\triangle t_{remaining} = \triangle t_{remaining} - \triangle t_{chem} \tag{4.77}$$

7. The primitive variables calculated after solving Equation (4.71) are used to estimate again the reaction rates and with them the chemical time step of each species using equation (4.74). If the smallest chemical time step ($\triangle t_{chem}$) is smaller than the remaining numerical time step step ($\triangle t_{remaining}$), $\triangle t_{chem}$ is used to solve equation (4.71) again. This process is repeated until the calculated chemical time step is higher than the remaining numerical time step.

8. When this happens, the remaining numerical time step step is the one used to solve equation (4.71) and the calculation goes to the next convective $\triangle t$ according to equation 4.72.

4.2.2.3 Numerical method to solve condensed phase energy governing equation

Finite volume method is used to obtain an approximate solution of equation (4.50), as was done for the gas phase. The energy equation of condensed phase can be written in vector form as,

$$\frac{\partial U}{\partial t} = S(U) \tag{4.78}$$

which will be solved by using the first-order Euler method as,

$$\overline{\boldsymbol{U}}_j^{n+1} = \boldsymbol{U}_j^n + \triangle t \boldsymbol{S}_j^n \tag{4.79}$$

where U is defined as,

$$U = \rho_c E_c \tag{4.80}$$

and $S(U)$ as,

$$S(U) = k_c \nabla^2 T_c \tag{4.81}$$

4.2.3 Results and discussion

The model previously described has been programmed in C++ using OpenFoam and to be able to validate it, the code has been run for different tests in two dimensions and their results have been compared against experimental data.

The first test is the burning of a strand of AP/HTPB uniformly distributed. In this case the results are compared with data from the experiments run in the facilities of National Spanish Institute of Aerospace Technology (INTA) [86]. In those experiments an AP/HTPB strand from EXPAL Systems (R&D Department) of 4 mm in diameter and 155 mm in length is burned in a Crawford Bomb Strand Burner for several room temperatures and in a pressure range from 4 to 19 MPa.

The second test is the burning of a strand composed by AP and HTPB in sandwich configuration as proposed by Cao et al. [47] who use the experimental results provided by Kohga [51] to validate their code. In his experiment, Kohga [51] studied the burning of AP/HTPB composite propellants using coarse and fine AP particles , 110 μm and 4 μm diameter respectively, with and without Fe_2O_3 in a pressure range of 0.5 - 7 MPa.

Finally, the same AP/HTPB geometry in sandwich configuration has been used to apply a pressure step test. The pressure will fall down abruptly from 7 MPa to 0.5 MPa at the open side of the tube and its influence in the main variables of interest is studied.

For all tests, the necessary thermophysical and chemical kinetic properties of composite AP/HTPB propellant are considered as input variables (see Tables table 4.2 and 4.3). These values are taken from Zhou et al. [59] and Ye et al. [46]. The melting temperature (T_{melt}) is assumed to be 800 K and the gas conductivity (k_g) equal to $4.4 \cdot 10^{-2}$ W·m^{-1}·K^{-1}.

Parameter	Unit	AP (1)	HTPB (2)
$n_{1,2}$		1.744	1.75
$D_{1,2}$	kg·m^{-3}·s^{-1}·Pa^{-n}	2.261·10^{-2}	2.294·10^{-2}
$Q_{g1,2}$	J·kg^{-1}	1.799·10^{6}	9.606·10^{6}
$E_{1,2}/R_u$	K^{-1}	8000	11000

Table 4.2: Chemical kinetics AP/HTPB composite propellant.

Parameter	Unit	AP	HTPB
ρ_c	kg·m^{-3}	1950	920
k_c	W·m^{-1} · K^{-1}	0.405	0.276
c	J·kg^{-1}·K^{-1}	1255.2	1255.2
M_g	kg·mol^{-1}	0.1174	0.0130
Q_c	J·kg^{-1}	4.186·10^{5}	1.967·10^{5}

Table 4.3: Thermophysical properties of AP/HTPB composite propellant.

4.2.3.1 Crawford Bomb Strand Burner test.

The first test run to validate the code is the burning of a homogeneous AP/HTPB strand at 4 MPa and 7 MPa and initial room temperatures of 220.15 K, 294.15 K or 347.15 K. The results are compared with those obtained in INTA facilities where a strand of AP/HTPB of 4 mm in diameter and 155 mm in length is burned in the same conditions.

The geometry simulated in this test (see Figure 4.29) consists in a tube of 156 mm in length and 4 mm in width in which 155 mm are considered homogeneous propellant composed by 74.41% of AP and 25.59% of HTPB. The remaining 1 mm is considered to be filled with air.

The tube is insulated all along their walls except the right one which is open therefore, there is not transference of mass and heat through the walls. On the one hand, zero gradient boundary conditions

have been considered for temperature, density, mass fractions and pressure along the walls despite the pressure at the exit of the tube which have been fixed either to 4 MPa or 7 MPa depending on the reproduced test. On the other hand, velocity have been fixed to zero in the left closed wall, to zero gradient in the right open wall and slip boundary condition have been considered in upper-bottom and front-back walls.

Regarding initial conditions, the control volume is assumed to be already initiated. The initial condition of temperature is described by a linear distribution from the value fixed on the left side, which can be 220.15 K, 294.15 K or 347.15 K depending on the test considered, to 811 K on the right side. Initial pressure in the gas domain have been set as the pressure at the right boundary. Finally, the initial velocity of the gas phase have been set to zero.

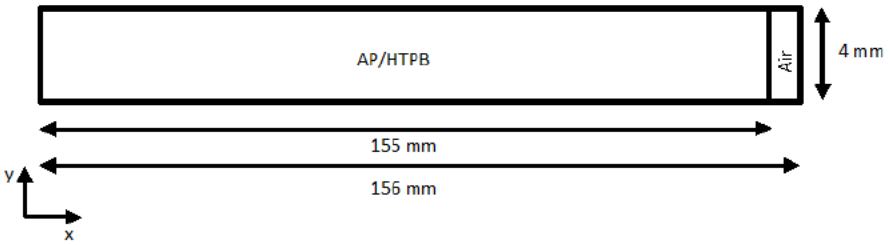

Figure 4.29: Geometry of AP/HTPB strand configuration.

The result of the calculation and their comparison with the experimental results from INTA facilities are plotted in Figure 4.30. Quantitative results, absolute and relative error scan be found in Tables 4.4 and 4.5.

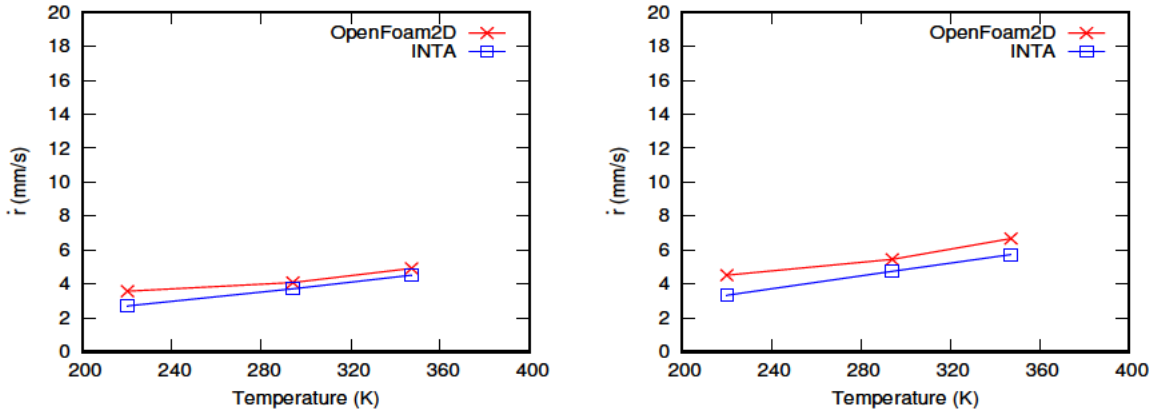

Figure 4.30: Comparison between calculated and experimental burning rate at 4 MPa (left) and 7 MPa (right).

Temperature (K)	OpenFoam Burning rate (mm/s)	INTA Burning rate (mm/s)	Absolute error (mm/s)	Relative error (%)
220.15	3.58	2.71	0.869	32.08
294.15	4.08	3.72	0.364	9.79
347.15	4.92	4.52	0.398	8.80

Table 4.4: Quantitative comparison of calculated and experimental burning rate for 4 MPa.

Temperature (K)	OpenFoam Burning rate (mm/s)	INTA Burning rate (mm/s)	Absolute error (mm/s)	Relative error (%)
220.15	4.52	3.34	1.180	35.34
294.15	5.45	4.75	0.704	14.83
347.15	6.68	5.73	0.949	16.57

Table 4.5: Quantitative comparison of calculated and experimental burning rate for 7 MPa.

For both pressures, the difference between numerical and experimental results for 294.15 K is lower than that obtained either for 347.15 K nor 220.15 K. Therefore, it can be said that the smallest absolute error is obtained when initial temperature is 294.15 K in the range of pressure studied. Moreover, the difference between the results obtained with the model and experimental ones when initial temperature is 220.15 K is higher than for 347.15 K. In addition, differences between code and experimental results increase with the pressure, obtaining a better agreement for 4 MPa than for 7 MPa being the magnitude of the absolute error less than 1 mm/s for 4 MPa and around 1 mm/s 7 MPa, being in the order of magnitude of the experimental error. However, the relative error, not only increases considerable for low initial temperatures independently of the pressure of the test, but also for low pressures up to reach values of 36%. This is due to the relation used to calculate error,

$$Relative\,error = \frac{|V_{experimental} - V_{numerical}|}{V_{experimental}} \tag{4.82}$$

where V is the value of the magnitude whose error is being calculated and $|V_{experimental} - V_{numerical}|$ is its absolute error. Despite the absolute error is mostly constant independently of the initial temperature, the relative error increases its magnitude drastically. This happens because experimental value of the burning rate decrease with the initial temperature chosen to run the test and this affects to the value calculated with expression (4.82).

As a conclusion, it can be said that the results obtained with the numerical model agree with the experimental ones for the pressure range considered.

4.2.3.2 Sandwich configuration test

Once the model has been validated when studying the burning of a strand made of composite AP/HTPB propellant homogeneously distributed in a Crawford Bomb Strand Burner, the following step is to see the performance of the model when burning a strand in which AP and HTPB are not uniformly distributed but placed in a sandwich configuration in a range of pressures from 0.5 MPa to 7 MPa. To validate the model, the results have been compared with those provided by Kohga [51].

The tube is insulated all along their walls except the right one which is open therefore, there is not transference of mass and heat through the walls. On the one hand, zero gradient boundary conditions have been considered for temperature, density, mass fractions and pressure along all walls despite the pressure at the exit of the tube which have been fixed in a range of 0.5 MPa to 7 MPa depending on the reproduced test. On the other hand, velocity have been fixed to zero in the left closed wall, to zero gradient in the right open wall and slip boundary condition have been considered in upper-bottom and front-back walls.

Regarding initial conditions, the control volume is assumed to be already initiated. The initial condition of temperature is described by a linear distribution from 300 K (T_1) fixed on the left side to 1315 K (T_2) fixed on the right side. Initial temperatures, as well as reference temperature and melting temperature are summarised in Table 4.6.

The geometry used (Figure 4.31) is that described by Ye et al. [46] in which half of its volume is composed of air and the other half of AP/HTPB composite propellant in sandwich configuration.

According to Cao et al. [47], the width of the domain is obtained as a function of both AP and HTPB particle and AP mass fraction as per the following two expressions,

$$L = d_{AP} + d_{HTPB} \tag{4.83}$$

$$\frac{\rho_{AP} \cdot d_{AP}}{\rho_{HTPB} \cdot d_{HTPB}} = \frac{\alpha}{(1-\alpha)} \tag{4.84}$$

A strand with 80% of AP content and particle average size of 110 μm was used for calculation, as it is also considered by Cao et al. [47]. In this case and according to equations (4.84) and (4.83), the widths obtained are 60 mm for HTPB and 170 μm for the total height. In order to define a 3D domain, both condensed and gas phase are set 500 μm height as seen in Figure 4.31. This first test is run in 2D configuration for several pressures in a range from 0.5 MPa to 7 MPa.

Variable	Unit	Value
T_0	K	300
T_{melt}	K	800
T_1	K	300
T_2	K	1315

Table 4.6: Initiation conditions.

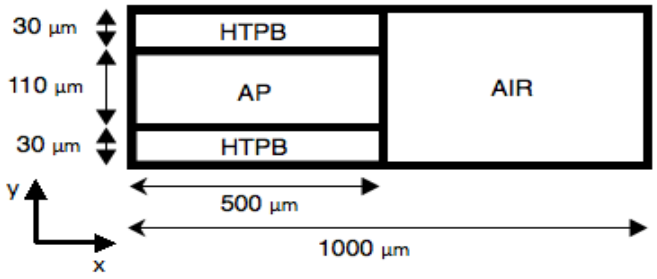

Figure 4.31: Geometry of AP/HTPB sandwich configuration.

Firstly, a comparison between the burning rate obtained using the proposed model and the experimental results from Kohga [51] is presented in Figure 4.32. The results obtained with the model previously explained agree well for the considered pressure range and the difference between calculated and experimental data maintains the same magnitude independently of the pressure considered which can be seen quantitatively in Table 4.7. The absolute error, remains constant and have a value around 0.5 mm/s being in the order of magnitude of the experimental error. However, the value of the relative error increases considerably with the pressure fall to reach up to 22%. This is due to expression (4.82) used to calculate error as explained in subsection 4.2.3.1.

Besides burning rate, other relevant variables such as gas velocity and AP and HTPB mass fraction distributions are obtained in Figures from 4.33 to 4.41. The first phenomenon that can be observed at glance in any of these figures is the decrease of the distance between the left side of the tube and the burning surface with the increase of the pressure. That means, the higher the pressure is, the faster the condensed phase changes from solid to gas which in absolute concordance with the results of Figure 4.32 where the direct relationship between burning rate and increase of pressure is plotted.

Velocity field is depicted in Figures 4.33, 4.34 and 4.35 for time equal to 0.02 s, 0.04 s and 0.06 s respectively. The behaviour of the gas velocity is opposed to the burning rate, the higher the pressure is, the lower gas velocity we have. The reason of this behaviour could be the increase of gas density

with pressure. By comparing the render views for 0.5 MPa of Figures 4.33, 4.34 and 4.35 against Figures 4.36, 4.37 and 4.38, it can be observed that an increase of AP mass fraction close to the burning surface leads to a local raise of the gas velocity. Since the increase of AP mass fraction is directly related with the increase of the burning rate, as it will be explained afterwards analysing Figures 4.43 and 4.42, and the gas velocity at the burning surface is calculated as $u_g = \frac{\rho_c \dot{r}}{\rho_g}$, a higher result of the local gas velocity is obtained at the areas where the burning rate is higher too.

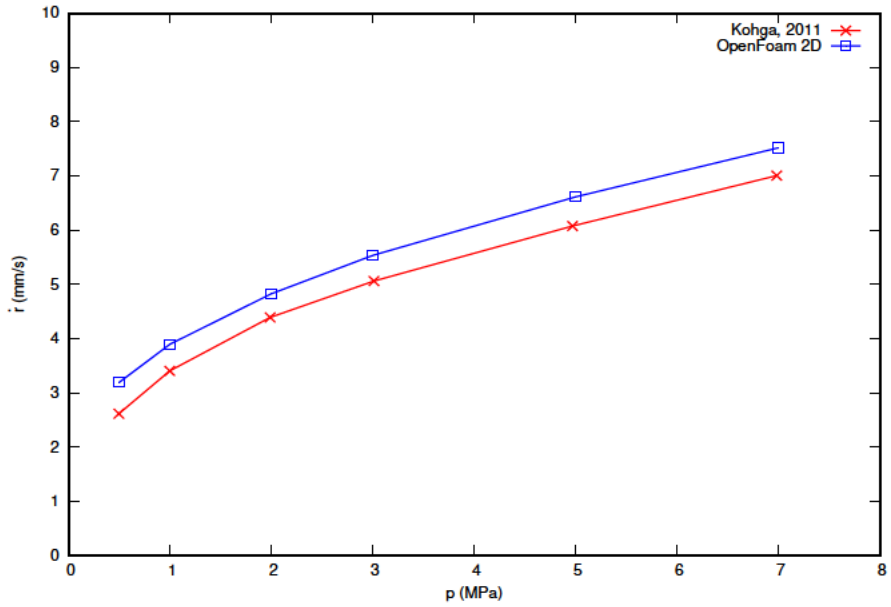

Figure 4.32: Comparison of calculated and experimental burning rate.

Pressure (MPa)	OpenFoam Burning rate (mm/s)	Kohga Burning rate (mm/s)	Absolute error (mm/s)	Relative error (%)
7	7.52	7.01	0.512	7.31
5	6.61	6.08	0.537	8.84
3	5.53	5.06	0.473	9.35
2	4.82	4.39	0.437	9.96
1	3.89	3.40	0.491	14.43
0.5	3.19	2.61	0.580	22.21

Table 4.7: Quantitative comparison of calculated and experimental burning rate.

AP mass fraction distributions for time equal to 0.02, 0.04 and 0.06 seconds are represented in Figures 4.36, 4.37 and 4.38 respectively. The very first visible attribute is the local concentration of AP in the cells close to burning surface which has not an uniform distribution along the tube unlike what happens with HTPB (see Figures 4.39, 4.40 and 4.41). This behaviour may be due to the facility that the first reaction (equation (4.44)) has to take place compared with second one (equation (4.45)). Since the activation energy which the oxidiser needs to be decomposed is not really high, it could be deduced that, as soon as condensed AP sublimates into AP in gas phase, the first reaction takes place and most of the AP is decomposed in P_1 (see equation (4.44)). However, binder combustion reaction (equation (4.45)) not only presents a higher activation energy, but also needs the products

from the first reaction to take place. This could lead to the conclusion that when HTPB sublimates to gas, it does not burn immediately and therefore, it has more time to spread along the gas domain and accumulate higher concentration in the cells than AP.

The figures show how the content of AP and HTPB increases as the pressure decreases as happened for gas velocity field. The increase of mass fraction of both binder and oxidiser with the fall of pressure could be assigned to the reaction rates formulation. Equations (4.61) and (4.62) are function of the pressure therefore, the higher the pressure, the higher reaction rate will be obtained. High values of R_1 and R_2 mean that the consumption of both, AP and HTPB. Therefore, it could be said that high pressures increase the reaction rate leading to a decrease of propellant mass fraction due to mass fraction conservation equation (4.49).

When the pressure is high, AP in gaseous form is located at the centre of the tube, close to AP in its condensed form, that means, at the same y-coordinate range values. However, the lower the pressure, the higher the AP gas is spread increasing the amount of cells containing AP in its gaseous form close to the burning surface. The increase of the diffusivity as the pressures falls down may be due to the rise in gas velocity with the reduction of pressure which drags AP throughout the domain. However, at 0.5 MPa, binder and oxidiser mass fractions present distributions with higher concentrations of each propellant close to their condensed phases respectively. At low pressures, the amount of propellant sublimating is very small. In addition, as has been already explained, the reaction rates of R1 and R2 decrease with the pressure. Therefore, the combustion of AP and HTPB close to the burning surface is reduced leading to an accumulation of both of them in those cells.

Since in this test, the AP and HTPB are placed in sandwich configuration, it is of high interest to study the burning rate and the mass fraction of both, binder and oxidiser, in the y-coordinate. Therefore, the regression rate at the burning surface and the AP and HTPB mass fractions along a cross section plane adjacent to the burning surface for a pressure of 7 MPa are represented in Figures 4.42 and 4.43 respectively where 0 is the minimum value and 1 the maximum one. The content of HTPB is mostly constant along y-direction however, the content of AP reaches its minimum value in the lower or upper sides of the sandwich and its maximum at $y = 30\,\mu m$ where the interface between AP and HTPB is located, having a symmetric distribution. The burning rate profile (see Figure 4.42) is similar to that of AP mass fraction unlike the upper and lower layers of the sandwich where the burning rate does not decrease as abruptly as AP mass fraction does. Both magnitudes, burning rate and propellant mass fractions decrease with time. The reason why HTPB is uniformly distributed and AP gas is localised close to its condensed phase has been already explained before.

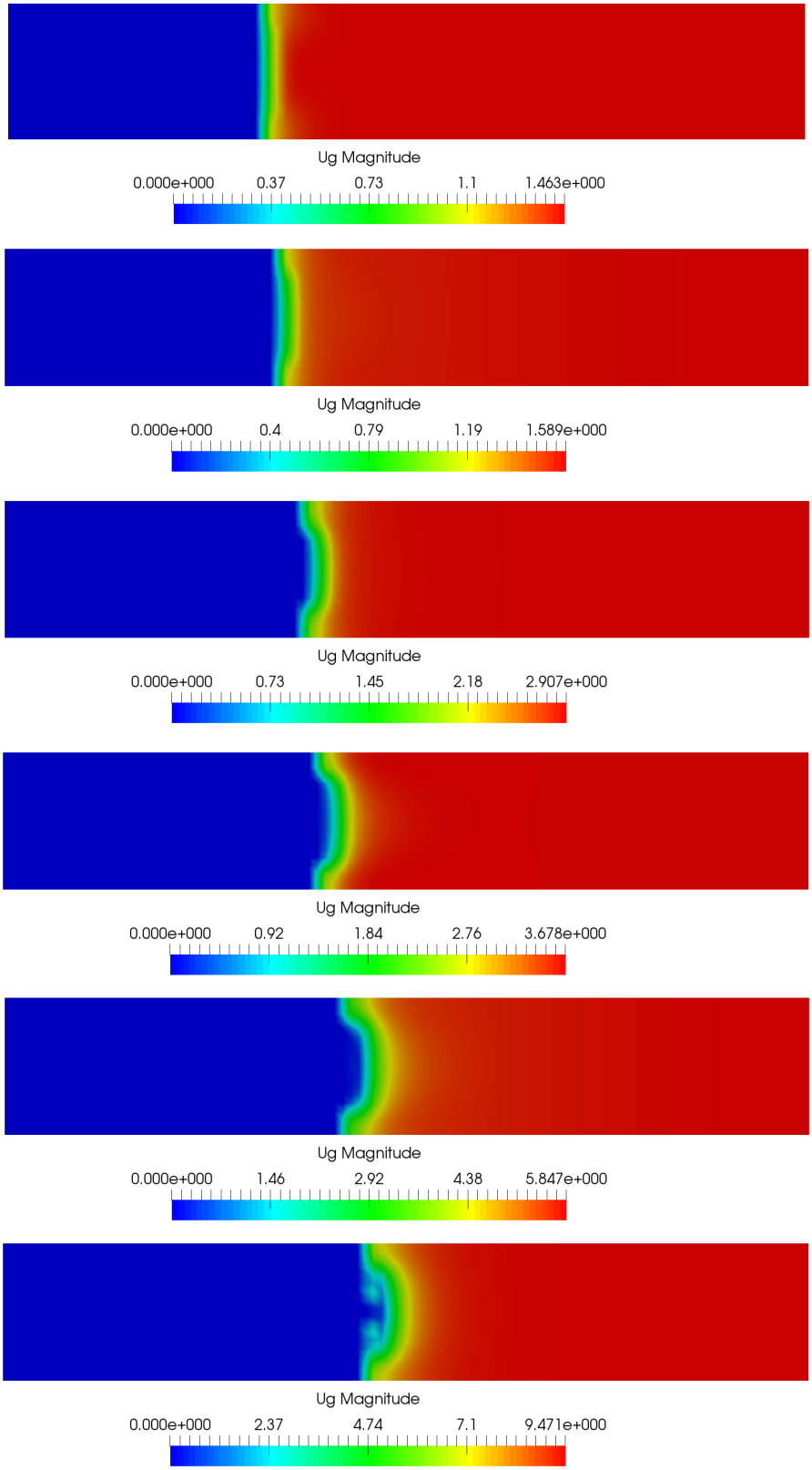

Figure 4.33: Velocity distribution of gas phase in t = 0.02 s at 7 MPa, 5 MPa, 3 MPa, 2 MPa, 1 MPa, 0.5 MPa (above-below).

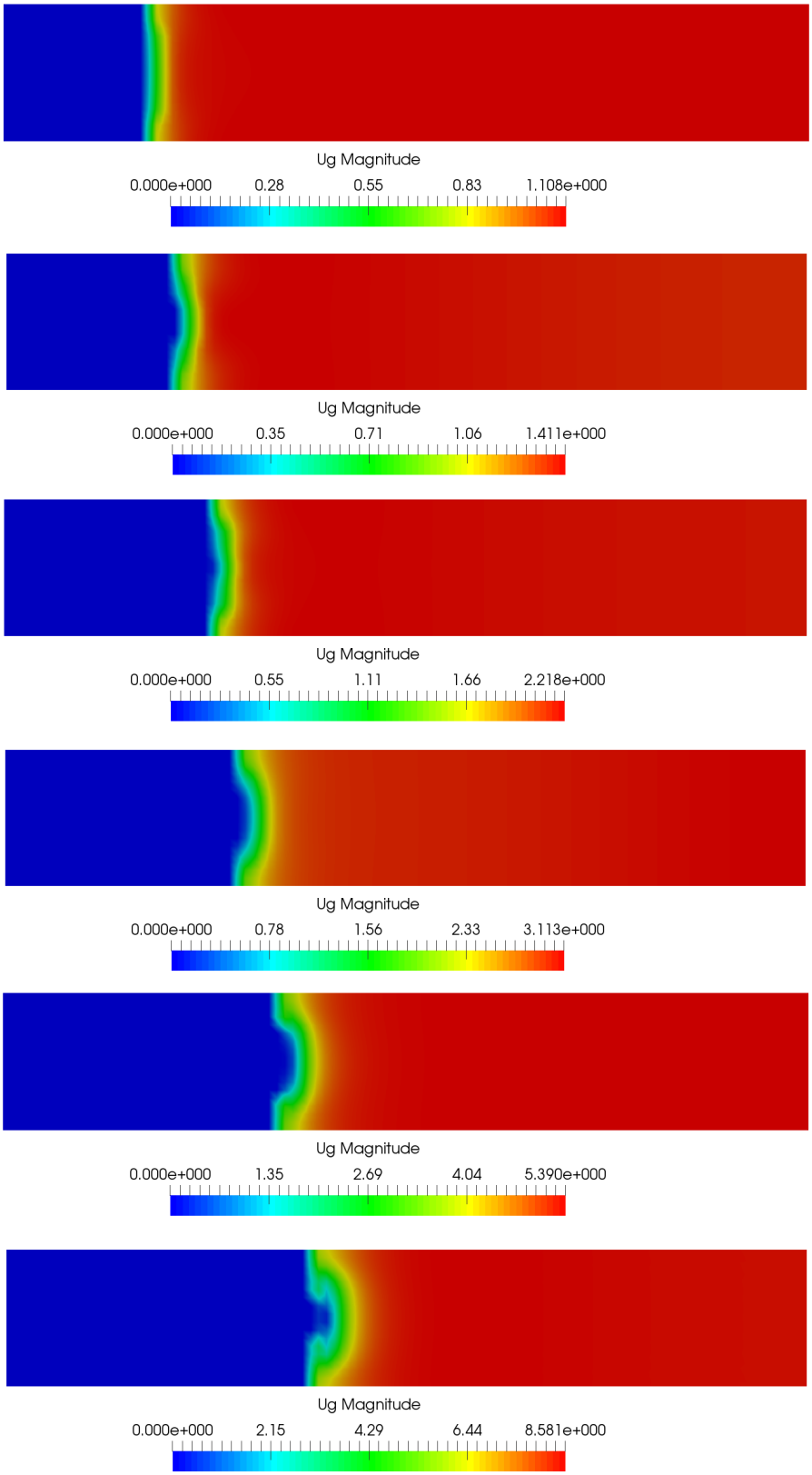

Figure 4.34: Velocity distribution of gas phase in t = 0.04 s at 7 MPa, 5 MPa, 3 MPa, 2 MPa, 1 MPa, 0.5 MPa (above-below).

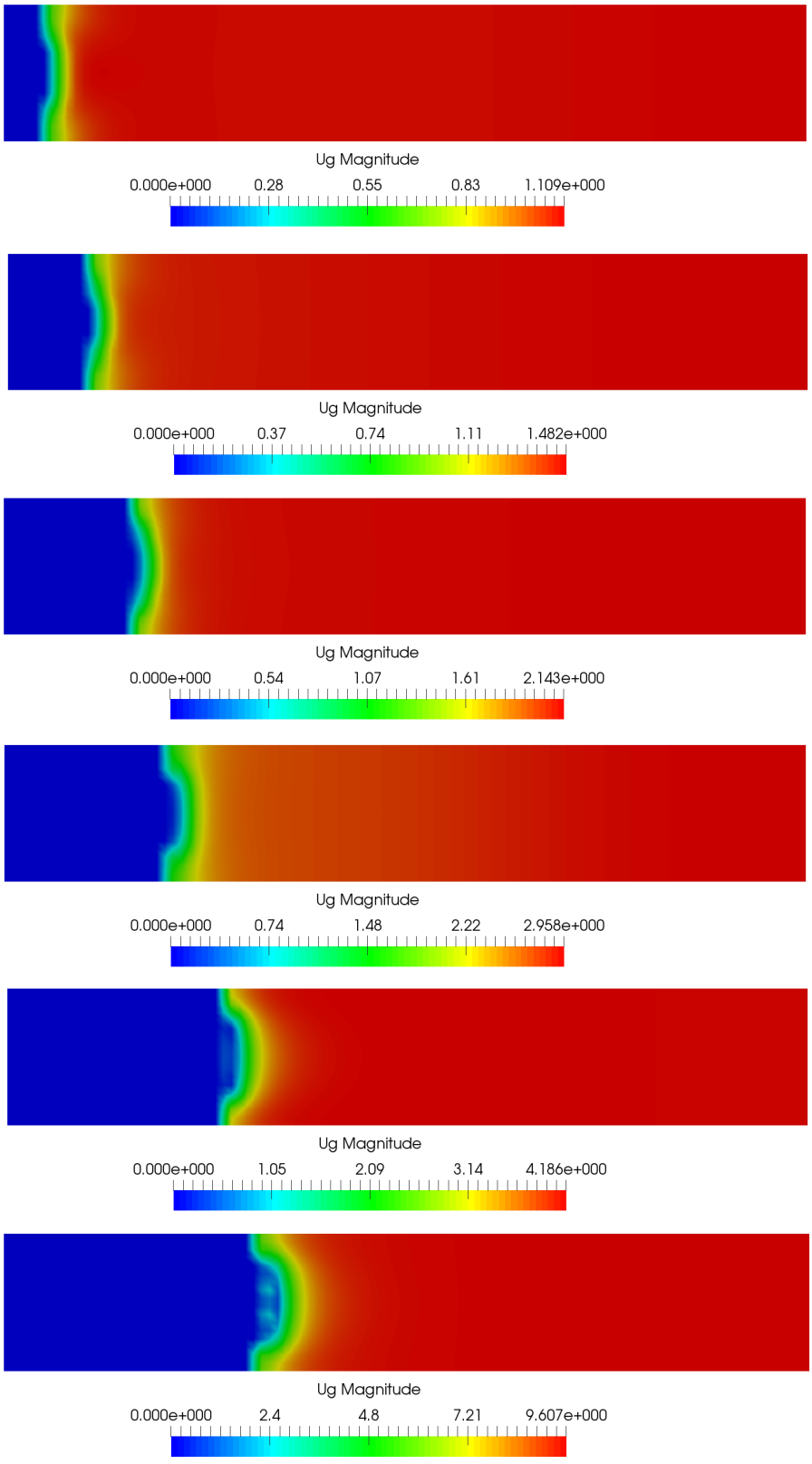

Figure 4.35: Velocity distribution of gas phase in t = 0.06 s at 7 MPa, 5 MPa, 3 MPa, 2 MPa, 1 MPa, 0.5 MPa (above-below).

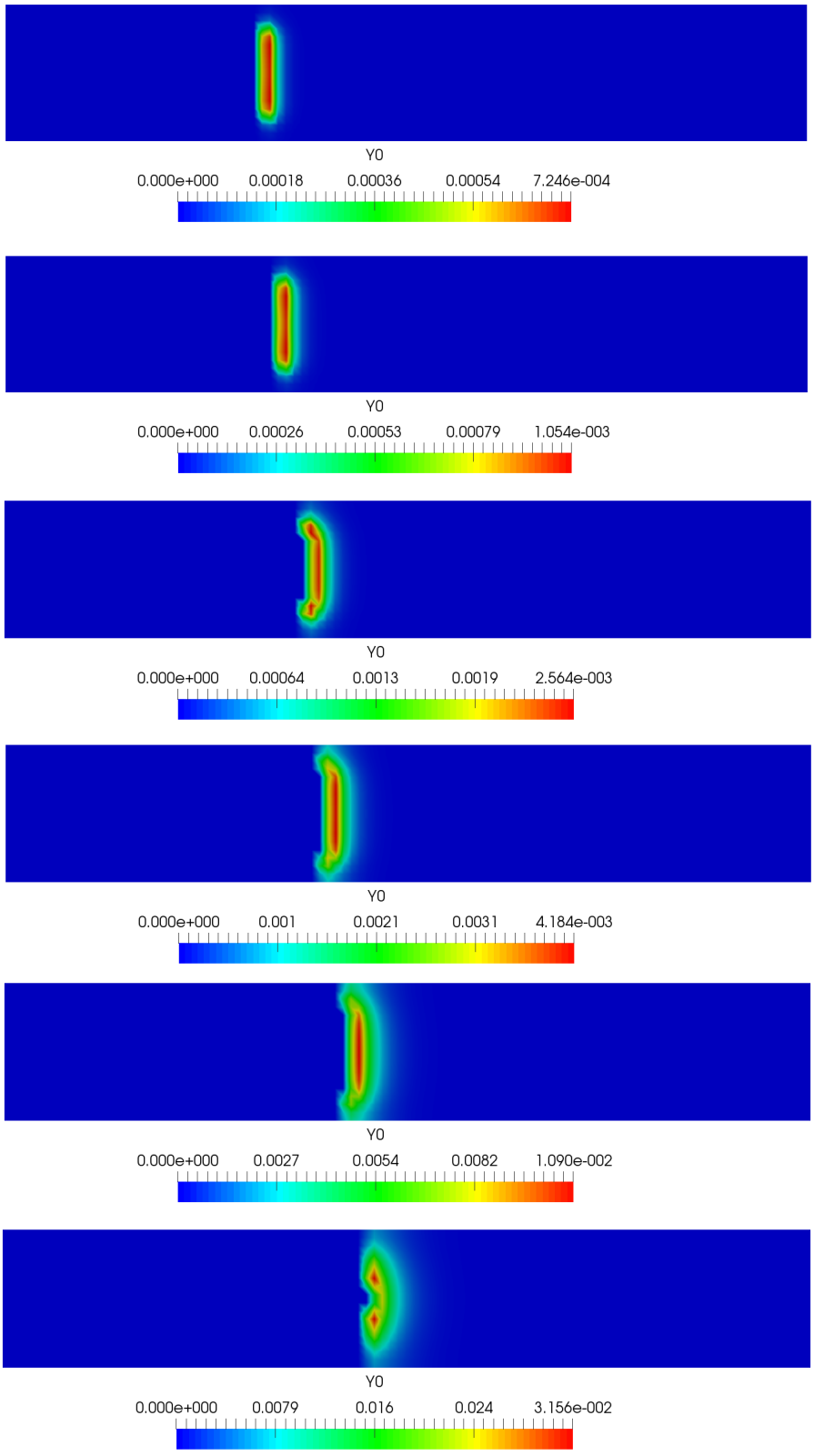

Figure 4.36: AP distribution in t = 0.02 s at 7 MPa, 5 MPa, 3 MPa, 2 MPa, 1 MPa, 0.5 MPa (above-below).

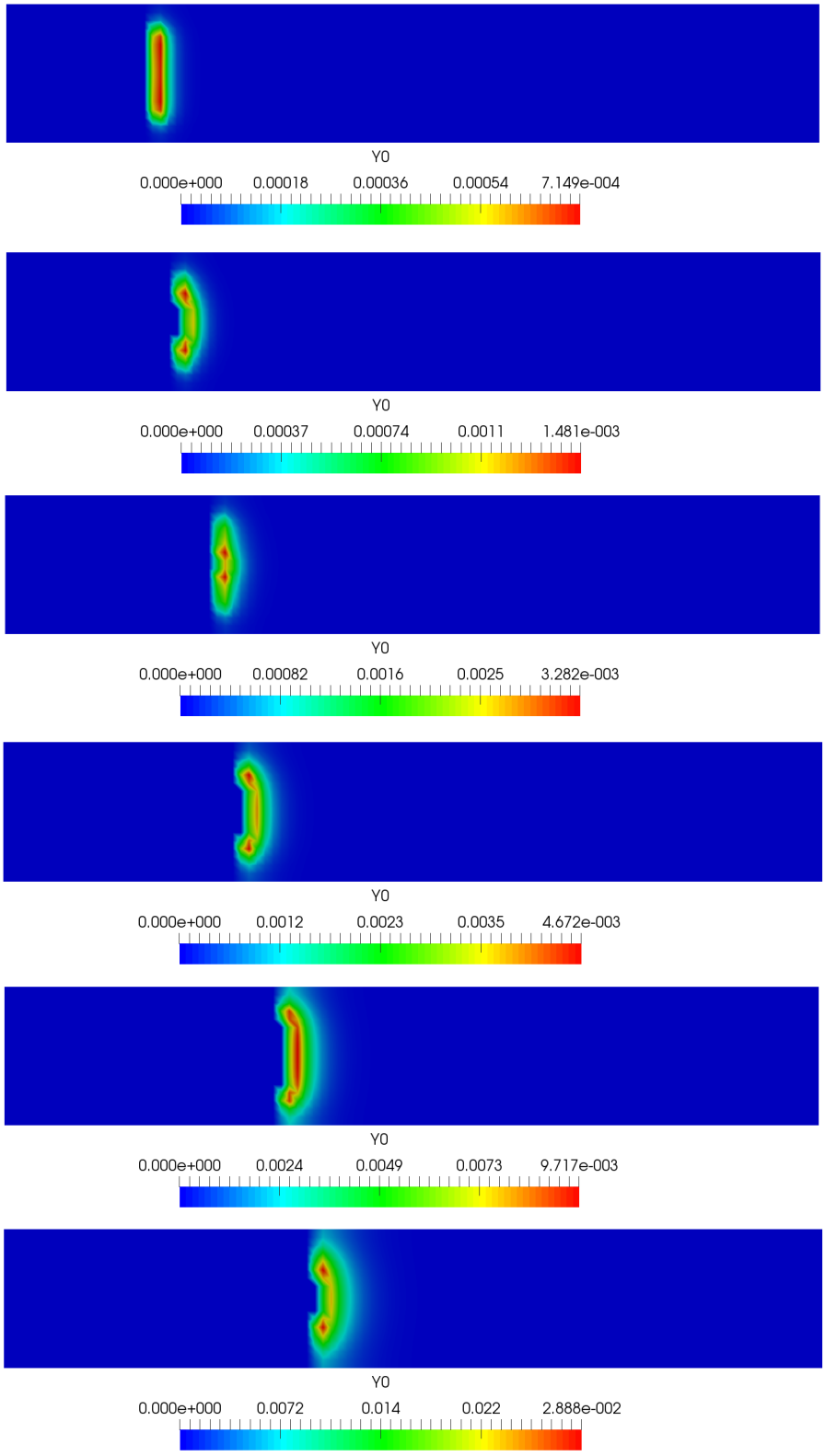

Figure 4.37: AP distribution in t = 0.04 s at 7 MPa, 5 MPa, 3 MPa, 2 MPa, 1 MPa, 0.5 MPa (above-below).

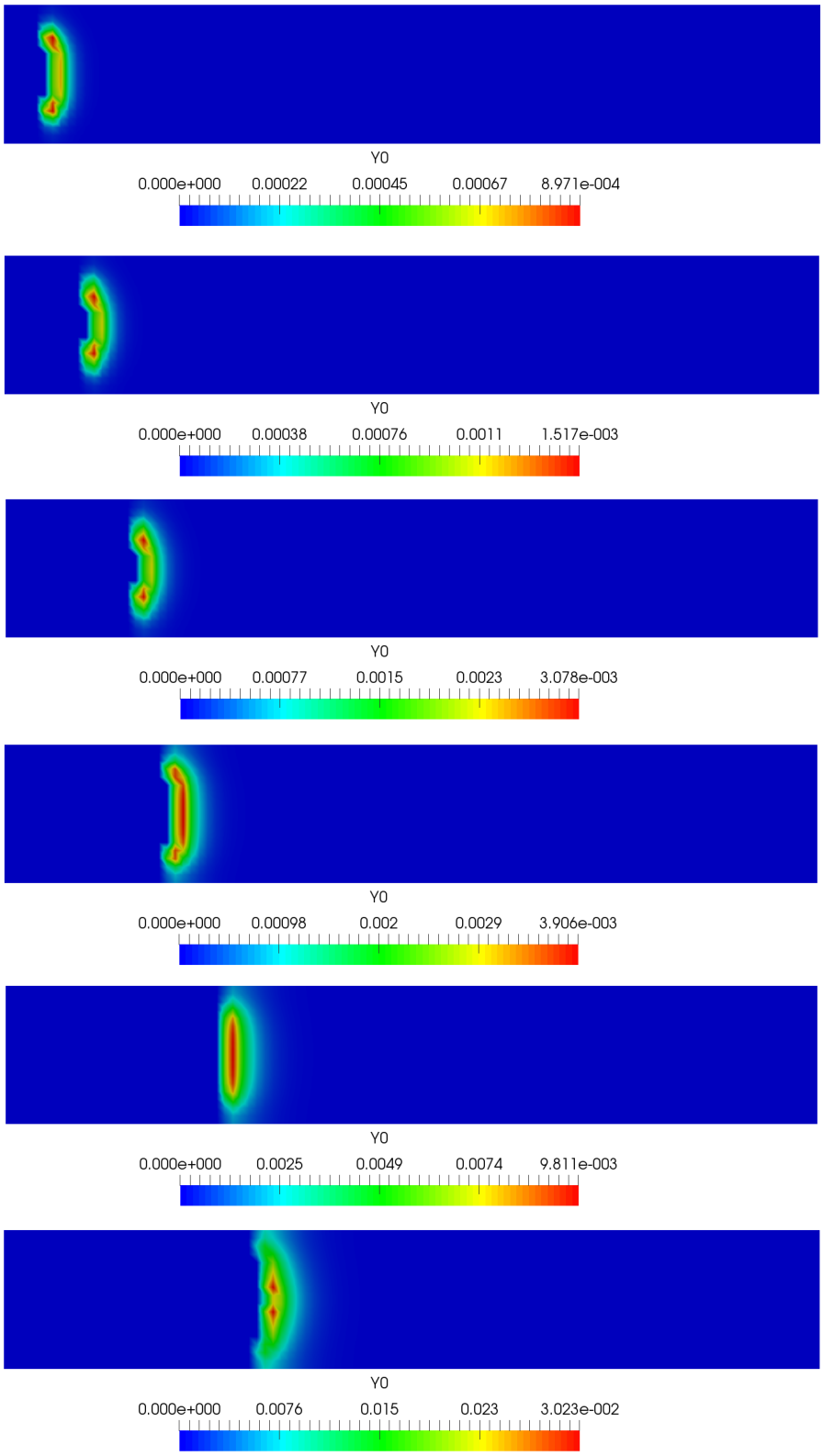

Figure 4.38: AP distribution in t = 0.06 s at 7 MPa, 5 MPa, 3 MPa, 2 MPa, 1 MPa, 0.5 MPa (above-below).

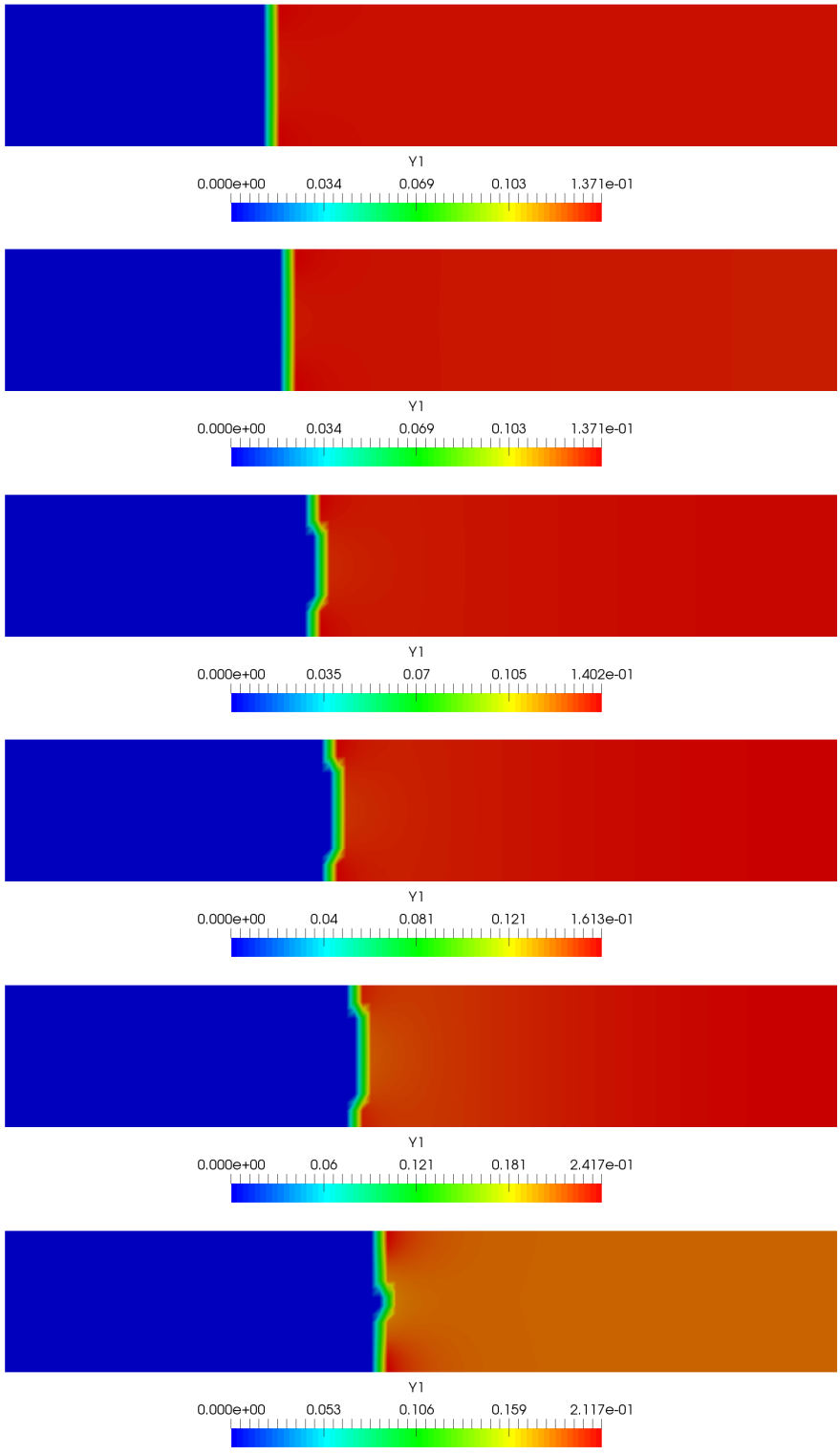

Figure 4.39: HTPB distribution in t = 0.02 s at 7 MPa, 5 MPa, 3 MPa, 2 MPa, 1 MPa, 0.5 MPa (above-below).

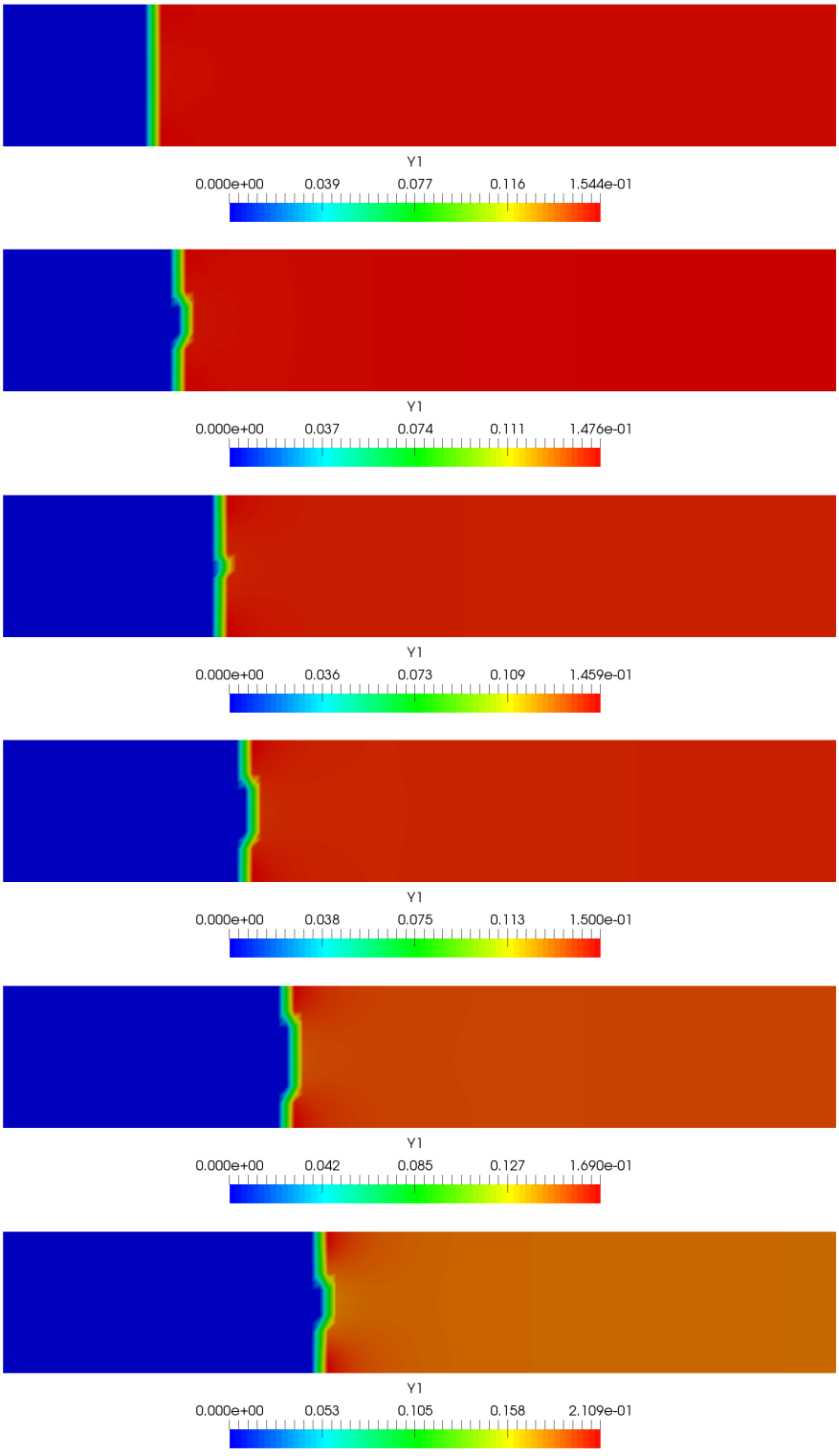

Figure 4.40: HTPB distribution in t = 0.04 s at 7 MPa, 5 MPa, 3 MPa, 2 MPa, 1 MPa, 0.5 MPa (above-below).

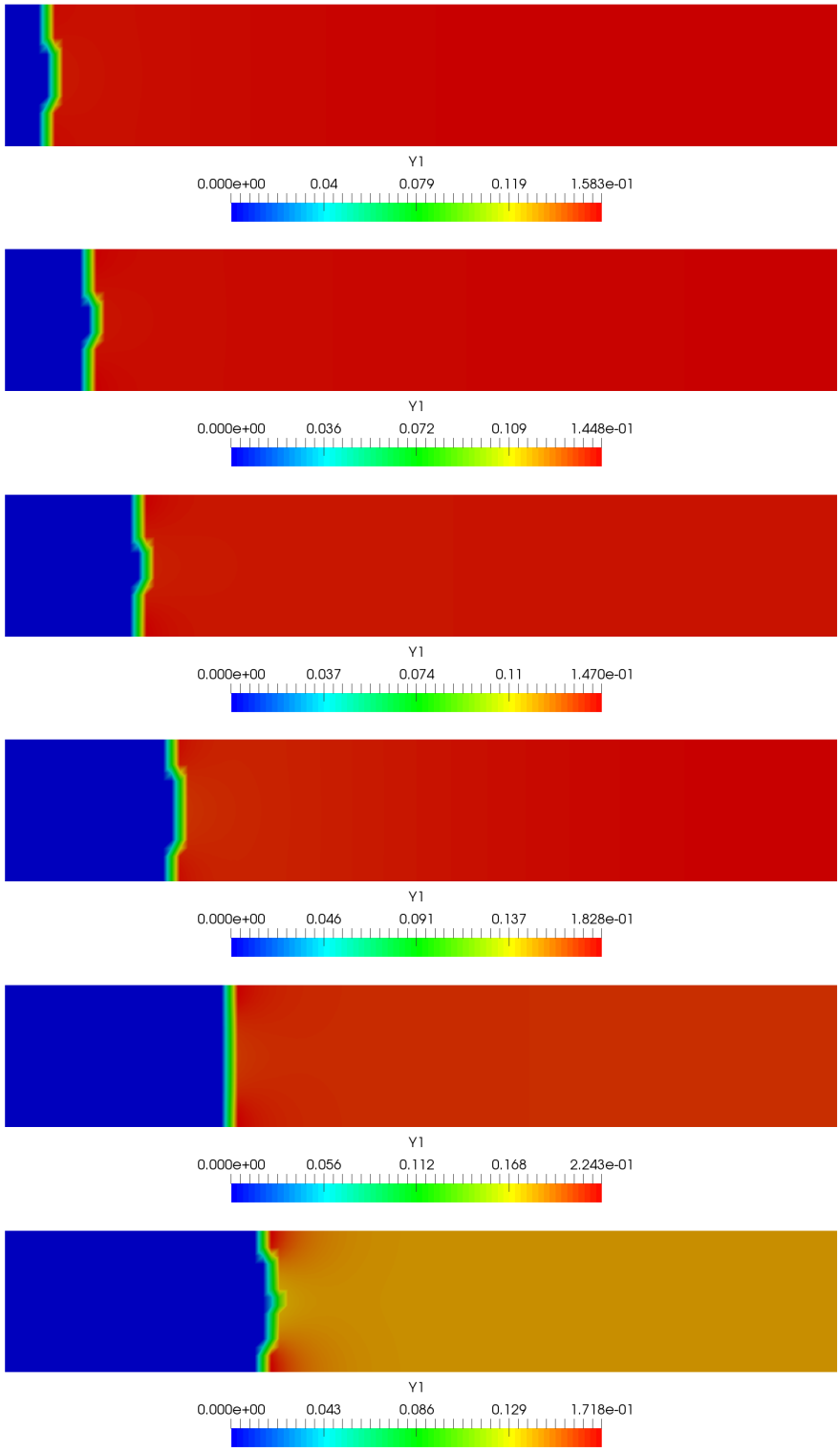

Figure 4.41: HTPB distribution in t = 0.06 s at 7 MPa, 5 MPa, 3 MPa, 2 MPa, 1 MPa, 0.5 MPa (above-below).

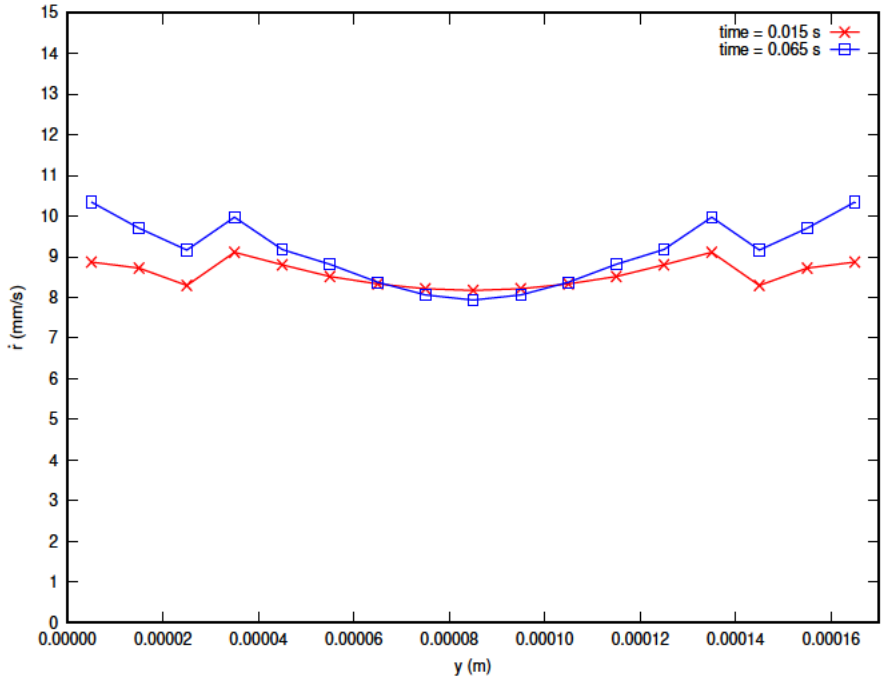

Figure 4.42: Burning rate distribution along the burning surface at t = 0.015 s and t = 0.065 s at 70 MPa.

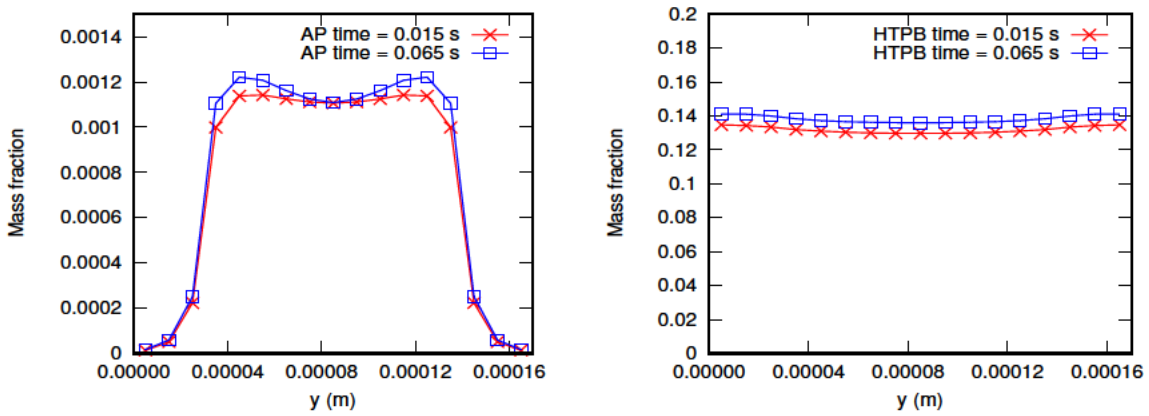

Figure 4.43: Mass fraction distribution after burning surface at t = 0.015 s and t = 0.065 s at 7 MPa for AP (left) and HTPB (right).

Finally, and before finishing this subsection, the results related to the global temperature and the heat flux analysis are detailed. A global variable temperature which takes the value of the condensed phase temperature or the gas temperature depending on the region considered is defined. This variable is firstly depicted in the x-direction for a pressure range from 0.5 to 7 MPa (see Figure 4.44, left) for time equal to 0.04 s. As observed, there is an abrupt raise of the temperature close to the burning surface and afterwards it remains stable. The value of constant temperature in gas phase increases slightly with the fall of pressure fixed at the right boundary. This phenomenon could take place because, as it was already discussed, the fall of pressure provokes a decrease of the reaction rates and therefore, there is a decrement in the combustion of AP and HTPB. As a consequence of the

loss of strength of AP and HTPB combustion reactions, the concentration of the reaction products (HCl, CO_2, H_2O, N_2) decreases mildly too. The slight decrement of the reaction products mass fractions is enough to make the density decrease its value provoking an increment of the temperature. Moreover, the effect of the temperature decrement with the raise of pressure can be also seen in Figure 4.44 (right), where the distributions in the y-direction of the condensed phase temperature at the cells adjacent to the burning surface when time is equal to 0.03 s are plotted for the each pressure of the considered range. Its distribution has a shape similar to the one of the regression rate at the burning surface plotted in Figure 4.42. This behaviour is exactly the one expected since the higher temperature the gas phase is, the higher will be the heat transferred to the solid along the burning surface.

Global temperature is depicted in colour diagrams as in Figures 4.45, 4.46 and 4.47 for times 0.02, 0.04 and 0.06 seconds. The behaviour observed in Figure 4.44 is repeated, temperature diagrams show how the decrement of pressure leads to a raise of the temperature far from the burning surface. In addition, it can be also seen how for low pressures, the temperature in the condensed phase increases more gradually than for higher ones. The global temperature variable is used afterwards to obtain the heat flux along the tube. Heat flux has been calculated by considering the heat conductivities of the different zones and multiplying by the temperature gradient. As expected, the main transference of heat is located at the burning surface where the solid changes its phase from condensed to gas (see Figures 4.48, 4.49 and 4.50). The remaining parts of the tube do not present a significant value of heat flux since in that volume the temperature remains mostly constant as it is already explained when analysing Figures 4.45, 4.46 and 4.47. Moreover, the greatest amount of energy is obtained in the central part of the sandwich where the change of phase of AP from condensed into gas phase and its combustion happen. The asymmetry encountered in the figures is due to the interpolation done by the software Paraview to obtain the point values in order to provide a smooth result. Cell values results can be found in Appendix.

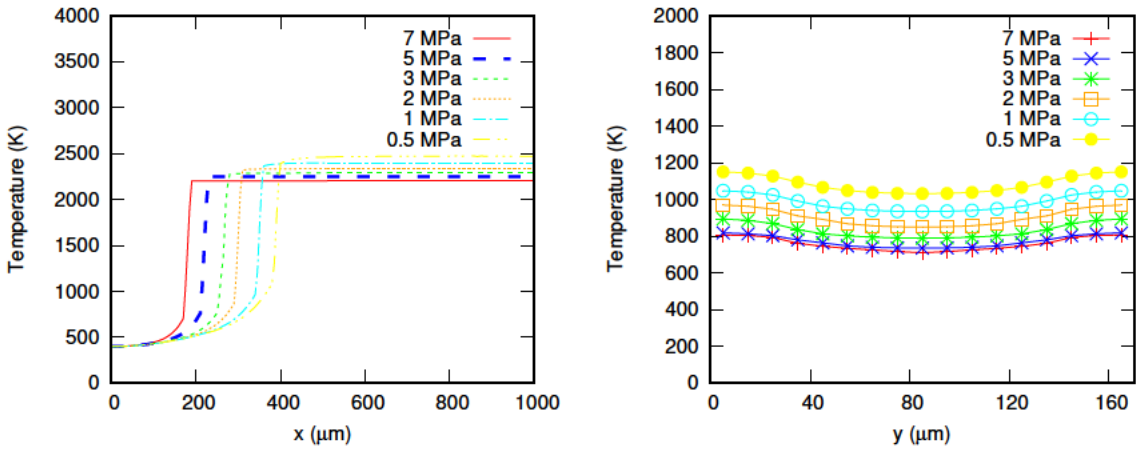

Figure 4.44: Temperature distribution for t = 0.04 s along x-direction (left) and temperature in condensed phase before burning surface at t = 0.03 s for 7 MPa to 0.5 MPa (right).

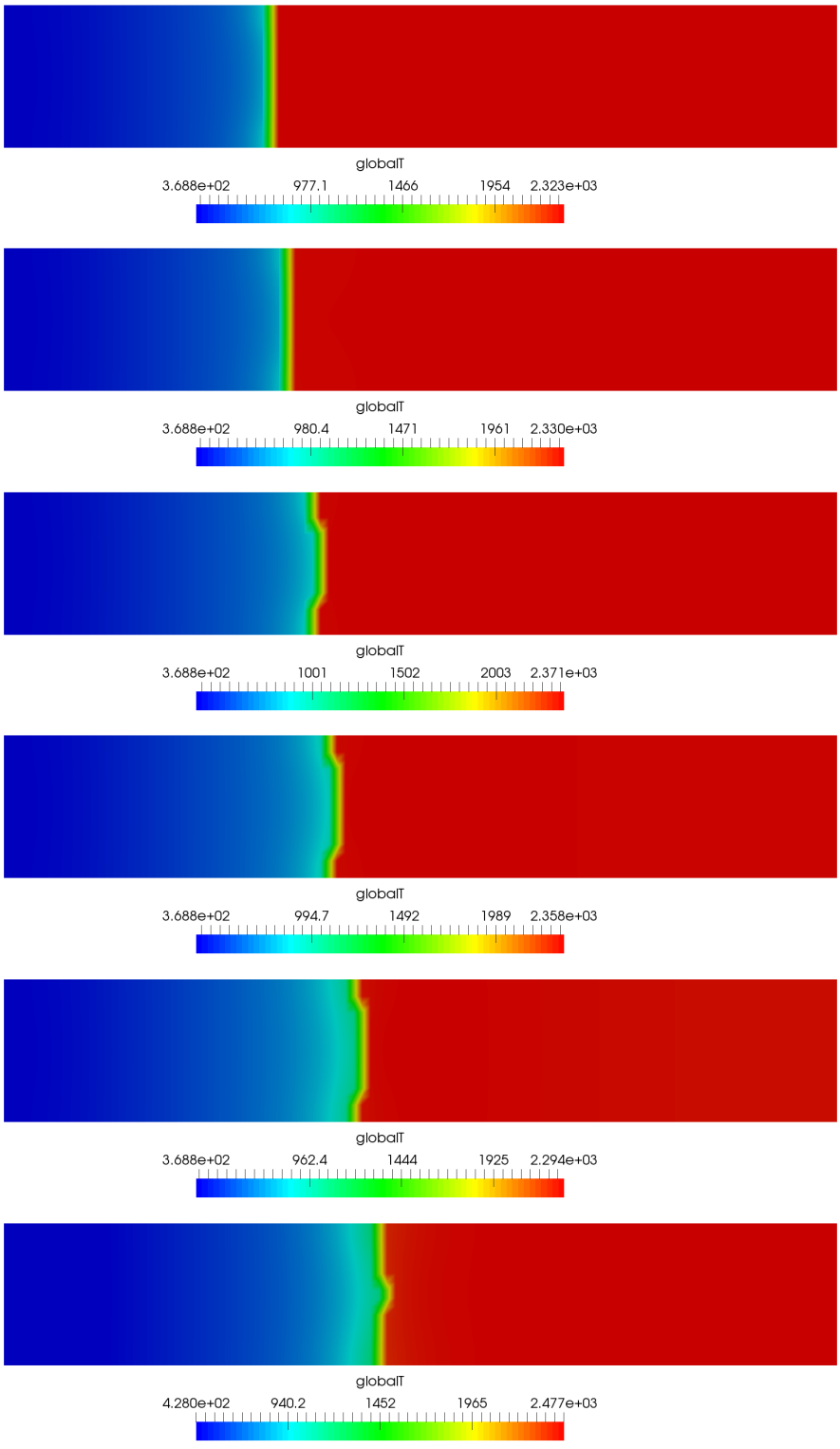

Figure 4.45: Temperature distribution in t = 0.02 s at 7 MPa, 5 MPa, 3 MPa, 2 MPa, 1 MPa, 0.5 MPa (above-below).

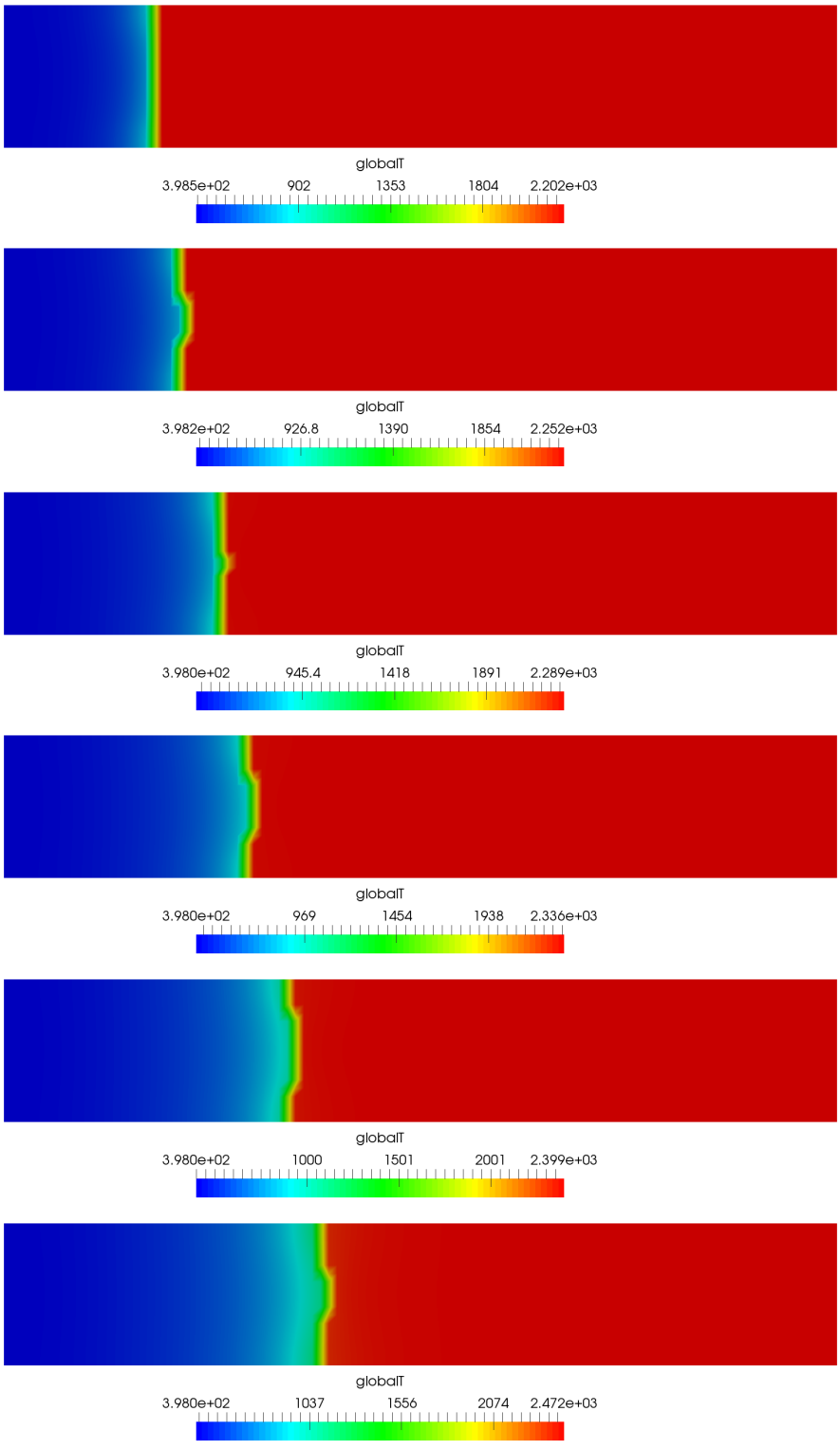

Figure 4.46: Temperature distribution in t = 0.04 s at 7 MPa, 5 MPa, 3 MPa, 2 MPa, 1 MPa, 0.5 MPa (above-below).

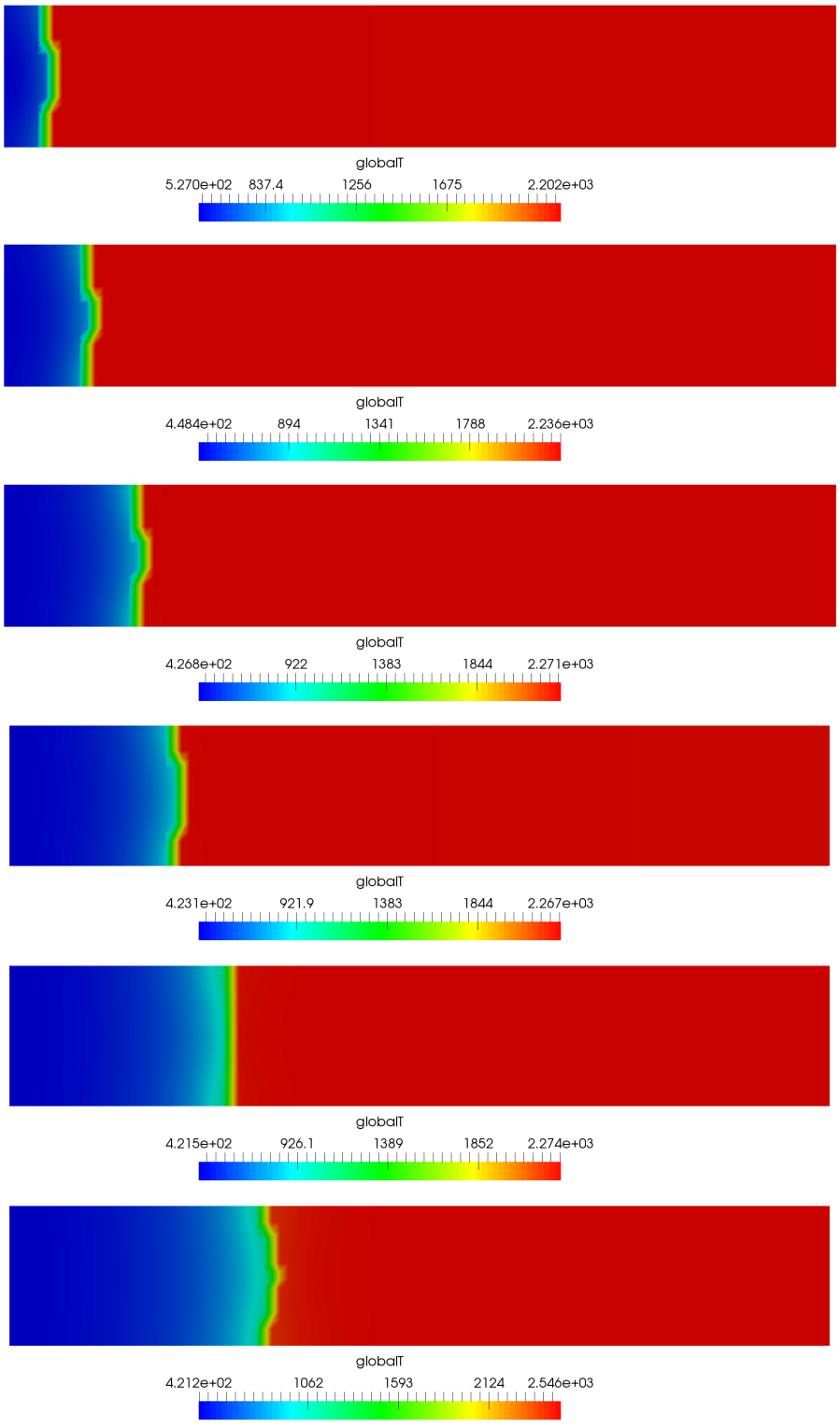

Figure 4.47: Temperature distribution in t = 0.06 s at 7 MPa, 5 MPa, 3 MPa, 2 MPa, 1 MPa, 0.5 MPa (above-below).

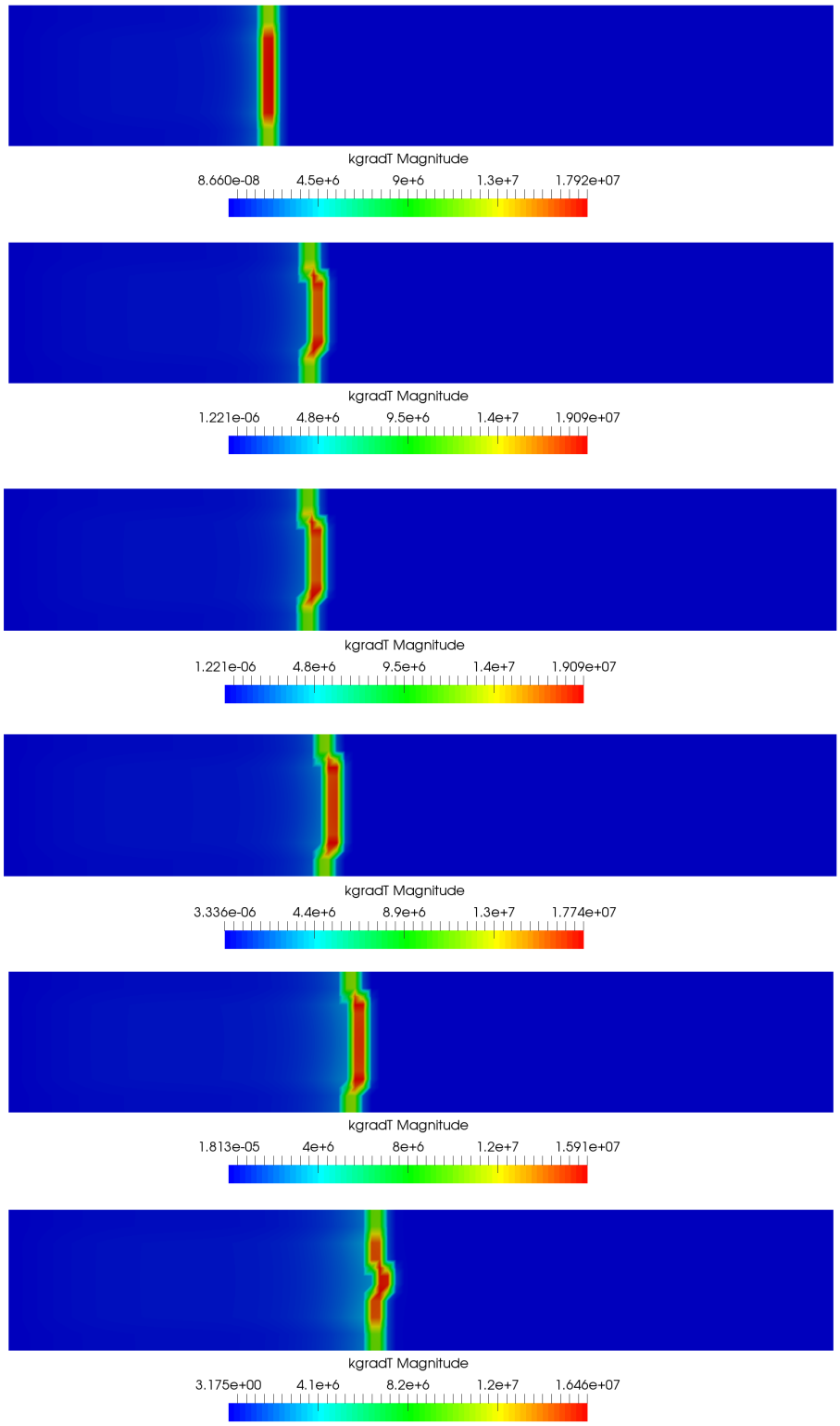

Figure 4.48: Heat flux distribution in t = 0.02 s at 7 MPa, 5 MPa, 3 MPa, 2 MPa, 1 MPa, 0.5 MPa (above-below).

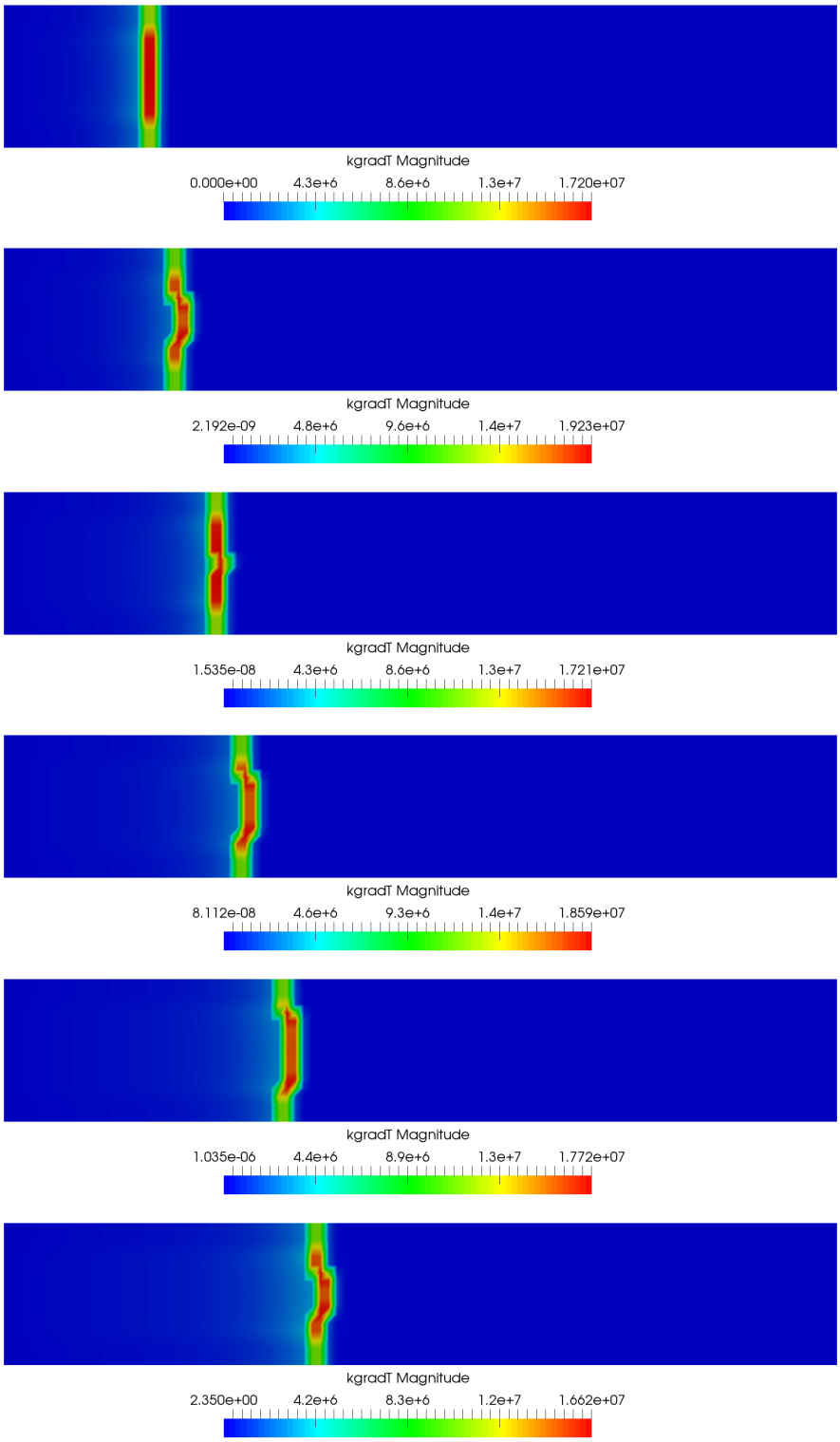

Figure 4.49: Heat flux distribution in t = 0.04 s at 7 MPa, 5 MPa, 3 MPa, 2 MPa, 1 MPa, 0.5 MPa (above-below).

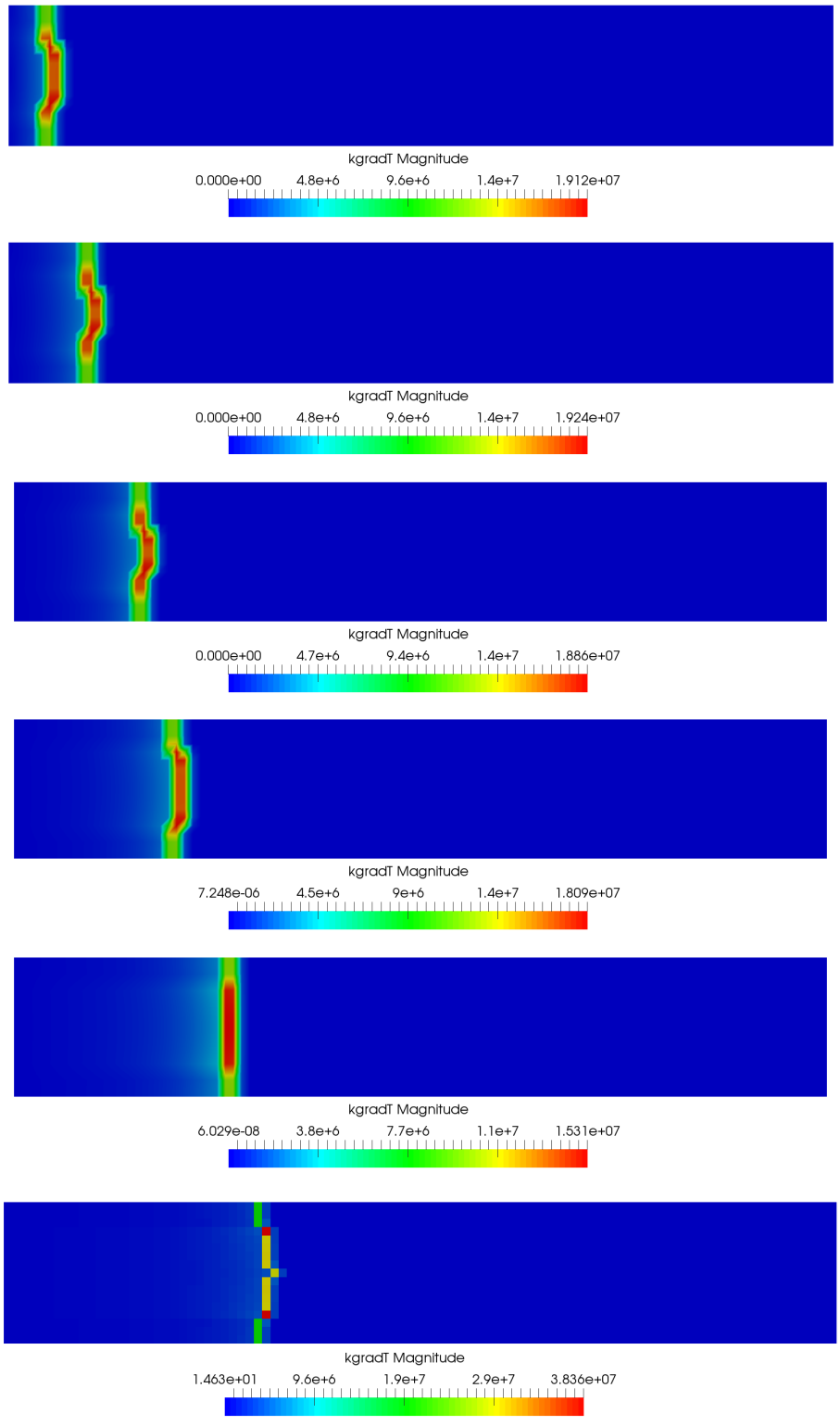

Figure 4.50: Heat flux distribution in t = 0.06 s at 7 MPa, 5 MPa, 3 MPa, 2 MPa, 1 MPa, 0.5 MPa (above-below).

4.2.3.3 Sandwich configuration test. Pressure ramp boundary conditions

Pressure oscillations produced in a rocket motor as well as depressurisation suffered in a combustion chamber and at the exit of a barrel, are very interesting technological problems which have not been deeply studied in the literature. Therefore, in this subsection the numerical modelling of transient combustion of solid composite propellant is presented. In order to perform this analysis, a last test is applied to the previous AP/HTPB sandwich configuration geometry (see 4.31) which consists in applying a pressure ramp as boundary condition at the end of the tube.

In this case, instead of fixing a constant pressure for the open side, as it is done in subsections 4.2.3.1 and 4.2.3.2, a sharp pressure ramp in the range of validated pressures (from 7 MPa to 0.5 MPa) is applied. This ramp will be produced in a very short time equal to 0.01 μs and it will start at 0.005 s. Therefore, before 0.005 s, the pressure will be fixed to 7 MPa and after 0.00500001 s the pressure will become 0.5 MPa. The effect provoked by this depressurisation is studied firstly in the pressure distribution, and afterwards in AP and HTPB mass fraction distributions, temperature, heat flux, burning rate and surface temperature. The ramp is depicted in Figure 4.52.

The first variable studied in this case is the pressure distribution. As can be seen in the colour diagrams from Figure 4.51, at t = 0.005 s, the pressure is 7 MPa and it has the same distribution as the test of subsection 4.2.3.2 for this pressure. When time is t = 0.005000005 s and t = 0.005000009 s the pressure at the end of the tube is in the middle of the ramp and therefore the pressure at this location is below 7 MPa. At t = 0.0051 the pressure wave has progressed from the open side of the tube to the middle of the gas area and at 0.0053 the final pressure of 0.5 MPa is reached and stable all along the tube. If instead of using colour diagram, the results of the pressure are plotted vs x-coordinate for an specific point in the middle of the tube, the jump of the pressure can be compared against 7 MPa and 0.5 MPa fixed pressure boundary conditions test (Figure 4.52). The point chosen for plotting is $P_1 = (515 \cdot 10^{-6}, 85 \cdot 10^{-6}, 85 \cdot 10^{-6})$. To be able to see in detail the variation of pressure, a zoom of time between 0.0052 to 0.007 s is provided in Figure 4.53. Pressure falls down sharply from 0.515 to 0.499 MPa and afterwards it increases its value smoothly until reaching equilibrium pressure of 0.5 MPa. It is relevant to remark that the pressure ramp induced at the right boundary leads to a decrease of the pressure below the one obtained at the same point when the boundary condition for pressure is fixed to 0.5 MPa reaching values even below the pressure at the boundary in that moment. Therefore, it can be said that, when the end of the chamber is put down rapid depressurisation the pressure wave evolves from the end to the beginning of the gas volume and comes back causing a depression under 0.5 MPa. How this phenomenon influences in the remaining variables of interest is studied hereafter.

AP and HPTB mass fractions obtained in gas area are the next variables to be analysed. When time is equal to 0.005 s, the distribution of AP mass fraction is the same as that obtained when applying 7 MPa fixed boundary condition but, as the time passes, the differences between fixed 7 MPa and 0.5 MPa and pressure ramp boundaries are perfectly visible (see Figures 4.55 and 4.56). As already observed in Figure 4.32the quickest movement of the burning surface is provided by the test which fixes a pressure 7 MPa at the right boundary. As expected, the burning surface x-coordinate location when applying pressure ramp boundary condition is in between the one of 7 MPa and the one of 0.5 MPa. As it was analysed in the previous section, the higher the pressure, the lower value of reactions rates and therefore, the higher AP mass fraction accumulated in gas area. Therefore, it is reasonable to think that the same phenomenon would be observed when comparing the quantity of AP mass fraction of ramp pressure against fixed pressure boundary conditions. The fall of pressure provoked by the depressurisation at the boundary leads to an increase of both AP mass fraction and its diffusivity (see Figure 4.57). This behaviour it is easily appreciated if the mass fraction of AP at P_1 is represented against time (see Figure 4.62) for 7 MPa, 0.5 MPa and pressure ramp boundary conditions. When pressure at the boundary is 7 MPa, the surface moves faster than when the pressure is 0.5 MPa and therefore, its burning surface is located further from P_1 than the burning surface for 0.5 MPa. For fixed 7 MPa test there is not AP mass fraction at this coordinate opposite to 0.5 MPa test which presents a content of AP around 2%. This happens because AP in gaseous form is located mostly at the cells close to the burning surface. The oxidiser mass fraction when depressurisation

is applied behaves exactly as 7 MPa fixed boundary one until time equal to 0.005 s. After this time, although its burning surface is located at the same position as 7 MPa one, AP mass fraction distribution at this point raises due to the increase of the diffusion of AP with the fall of pressure.

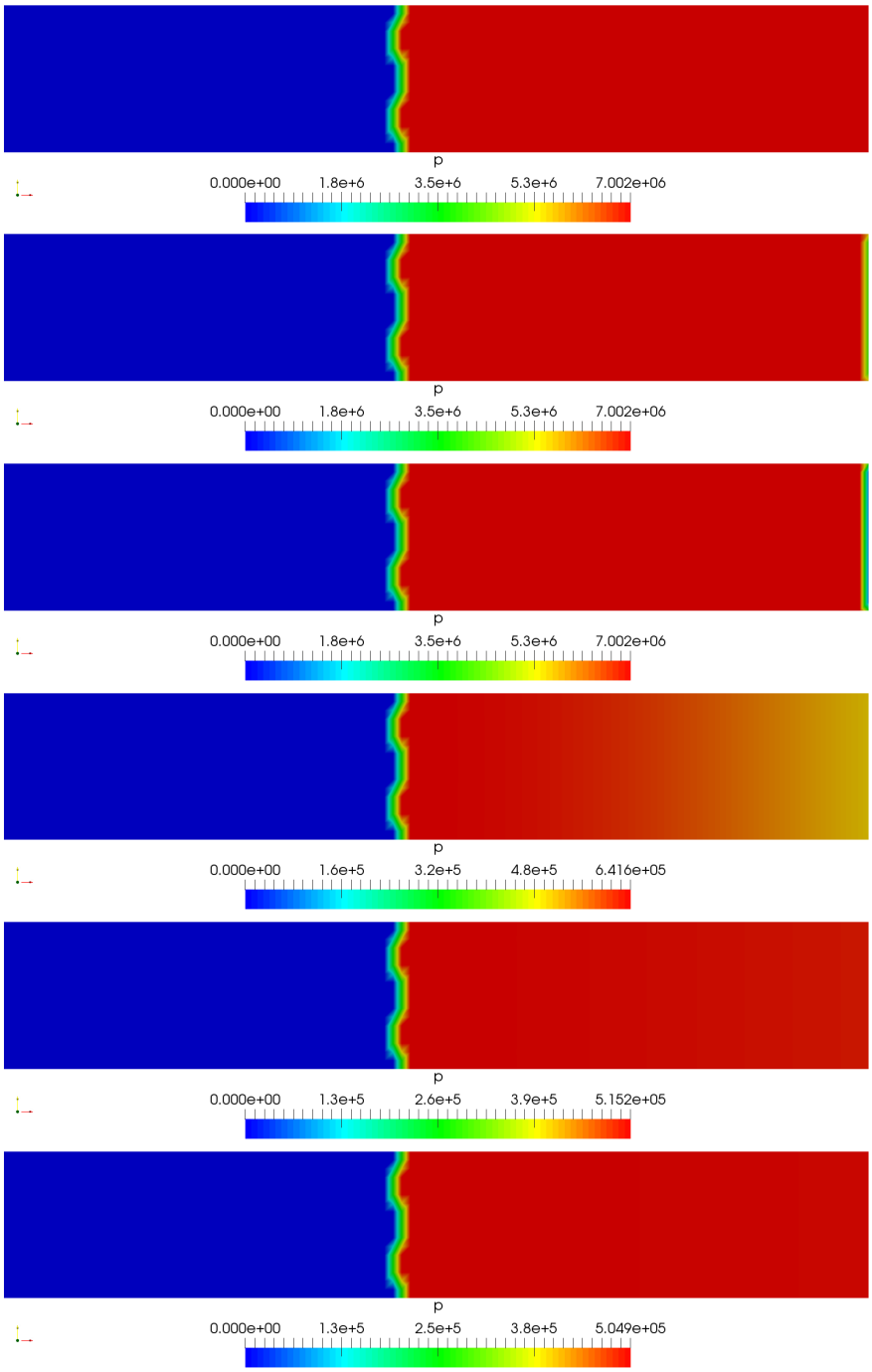

Figure 4.51: Pressure distribution in t = 0.005 s, t = 0.005000005 s, t = 0.005000009 s, t = 0.0051 s, t = 0.0052 s, t = 0.0053 s (above-below).

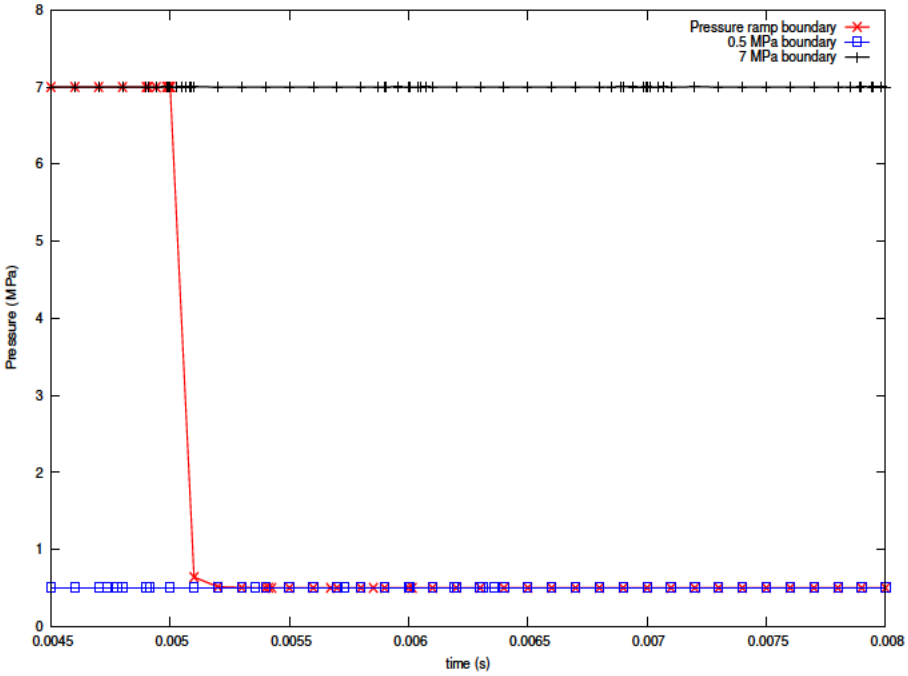

Figure 4.52: Pressure distribution against time for $P_1 = (515 \cdot 10^{-6}, 85{\cdot}10^{-6}, 85{\cdot}10^{-6})$.

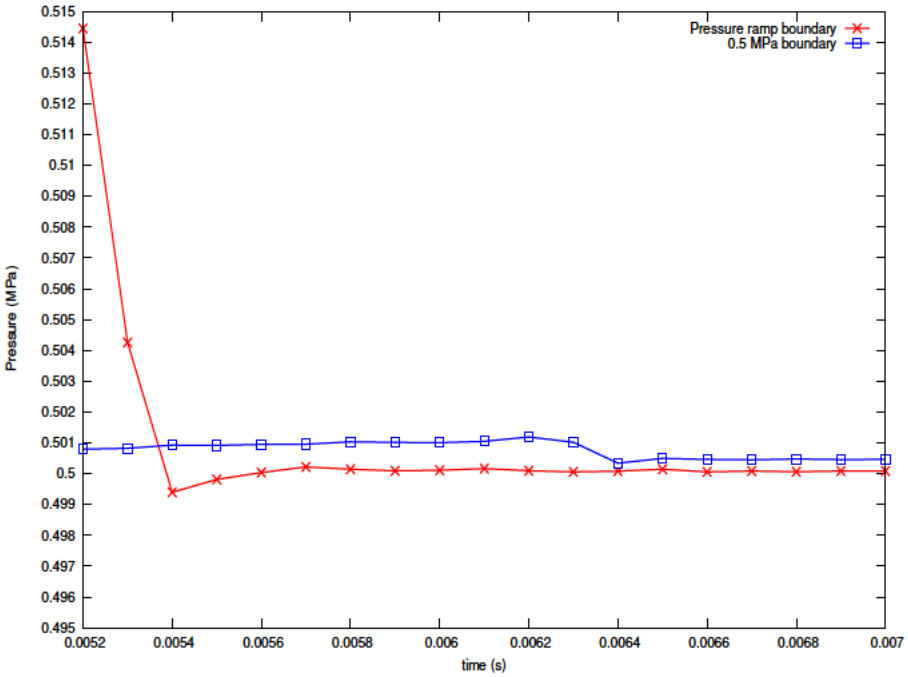

Figure 4.53: Zoom of pressure distribution against time for $P_1 = (515 \cdot 10^{-6}, 85{\cdot}10^{-6}, 85{\cdot}10^{-6})$.

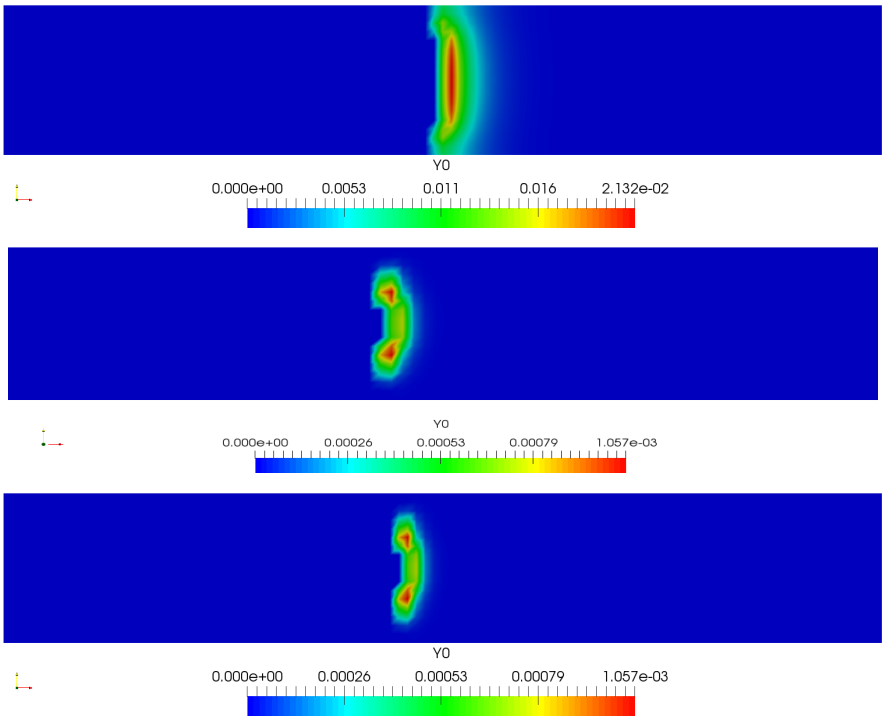

Figure 4.54: AP mass fraction distribution in t = 0.005 for 0.5 MPa, the pressure ramp and 7 MPa boundary conditions (above-below).

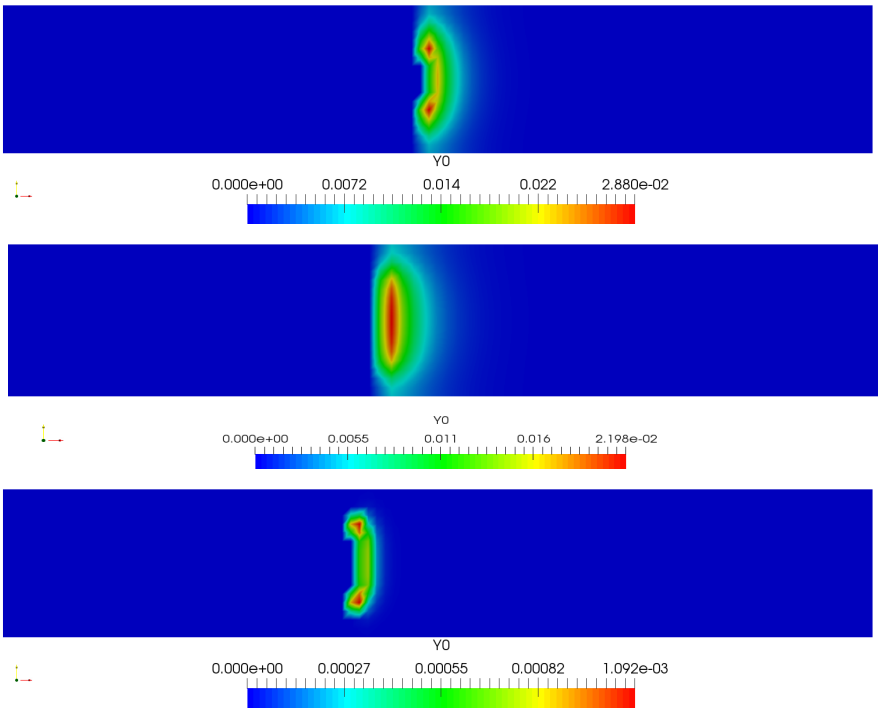

Figure 4.55: AP mass fraction distribution in t = 0.01 for 0.5 MPa, the pressure ramp and 7 MPa boundary conditions (above-below).

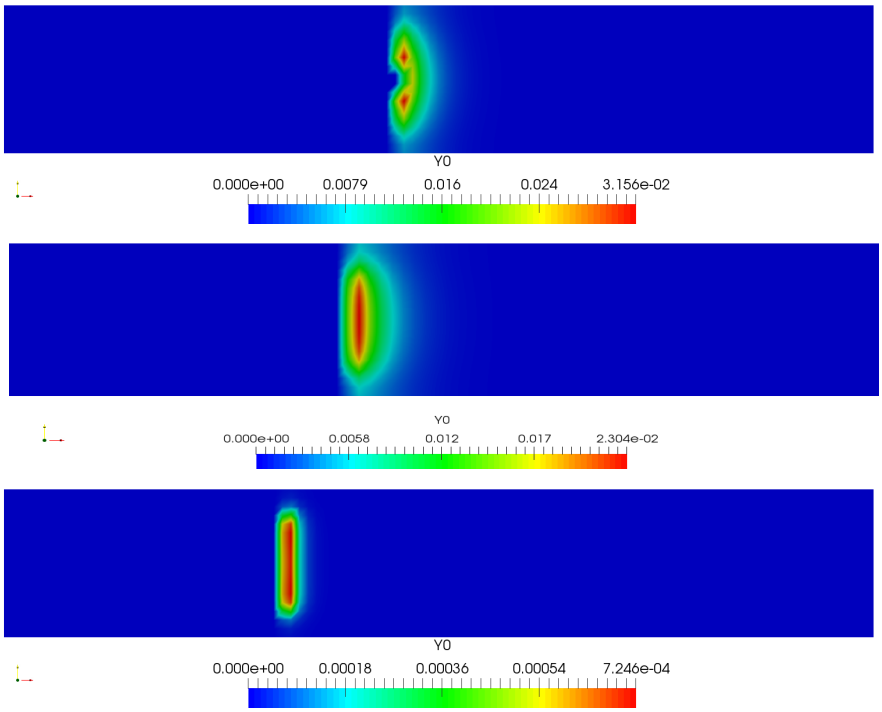

Figure 4.56: AP mass fraction distribution in t = 0.02 for 0.5 MPa, the pressure ramp and 7 MPa boundary conditions (above-below).

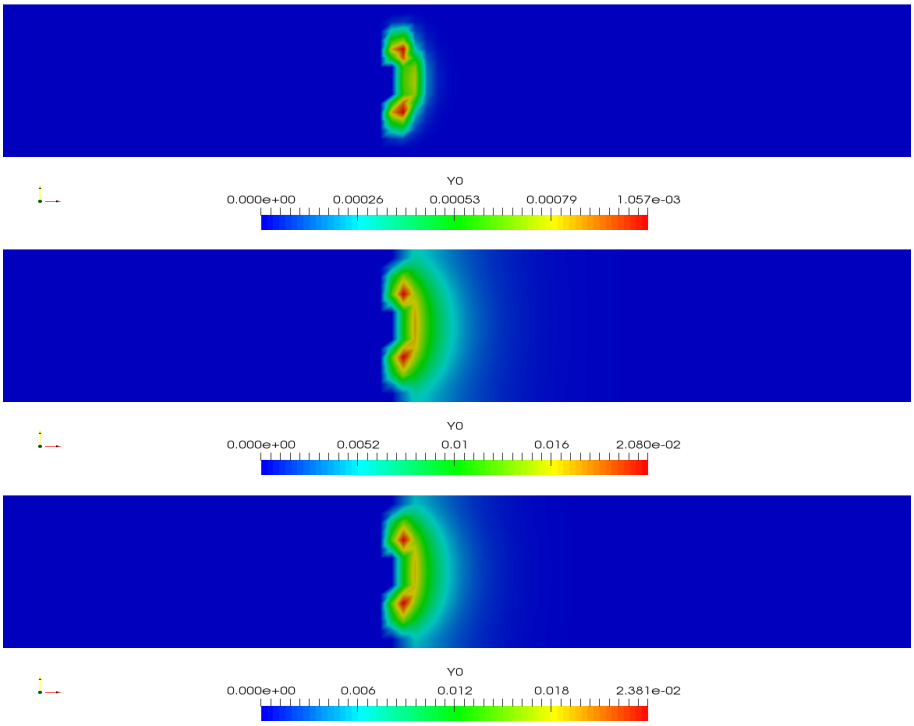

Figure 4.57: AP mass fraction distribution in t = 0.005 s, t = 0.0051 s and t = 0.0052 s (above-below).

The behaviour of HTPB in gas phase in case of considering a pressure ramp boundary condition, as it happens for fixed pressure boundary condition, it is completely opposed to the one of AP. Unlike AP which is mostly close to the burning surface, HTPB in gaseous form is uniformly distributed along the gas domain. Since the activation energy which the oxidiser needs to be decomposed is not really high, as soon as condensed AP sublimates to AP in gas phase, the first reaction takes place and most of the AP is decomposed in reaction products. However, binder combustion reaction, not only presents a higher activation energy, but also needs the products from the first reaction to take place. This could lead to the conclusion that when HTPB sublimates to gas, it does not burn immediately and therefore, it has enough time to spread along the control volume.

By observing HTPB mass fraction distributions from Figures 4.58, 4.59 and 4.60 the same conclusion about the burning rate is obtained. For each time considered, the position of the burning surface when a fixed boundary condition of 7 MPa is applied is closer to the beginning of the condensed phase domain which means that the propellant is burning quicker at high pressures. When time is 0.005 s, the position of the burning surface is the same for fixed 7 MPa and pressure ramp boundary conditions since during this time the same value of the pressure is applied at the end of the tube. However, at 0.01 s the pressure ramp test has already suffered the depression at the end of the tube and the pressure is established to 0.5 MPa. Therefore, the position of the burning surface in x-direction for pressure ramp is further from the left side than for 7 MPa fixed boundary test but closer than for fixed 0.5 MPa boundary condition case, as expected.

As happens with AP mass fraction, HTPB mass fraction increases with fall of pressure. As explained in subsection 4.2.3.2, the increase of mass fraction of both binder and oxidiser when the pressure decreases could be assigned to the reaction rates formulation. Since equations (4.61) and (4.62) are functions of the pressure, the higher the pressure, the higher reaction rate will be obtained. High values of R_1 and R_2 mean that the consumption of both, AP and HTPB. Therefore, due to mass fraction conservation equation (4.49), it could be said that high pressures increase the reaction rate leading to a decrease of propellant mass fraction in the domain.

It is of high interest to remark the phenomenon observed in Figure 4.63 as result of plotting the mass fraction of HTPB for the same specific point in the geometry used in Figure 4.62 (P_1). From 0.0045 s to 0.005 s, the behaviour of the pressure ramp boundary is exactly the same as that of 7 MPa fixed pressure boundary. However, together with the sharp fall of pressure, comes the strong raise of HTPB mass fraction. Comparing this figure with 4.53, the similarities are easily visible. The depressurisation at the boundary provokes a fall of pressure close to the burning surface even below 0.5 MPa. This decrement of pressure will lead to a raise of the value of HTPB mass fraction over the one obtained for 0.5 MPa fixed boundary test. This is the expected behaviour since it has been already concluded that the fall of pressure brings an increase of propellant in gas phase along the geometry. The mass fraction values obtained for both tests will come closer as the pressure for the pressure ramp boundary condition test becomes closer to 0.5 MPa. However, due to the fact that the mass fraction of HTPB present in the gas phase before reaching equilibrium is higher for the depressurisation test than for fixed pressure test, the mass fraction of binder obtained along the tube is higher when applying transient combustion although the final pressure of both tests is the same.

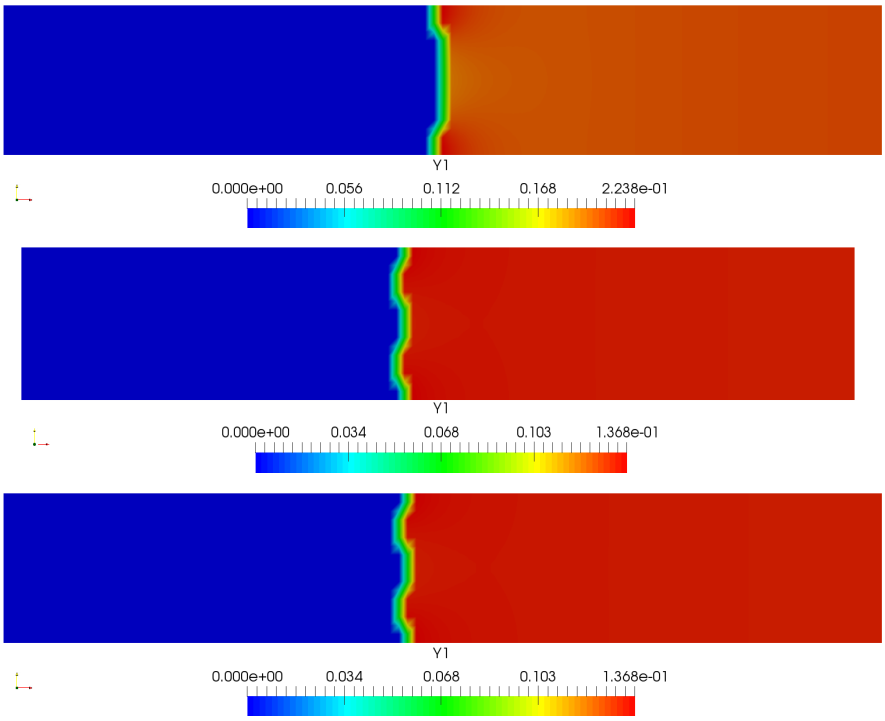

Figure 4.58: HTPB mass fraction distribution in t = 0.005 for 0.5 MPa, the pressure ramp and 7 MPa boundary conditions (above-below).

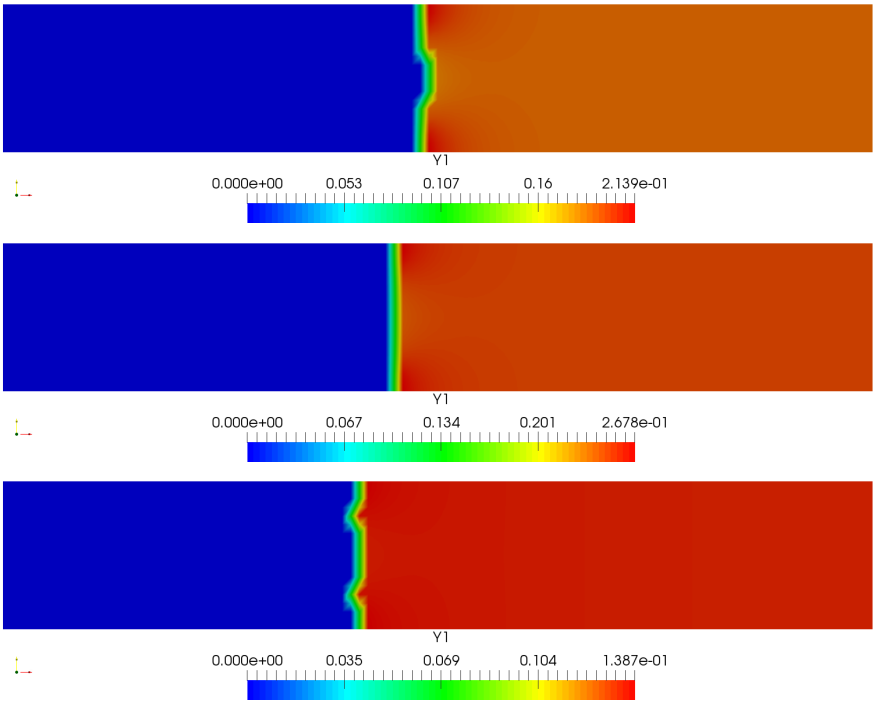

Figure 4.59: HTPB mass fraction distribution in t = 0.01 for 0.5 MPa, the pressure ramp and 7 MPa boundary conditions (above-below).

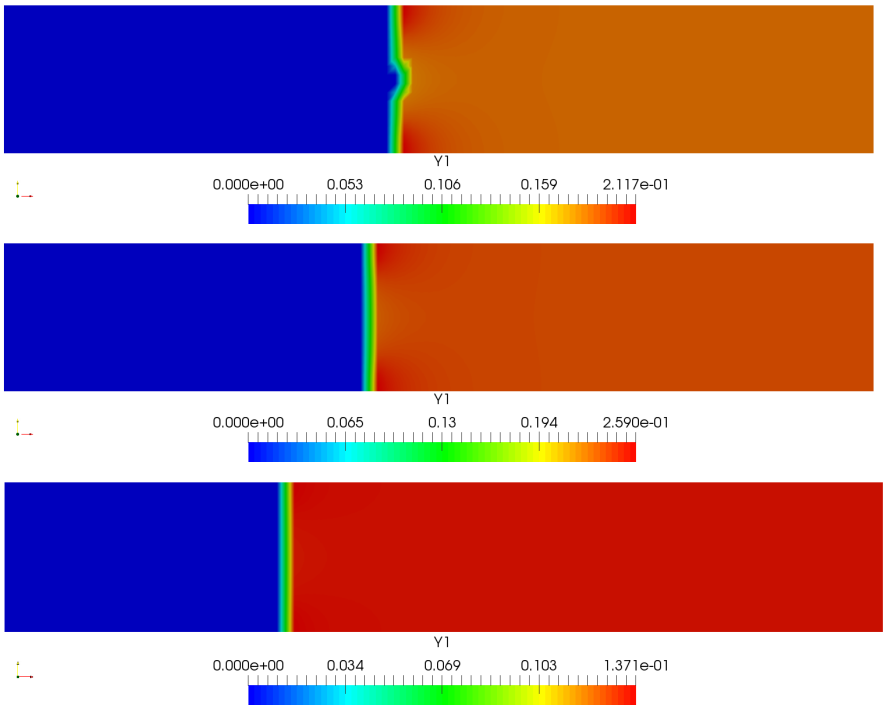

Figure 4.60: HTPB mass fraction distribution in t = 0.02 for for 0.5 MPa, the pressure ramp and 7 MPa boundary conditions (above-below).

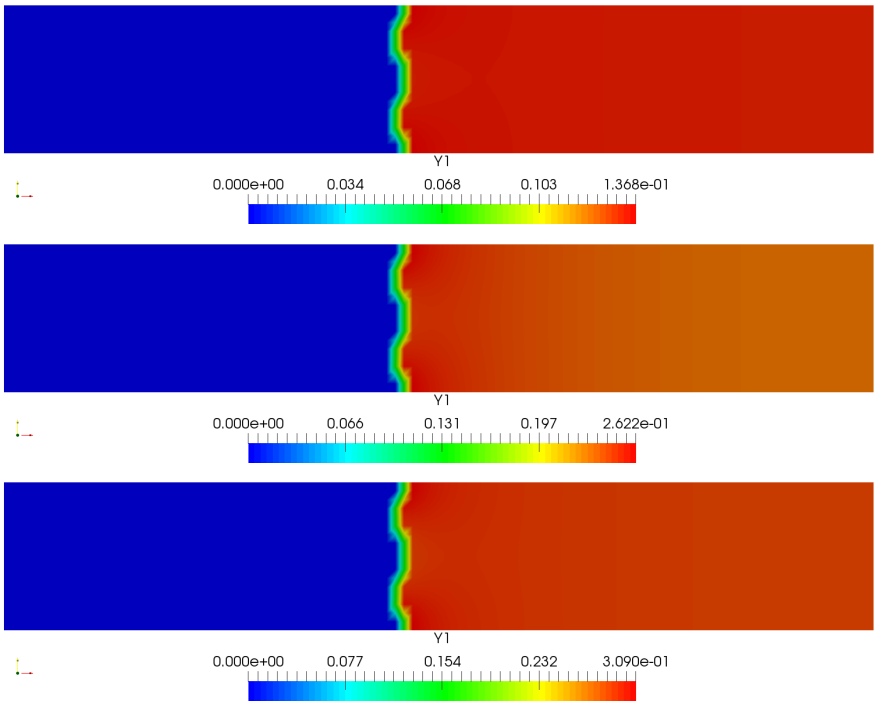

Figure 4.61: HTPB mass fraction distribution in t = 0.005 s, t = 0.0051 s and t = 0.0052 s (above-below).

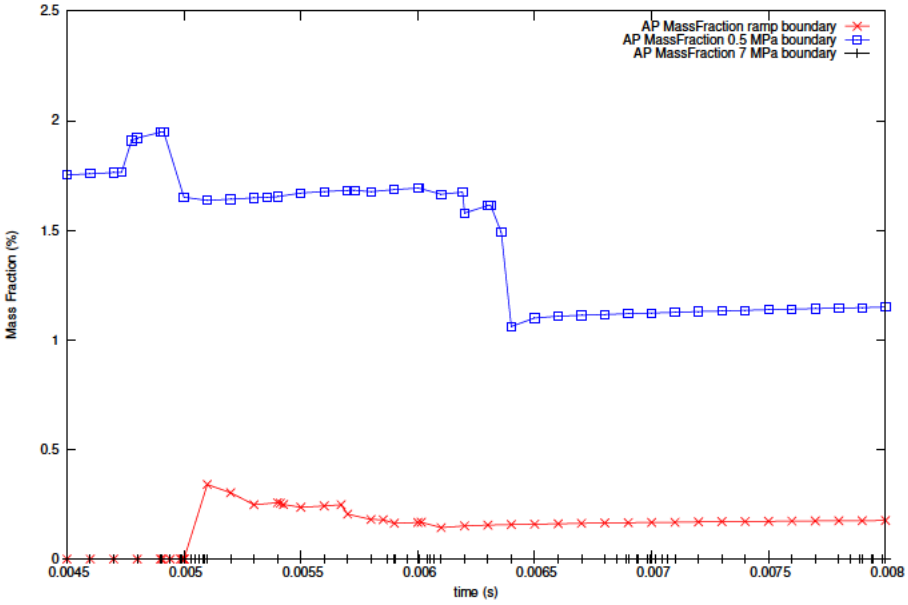

Figure 4.62: AP mass fraction (%) distribution against time for $P_1 = (515 \cdot 10^{-6}, 85{\cdot}10^{-6}, 85{\cdot}10^{-6})$.

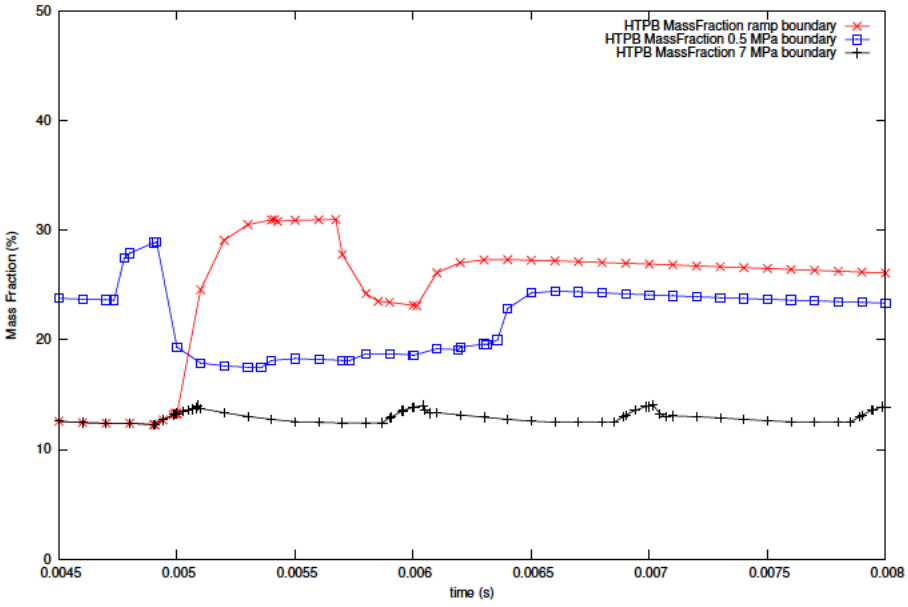

Figure 4.63: HTPB mass fraction (%) distribution against time for $P_1 = (515{\cdot}10^{-6}, 85{\cdot}10^{-6}, 85{\cdot}10^{-6})$.

As in subsection 4.2.3.2, global temperature and heat flux distribution are depicted. Firstly, the temperature distribution obtained when applying the ramp pressure boundary condition are shown in Figure 4.64. The immediate effect of the sharp fall of pressure at the end of the tube is the decrease of the temperature is this location as expected due to ideal gas law as it is visible in time equal to 0.0051 s. Afterwards, temperature raises again remaining mostly stable in all gas domain (see Figures 4.64, 4.65 and 4.66). As can be seen, the highest value of temperature reached at the end of the tube results when pressure applied at the right boundary is that obtained when fixing the

pressure at the right boundary to 0.5 MPa followed by the depressurisation test and finally, the 7 MPa fixed boundary test. The raise of the temperature field at the right side of of the tube when the pressure at the boundary falls down has been already explained in section 4.2.3.2. Since the reaction rates depend on the pressure, the lower the pressure, the lower reaction rate, leading to a decrease of the mass fractions of the reaction products with the consequent decrease of density and therefore, an increment of temperature. The temperature obtained when pressure is fixed to 0.5 MPa at the right boundary is slightly higher than that in the depressurisation test. This happens because before applying the pressure ramp at the right boundary, the pressure is fixed to 7 MPa and therefore, its density is higher than in 0.5 MPa test. The difference between the temperature obtained for 0.5 MPa fixed pressure and depressurisation boundary condition tests is narrowed with the time since the density of both, depressurisation and 0.5 fixed boundary condition tests, comes closer too. In addition, at low pressures, the evolution of the temperature along the control volume is softer than at high ones. This effect occurs immediately after applying depressurisation at the boundary (see Figure 4.64) and it is maintained with time as visible in Figures 4.65 and 4.66.

As expected, the main transference of heat is located at the burning surface where the propellant changes its phase from condensed into gas (see Figures 4.67, 4.68 and 4.69). The remaining parts of the tube do not present a significant value of heat flux since in that volume the temperature remains mostly constant as it is already explained analysing Figures 4.64, 4.65 and 4.66. In addition, the greatest amount of energy is obtained in the central part of the sandwich where the change of phase of AP from condensed to gas phase and its combustion happen. These are the same conclusions than those obtained in subsection 4.2.3.2 therefore, it can be said that the depressurisation of the ramp it has not a significant impact in the heat flux distribution. However, the magnitude of heat flux obtained for the pressure ramp test is smaller than that obtained when fixing the pressure to 7 MPa. This may be due to the smoother evolution of temperature along the domain produced at low pressure against the sharp increase of temperature at high ones.

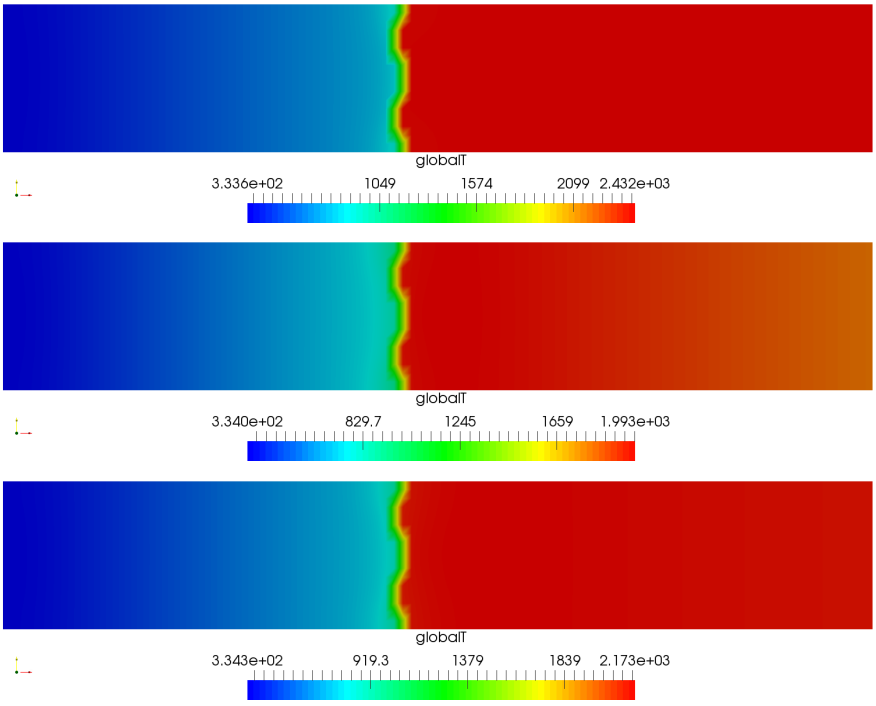

Figure 4.64: Temperature distribution in t = 0.005 s, t = 0.0051 s and t = 0.0052 s (above-below).

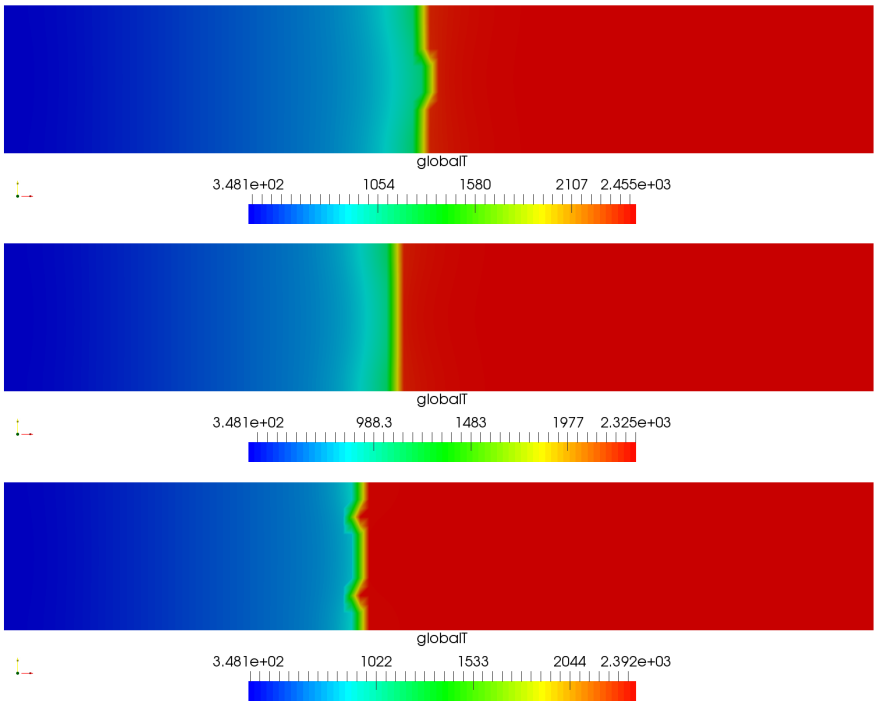

Figure 4.65: Temperature distribution in t = 0.01 s for 0.5 MPa, the pressure ramp and 7 MPa boundary conditions (above-below).

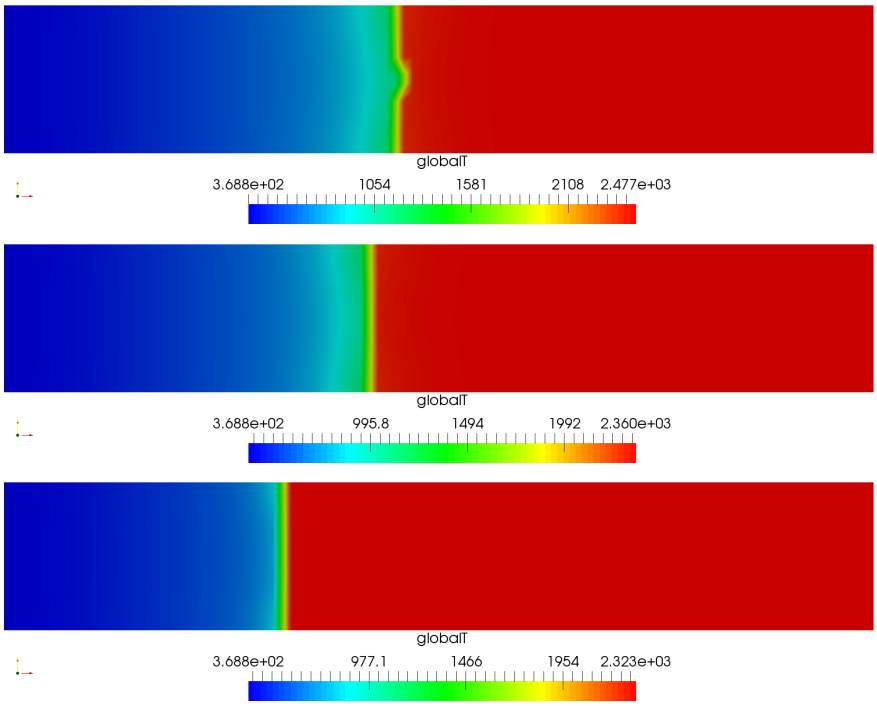

Figure 4.66: Temperature distribution in t = 0.02 s for for 0.5 MPa, the pressure ramp and 7 MPa boundary conditions (above-below).

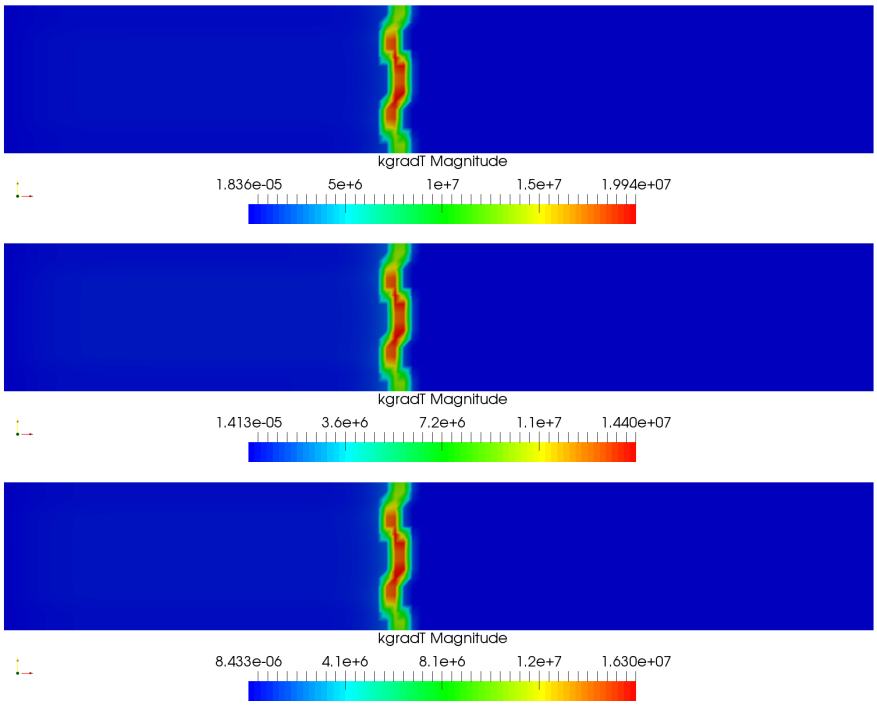

Figure 4.67: Heat flux distribution for ramp pressure boundary condition in t = 0.005 s, t = 0.0051 s and t = 0.0052 s (above-below).

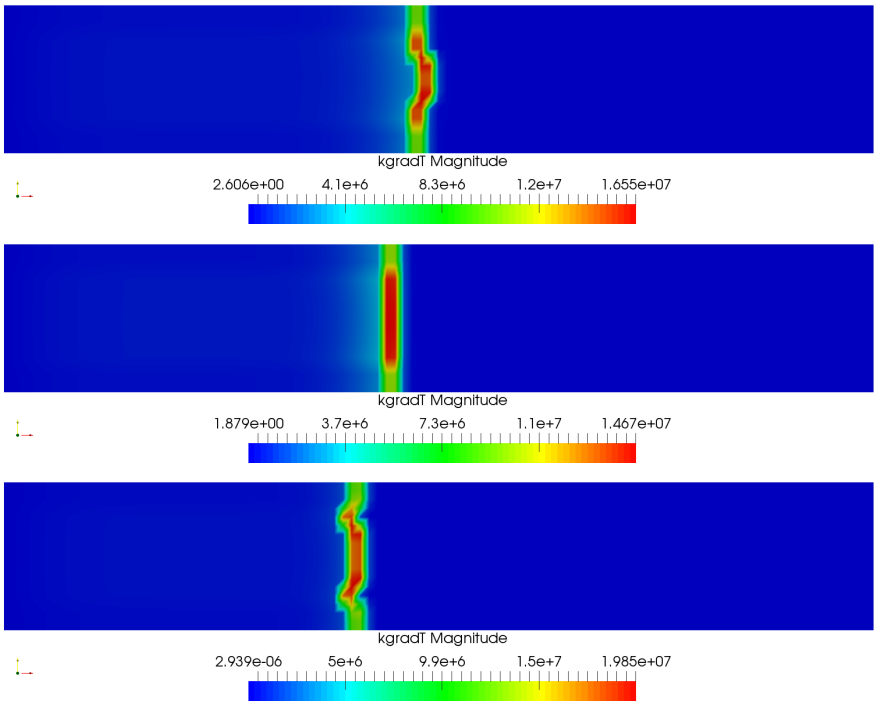

Figure 4.68: Heat flux distribution in t = 0.01 s for 0.5 MPa, the pressure ramp and 7 MPa boundary conditions (above-below).

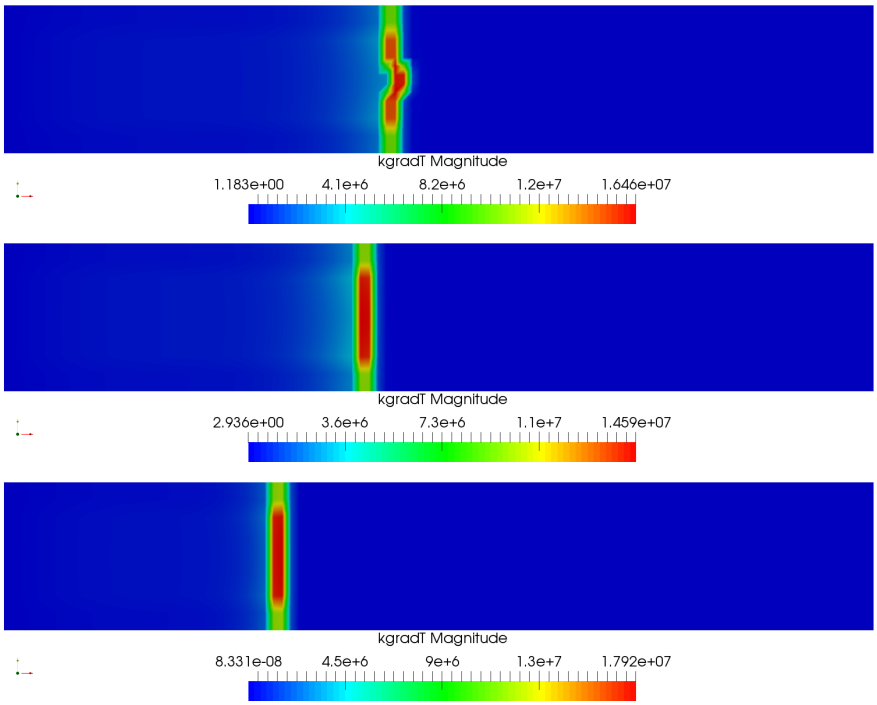

Figure 4.69: Heat flux distribution in t = 0.02 s for for 0.5 MPa, the pressure ramp and 7 MPa boundary conditions (above-below).

Finally, burning rate and temperature are plotted along the burning surface for times equal to 0.0021 s (before the pressure ramp is applied) and 0.0081 (after the pressure ramp boundary condition is applied). As in Figure 4.32 from subsection 4.2.3.1, it is observed how the burning rate decreases with pressure. Before applying the pressure ramp, the burning rate obtained at the burning surface is the same as the test cases in which the pressure is fixed to 7 MPa (see Figure 4.70) being the difference with the one for fixed 0.5 MPa very high. When the pressure ramp boundary condition is applied, the burning rate decreases reaching a value even lower than that of fixed 0.5 MPa boundary condition (see Figure 4.71). This phenomenon occurs because applying a sharp depressurisation at the boundary leads to obtaining lower values of pressure closer to the burning surface than those obtained when fixing the pressure to 0.5 MPa. Since burning rate is directly related with the pressure, together with a decrease of pressure below 0.5 MPa a fall of the burning rate below the value obtained for 0.5 MPa fixed pressure test will come. As the difference between the pressure obtained after depressurisation and the pressure obtained with fixed 0.5 MPa boundary is not really high, the gap between both burning rates is mild too.

Regarding the temperature at the burning surface, before applying the pressure ramp at the right boundary, the maximum value of temperature is that obtained when fixing the pressure of the right boundary to 0.5 MPa (see Figure 4.72). When the depressurisation is applied, the temperature of the burning surface for this test increases (see Figure 4.73) until reaching a value very close to that obtained for 0.5 MPa fixed pressure but lower. As a result, the distribution of the surface temperature when applying depressurisation is located between those obtained for 0.5 and 7 MPa fixed pressure boundary conditions tests. The same behaviour is noticed when analysing global temperature variable distribution in Figures 4.65 and 4.66.

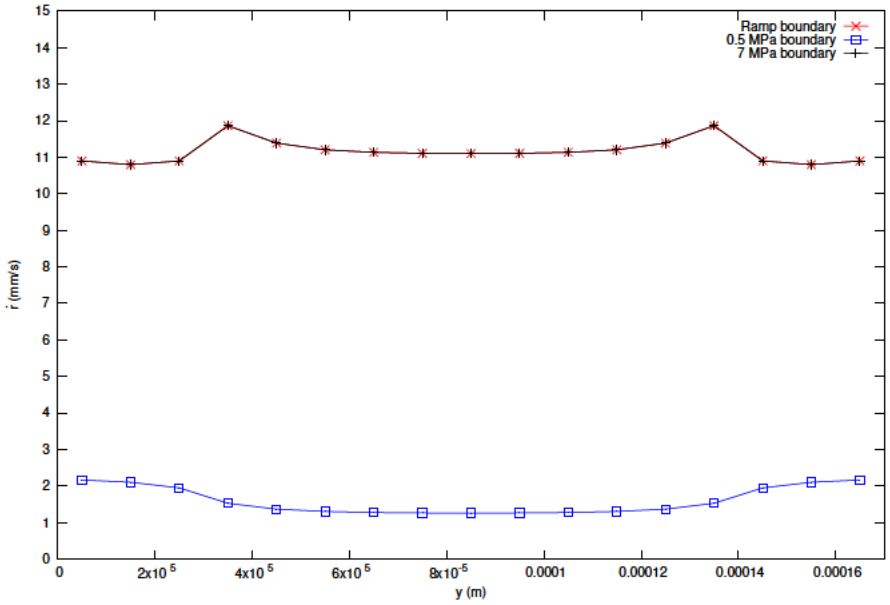

Figure 4.70: Burning rate distribution along the burning surface at t = 0.021 s for fixed 7 MPa, fixed 0.5 MPa and pressure ramp boundary conditions.

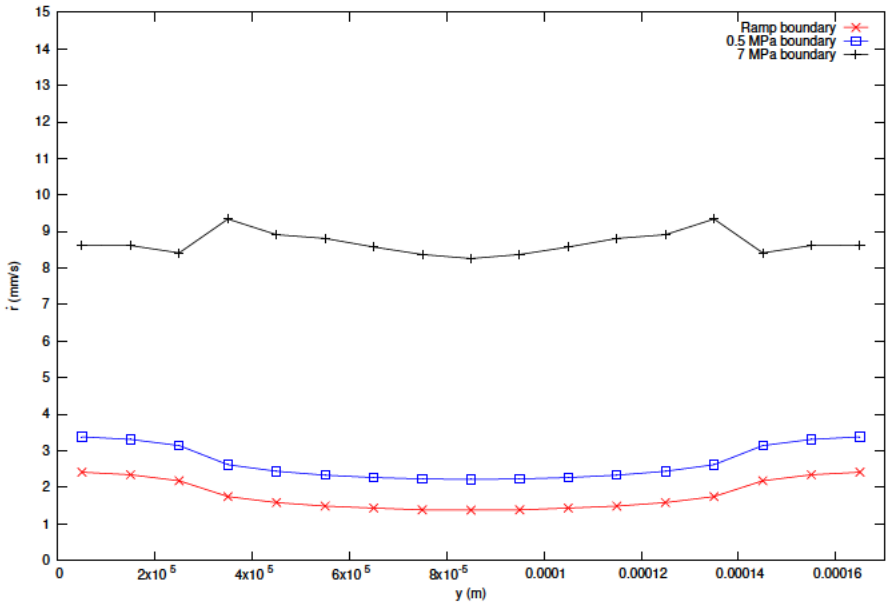

Figure 4.71: Burning rate distribution along the burning surface at t = 0.081 s for fixed 7 MPa, fixed 0.5 MPa and pressure ramp boundary conditions.

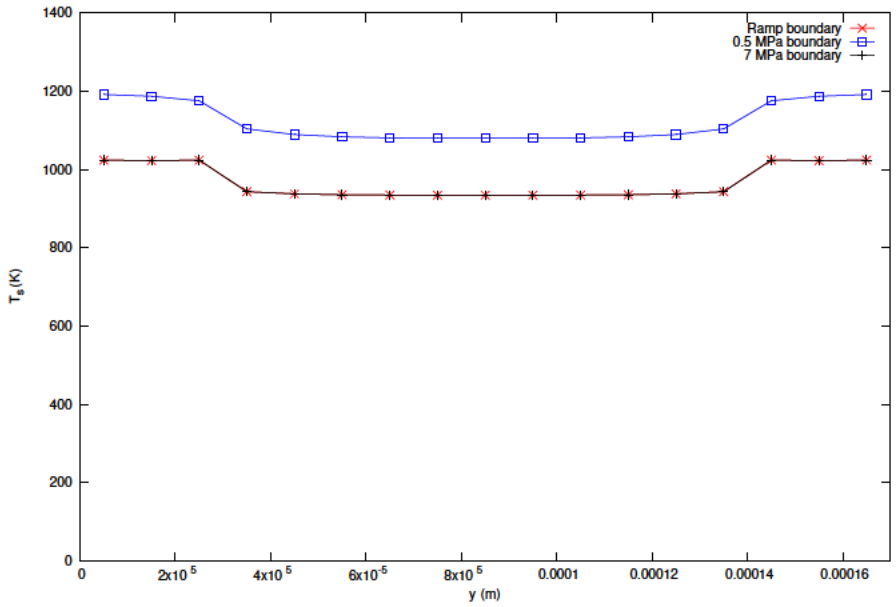

Figure 4.72: Temperature at the burning surface at t = 0.021 s for fixed 7 MPa, fixed 0.5 MPa and pressure ramp boundary conditions.

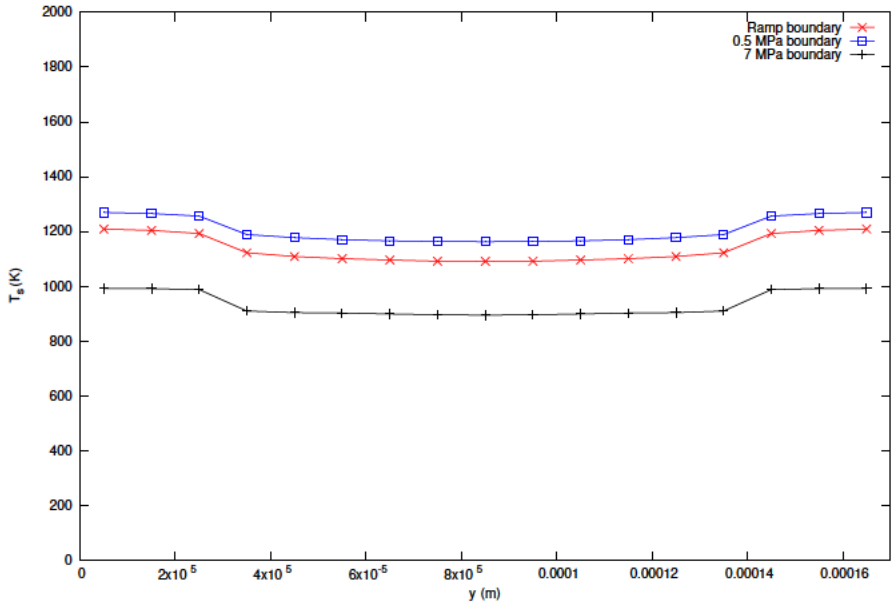

Figure 4.73: Temperature at the burning surface at t = 0.081 s for fixed 7 MPa, fixed 0.5 MPa and pressure ramp boundary conditions.

4.2.4 Conclusions

A code to study the multidimensional modelling of unsteady combustion of AP/HTPB propellants has been developed in OpenFoam. The code employs Rusanov numerical scheme to solve the homogeneous system of differential equations and afterwards, a first-order Euler methods to solve the ordinary differential equations including the source terms. The kinetics of the model is described by considering firstly, a change of phase of the solid propellant from condensed to gas and secondly, a reduced chemistry scheme which defines simplified chemical reactions to represent the combustion itself. To couple both processes, mass and species conservation, as well as temperature continuity are imposed in the burning surface in which the burning rate will represent a key factor. Moreover, an energy balance is also applied at the burning surface which represents that heat that the gas transfers to the burning surface is invested firstly, in raising the surface temperature to produce the phase change and secondly, in warming the condensed phase by conduction.

The first step done to validate the code is to perform a test which simulates the problem of combustion of a homogeneous AP/HTPB strand in a Crawford bomb strand burner. The simulation assumes that the tube is insulated and there is no transference of mass or energy in any boundary despite the right cross-section which open to atmosphere. The simulation has been performed twice by fixing the pressure in the right cross-section to 4 MPa and 7 MPa. The values obtained for the burning rate have been compared against experimental data from INTA facilities [86] obtaining positive results. Once this analysis has been concluded, the configuration of the binder and oxidiser is changed from a homogeneous strand to a geometry in which a layer of AP is located in between two layers of HTPB, called sandwich configuration. In this case the condensed control volume presents two different regions, one containing AP and other of HTPB, which have different thermophysical properties. As in the Crawford Strand Burner test, the simulation assumes that the tube is insulated and there is no transference of mass or energy in any boundary despite the right one which is open to atmosphere. The pressure at the right side of the tube has been fixed for this test and a range of pressures between 0.5 MPa to 7 MPa have been tested. Finally, the same geometry has been used to study the combustion of AP/HTPB propellant in sandwich configuration when a depressurisation ramp is performed. Instead of having a fixed pressure in the open side of the tube, a ramp boundary condition have been applied in which, in a very short interval of time, the pressure decreases from 7MPa to 0.5 MPa.

Regarding the first test considered in this subsection, it can be said that the results obtained in the simulation of the burning of an AP/HTPB homogeneous strand in a Crawford Bomb Strand Burner at 4 MPa and 7 MPa for several initial temperatures agree with the experimental ones. The absolute error present a range of values between 0.4 mm/s to 1.1 mm/s, being in the order of magnitude of the experimental error. However, the calculated relative error around 36% for 220.15K and 7 MPa and decreasing with the decrement of pressure and the increment of temperature to values around 10% at 4 MPa for 294.15 K and 347.15 K. As explained throughout subsection 4.2.3.1, the high magnitude obtained for the relative error is due to the low value of experimental burning rate for low temperatures. Therefore, although the absolute error remains around 1 mm/s, or even 0.4 mm/s for 294.15 K and 347.15 K, the decrease of the experimental burning rate raises the relative error.

Once the code have been validated against experimental data, the combustion of an AP/HTPB propellant in sandwich configuration fixing the pressure at the open side of the tube has been performed for a pressure range from 0.5 to 7 MPa. Distributions of the main parameters of interest such as, burning rate, gas velocity, mass fraction of AP and HTPB distributions, global temperature and heat flux have been studied. The main conclusions extracted from the analysis can be summarised in the following lines:

1. The burning rate results obtained with the developed two-dimensional model of this work applied to the combustion of AP/HTPB composite propellant in sandwich configuration agree well with the experimental ones from Kohga [51] for the considered pressure range. The relative error obtained from the results is less than 10% for a pressure range between 7 MPa and 2 MPa and below 25% between 0.5 MPa and 2 MPa. However, the absolute error remains constant

with a value around 0.5 mm/s, being in the order of magnitude of the experimental error. As it has been already explained, the increase in the relative error with the fall of pressure is due to the low values of burning rate obtained for the pressure range of 0.5 MPa to 2 MPa.

2. Despite the raise of the burning rate with the pressure, the higher the pressure, the lower the gas velocity has been obtained. This behaviour may be due to the increase of the gas density with the pressure. However, it is also observed that an increase of AP mass fraction close to the burning surface leads to a local raise of the gas velocity. This behaviour is attributed to the relationship between burning rate and gas velocity at the burning surface (4.54).

3. The behaviour of AP and HTPB mass fraction distribution along the gas domain is completely opposed. AP mass fraction presents a local concentration in the cells close to burning surface which has not an uniform distribution along the tube like it happens for HTPB. This behaviour may be due to the facility that the first reaction has to take place compared with second one. Since the activation energy that the oxidiser needs to be decomposed is not high, compared with the one from HTPB, it could be deduced that, as soon as condensed AP sublimates to AP in gas phase, the first reaction takes place and most of the AP is decomposed in reaction products. However, binder combustion reaction, not only presents a higher activation energy, but also needs the products from the first reaction to take place. This could lead to the conclusion that when HTPB sublimates to gas, it does not burn immediately and therefore, it has enough time to spread along the gas domain making possible for the cells far from the burning surface to accumulate higher concentrations of binder than oxidiser.

4. The content of AP and HTPB in gas phase increases with the pressure decrement as happened for gas velocity field. The increase of mass fraction of both binder and oxidiser with the fall of pressure could be assigned to the dependency of reaction rates expressions with the pressure. Therefore, the higher the pressure, the higher reaction rate will be obtained. A large value of reaction rates means that the consumption of both, binder and oxidiser, will be high. Therefore, due to mass fraction conservation equation, it could be said that high pressures increase the reaction rate leading to a consumption of propellant mass fraction.

5. The diffusivity of AP increases at low pressures. The rise in gas velocity at low pressure could increase the movement of AP throughout the domain. However, it is observed that, at 0.5 MPa, both binder and oxidiser mass fractions present a nonuniform distribution with higher concentrations in the cells of gas adjacent to their condensed phases respectively. This could happen because at low pressures, the degradation of the propellant is less intense and, in addition, R1 and R2 reaction rates of decrease. Therefore, the combustion of AP and HTPB in the cells close to the burning surface is reduced increasing as a result the mass fractions of binder and oxidiser in these cells.

6. Analysing the gas species distribution along a cross section plane close to the burning surface for a pressure of 7 MPa provides an almost constant content of HTPB. However, the content of AP reaches its minimum value in the lower or upper sides of the sandwich and its maximum at $y = 30\ \mu m$ where the interface between AP and HTPB is located, having a symmetric distribution. The burning rate profile is similar to that obtained for AP mass fraction despite for upper and lower layers of the sandwich where the burning rate does not decrease as abruptly as AP mass fraction does but softer due to the presence of HTPB which contribute to enhance the burning rate.

7. The value of constant temperature in gas phase increases slightly with the fall of pressure fixed at the right boundary. This phenomenon could take place because, as have been already discussed, the fall of pressure provokes a decrease of reaction rates and therefore, there is a decrement in the combustion of AP and HTPB. As consequence of the loss of strength of AP and HTPB combustion reactions, the concentration of the reaction products (HCl, CO_2, H_2O N_2)

decreases mildly too. The slight decrement of the reaction products mass fractions is enough to make the density decrease its value provoking an increment of the temperature.

8. The main transference of heat is located at the burning surface where the solid changes its phase from condensed to gas phase. In the rest of the tube, no significant change have been appreciated in the heat flux. This behaviour is the one expected since the temperature remains mostly stable all along the condensed phase and the gas phase presenting the only step in the burning surface.

Finally, the combustion simulation of AP/HTPB composite propellant in sandwich configuration has been performed applying a depressurisation ramp at the open side of the tube in order to see how it influences in the main variables of interest. The conclusions obtained are the following:

1. The pressure ramp induced at the right boundary leads to a decrease of the pressure value below 0.5 MPa at the cells located in the middle of the tube. Therefore, it can be said, that when the end of the chamber is put down to a rapid depressurisation the pressure wave evolves from the end to the beginning of the gas control volume and comes back causing a depression under 0.5 MPa.

2. As has been remarked in the previous conclusions, the higher the pressure, the higher the burning rate and therefore, the quicker the burning surface moves to the left side of the tube. As expected, the x-coordinate of the burning surface has an intermediate value between those of 7 MPa and 0.5 MPa tests.

3. The fall of pressure provoked by the depressurisation at the boundary leads to an increase of both AP mass fraction and its diffusivity. As expected, the distribution of oxidiser mass fraction obtained before applying the ramp boundary condition behaves exactly as that obtained for 7 MPa fixed boundary one. After applying the pressure ramp, AP mass fraction distribution raises due to the increase of the AP diffusivity with the fall of pressure although the burning surface is located at the same position as the one of 7 MPa test.

4. HTPB mass fraction also increases with the fall of pressure. Before the depressurisation is applied, the distribution of HTPB is exactly the same as that obtained in the 7 MPa fixed pressure boundary test. However, together with the sharp fall of pressure, comes a raise of HTPB mass fraction. The depressurisation at the boundary provokes a fall of pressure close to the burning surface even below 0.5 MPa. This decrement of pressure will lead to a raise of the value of HTPB mass fraction over the one obtained for 0.5 MPa fixed boundary test. The mass fraction values obtained for both tests will come closer as the pressure for the pressure ramp boundary condition test becomes closer to 0.5 MPa.

5. The immediate effect of the sharp fall of pressure at the end of the tube is the decrease of the temperature at this location as could be expected by taking into account ideal gas law. Afterwards, temperature raises again remaining mostly stable. The highest value of temperature reached at the end of the tube is that obtained when fixing the pressure at the right boundary to 0.5 MPa followed by the depressurisation test and finally, the value obtained for the 7 MPa fixed boundary test. Since the reaction rates depend on pressure, the lower the pressure, the lower reaction rate. This leads to a decrease of the reaction products mass fractions with the consequent decrease of density and therefore, an increment of temperature. The temperature obtained when pressure is fixed to 0.5 MPa at the right boundary is slightly higher than that of the depressurisation test. This happens because before applying the pressure ramp at the right boundary, the pressure is fixed to 7 MPa and therefore, its density is higher than in 0.5 MPa test. The difference between the temperature obtained for the 0.5 MPa fixed pressure test and the depressurisation test is narrowed with the time since the density of both, depressurisation and 0.5 fixed boundary condition tests, comes closer too.

6. The large value of heat transference is located at the burning surface where the propellant changes its phase from condensed to gas. The greatest amount of energy is obtained in the central part of the sandwich where degradation of condensed AP takes place. Since, the behaviour is the same than that obtained for the fixed pressure boundary condition, it can be said that the depressurisation of the ramp has not a significant impact in the heat flux. However, the magnitude of the heat flux obtained for the pressure ramp test is smaller than that obtained when fixing the pressure to 7 MPa. This may be due to the smoother evolution of temperature along the domain produced at low pressure against the sharp increase of temperature at high ones.

7. The burning rate decreases with pressure. Before applying the pressure ramp, the burning rate obtained at the burning surface is the same for fixed 7 MPa and pressure ramp boundary conditions. When the pressure ramp boundary condition is applied, the burning rate decreases reaching a value even lower than that obtained for the 0.5 MPa fixed boundary test. This phenomenon occurs because applying a sharp depressurisation at the boundary leads to obtaining lower values of pressure closer to the burning surface than those obtained by fixing the pressure to 0.5 MPa. Since burning rate is directly related with the pressure, together with a decrease of pressure below 0.5 MPa, a fall of the burning rate below the value obtained for 0.5 MPa fixed pressure test will come.

8. When the depressurisation is applied, the temperature of the burning surface increases until reaching a value very close to that obtained for 0.5 MPa but lower. As a result, when applying depressurisation, the distribution for the surface temperature is located between those obtained for 0.5 and 7 MPa fixed pressure tests. The same behaviour was encountered when analysing the distribution of global temperature variable.

4.3 Combustion of double-base homogeneous propellant

In this section, the model already tested in homogeneous and heterogeneous composite AP/HTPB propellant is adapted to simulate the burning of double-base homogeneous propellants widely used in Rocket Motors.

Firstly, the physical model with the governing equations, source terms and the coupling at the burning surface is presented. Finite volume method is used in which the fluxes are evaluated with Rusanov numerical scheme, as done to solve AP/HTPB system of equations. This is followed by the study of the combustion test of a double-base homogeneous propellant in which pressure is fixed at the boundary. The same model is applied to the simulation of a test in which the right boundary suffers depressurisation. Finally, conclusions are also presented.

4.3.1 Physical model

The combustion of double-base propellant is modelled, as done with AP/HTPB, by considering a solid phase zone (hereafter cited as condensed phase) and a gas phase zone. Both zones are assumed to be insulated excepting the surface of contact between gas and condensed phases which is called burning surface.

To model double-Base propellant, the condensed phase is assumed to be composed by fuel (F), oxidiser (O) and a group of delayed reaction species DR1 (defined by Tseng and Yang [72]). When the condensed phase located at the burning surface reaches the melting temperature (T_{melt}), these three species change their phase from condensed to gas phase. The combustion process of these species in their gaseous form is described by a reaction mechanism defined by Tseng and Yang [72] chemical kinetic scheme,

$$c_F F + c_O O \longrightarrow c_{DR2} DR2 \ (R1) \tag{4.85}$$

$$c_{DR1} DR1 \longrightarrow c_P P \ (R2) \tag{4.86}$$

$$c_{DR2} DR2 \longrightarrow c_P P \ (R3) \tag{4.87}$$

On the one hand, in R1, fuel (CH_2O) and oxidiser (NO_2) react to produce an intermediate group of delayed reaction species DR2 (Tseng and Yang [72]). On the other hand, these species together with DR1 react to produce the final products (N_2, CO, CO_2, H_2O, $H_2, etc.$) . Therefore, the gas phase will be formed initially by air but after the reactions take place, fuel, oxidiser, DR1, DR2 as well as final products will be part of it. Reaction coefficients are detailed in Table 4.8.

Parameter	Value
c_F	1
c_O	1.4
$c_{DR1,DR2}$	3.4
c_P	3.9

Table 4.8: Reaction coefficients [72].

4.3.1.1 Governing equations

The mathematical model applied to reproduce the combustion problem considers mass, momentum, energy and species mass fraction governing equations for the gas phase and energy equation for the solid phase as in the following equation system,

$$\frac{\partial \rho_g}{\partial t} + \overrightarrow{\nabla} \cdot (\rho_g \overrightarrow{u}_g) = 0 \tag{4.88}$$

$$\frac{\partial\left(\rho_g \overrightarrow{u}_g\right)}{\partial t} + \overrightarrow{\nabla}\cdot\left(\rho_g \overrightarrow{u}_g \otimes \overrightarrow{u}_g + p\overrightarrow{I}\right) = 0 \tag{4.89}$$

$$\frac{\partial\left(\rho_g E_g\right)}{\partial t} + \overrightarrow{\nabla}\cdot\left(\rho_g \overrightarrow{u}_g\left(E_g + \frac{p}{\rho_g}\right)\right) = k_g\nabla^2 T_g + \sum_{j=1}^{N} Q_{g,j}R_j \tag{4.90}$$

$$\frac{\partial\left(\rho_g Y_i\right)}{\partial t} + \overrightarrow{\nabla}\cdot\left(\rho_g \overrightarrow{u}_g Y_i\right) = \frac{k_g}{\gamma_g c_{vg}}\nabla^2 Y_i + \phi_i \qquad i = 1, 2, ..., n-1 \tag{4.91}$$

$$\frac{\partial\left(\rho_c E_c\right)}{\partial t} = k_c\nabla^2 T_c \tag{4.92}$$

where the subscripts i and j stand for the ith-species from 1 to n-1 and for reaction number from 1 to N respectively. The specific heat at constant volume for a mixture of gases is defined with the following expression,

$$c_{vg} = \sum_{i=0}^{n} Y_i c_{vg,i} \tag{4.93}$$

which is exactly the same equation system detailed in subsection 4.2.1.1.

4.3.1.2 Burning surface coupling

Gas and condensed phase variables are related to each other by coupling them at the burning surface in the same way as is done for AP/HTPB propellant:

1. Gas and solid temperature must be the same and equal to the surface temperature (T_s),

$$T_g = T_c = T_s \tag{4.94}$$

2. Energy balance at the burning surface is required,

$$k_g\nabla T_g\big|_s = k_c\nabla T_c\big|_s + \rho_c\dot{r}\left(Q_c - c_c\left(T_s - T_0\right)\right) \tag{4.95}$$

3. The continuity of mass must be ensured. When the temperature of the surface is higher than the melting temperature (T_{melt}), the solid changes phase to gas. Otherwise the velocity in the burning surface must be zero. Therefore, the following relationship is set,

$$u_g = \begin{cases} \frac{\rho_c\dot{r}}{\rho_g}, & T_s > T_{melt} \\ 0, & T_s < T_{melt} \end{cases} \tag{4.96}$$

4. Finally, species conservation must be ensured too.

$$\rho_c\dot{r}Y_{s,i} = \rho_c\dot{r}\ Y_{c,i}\big|_{0^-} + \frac{k_g}{\gamma_g c_{vg}}\ \nabla Y_i\big|_{0^+} \tag{4.97}$$

The velocity at which the burning surface of the condensed phase changes into gas is called the burning rate ($\dot{r}$). The formula that Tseng and Yang [72] use to describe the burning velocity is written as,

$$\dot{r}^2 = \frac{\frac{E_{a,c}}{R_u T_s}\alpha_c A_c e^{-\frac{E_{a,c}}{R_u T_s}}}{1 - \frac{T_0}{T_s} - \frac{Q_c}{2c_c T_s}} \tag{4.98}$$

where A_c,$E_{a,c}$, c_s and Q_c are the pre-exponential factor, activation energy, specific heat and specific heat release of the condensed phase respectively and their values are provided in Tseng and Yang [72]. Since the propellant is homogeneous, all points of the burning surface will progress at the same velocity.

4.3.1.3 Source terms

To solve the equation system 4.88-4.92 several source terms will be needed.

The gases, as for AP/HTPB model, are assumed to behave like ideal gas and therefore, the equation of state is defined as,

$$p = \rho_g R_g T_g \tag{4.99}$$

being R_g the specific constant of gases which for a mixture of gases is as calculated as,

$$R_g = R_u \sum_{i=0}^{n} Y_i / M_{g,i} \tag{4.100}$$

The modelling of the kinetic scheme detailed at the beginning of subsection 4.3.1 is done by calculating firstly, the reaction rates of R1, R2 and R3 which are equations (4.85), (4.86) and (4.87), and afterwards the rate of production or consumption of each specie due to the combustion process. The reaction rates have an Arrhenius form however, opposite to the model used for AP/HTPB composite propellant, they are not function of the gas pressure but the density, the temperature and the mass fraction of the species involve in the following form,

$$R_1 = -D_1 \rho_g^2 \frac{Y_F Y_O}{M_{g,O}} e^{\left(-\frac{E_1}{R_u T_g}\right)} \tag{4.101}$$

$$R_2 = -D_2 \rho_g^2 \frac{Y_{DR1}}{M_{g,DR1}} e^{\left(-\frac{E_2}{R_u T_g}\right)} \tag{4.102}$$

$$R_3 = -D_3 \rho_g^2 \frac{Y_{DR2}}{M_{g,DR2}} e^{\left(-\frac{E_3}{R_u T_g}\right)} \tag{4.103}$$

where D_1, D_2 and D_3 are the pre-exponential factors, and E_1, E_2 and E_3 are the activation energies of the reaction rates.

Once the reaction rates are defined, and in order to solve equation (4.91), the following step is to calculate the rate of production or consumption of each species involved in the combustion process,

$$\phi_F = R_1 \tag{4.104}$$

$$\phi_O = \phi_F \frac{c_O M_{g,O}}{c_F M_{g,F}} \tag{4.105}$$

$$\phi_{DR1} = R_2 \tag{4.106}$$

$$\phi_{DR2} = R_3 - (\phi_F + \phi_O) \tag{4.107}$$

$$\phi_P = -R_2 - R_3 \tag{4.108}$$

$$\phi_{air} = 1 - \phi_F - \phi_O - \phi_{DR1} - \phi_{DR2} - \phi_P \tag{4.109}$$

4.3.2 Numerical method and time integration applied

Finite volume method in which the fluxes are evaluated with Rusanov numerical scheme, is applied to solve the system of governing equation which represents the gas phase, as done to solve AP/HTPB system of equations. The solution to the condensed phase energy equation is obtained as for AP/HTPB propellant. Both processes are described in subsections 4.2.2.1 and 4.2.2.3 and they will not be rewritten.

The calculation steps of the time integration are exactly the same as described 4.2.2.2. However, due to the differences in the programming of the reaction rates and species rate, the detailed expression of the time step associated to the ith-speciess is written as follows,

$$\triangle t_{chem,i} = \frac{\rho_g Y_i}{|\phi_i|} \tag{4.110}$$

4.3.3 Results and discussion

The model previously described is programmed in C++ using OpenFoam as done for AP/HTPB solid propellant. The code has been run for two different tests in two dimensions. The first test performed is the combustion of the propellant when the pressure in the open side of the tube is fixed in a range from 1 MPa to 9 MPa. The results obtained are compared with those of Tseng and Yang [72] and Aoki and Kubota [77].

In the second test, a pressure step boundary condition is applied at the right side of the control volume. As it is done in subsection 4.2.3.3, the test is modelled by considering that the pressure at the open side of the tube decreases abruptly from 9 MPa to 1 MPa in a very short time. Its influence in the main variables of interest is studied.

The geometry is that described by Ye et al. [46] as used in AP/HTPB sandwich combustion but in this case half of its volume is composed of air and the other half of homogeneously distributed double-base solid propellant. The total length and height of the domain are 1000 μm and 170 μm respectively. Both condensed and gas phase are set 500 μm height as seen in Figure 4.31.

The tube is insulated all along their walls except the right one which is open therefore, there is not transference of mass and heat through the walls. On the one hand, zero gradient boundary conditions have been considered for temperature, density, mass fractions and pressure along all walls despite the pressure at the exit of the tube which have been fixed in a range of 1 MPa to 9 MPa depending on the reproduced test. On the other hand, velocity have been fixed to zero in the left closed wall, to zero gradient in the right open wall and slip boundary condition have been considered in upper-bottom and front-back walls.

Regarding initial conditions, the control volume is assumed to be already initiated. The initial condition of temperature is described by a linear distribution from 294 K (T_1) fixed on the left side to 1100 K (T_2) fixed on the right side. Initial temperatures, as well as reference temperature and melting temperature are summarised in Table 4.9. In order to study the effect that the initial temperature distribution has in the burning rate, the code has been run considering several values final temperatures 950K, 1000K, 1100 K and 1300 K in a range from 1 MPa to 9 MPa. The results obtained have been compared with those of Tseng and Yang [72] and Aoki and Kubota [77].

Variable	Unit	Value
T_0	K	294
T_{melt}	K	660
T_1	K	294
T_2	K	1100

Table 4.9: Initiation conditions.

The first test performed is the combustion of the propellant when the pressure in the open side

of the tube is fixed in a range from 1 to 9 MPa. The results obtained are compared with the ones obtained by Tseng and Yang [72] and Aoki and Kubota [77].

In the second test the burning of the same strand when a pressure step boundary condition is applied at the right side of the control volume is simulated. Firstly the pressure at the right boundary is fixed to 9 MPa and afterwards, it decreases abruptly until reaching 1 MPa at the open side of the tube as it is done in subsection 4.2.3.3.

The necessary thermophysical and chemical kinetic properties of double-base propellant considered as input variables are taken from bibliography and detailed in Tables table 4.10, 4.11 and 4.12 .

Parameter	Unit	Value
D_1	$m^3 \cdot (mol \cdot s)^{-1}$	$1 \cdot 10^4$
D_2	$m^3 \cdot (mol \cdot s)^{-1}$	$1 \cdot 10^7$
D_3	$m^3 \cdot (mol \cdot s)^{-1}$	$1 \cdot 10^7$
E_1	J/mol	$33.5 \cdot 10^3$
E_2	J/mol	$209 \cdot 10^3$
E_3	J/mol	$209 \cdot 10^3$

Table 4.10: Chemical kinetics data of double-base solid propellant [72].

Parameter	Unit	Value
ρ_c	$kg \cdot m^{-3}$	1600
k_c	$W \cdot m^{-1} \cdot K^{-1}$	0.21376
c_c	$J \cdot kg^{-1} \cdot K^{-1}$	1670
A_c	s^{-1}	$1 \cdot 10^{17}$
$E_{a,c}$	J/mol	$167.2 \cdot 10^3$
Q_c	$J \cdot kg^{-1}$	$418.4 \cdot 10^3$
α_c	$J \cdot kg^{-1}$	$8 \cdot 10^{-8}$

Table 4.11: Thermophysical properties of double-base solid propellant [72].

Parameter	Unit	Value
k_g	$W \cdot m^{-1} \cdot K^{-1}$	0.1045
$c_{p,F}$	$J \cdot kg^{-1} \cdot K^{-1}$	2320
$c_{p,O}$	$J \cdot kg^{-1} \cdot K^{-1}$	1190
$c_{p,DR1,DR2}$	$J \cdot kg^{-1} \cdot K^{-1}$	1480
$c_{p,P}$	$J \cdot kg^{-1} \cdot K^{-1}$	1940
$M_{g,F}$	$kg \cdot mol^{-1}$	0.03003
$M_{g,DR1,DR2}$	$kg \cdot mol^{-1}$	0.02778
$M_{g,O}$	$kg \cdot mol^{-1}$	0.04601
$M_{g,P}$	$kg \cdot mol^{-1}$	0.02418
$h^0_{f,F}$	$J \cdot kg^{-1}$	$-3862 \cdot 10^3$
$h^0_{f,DR1}$	$J \cdot kg^{-1}$	$-5384 \cdot 10^3$
$h^0_{f,DR2}$	$J \cdot kg^{-1}$	$-3592 \cdot 10^3$
$h^0_{f,O}$	$J \cdot kg^{-1}$	$736.5 \cdot 10^3$
$h^0_{f,P}$	$J \cdot kg^{-1}$	$-6184 \cdot 10^3$

Table 4.12: Thermophysical properties of double-base solid propellant [59].

Parameter	Value
$Y_{s,F}$	0.1662
$Y_{s,O}$	0.3576
$Y_{s,DR1}$	0.4762
$Y_{s,DR2}$	0
$Y_{s,P}$	0

Table 4.13: Composition of propellant condensed phase [72].

The heat of the chemical reactions in the combustion of the double-base propellant is not provided in the bibliography as is done for AP/HTPB propellant. However, the heat of formation of each component is known (see Table 4.12). Therefore, the heat of each jth-reaction is obtained as,

$$Q_{g,j} = \sum h^0_{f,products} - \sum h^0_{f,reactives} \tag{4.111}$$

The final values in $J{\cdot}kg^{-1}$ are represented in Table 4.14.

Variable	Unit	Value
$Q_{g,1}$	$J{\cdot}kg^{-1}$	$-8.90 \cdot 10^6$
$Q_{g,2}$	$J{\cdot}kg^{-1}$	$-7.90{\cdot}10^5$
$Q_{g,3}$	$J{\cdot}kg^{-1}$	$-2.58{\cdot}10^6$

Table 4.14: Heat of reactions.

To run the test, initial conditions of temperature need to be established. The tube is assumed initialised therefore, the left side of the domain is set at 294 K (T_1) and the right side at 1100 K (T_2) and the rest of the control volume will have the temperature determined by the linear equation between these two values. Initial temperatures, as well as reference temperature and melting temperature are summarised in Table 4.15. Melting temperature (T_{melt}) and reference temperature (T_0) values are obtained from Wu et al. [71]. The value adopted for the temperature at the right side of the control volume is justified throughout this subsection.

Variable	Unit	Value
T_0	K	294
T_{melt}	K	660
T_1	K	294
T_2	K	1100

Table 4.15: Initiation conditions.

4.3.3.1 Combustion of Double-Base Propellant with fixed pressure boundary conditions

The first test performed with the developed model to simulate the combustion of double-base propellants is similar to that described in subsection 4.2.3.2. The pressure of all the gas zone is assumed to have the same value and at the end of the tube, in the right and opened side, the pressure will be fixed with this value during all the test. The test is performed for several pressures in a range from 1 MPa to 9 MPa.

Firstly, the results obtained with this model, are compared with those obtained by Tseng and Yang [72] and Aoki and Kubota [77]. Afterwards, after crosschecking the good agreement of the model, the main variables of interest will be represented. Finally, a brief comparison between AP/HTPB and double-base Propellant is provided.

The appropriate behaviour of the developed model is crosschecked by studying the burning rate obtained for the already mentioned range of pressure and establishing a comparison against the values

found in the literature. Aoki and Kubota [77] presented in their work, among other variables, the burning rate versus the pressure for 12 propellants each one of them with a different content of nitroglycerine and nitrogen dioxide. As can be seen in their Table 1, EC-1 has a mass fraction of nitrogen dioxide of 0.466 being the closest that which Tseng and Yang [72] use in their study. Due to the amount of initial necessary data provided their paper, this propellant has been the one used to validate the model on double-base propellant.

Moreover, as has explained before, the control volume is assumed already initiated, therefore, in order to study the effect that the initial temperature distribution has in the burning rate, the results from Aoki and Kubota [77] and the ones from Tseng and Yang [72] are plotted together with the burning rates obtained when final temperature is 950K, 1000K, 1100 K and 1300 K in Figure 4.74. As can be seen, the temperature at which the domain is considered initiated has an effect in the burning rate. The higher the final temperature is assumed, the better adjust the results of the calculated burning rate to the results from Aoki and Kubota [77] for high and low pressures. However, when the temperature is high, the results obtained differ from those of the literature in the range from 2 MPa to 6 MPa. The quantitative values and their comparison with the results from Aoki and Kubota [77] together with absolute and relative error depending is described in Tables 4.16, 4.17, 4.18 and 4.19.

The results obtained agree well with those from Aoki and Kubota [77] independently of the initial temperature chosen for calculation . On the one hand, the absolute error is less than 1 mm/s in each case except for high pressures where, as seen in Figure 4.74, the curves start to diverge reaching a value around 1.7 mm/s at 950 K. On the other hand, the relative error present a high value compared with the absolute one. This is due to the expression used to calculate it, as it as already explained in subsection 4.2.3.1 when describing the burning rate results obtained for the combustion of an AP/HTPB homogeneously distributed in a Crawford Strand Burner. When the initial temperature chosen for the right boundary is high, the calculated burning rate agrees well with the experimental ones for low and high pressures (see Tables 4.16, 4.17, 4.18 and 4.19).

Analysing in detail the quantitative results obtained in Tables 4.16, 4.17, 4.18 and 4.19 it can be seen that when the pressure is 9 MPa, the higher the temperature, the lower the absolute error. The same phenomenon is observed when running the test at 1.1 MPa. In case of having a temperature of 1300 K, the relative and absolute errors obtained at 9.1 MPa and 1.1 MPa, are less than 11% and 0.8 mm/s respectively. However, in this case, the relative error obtained for pressures range from 2 MPa to 6 MPa increases being even 26 % for 2 MPa. The results obtained for 950 K and 1000 K are very similar: around 14% of relative error for the results at 9.1 MPa, around 20 % for 1.1 MPa and less than 9% for intermediate pressures, which means a very good agreement between the calculated and literature results. When the temperature is increased to 1100 K, not only the relative error for high pressure but also for low pressure is reduced to 10% and the for intermediate pressures, the relative error is maintained under 9%. Therefore, the final temperature of 1100 K is the one chosen to present the results hereafter.

The first variable to be analysed is the velocity field in the gas domain which is represented in Figures 4.75, 4.76 and 4.77 for 0.01 s, 0.02 s and 0.05 s respectively. The first phenomenon observed is the big difference between the burning rate for high pressures compared with the one of low pressures since, for example for time equal to 0.05 (Figure 4.77), the burning surface for 9.1 MPa has arrived almost to the beginning of the control volume, which means that most of the condensed phase has been already consumed, while for 1.1 MPa, the burning surface is still at the half of the tube. Therefore, it could be stated that the higher the pressure is, the quicker the condensed phase changes from solid to gas form. However, the behaviour of the gas velocity is opposed to the burning rate, the higher the pressure is, the lower gas velocity we have. This could be due, as explained in AP/HTPB subsection, to the increment of the gas density with the pressure which leads to a reduction of the gas velocity field as a result of solving equation (4.89). The velocity fields behaves differently depending on the pressure fixed at the right boundary. There are 3 mm/s gap between the burning rate of 3.4 MPa and the one of 9.1 MPa however, the difference in burning rate between 3.4 MPa and 1.1 MPa is close to 4.5 mm/s (see Table 4.18). This behaviour affects on the first hand, to the position of the burning surface in the x-coordinate, being almost the same for the first two time steps considered

and slightly different for 3.4 MPa at 0.05 s. On the other hand, this behaviour affects to how the velocity of the gas phase increases with time. For the first range of pressures (3.4 MPa to 9.1 MPa) the velocity magnitude remains almost constant for each of the time steps considered. However, for 2 MPa and 1.1 MPa fixed boundary tests, an increment with time is observed. This phenomenon could take place because chemical reactions at low pressures need some time to start the reaction and therefore, for the gas velocity to increase while for high pressures the reaction mechanism is activated from the very beginning of the combustion process.

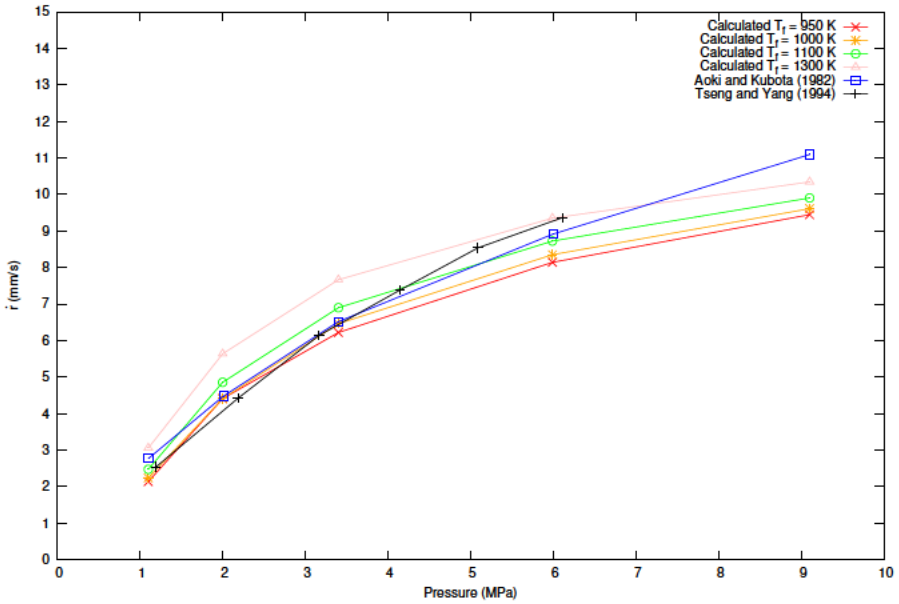

Figure 4.74: Comparison of calculated and experimental burning rate.

Pressure (MPa)	OpenFoam Burning rate (mm/s)	Aoki and Kubota Burning rate (mm/s)	Absolute error (mm/s)	Relative error (%)
9.1	9.447	11.098	1.651	14.879
5.99	8.142	8.917	0.776	8.698
3.4	6.222	6.523	0.301	4.622
2	4.4122	4.483	0.071	1.577
1.1	2.141	2.776	0.635	22.880

Table 4.16: Quantitative comparison of calculated and experimental burning rate for 950 K.

Pressure (MPa)	OpenFoam Burning rate (mm/s)	Aoki and Kubota Burning rate (mm/s)	Absolute error (mm/s)	Relative error (%)
9.1	9.611	11.098	1.486	13.40
5.99	8.351	8.917	0.565	6.34
3.4	6.465	6.523	0.058	0.90
2	4.412	4.483	0.070	1.58
1.1	2.243	2.776	0.533	19.21

Table 4.17: Quantitative comparison of calculated and experimental burning rate for 1000 K.

Pressure (MPa)	OpenFoam Burning rate (mm/s)	Aoki and Kubota Burning rate (mm/s)	Absolute error (mm/s)	Relative error (%)
9.1	9.905	11.098	1.193	10.75
5.99	8.726	8.917	0.191	2.15
3.4	6.900	6.523	0.376	5.76
2	4.855	4.483	0.372	8.30
1.1	2.478	2.776	0.298	10.73

Table 4.18: Quantitative comparison of calculated and experimental burning rate for 1100 K.

Pressure (MPa)	OpenFoam Burning rate (mm/s)	Aoki and Kubota Burning rate (mm/s)	Absolute error (mm/s)	Relative error (%)
9.1	10.347	11.098	0.751	6.772
5.99	9.351	8.917	0.432	4.865
3.4	7.666	6.523	1.146	17.577
2	5.641	4.483	1.161	25.907
1.1	3.061	2.776	0.285	10.264

Table 4.19: Quantitative comparison of calculated and experimental burning rate for 1300 K.

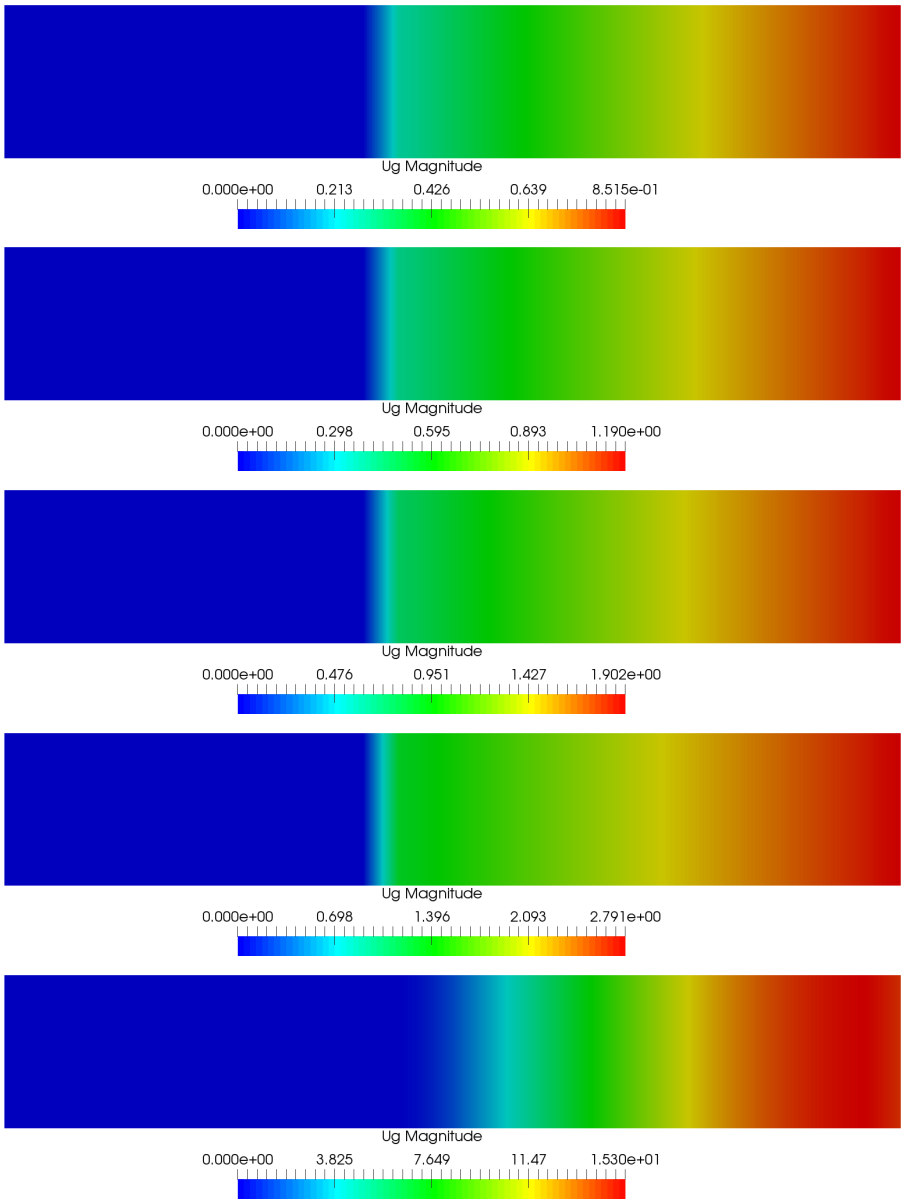

Figure 4.75: Velocity distribution of gas phase in t = 0.01 s at 9.1 MPa, 5.99 MPa, 3.4 MPa, 2 MPa, 1.1 MPa (above-below).

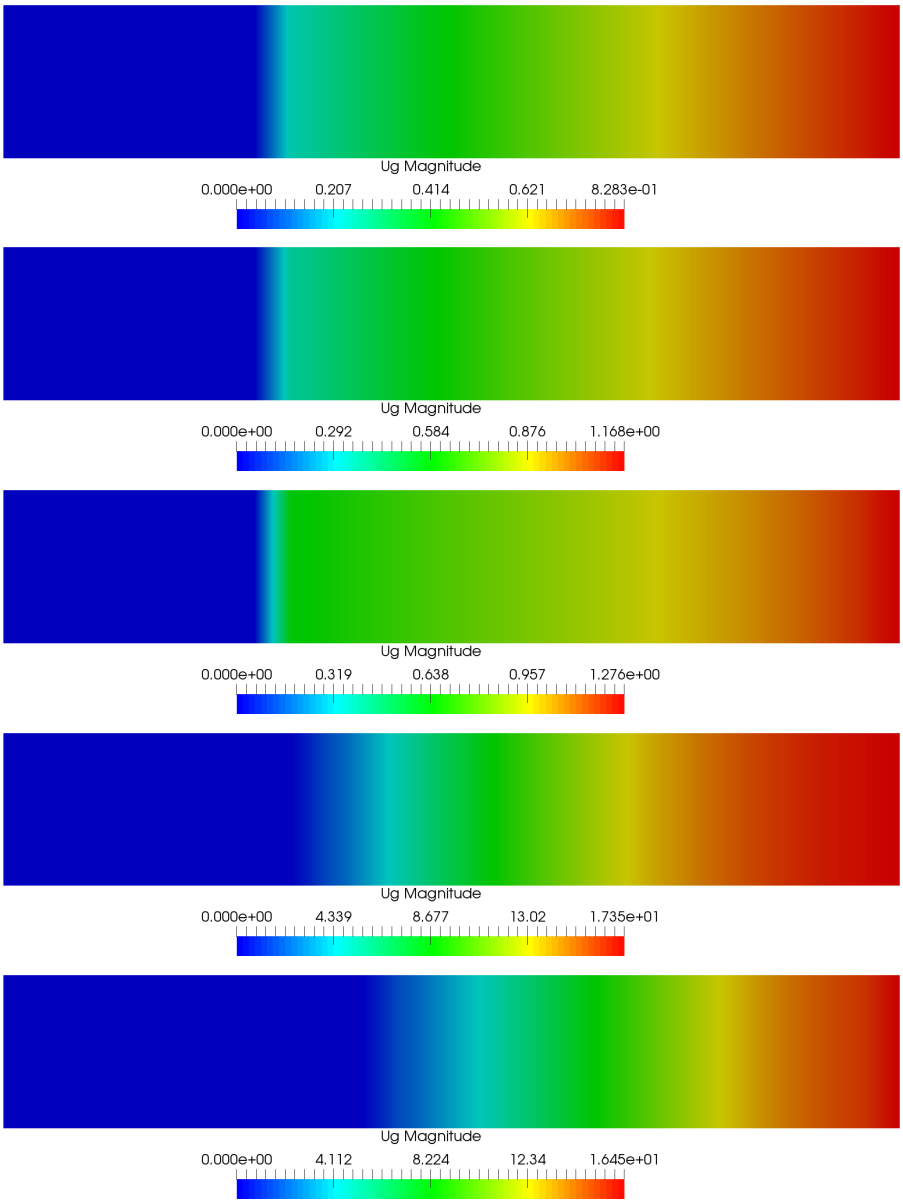

Figure 4.76: Velocity distribution of gas phase in t = 0.02 s at 9.1 MPa, 5.99 MPa, 3.4 MPa, 2 MPa, 1.1 MPa (above-below).

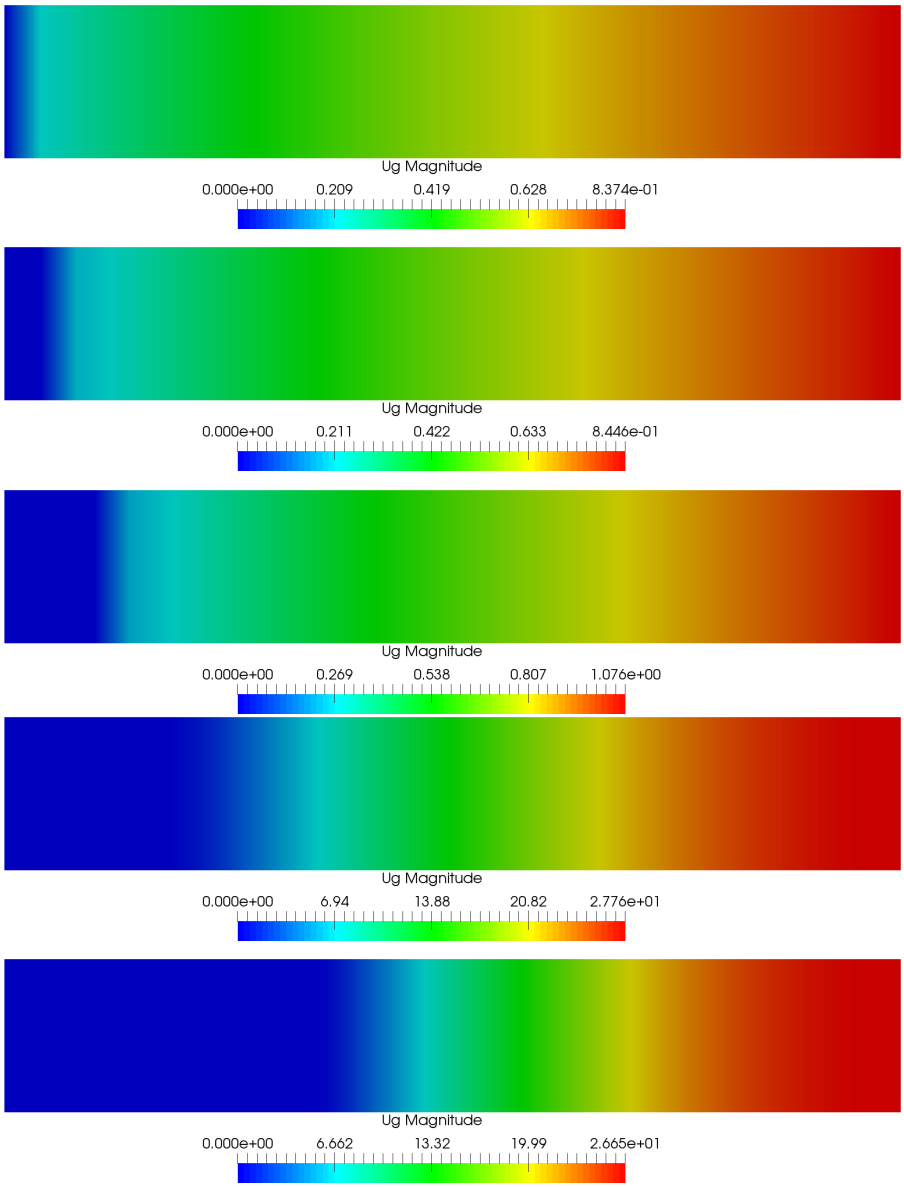

Figure 4.77: Velocity distribution of gas phase in t = 0.05 s at 9.1 MPa, 5.99 MPa, 3.4 MPa, 2 MPa, 1.1 MPa (above-below).

Oxidiser and fuel mass fractions along the control volume are the next variables to be studied. As can be observed in Figures 4.78, 4.79 and 4.80 independently of the considered pressure, the highest amount of fuel and oxidiser is located close to to the burning surface decreasing the mass fraction smoothly with x-coordinate. The maximum value of fuel mass fraction obtained for each pressure decreases slightly with the time. Figures show how the increase of the time leads to a fall of the fuel mass fraction at the end of the tube. The same behaviour is observed for the oxidiser mass fraction, being the expected behaviour since both, fuel and oxidiser, react together in reaction 1 (see equation (4.101)) and need each other for the reaction to take place. Regarding the mass fraction values obtained for each one of the species analysed, depending on the pressure at which the boundary is fixed, both fuel and oxidiser present an increase in their maximum values of mass fraction with the fall of pressure. The same effect was observed when analysing the combustion of

AP/HTPB composite propellant. Equations (4.101), (4.102) and (4.102), which correspond to the chemical kinetics reaction rates, depend on the density of the gas. In consequence, the higher the pressure, the higher the density and therefore, the higher reaction rate will be obtained. A raise of reaction rates means an increment in the consumption of fuel, oxidiser and intermediate products DR1 and a decrement in opposite case. Therefore, since low pressure means a decrease in the combustion of fuel and oxidiser, the mass fraction of both will increase.

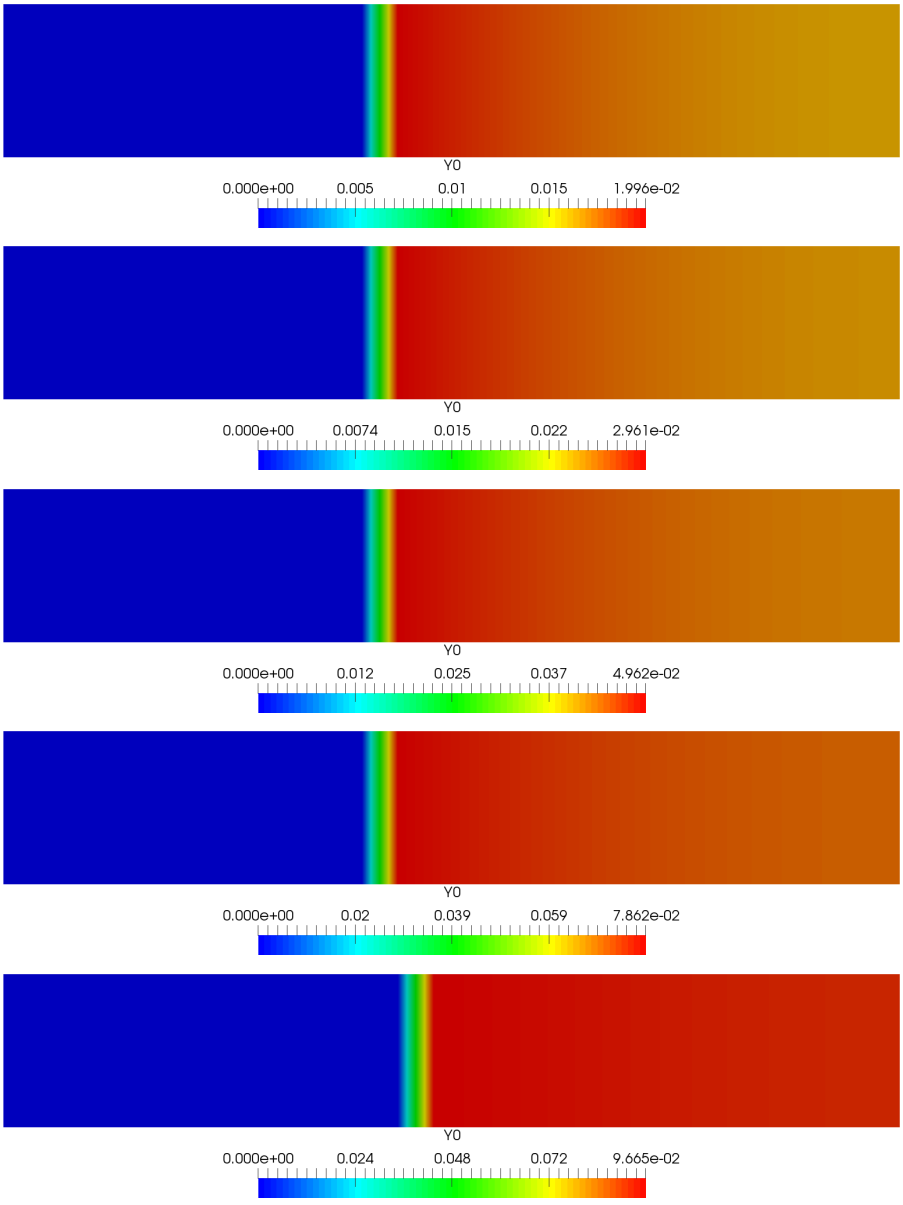

Figure 4.78: Fuel distribution in t = 0.01 s at 9.1 MPa, 5.99 MPa, 3.4 MPa, 2 MPa, 1.1 MPa (above-below).

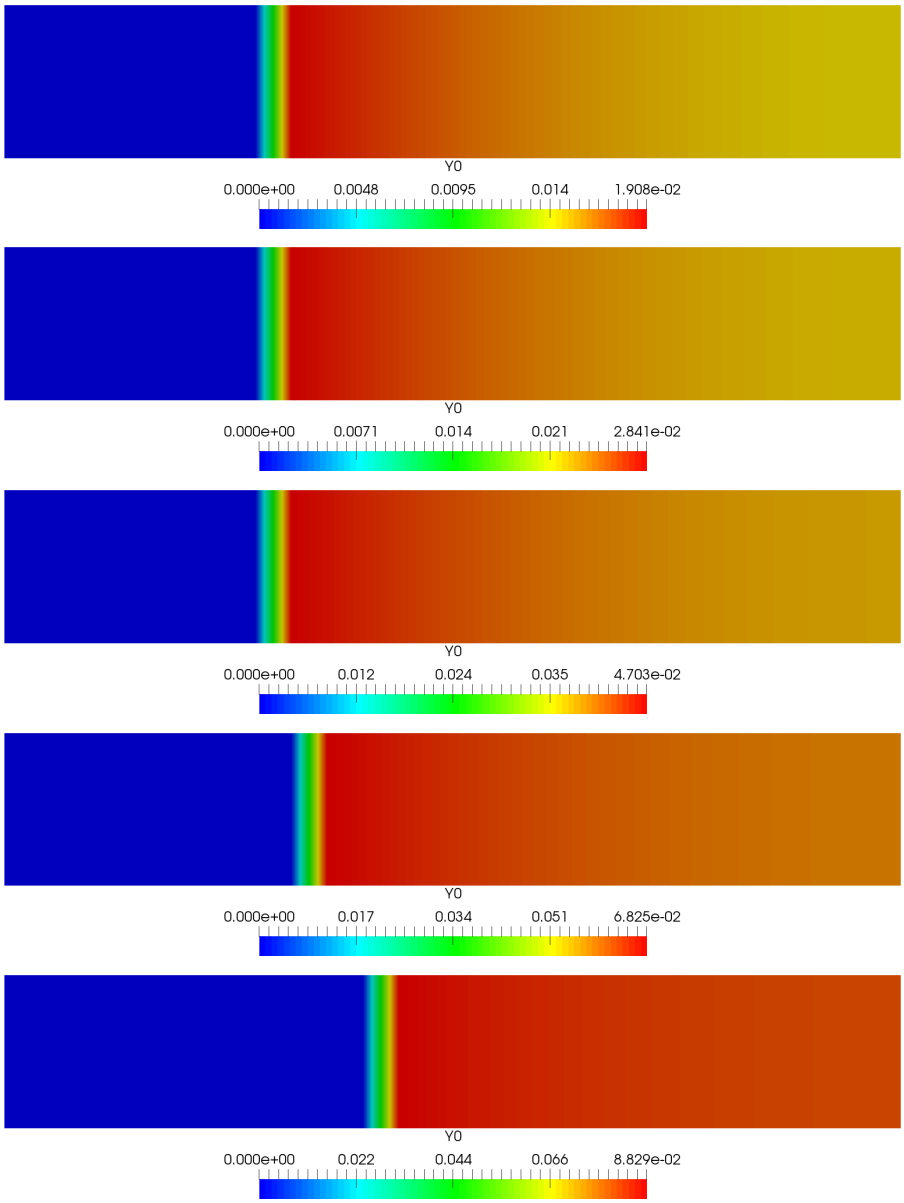

Figure 4.79: Fuel distribution in t = 0.02 s at 9.1 MPa, 5.99 MPa, 3.4 MPa, 2 MPa, 1.1 MPa (above-below).

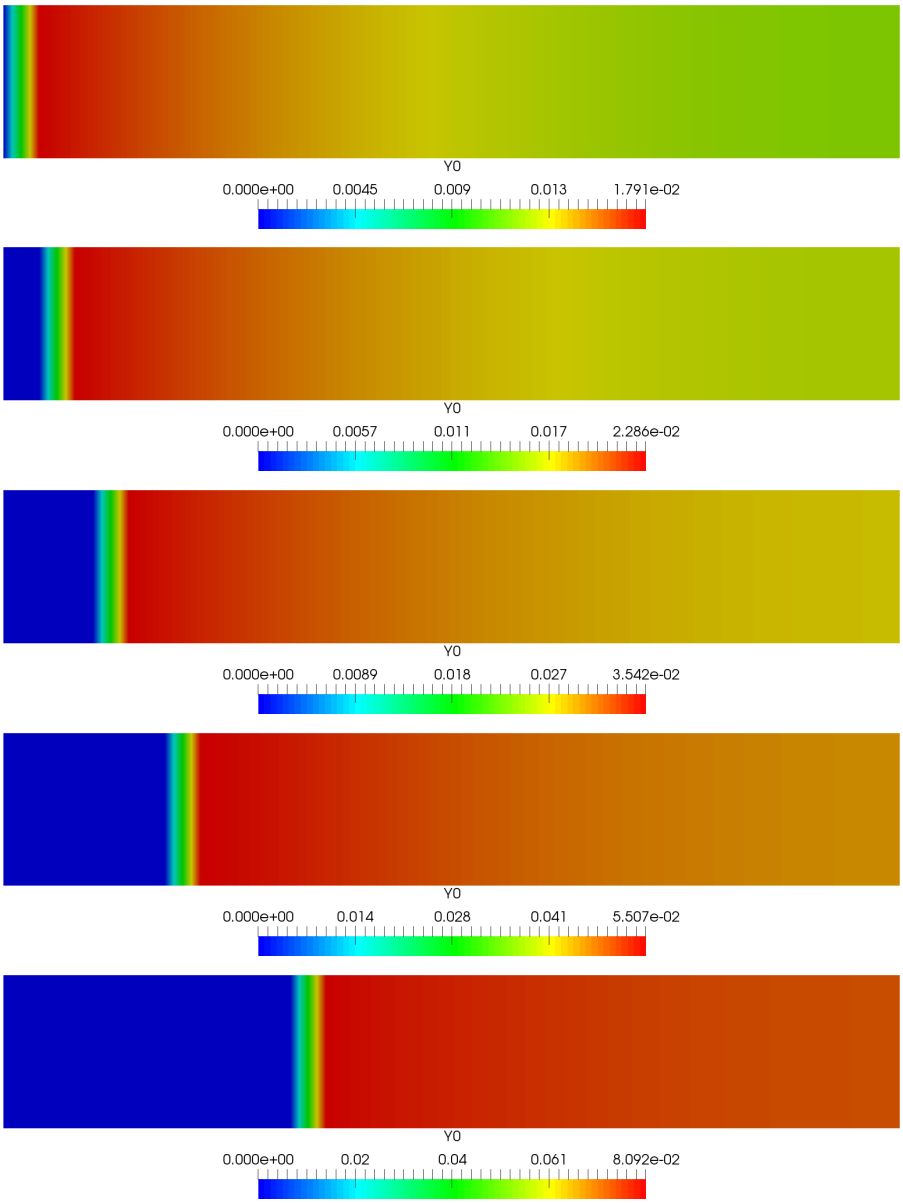

Figure 4.80: Fuel distribution in t = 0.05 s at 9.1 MPa, 5.99 MPa, 3.4 MPa, 2 MPa, 1.1 MPa (above-below) (above-below).

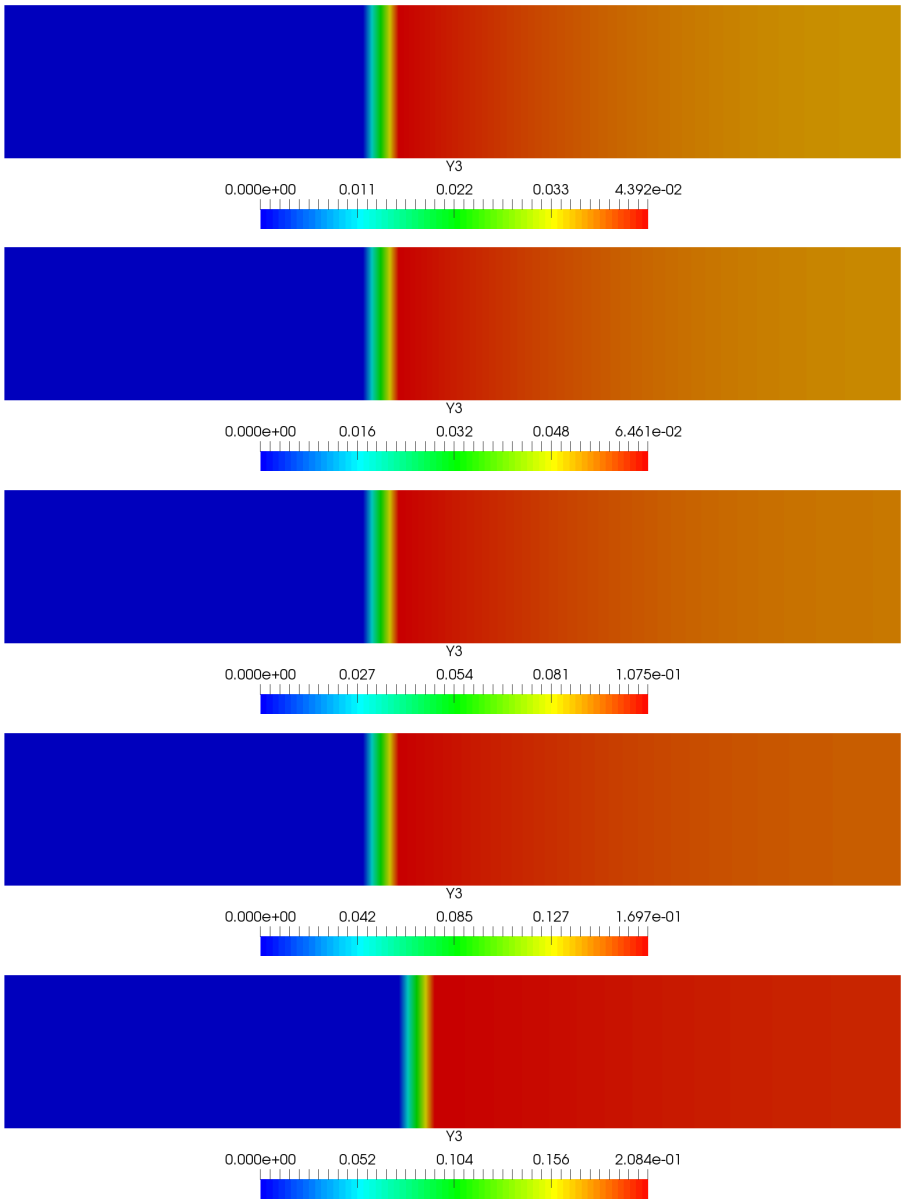

Figure 4.81: Oxidiser distribution in t = 0.01 s at 9.1 MPa, 5.99 MPa, 3.4 MPa, 2 MPa, 1.1 MPa (above-below).

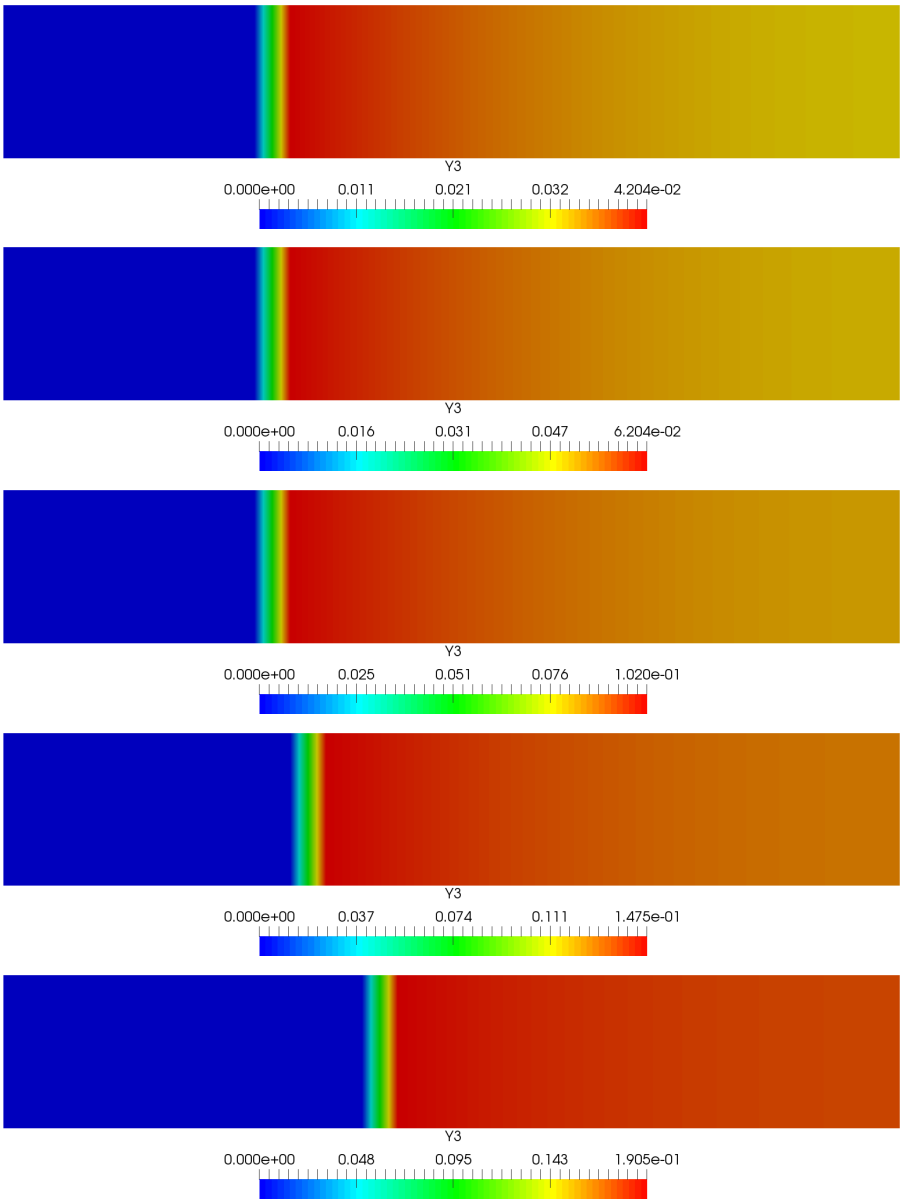

Figure 4.82: Oxidiser distribution in t = 0.02 s at 9.1 MPa, 5.99 MPa, 3.4 MPa, 2 MPa, 1.1 MPa (above-below).

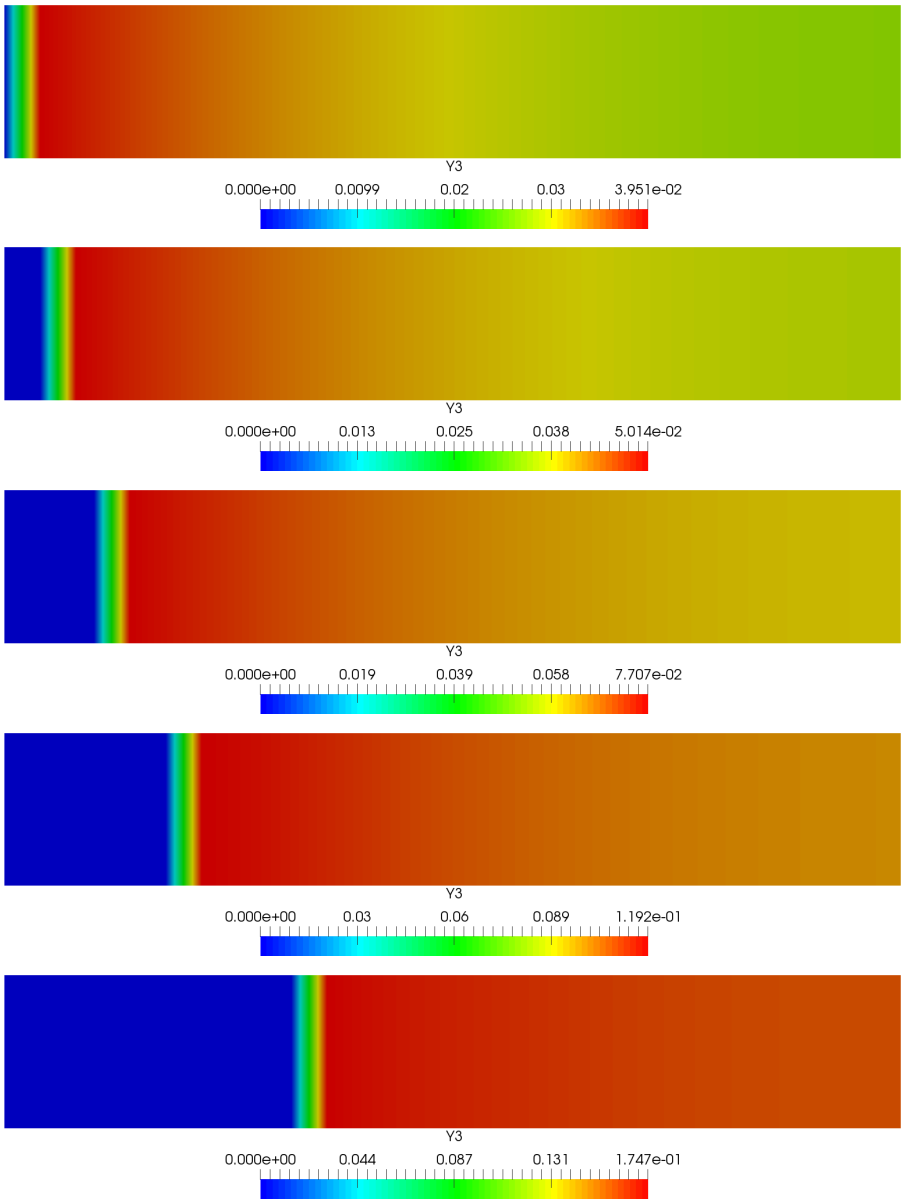

Figure 4.83: Oxidiser distribution in t = 0.05 s at 9.1 MPa, 5.99 MPa, 3.4 MPa, 2 MPa, 1.1 MPa (above-below).

The mass fraction distributions of the intermediate species DR1 and DR2, as well as the mass fraction of the final products, are depicted from Figures from 4.84 to 4.92. Figures 4.90, 4.91 and 4.92, show that final products (P) mass fraction increases with the pressure, which means that, the higher the pressure, the higher reaction rates of R2, R3 or both there will be. On the one hand, the higher the pressure, the higher reaction rate of reaction 2 and therefore, the higher amount of DR1 will react to become final products leading to a decrease of DR1 mass fraction with the pressure (see Figures 4.84, 4.85 and 4.86). On the other hand, the mass fraction of the intermediate specie DR2 increases with the reaction of fuel and oxidiser (R1) and decreases when it changes to final products (R3). Therefore, the amount of mass fraction in the control volume be function of the reaction rates of both reactions (equations (4.101) and (4.103)). According to Figures 4.87, 4.88 and 4.89, the

mass fraction of DR2 increases with the pressure despite for the value obtained at 9.1 MPa which suffers a slight decrement in comparison with that at 5.9 MPa. This could be due to the fact that, since reaction rates get stronger with the increase of pressure, the reaction rate of R3 provokes a consumption of DR2 high enough to decrease the content produced by R1.

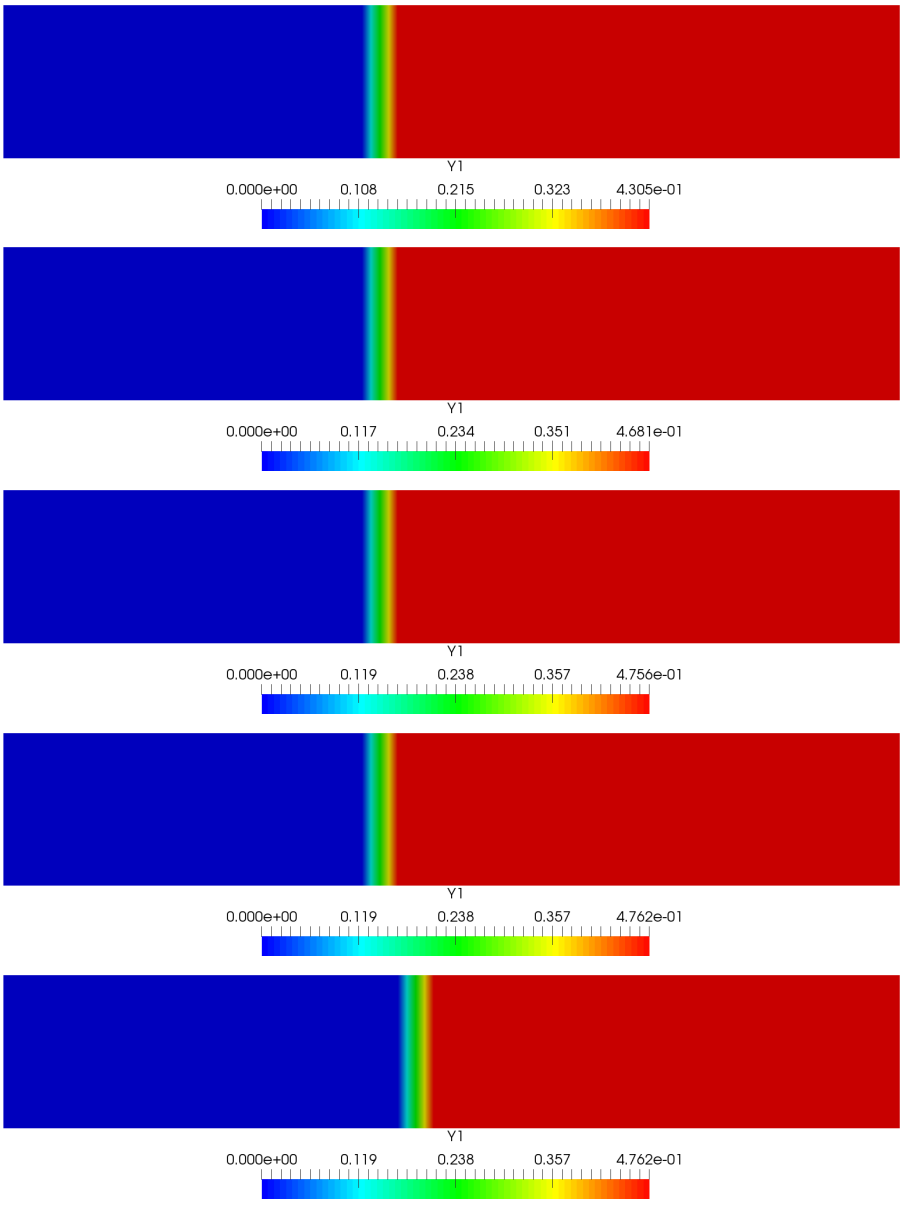

Figure 4.84: DR1 distribution in t = 0.01 s at 9.1 MPa, 5.99 MPa, 3.4 MPa, 2 MPa, 1.1 MPa (above-below).

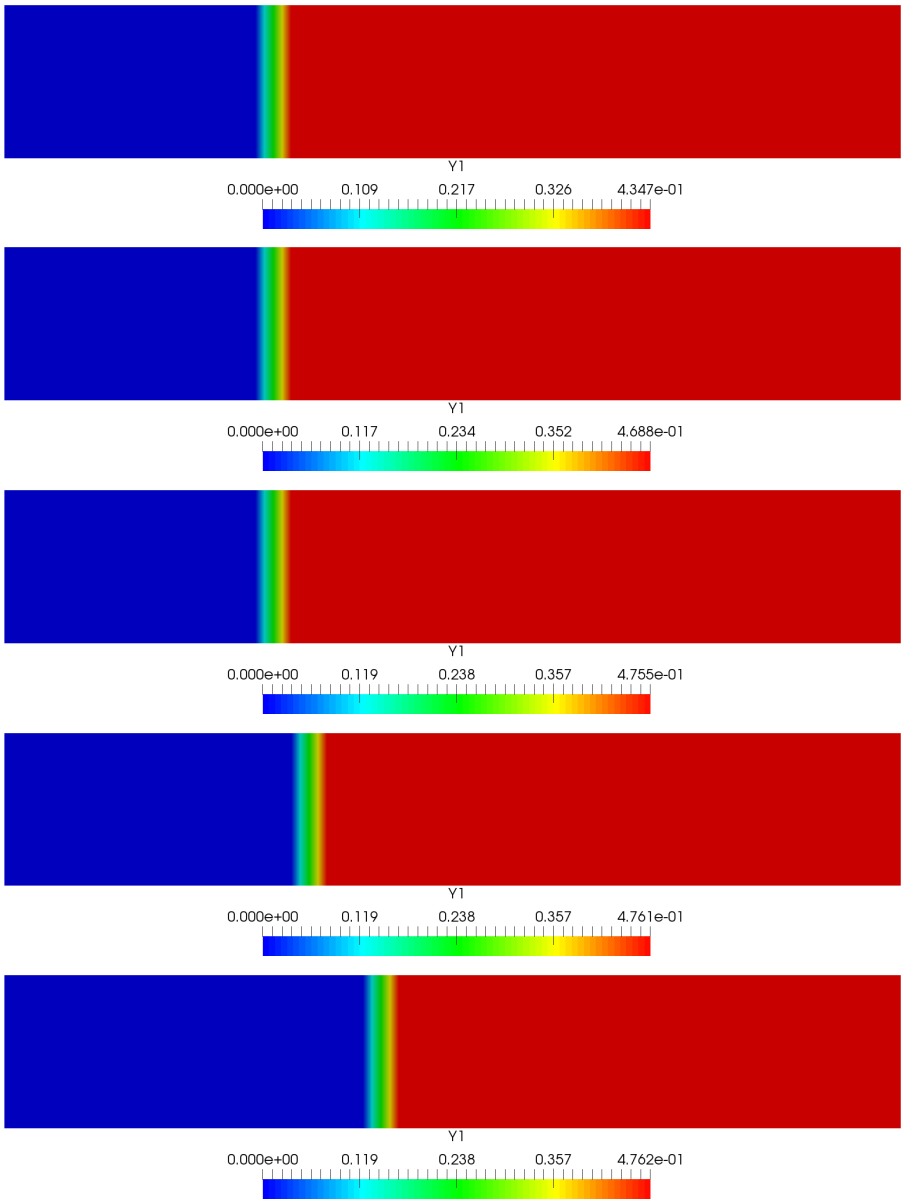

Figure 4.85: DR1 distribution in t = 0.02 s at 9.1 MPa, 5.99 MPa, 3.4 MPa, 2 MPa, 1.1 MPa (above-below).

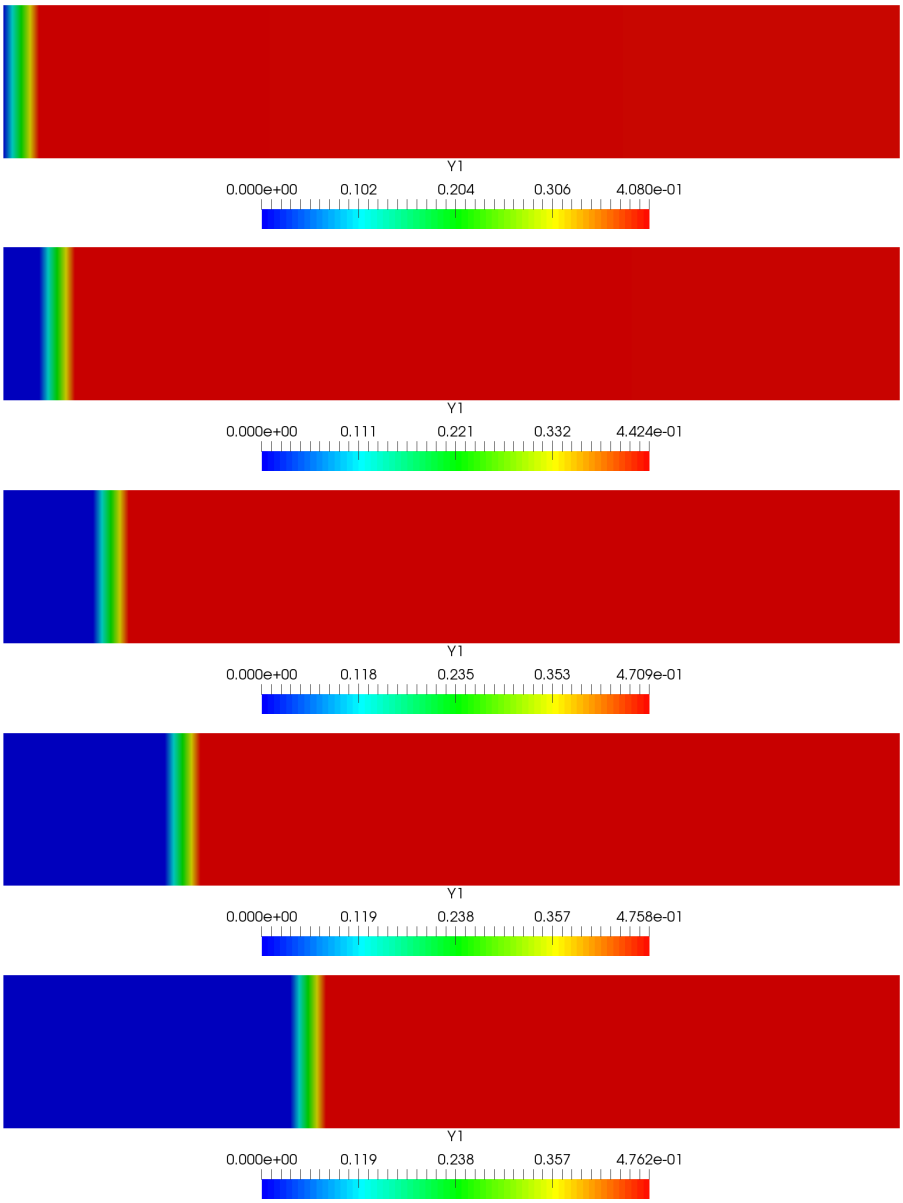

Figure 4.86: DR1 distribution in t = 0.05 s at 9.1 MPa, 5.99 MPa, 3.4 MPa, 2 MPa, 1.1 MPa (above-below).

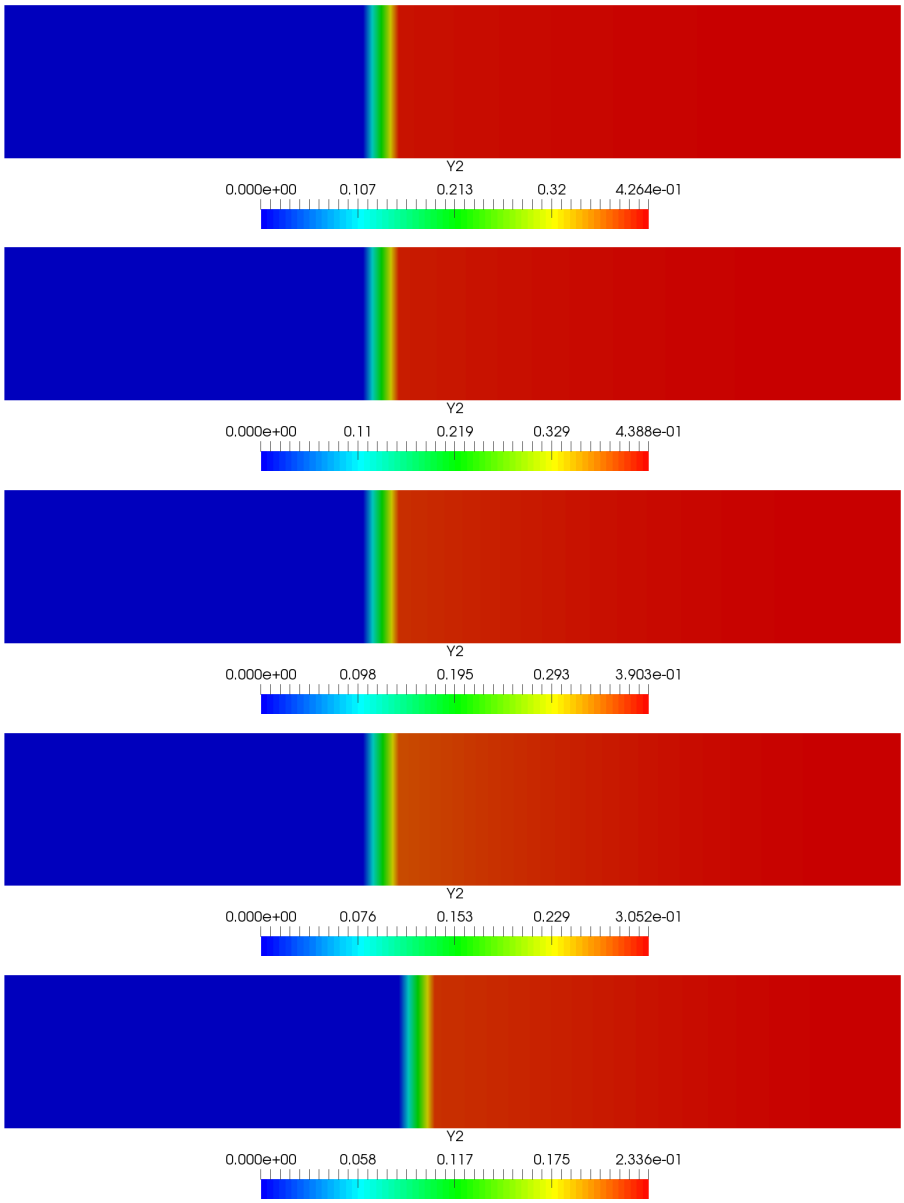

Figure 4.87: DR2 distribution in t = 0.01 s at 9.1 MPa, 5.99 MPa, 3.4 MPa, 2 MPa, 1.1 MPa (above-below).

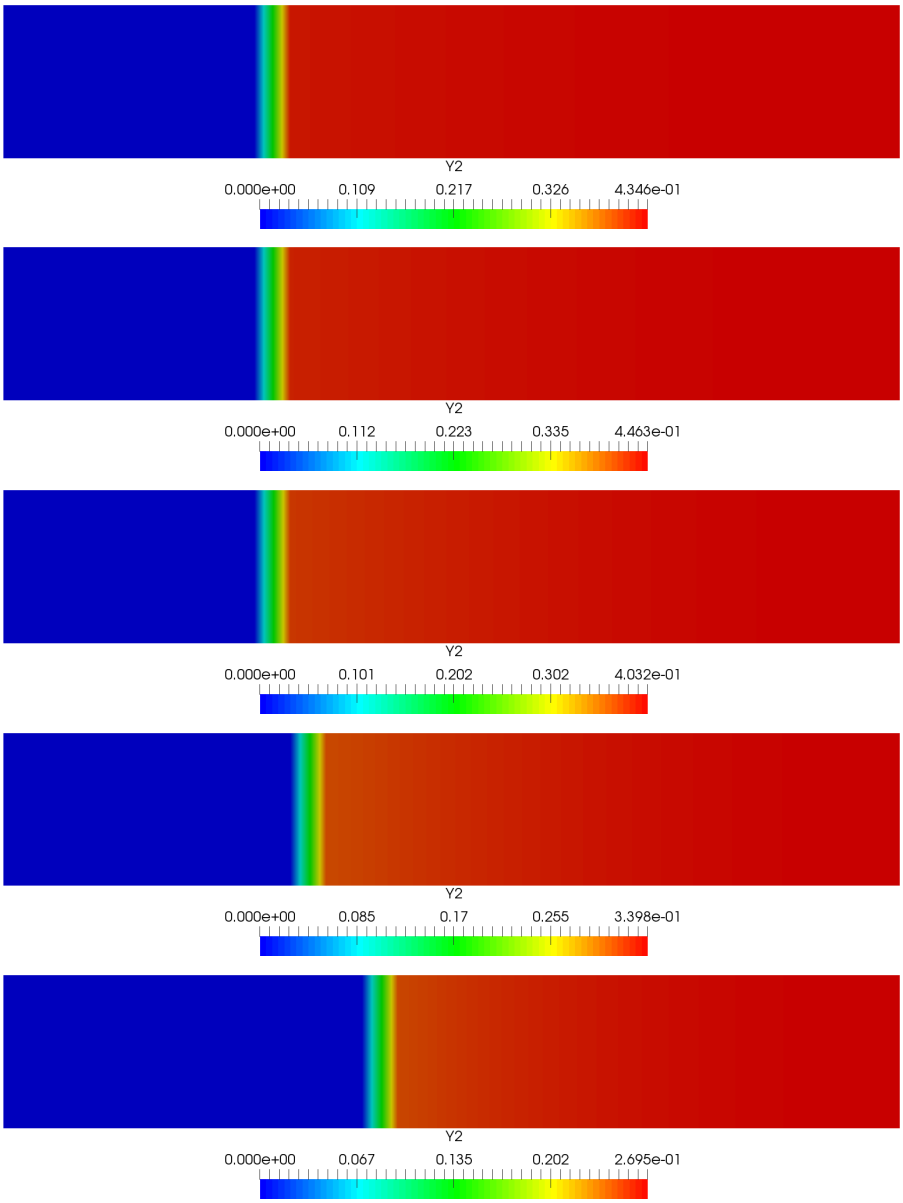

Figure 4.88: DR2 distribution in t = 0.02 s at 9.1 MPa, 5.99 MPa, 3.4 MPa, 2 MPa, 1.1 MPa (above-below).

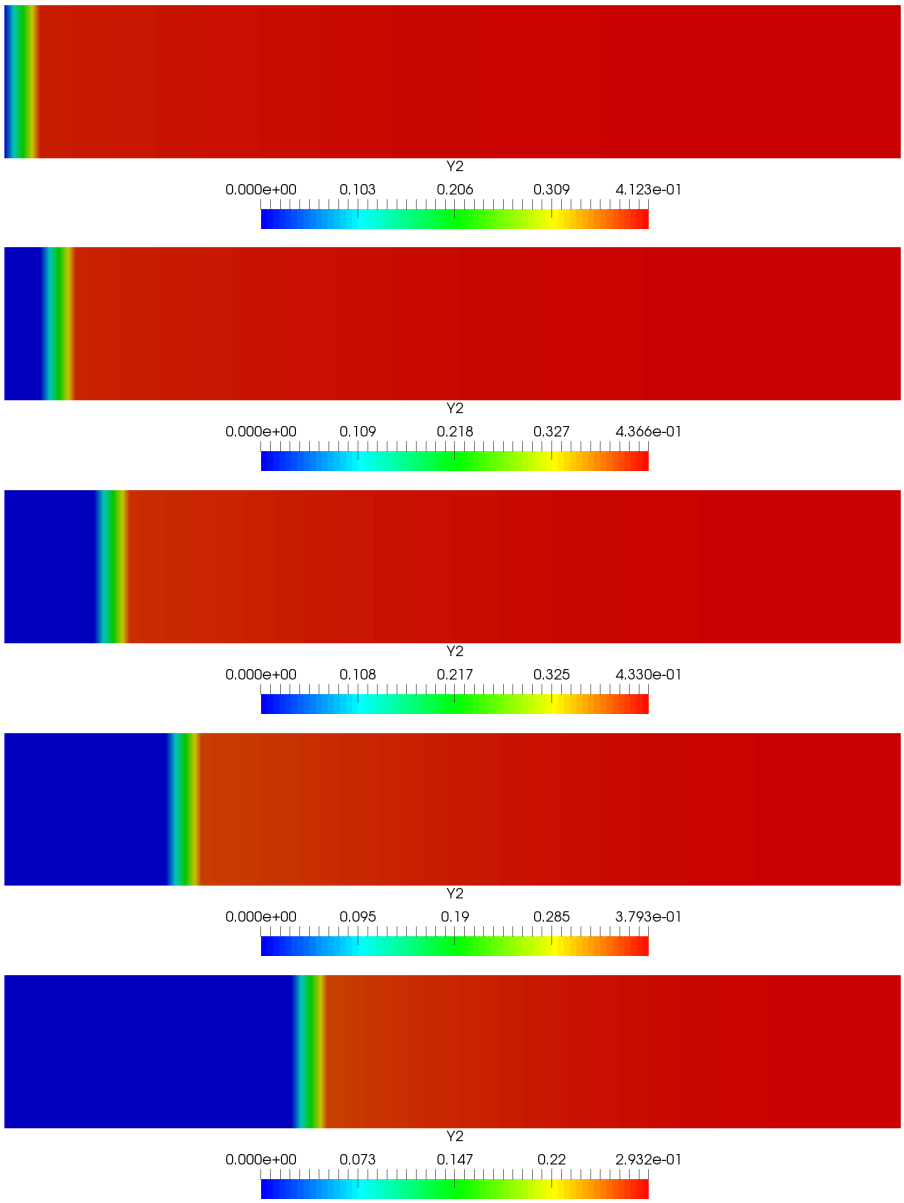

Figure 4.89: DR2 distribution in t = 0.05 s at 9.1 MPa, 5.99 MPa, 3.4 MPa, 2 MPa, 1.1 MPa (above-below).

As general rule, it can be assumed that the final products mass fractions increase with the time. However, when pressure is fixed between 9.1 MPa to 5.99 MPa, the mass fraction of the final products decreases slightly from 0.01 s to 0.02 s (hereafter first slot) and presents the raise between 0.02 s and 0.05 s (hereafter second slot). This phenomenon could be explained taking into account that final products are the result of R2 and R3 and R3 depends strongly on R1. Figures 4.84, 4.85 and 4.86 show how DR1 mass fraction is maintained between the first slot and decreased in the second one which means that reaction 2 needs some time to increase their effect. Moreover, observing Figures from 4.78 to 4.83, two behaviours can be observed. On the one hand, at high pressures, the mass fraction of DR2 increases slightly in the first time slot while decreasing in the second one. On the one hand, at high pressures, the mass fraction of DR2 increases slightly in the first time slot while

decreasing in the second one. On the other hand, at low pressures, DR2 mass fraction increases with the time which means that, during the first slot, reaction 1 produces more intermediate species than reaction 3 can consume and therefore, there is an increment of DR2 mass fraction. The same is happening at high pressures for the first time slot. However, between 0.02 s and 0.05 s, the amount of DR2 mass fraction when pressure is high suffers a decrement. Since during the second time slot and the pressure fixed is high there is a strong increment of the final products mass, it can be concluded that, reaction 3 increase its strength with pressure and time.

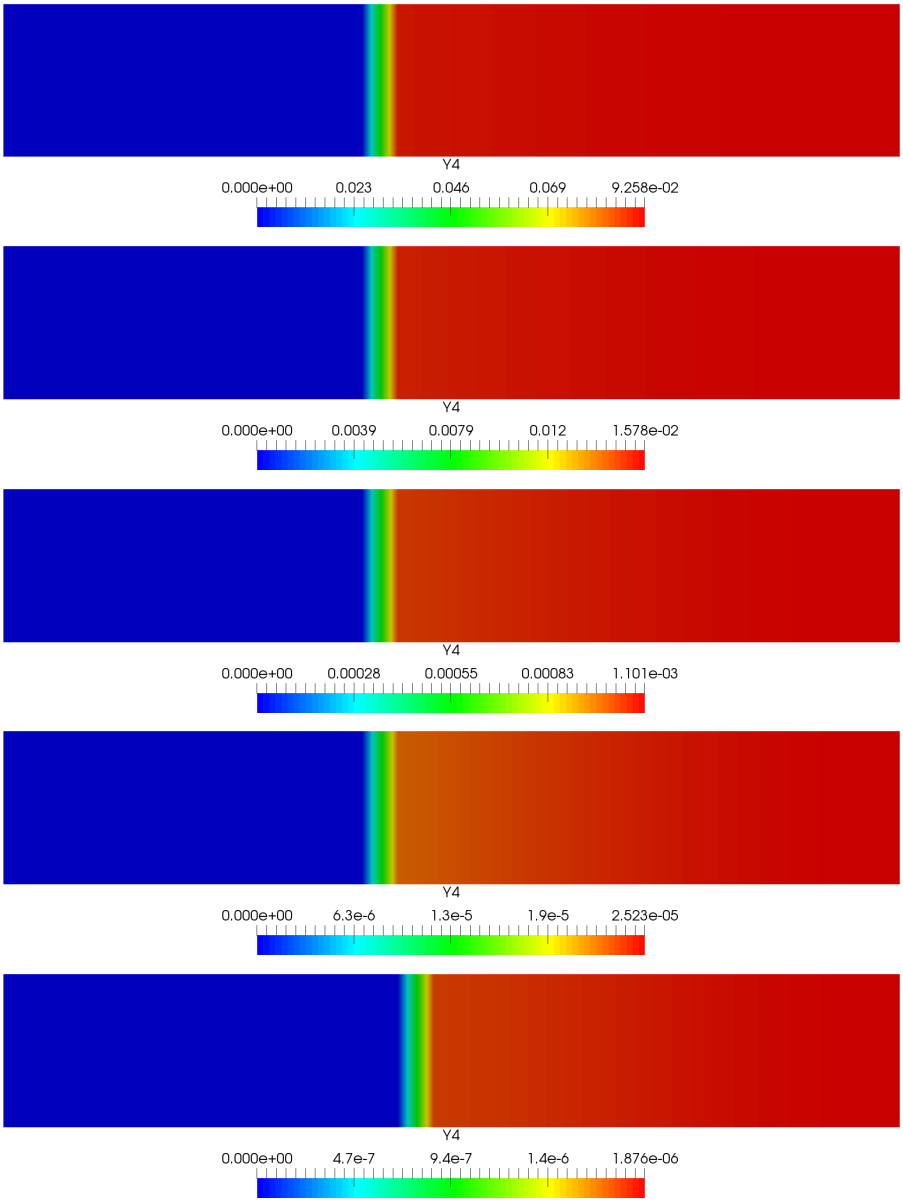

Figure 4.90: Final products distribution in t = 0.01 s at 9.1 MPa, 5.99 MPa, 3.4 MPa, 2 MPa, 1.1 MPa (above-below).

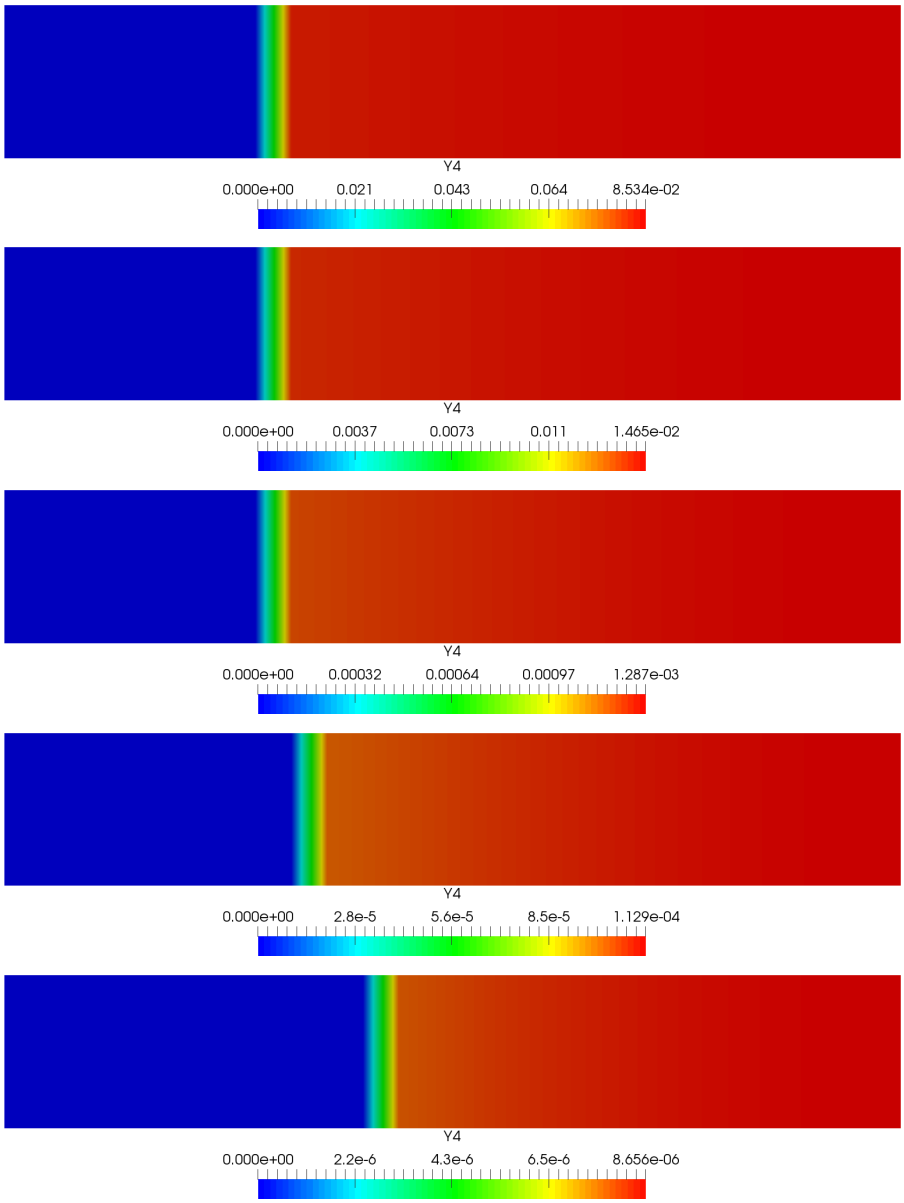

Figure 4.91: Final products distribution in t = 0.02 s at 9.1 MPa, 5.99 MPa, 3.4 MPa, 2 MPa, 1.1 MPa (above-below).

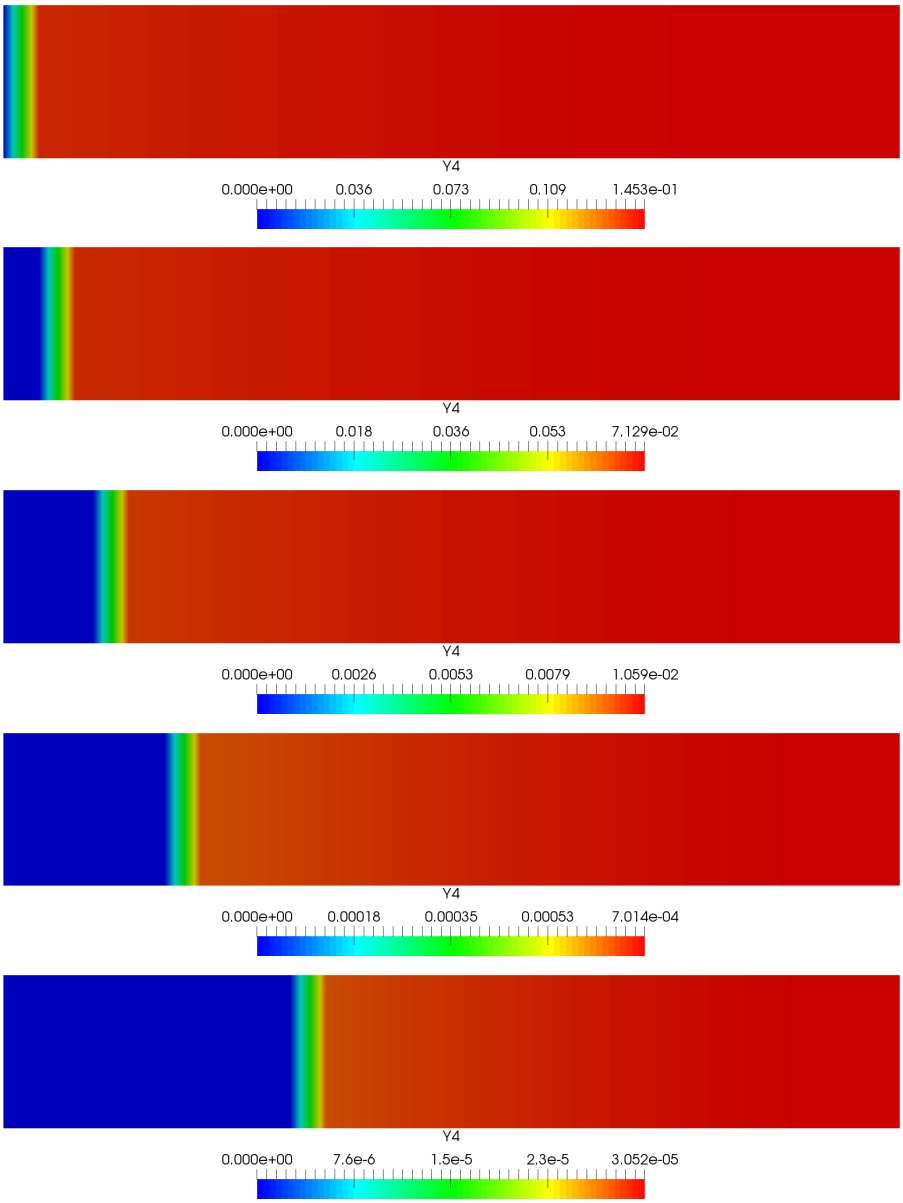

Figure 4.92: Final products distribution in t = 0.05 s at 9.1 MPa, 5.99 MPa, 3.4 MPa, 2 MPa, 1.1 MPa (above-below).

A global temperature variable which takes the condensed phase or the gas value depending on each domain is defined. As visible in Figures 4.93, 4.94 and 4.95, the location of the burning surface depends on the pressure fixed at the right boundary. The first conclusion extracted from these figures is the increment of the temperature with the pressure. Another effect very visible is the temperature evolution along the control volume. The lower the pressure, the softer is the transition between minimum and maximum temperature. However, this effect behaves in an opposite manner with the time evolution. As the time passes, the jump between hot temperature at the gas phase and cold temperature in the condensed phase becomes more abrupt which means that, the transference of heat in the solid decreases with the fall of pressure and increases when the time passes. By studying the already mentioned figures, it can be concluded that there is an increment of the temperature with

the time. This effect seems to be more visible at low than high pressures.

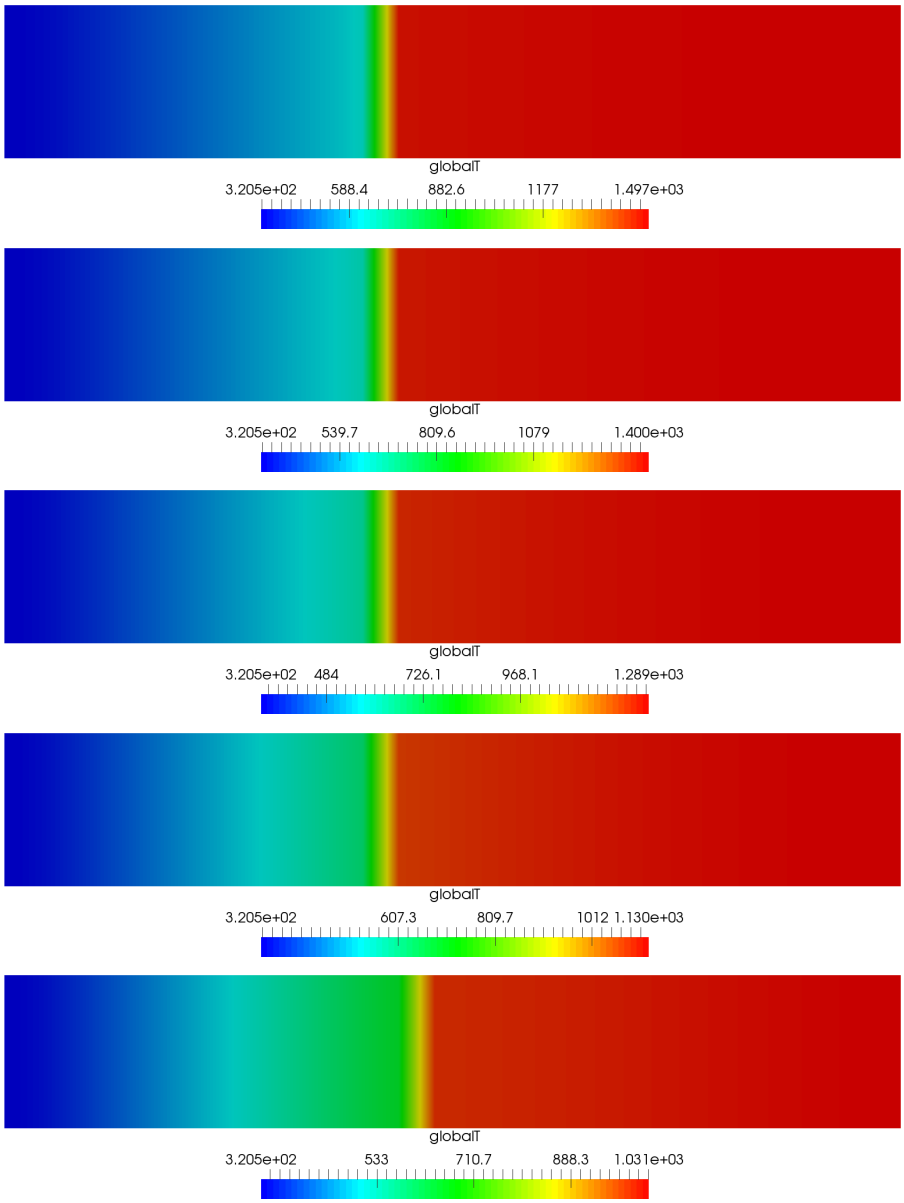

Figure 4.93: Temperature in t = 0.01 s at 9.1 MPa, 5.99 MPa, 3.4 MPa, 2 MPa, 1.1 MPa (above-below).

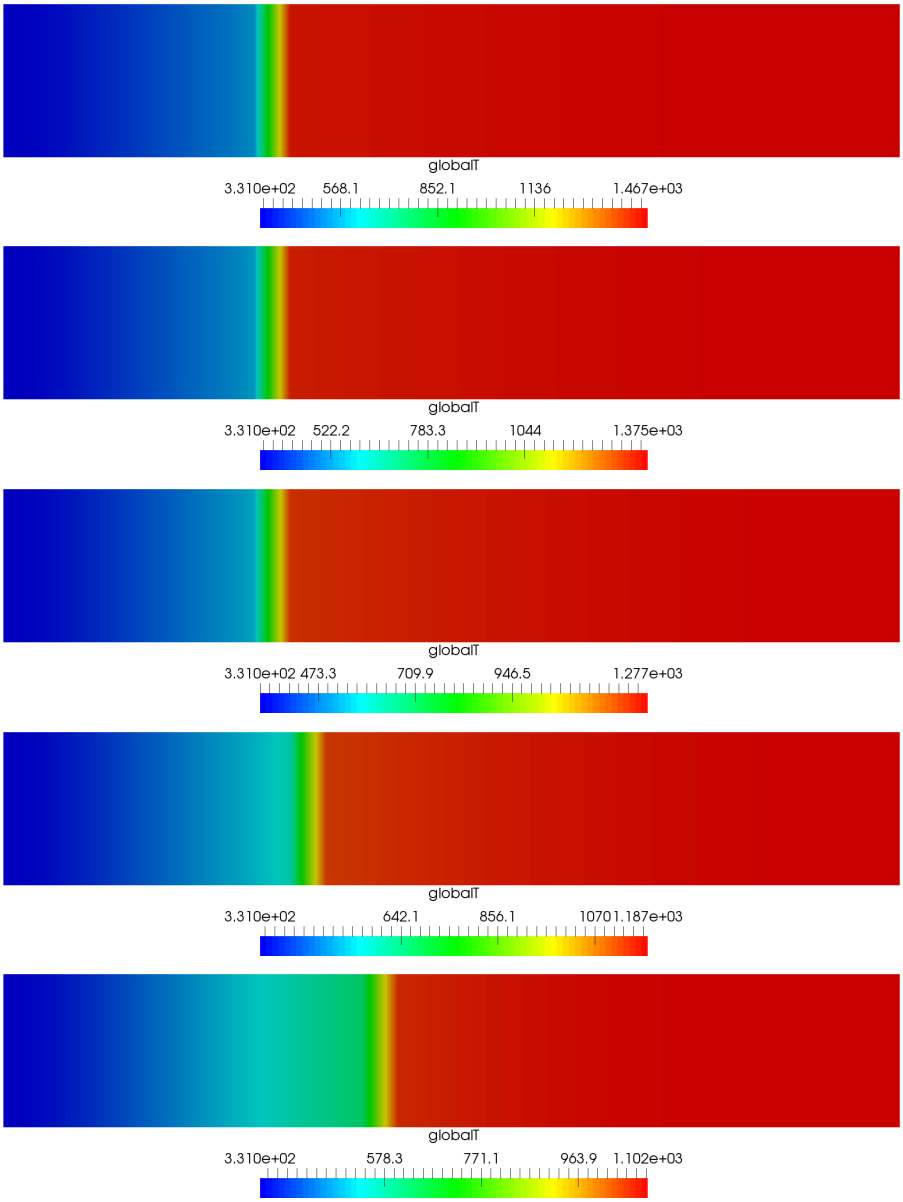

Figure 4.94: Temperature in t = 0.02 s at 9.1 MPa, 5.99 MPa, 3.4 MPa, 2 MPa, 1.1 MPa (above-below).

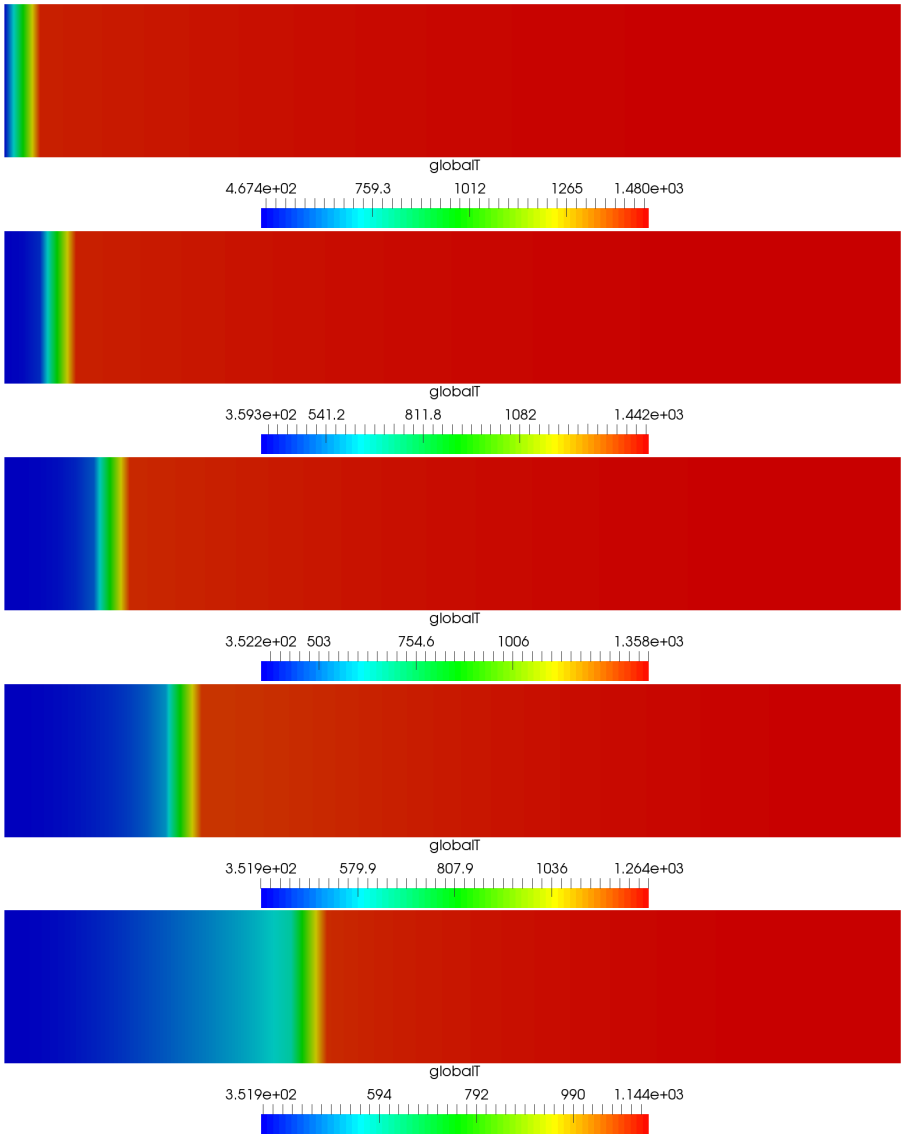

Figure 4.95: Temperature in t = 0.05 s at 9.1 MPa, 5.99 MPa, 3.4 MPa, 2 MPa, 1.1 MPa (above-below).

Finally, the heat flux is analysed by depicting its value in Figures 4.96, 4.97 and 4.98. The behaviour of the heat transfer is in perfect consonance with all previous statements. The heat flux increases with pressure and with time. The greatest amount of heat is transferred in the burning surface between the solid and the gas.

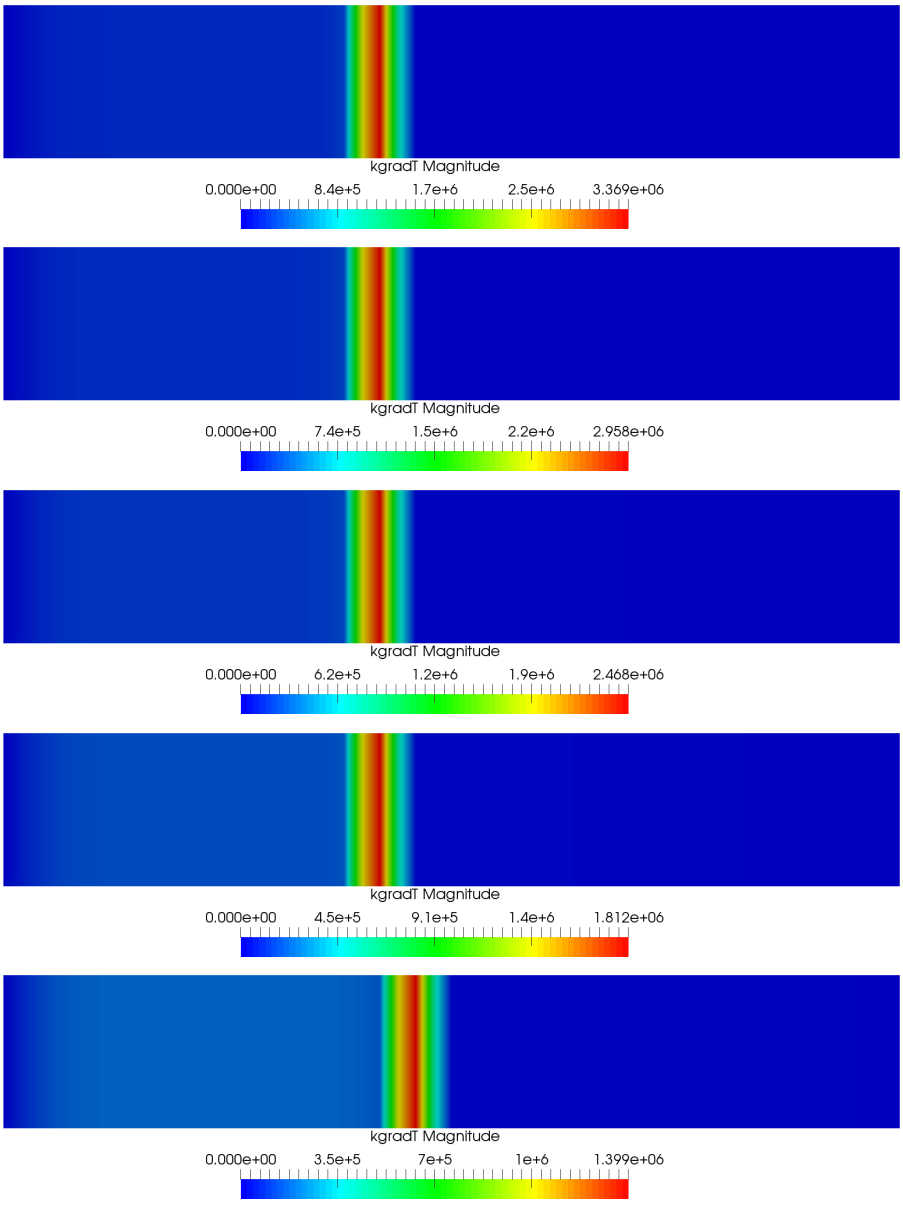

Figure 4.96: Heat flux in t = 0.01 s at 9.1 MPa, 5.99 MPa, 3.4 MPa, 2 MPa, 1.1 MPa (above-below).

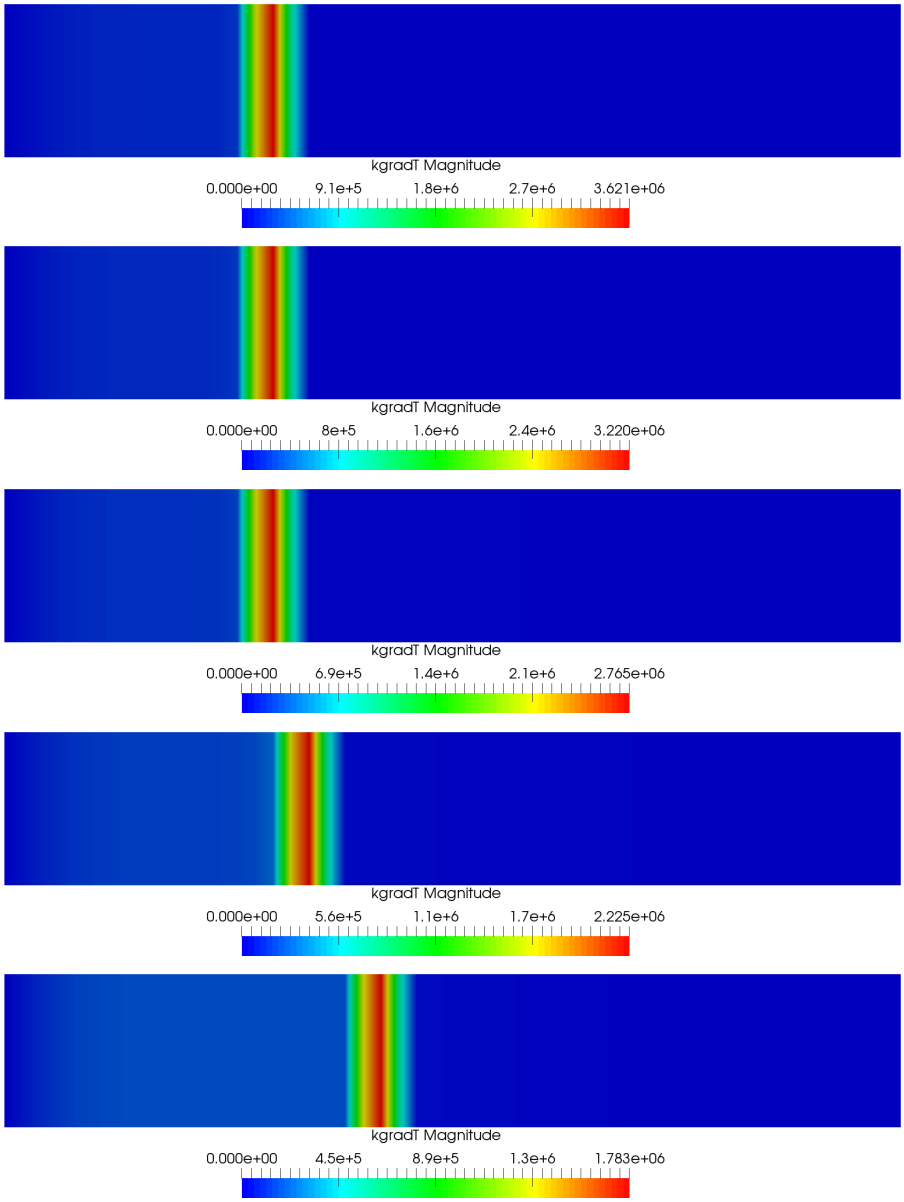

Figure 4.97: Heat flux in t = 0.02 s at 9.1 MPa, 5.99 MPa, 3.4 MPa, 2 MPa, 1.1 MPa (above-below).

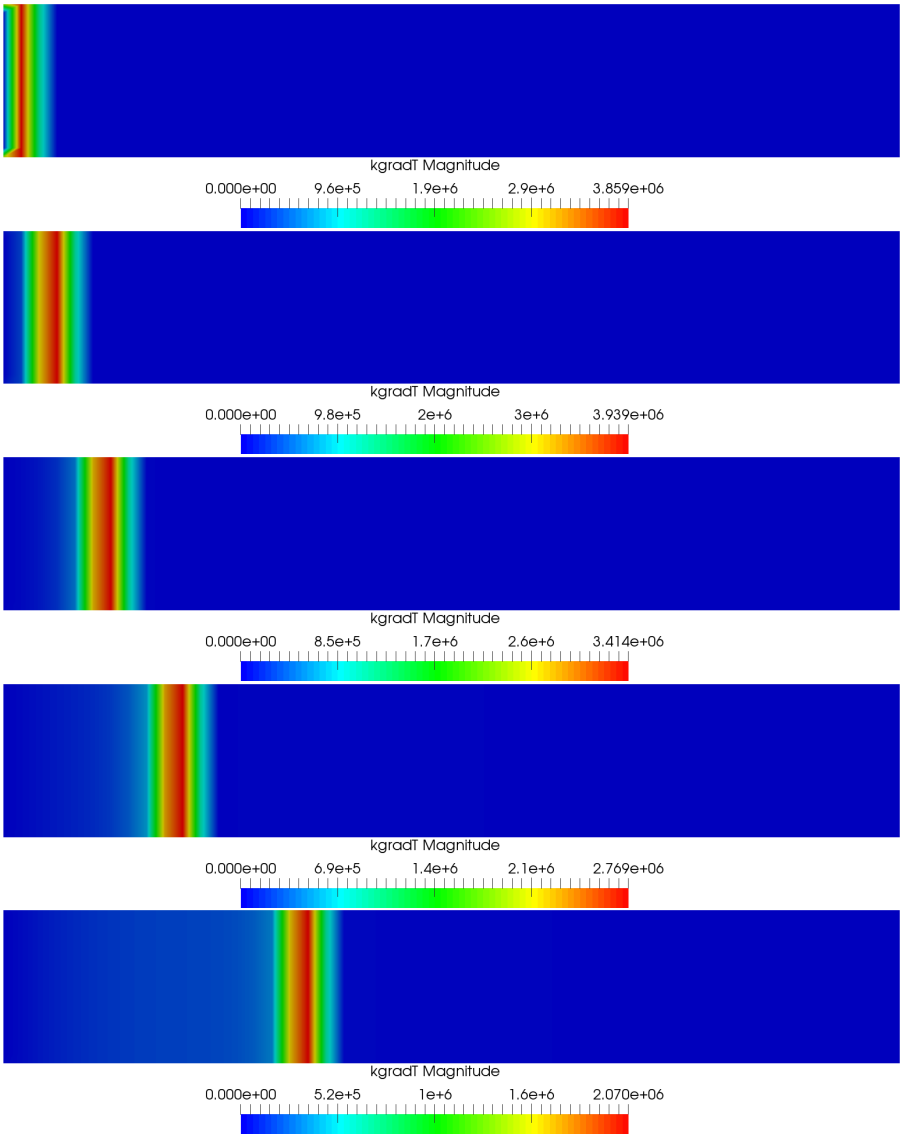

Figure 4.98: Heat flux in t = 0.05 s at 9.1 MPa, 5.99 MPa, 3.4 MPa, 2 MPa, 1.1 MPa (above-below).

4.3.3.2 Double-base propellant pressure ramp boundary conditions

The effect of depressurisation suffered in a combustion chamber has been studied when burning double-base propellant. In order to perform this analysis, a last test is applied to the previous double-base configuration geometry which consists in applying a pressure ramp as boundary condition at the end of the tube. In this case, instead of fixing a constant pressure for the open side, a sharp pressure ramp in the range of validated pressures (from 9.1 MPa to 1.1 MPa) is applied. This ramp will be produced in a very short time equal to 0.01 μs and it will start at 0.01 s. Therefore, before 0.01 s, the pressure will be fixed to 9.1 MPa and after 0.01000001 s the pressure will become 1.1 MPa. How the depressurisation influences to the pressure distribution, mass fraction of fuel and oxidiser as well as intermediate species and reaction products, temperature and heat flux is studied throughout this subsection.

The first variable to be analysed is the pressure distribution. To achieve this, the evolution of the pressure just after depressurisation in the right side of the tube is depicted in first place (see Figure 4.99). As can be seen in the first render of Figure 4.99, at the very first moment depressurisation is applied at the end of the tube, the pressure suffers a jump between the pressure along the tube with a value of 9.1 MPa to the value of the right side. When time is 0.01001 s, the pressure wave has progressed to the middle of the tube and almost half of the gas zone is already at low pressure. When 0.00001 more seconds take place, the pressure wave goes back to the right side of the tube creating a depression close to the burning effect as was observed when analysing depressurisation effect on the burning of AP/HTPB propellant. Again, at 0.01003 seconds the wave travels left until finally the gas remains at equilibrium pressure. This behaviour could be easily observed when plotting the results of the pressure for an exact point of the geometry. Three points have been chosen to study the behaviour of pressure. The first one, named $P_1 = (510 \cdot 10^{-6}, 85{\cdot}10^{-6}, 85{\cdot}10^{-6})$, is set very close to the burning surface of 1.1 MPa fixed boundary condition test. The second one ($P_2 = (750{\cdot}10^{-6}, 85{\cdot}10^{-6}, 85{\cdot}10^{-6})$) is located at the half of gas domain and finally, the last one is close to the end of the tube and named $P_3 = (950 \cdot 10^{-6}, 85{\cdot}10^{-6}, 85{\cdot}10^{-6})$. In order to study the behaviour as precise as possible, for each point the pressure has been represented firstly from 0.01 to 0.02 seconds and afterwards, from 0.01 to 0.011 seconds to have a detailed view of the distribution just after the depressurisation is created. By observing Figures 4.100 and 4.101 it can be seen how, for the 1.1 MPa fixing boundary condition test, the pressure at P_1 fluctuates around this value. However, the pressure at the same point for the 9.1 MPa fixed boundary condition test remains stable. This could be explained due to the distance between the first point and the burning surface. On the one hand, the burning surface when the pressure in the boundary is fixed to 1.1 MPa is located close to P_1 while on the other hand, when the pressure fixed at the boundary is high, the burning surface is located further, closer to the left boundary. The cells close burning surface are the first ones to receive the sublimated gas species from the burning surface and, as a result, the fuel, oxidiser and intermediate species combust firstly in these cells. Therefore, the density of cells located close to the burning surface will fluctuate and that will influence the temperature and pressure distributions. In order to crosscheck this statement, the pressure at the second (P_2) and third point (P_3) is represented in Figures 4.102, 4.103, 4.104 and 4.105 respectively. How the pressure fluctuation observed for the 1.1 MPa fixed pressure case disappears with the increase of the x-coordinate is perfectly visible in the already mentioned figures. To conclude, it can be said that the further from the burning surface the pressure is measured, the more stable will be the pressure. The pressure obtained for the ramp boundary test is compared against that of the 1.1 MPa fixed boundary test in Figure 4.101 in which sharp decrease of pressure can be seen. Afterwards, the pressure value in this point oscillate around 1.1 MPa reaching even lower pressure values. Therefore, a strong pressure jump applied at the exit of the chamber leads to an immediate depressurisation in the cells close to the burning surface even lower than the minimum value of the pressure step. After 0.0101 s, the pressure remains around 1.1 MPa being the fluctuations less visible than those seen in the 1.1 MPa fixed boundary test. The reason of this phenomenon is attributed again to the position of the burning surfaces for the different tests. Before suffering depressurisation, the pressure of the ramp test was fixed to 9.1 MPa, as consequence, when time is equal to 0.01 seconds its burning surface it is located in the same position than that of the 9.1 MPa fixed pressure test,

far from point one. Therefore, as happened for the 9.1 fixed boundary condition test, fluctuations of pressure are less visible. The evolution of pressure with time when ramp boundary conditions are established and its comparison with the 1.1 MPa and the 9.1 MPa boundary tests are represented in Figures 4.106 and 4.107.

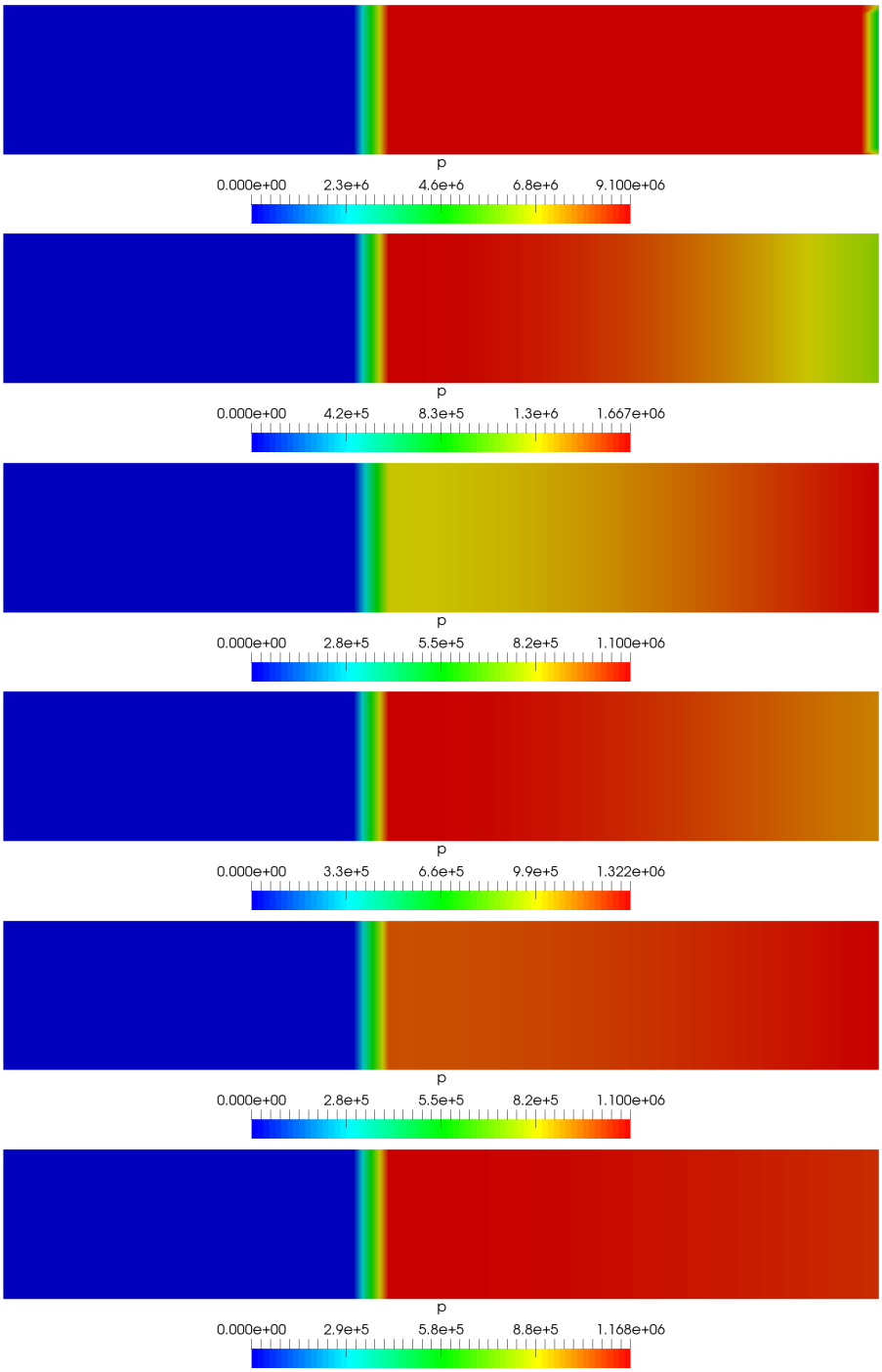

Figure 4.99: Pressure distribution for t = 0.01000001, t = 0.01001 s, t = 0.01002, t = 0.01003, t = 0.001004 s and t = 0.01005 s (above-below).

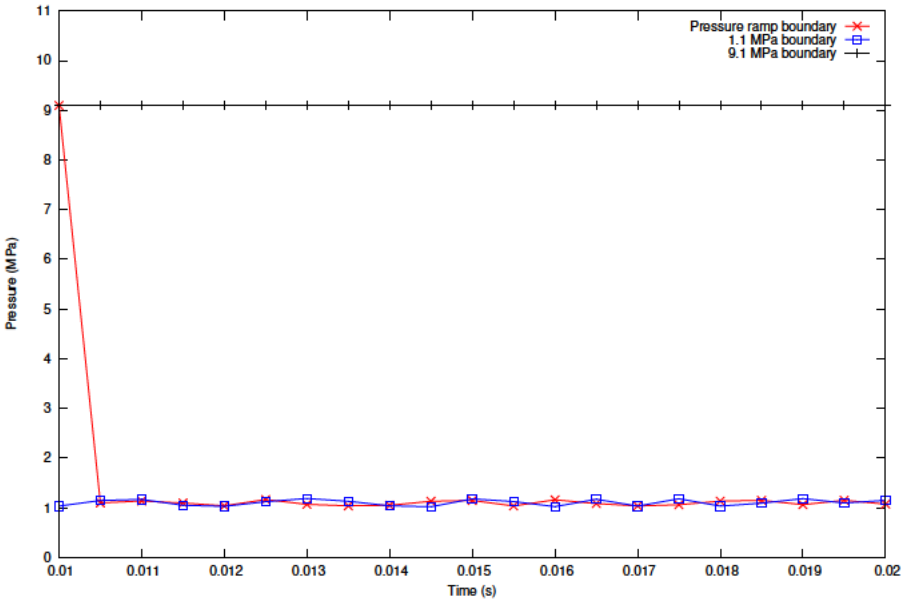

Figure 4.100: Pressure distribution for $P_1 = (510 \cdot 10^{-6}, 85{\cdot}10^{-6}, 85{\cdot}10^{-6})$.

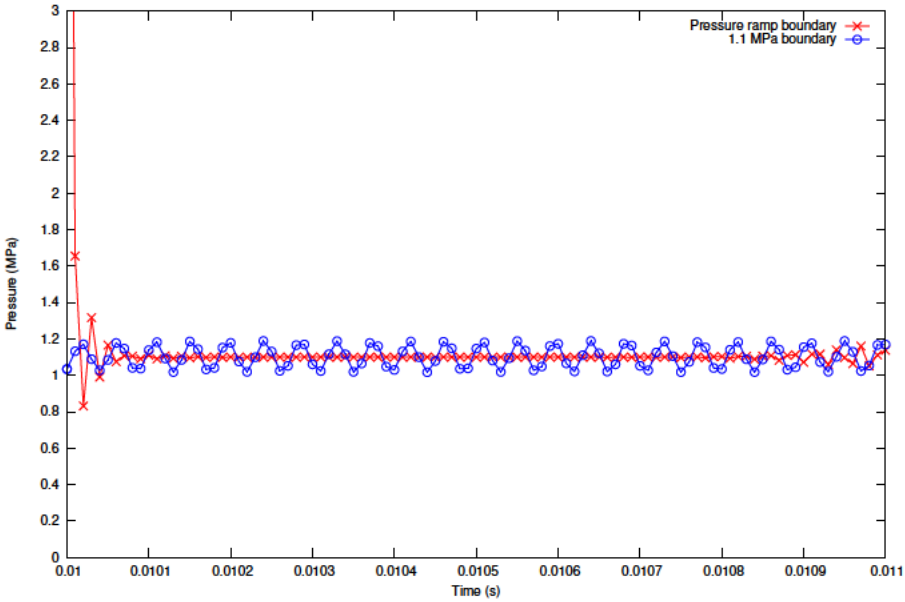

Figure 4.101: Pressure distribution for $P_1 = (510 \cdot 10^{-6}, 85{\cdot}10^{-6}, 85{\cdot}10^{-6})$.

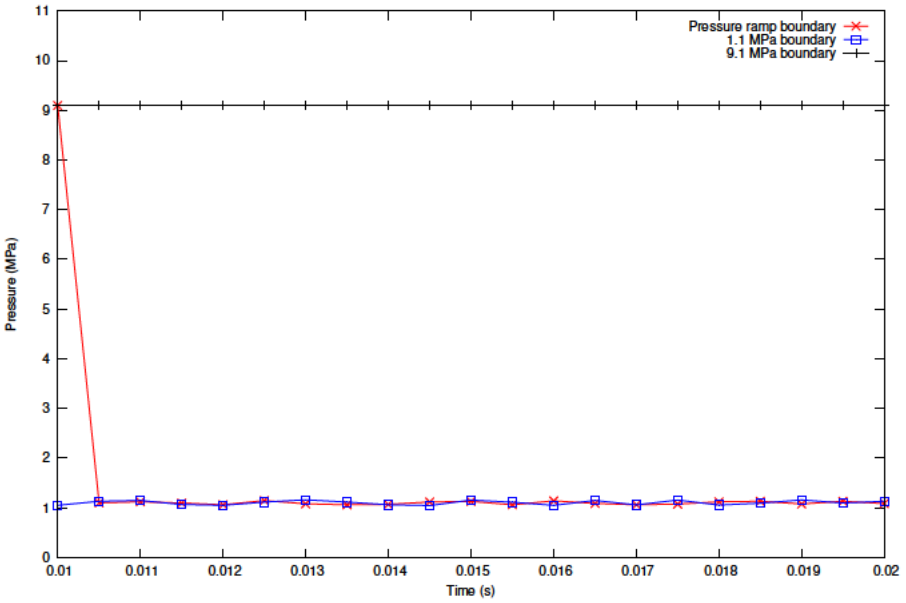

Figure 4.102: Pressure distribution for $P_2 = (750 \cdot 10^{-6}, 85{\cdot}10^{-6}, 85{\cdot}10^{-6})$.

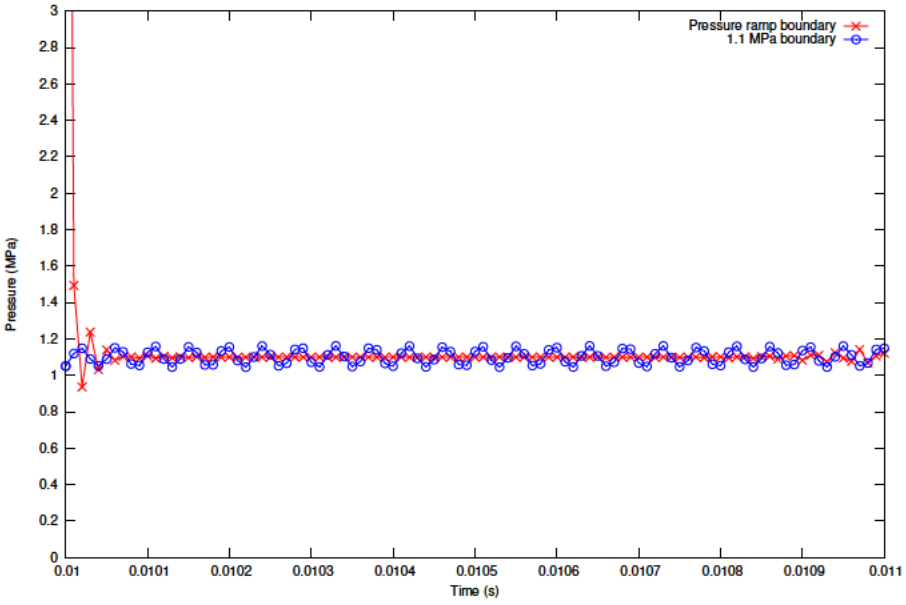

Figure 4.103: Pressure distribution for $P_2 = (750 \cdot 10^{-6}, 85{\cdot}10^{-6}, 85{\cdot}10^{-6})$.

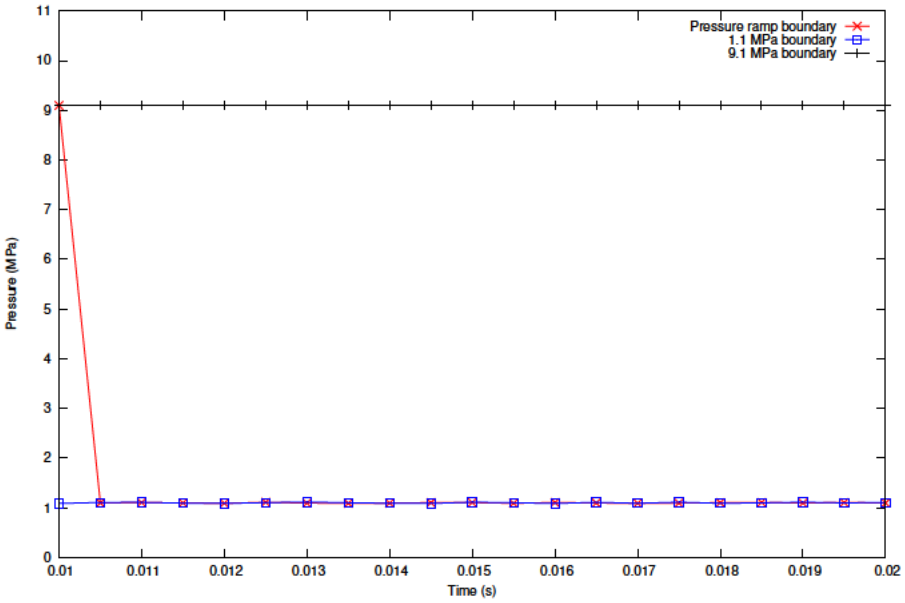

Figure 4.104: Pressure distribution for $P_4 = (510 \cdot 10^{-6}, 85{\cdot}10^{-6}, 85{\cdot}10^{-6})$.

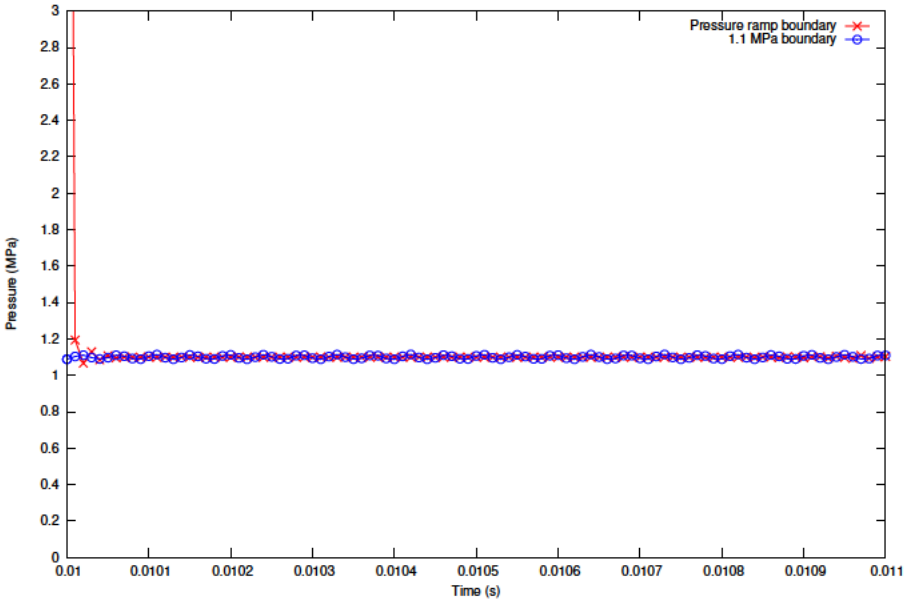

Figure 4.105: Pressure distribution for $P_3 = (950 \cdot 10^{-6}, 85{\cdot}10^{-6}, 85{\cdot}10^{-6})$.

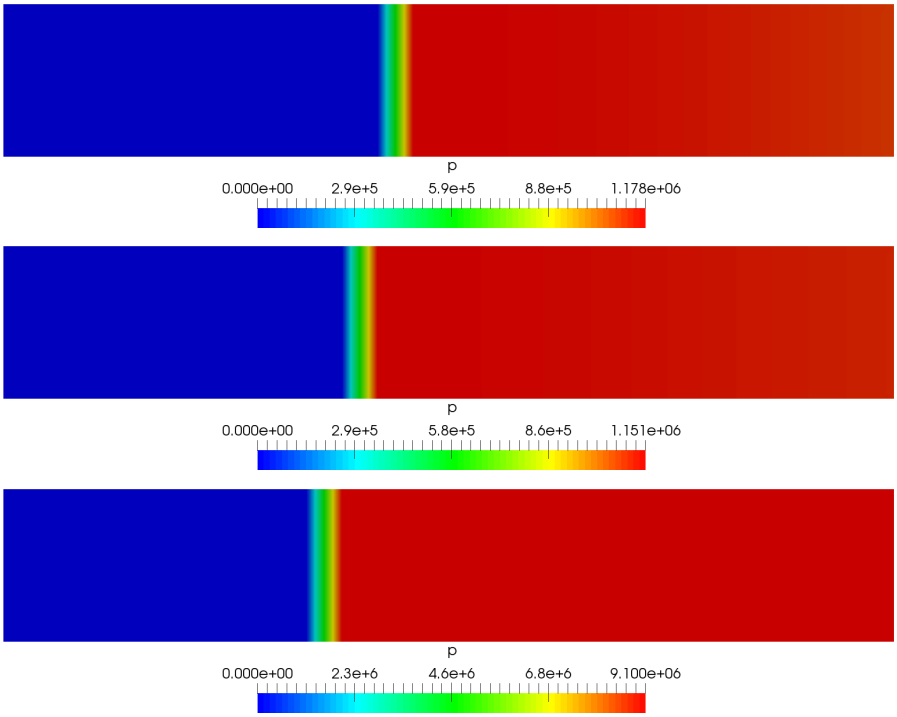

Figure 4.106: Pressure distribution for fixed 1.1 MPa, ramp and fixed 9.1 MPa boundary conditions at t= 0.015 s (above-below).

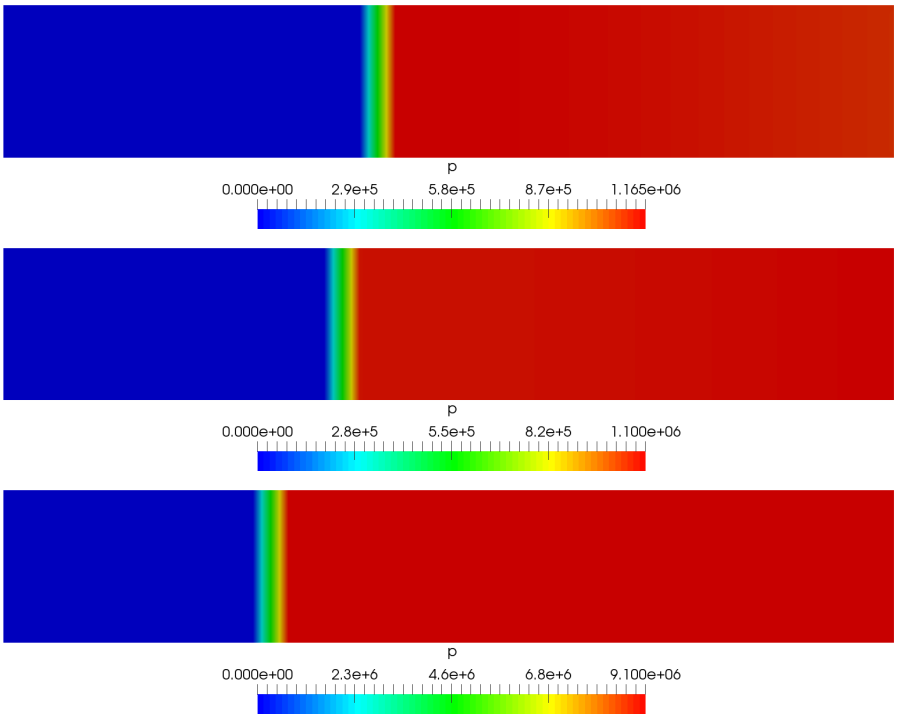

Figure 4.107: Pressure distribution for fixed 1.1 MPa, ramp and fixed 9.1 MPa boundary conditions at t = 0.02 s (above-below).

The same analysis performed for the pressure, will be done for mass fractions of fuel and oxidiser, intermediate species and products of chemical reaction in order to study how the depressurisation affects to the combustion process. The first two distributions of species mass fraction analysed are those corresponding to fuel and oxidiser (Figures 4.108 and 4.109) observing an increase of their concentrations during the time after applying depressurisation. By studying the other species, it can be seen how DR1, remains almost constant for the considered time slot (see Figure 4.84) increasing slightly its concentration too. However, Figure 4.111 shows the decrement of DR2 mass fraction from 0.01 s to 0.01005 s. Finally, products mass fraction distribution is plotted in Figure 4.112 where the fall of the specie concentration after applying depressurisation is observed too. How the depressurisation affect the mass fraction of the gas species can be explained with the same argument of subsection 4.3.3.1. The magnitude of the mixture density is smaller for low than for high pressures. Since the reaction rates which represent the chemical kinetics of the combustion process depend on the density, with the fall of pressure, the reaction rates decrease too. As a result, when depressurisation is applied, not only less fuel and oxidiser react to form intermediate product DR2, but also less DR1 and DR2 change to become final products. The sublimation of condensed phase and the decrease of reaction rates are the reason of the increment of fuel, oxidiser and intermediate products DR1. As a result, there creation of new final products will fall down and part of them will be lost by the exit of the tube concluding in a reduction of their mass fraction. The same phenomenon is suffered by intermediate specie DR2 just after depressurisation until time is equal to 0.001004 s. At this time pressure stabilised to 1.1 MPa (see Figure 4.99) and therefore, the mass fraction of DR2 remains almost constant too. In order to study in detail the evolution of fuel and oxidiser mass fractions, not only immediately after depressurisation, but also once pressure stability is reached, fuel and oxidiser mass fraction distribution for pressure ramp test have been plotted together with the ones of 1.1 MPa and 9.1 MPa fixed boundary condition test for 0.015 and 0.02 s in Figures 4.113, 4.114, 4.115 and 4.116. The maximum values of fuel and oxidiser mass fraction remain almost constant between the considered interval of time. As is done for pressure, mass fraction distributions are also studied at the three points of interest and the results are depicted from Figures 4.117 to 4.122. Figure 4.117 and its zoom in time (Figure 4.118) show very clearly how the mass fraction of both, fuel and oxidiser for depressurisation test behaves exactly the same. At the beginning their values are the same that the ones obtained for 9.1 MPa fixed boundary condition however, when depressurisation is applied, both mass fractions start to increase until reaching the ones obtained at 1.1 MPa fixed boundary condition. As observed when analysing the pressure, fuel and oxidiser mass fraction values in the first point of interest when pressure at the boundary is fixed to 1.1 MPa fluctuate slightly and being less visible for point two and three. Afterwards, intermediate species DR1 and DR2, and final products are also represented in these points (Figures 4.123, 4.124 and 4.125) obtaining the same evidences, both variables remain almost stable during the interval between 0.01 s and 0.02 s for the fixed boundary condition test. In the case of applying a ramp boundary condition, the mass fraction of DR1 starts with the value of 9.1 MPa fixed pressure and it increases when depressurisation is applied until reaching the value of 1.1 MPa fixed pressure test. However, DR2 mass fraction starts with the same percentage than the test of 9.1 MPa, and with the depressurisation, instead of increasing its value, it falls down until reaching the amount of DR2 obtained in 1.1 MPa fixed boundary condition test. Finally, to end this analysis, final products mass fraction at the three considered points are plotted in three graphs collected in Figure 4.129. As happened with the other species, no visible differences are observed during the selected interval of time in case of fixing the pressure at the boundaries but a slight decrement for 9.1 MPa test. The behaviour for the ramp test is exactly the one expected, the mass fraction of products start with a value close to 9% which corresponds to 9.1 MPa fixed boundary condition. When depressurisation is applied, chemical reaction lose their strength and as a result, less amount of products are obtained. The value of 9% will fall gradually until reaching that obtained for 1.1 MPa fixed boundary condition.

Before analysing temperature distribution and heat flux, it is of high interest to study how the surface temperature varies when strong pressure step is applied at the right boundary. As expected, when the depressurisation is applied, the temperature decreases sharply from the value of 9.1

fixed boundary condition test and starts to fluctuate slightly to finally reach stability around 650 K presenting the same behaviour as the already mentioned variables.

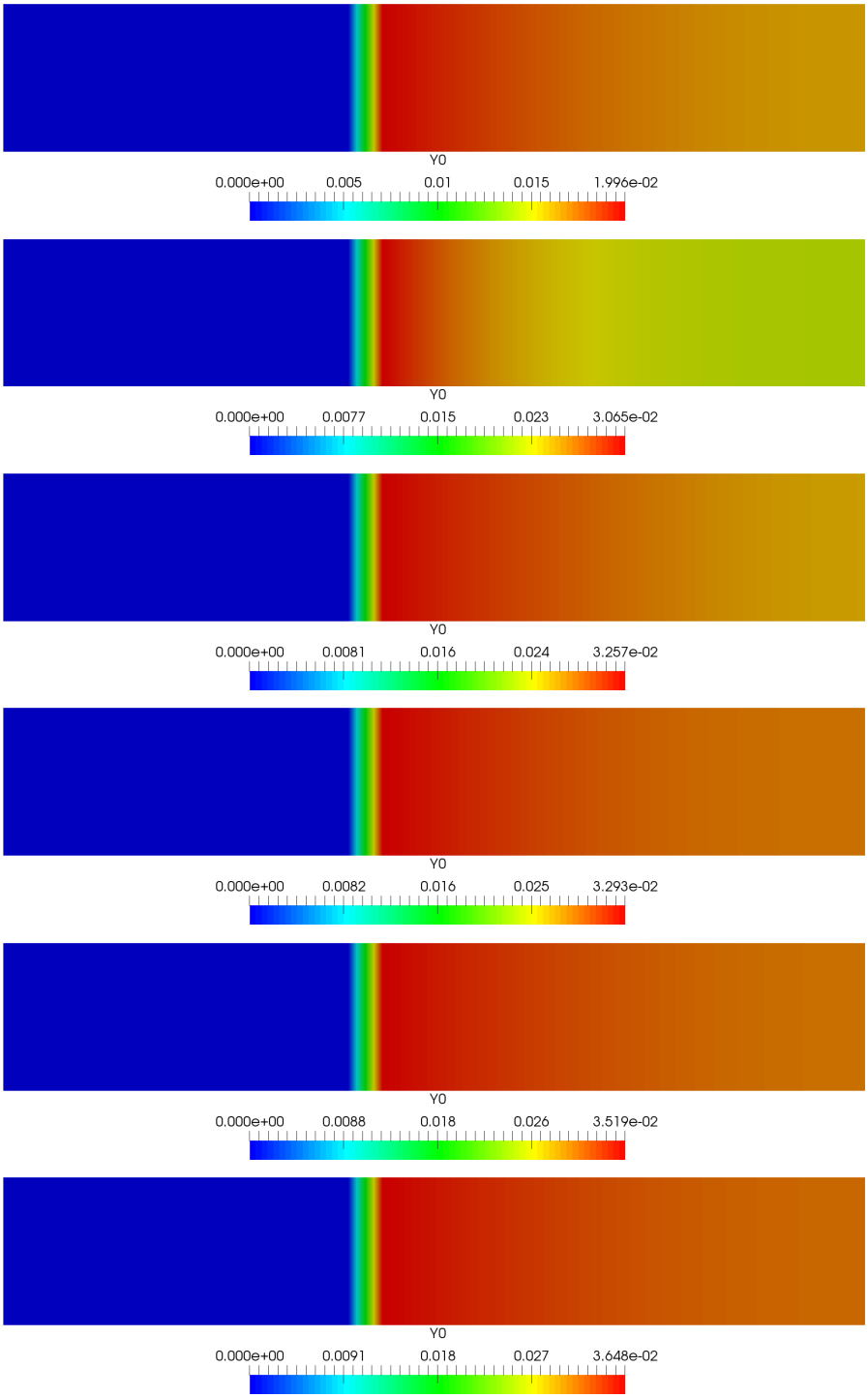

Figure 4.108: Fuel distribution for t = 0.01000001, t = 0.01001 s, t = 0.01002, t = 0.01003, t = 0.001004 s and t = 0.01005 s (above-below).

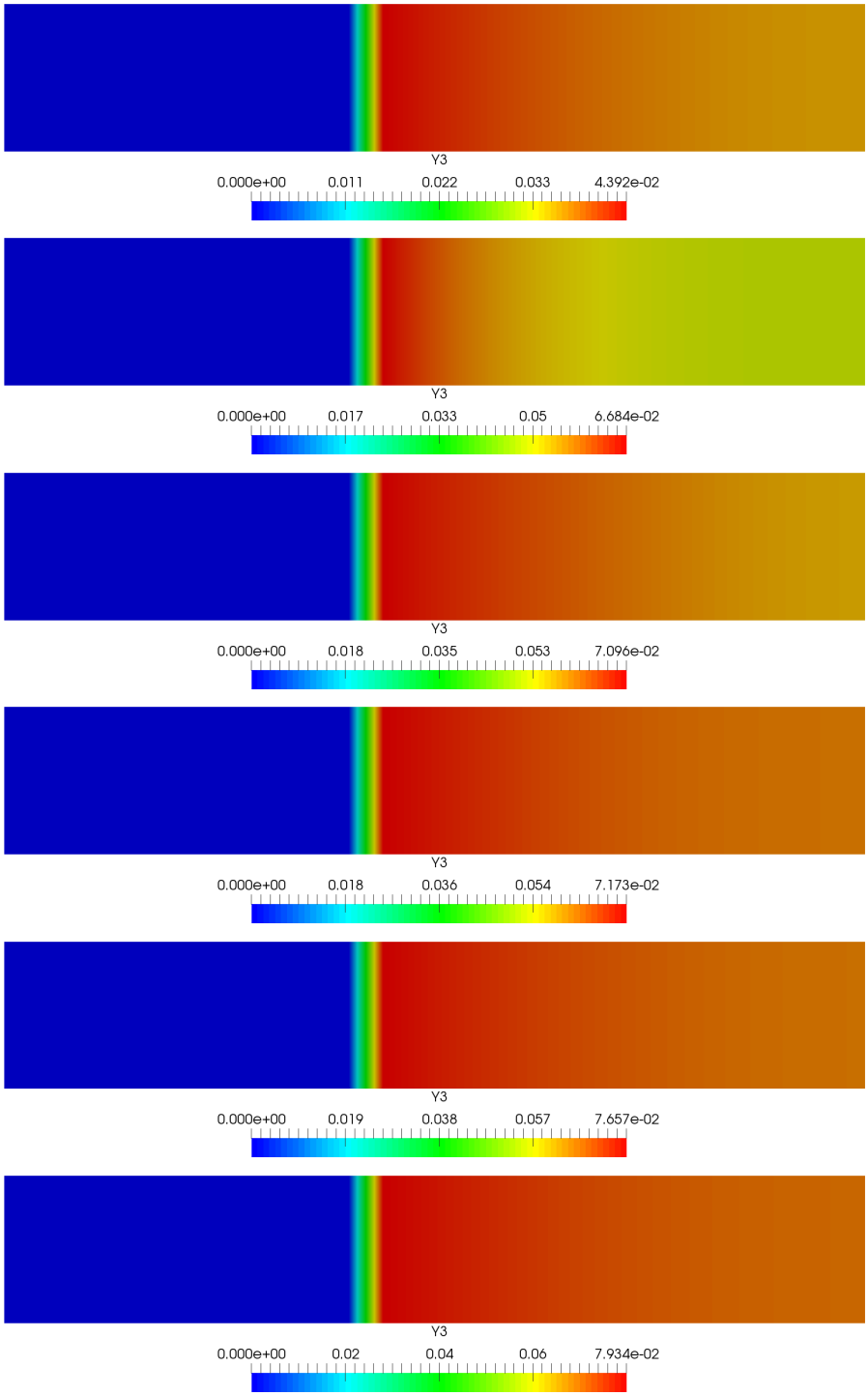

Figure 4.109: Oxidiser distribution for t = 0.01000001, t = 0.01001 s, t = 0.01002, t = 0.01003, t = 0.001004 s and t = 0.01005 s (above-below).

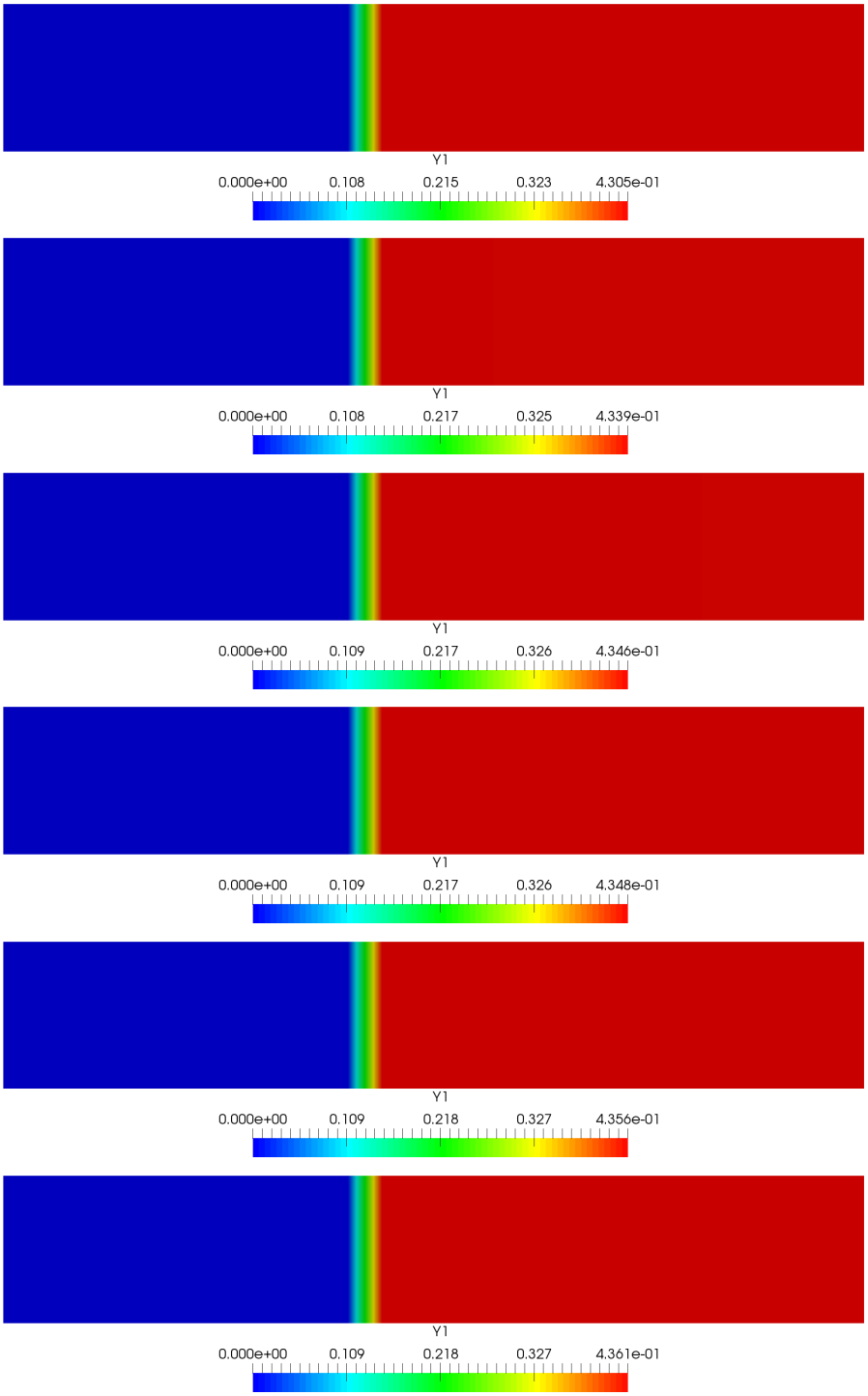

Figure 4.110: DR1 distribution for t = 0.01000001, t = 0.01001 s, t = 0.01002, t = 0.01003, t = 0.001004 s and t = 0.01005 s (above-below).

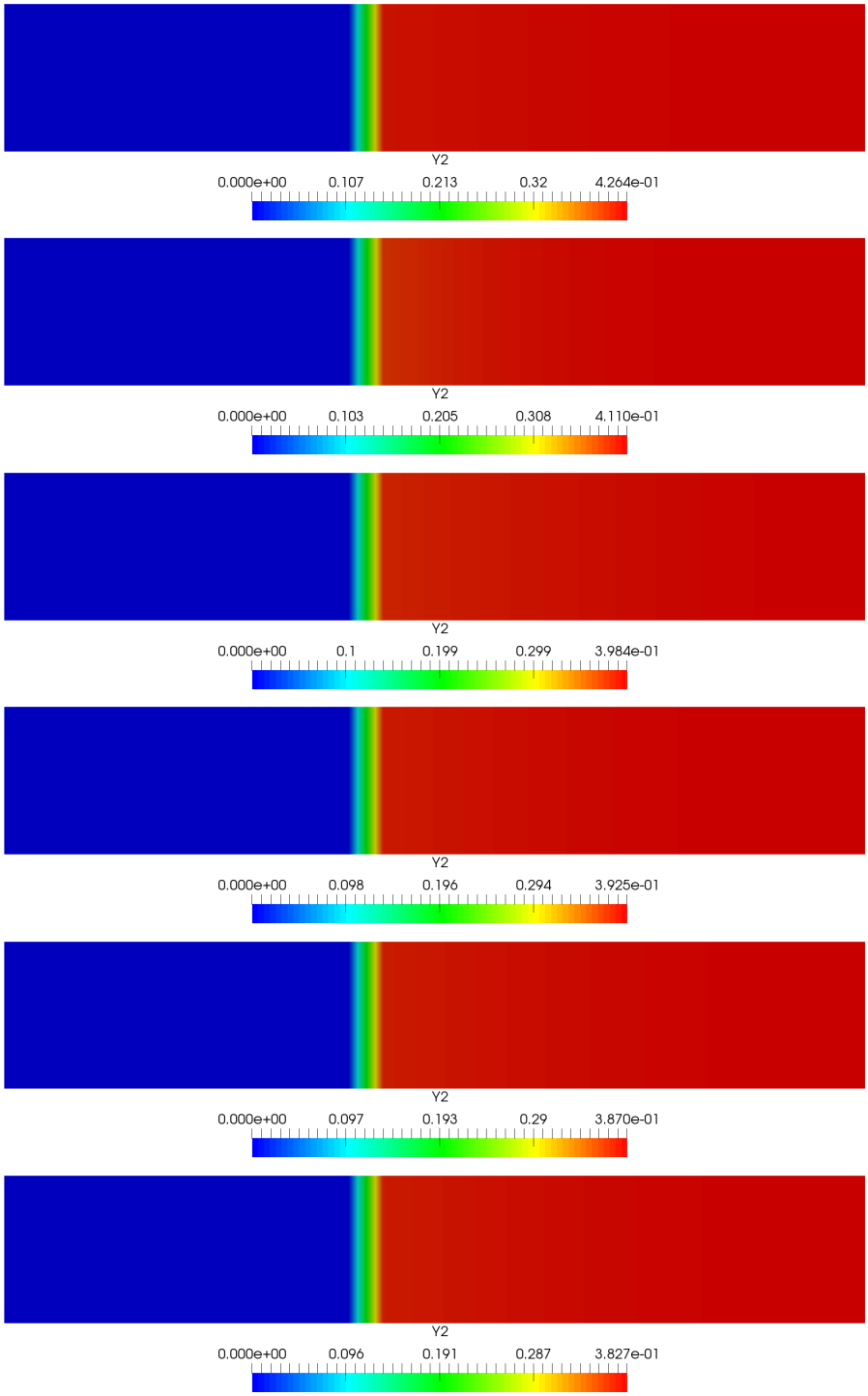

Figure 4.111: DR2 distribution for t = 0.01000001, t = 0.01001 s, t = 0.01002, t = 0.01003, t = 0.001004 s and t = 0.01005 s (above-below).

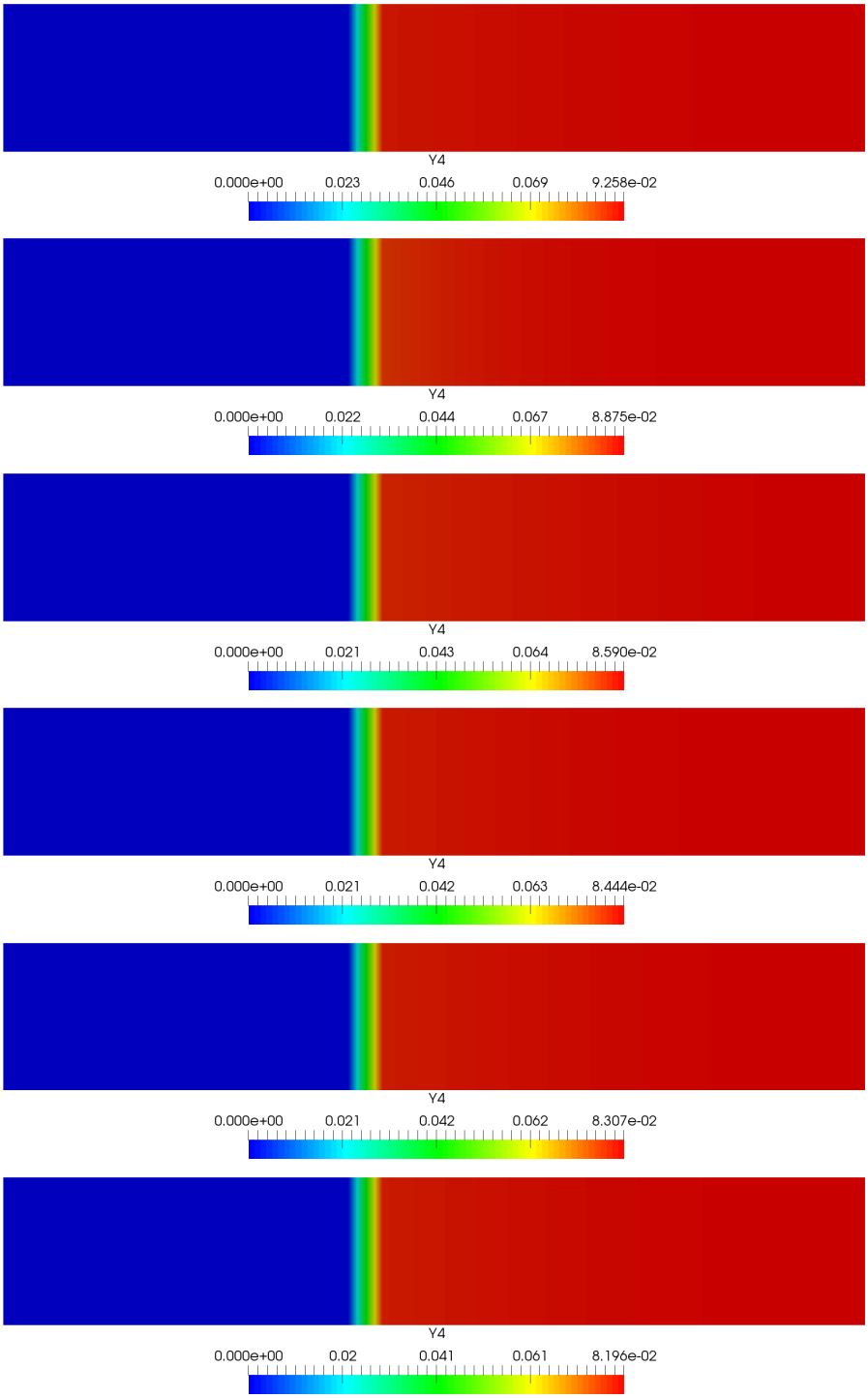

Figure 4.112: Products distribution for t = 0.01000001, t = 0.01001 s, t = 0.01002, t = 0.01003, t = 0.001004 s and t = 0.01005 s (above-below).

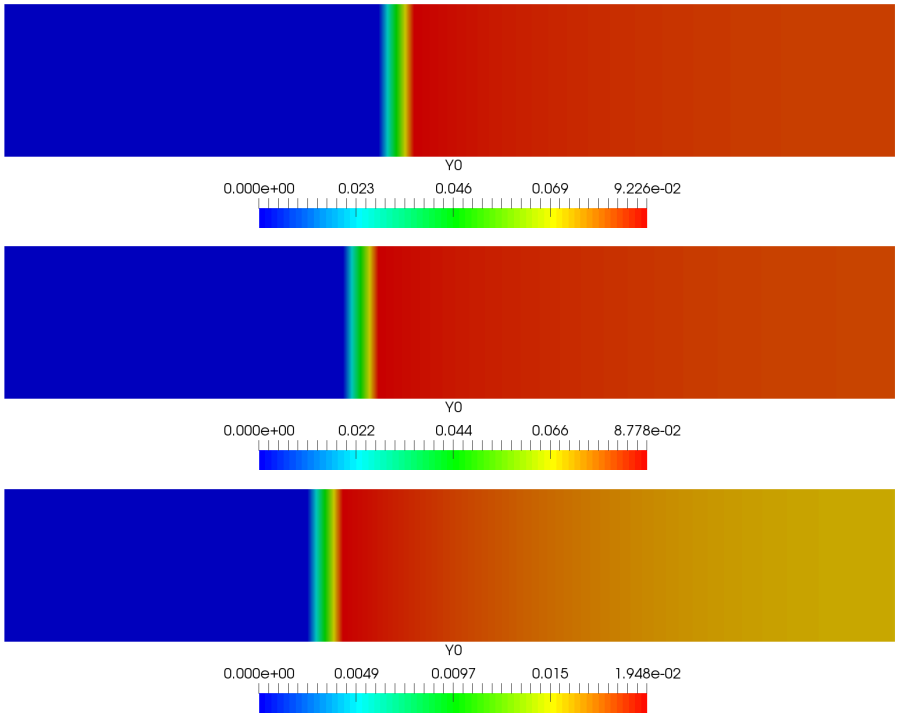

Figure 4.113: Fuel mass fraction distribution for fixed 1.1 MPa, ramp and fixed 9.1 MPa boundary conditions at t= 0.015 s (above-below).

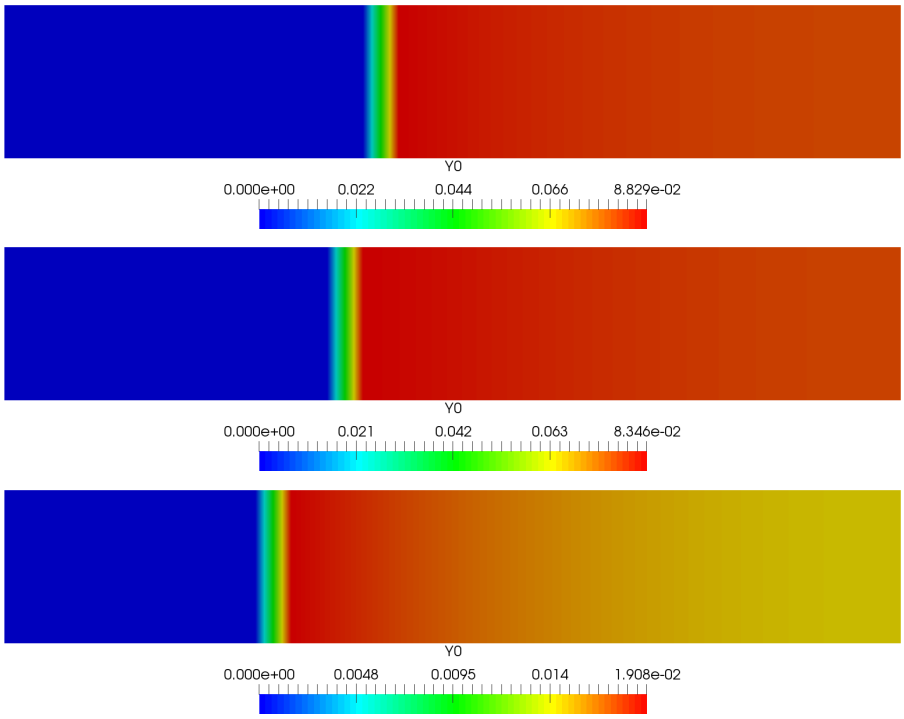

Figure 4.114: Fuel mass fraction distribution for fixed 1.1 MPa, ramp and fixed 9.1 MPa boundary conditions at t= 0.02 s (above-below).

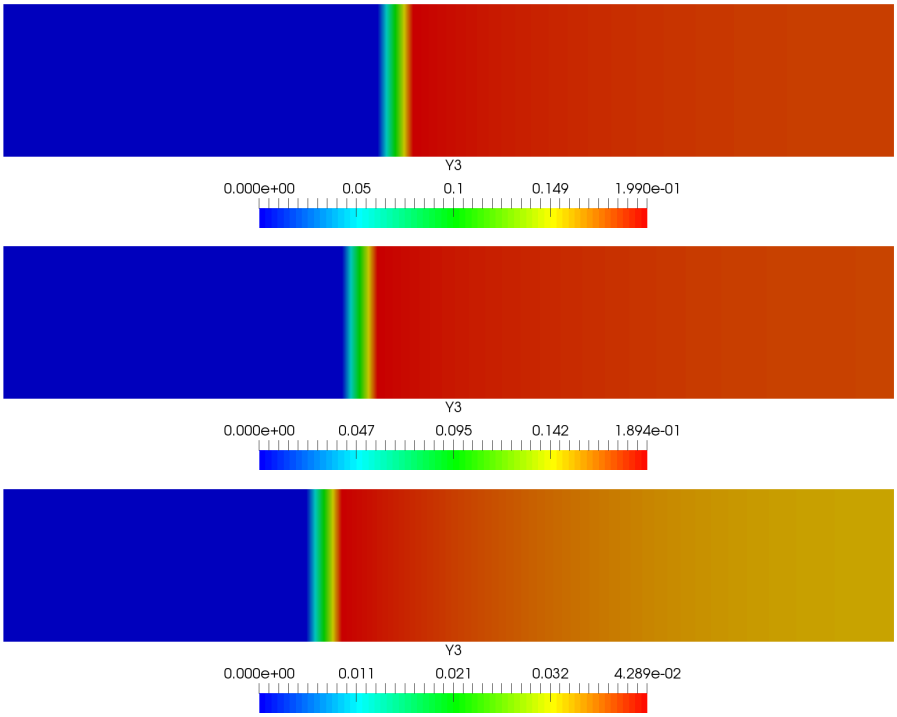

Figure 4.115: Oxidiser mass fraction distribution for fixed 1.1 MPa, ramp and fixed 9.1 MPa boundary conditions at t = 0.015 s (above-below).

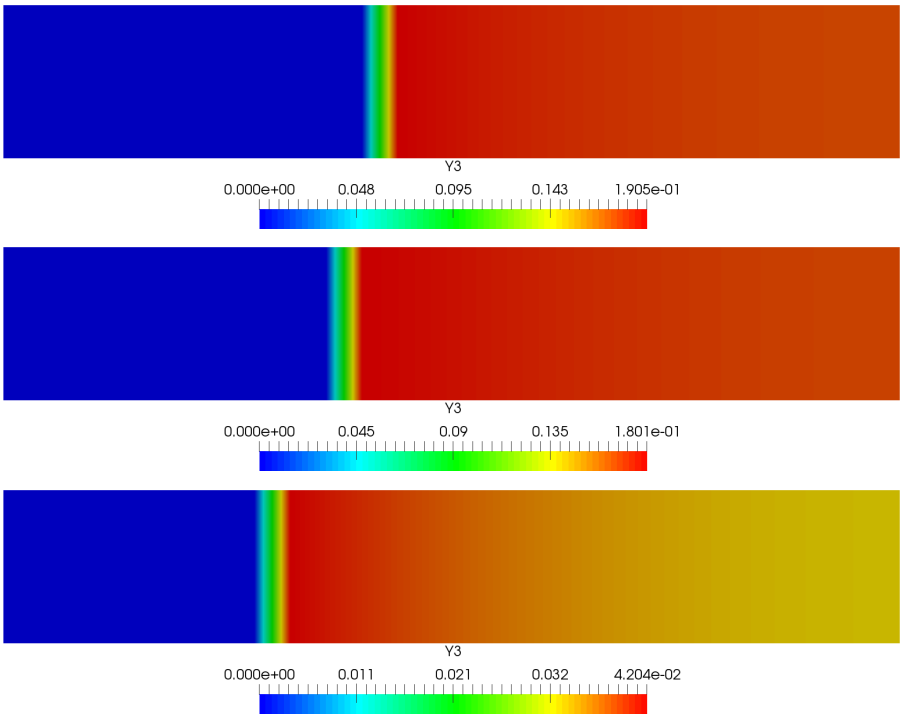

Figure 4.116: Oxidiser mass fraction distribution for fixed 1.1 MPa, ramp and fixed 9.1 MPa boundary conditions at t = 0.02 s (above-below).

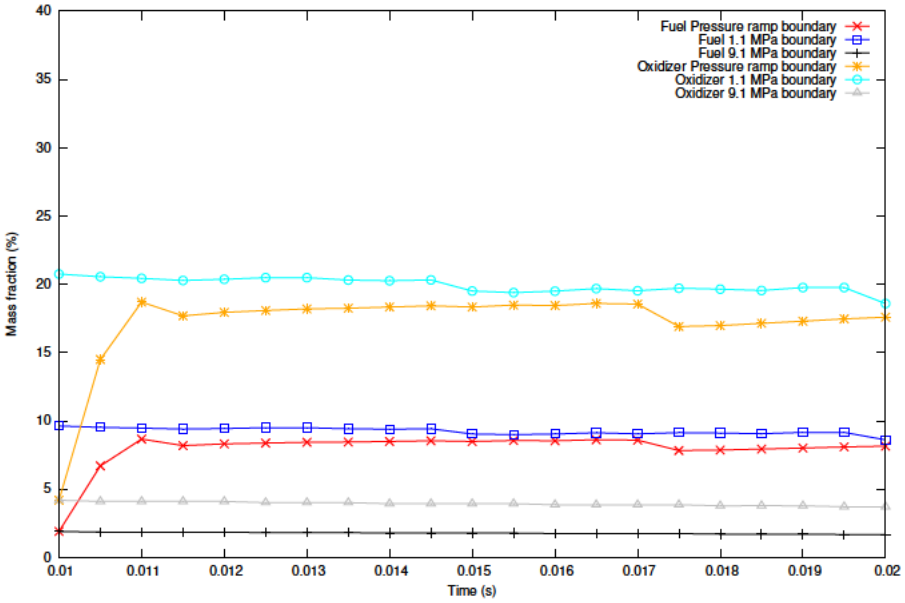

Figure 4.117: Fuel and oxidiser distribution for $P_1 = (510 \cdot 10^{-6}, 85{\cdot}10^{-6}, 85{\cdot}10^{-6})$.

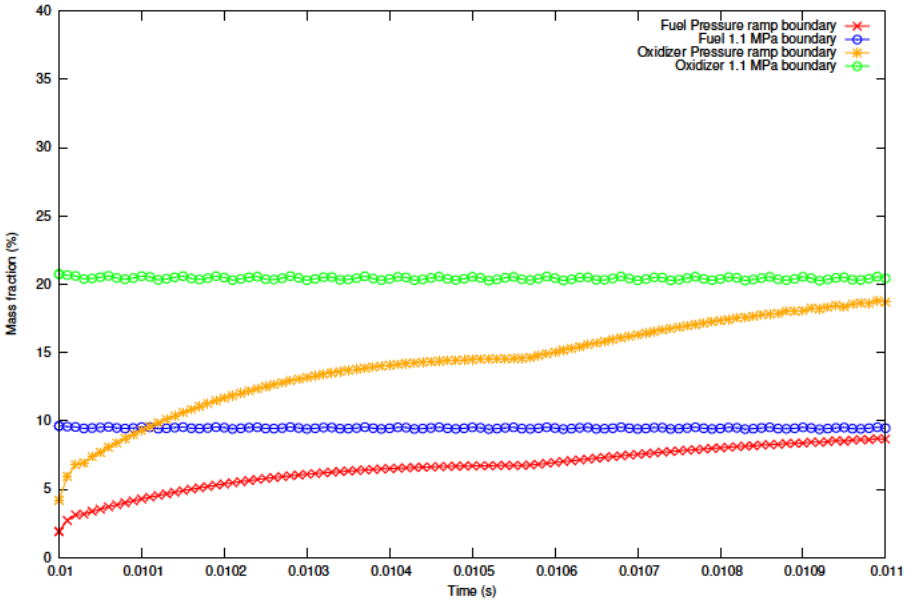

Figure 4.118: Fuel and oxidiser distribution for $P_1 = (510 \cdot 10^{-6}, 85{\cdot}10^{-6}, 85{\cdot}10^{-6})$.

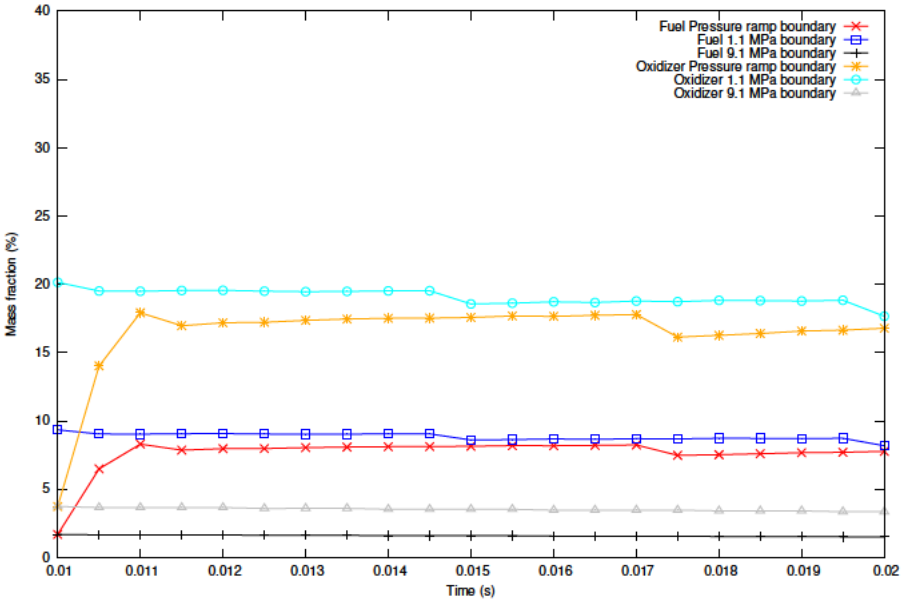

Figure 4.119: Fuel and oxidiser distribution for $P_2 = (750 \cdot 10^{-6}, 85{\cdot}10^{-6}, 85{\cdot}10^{-6})$.

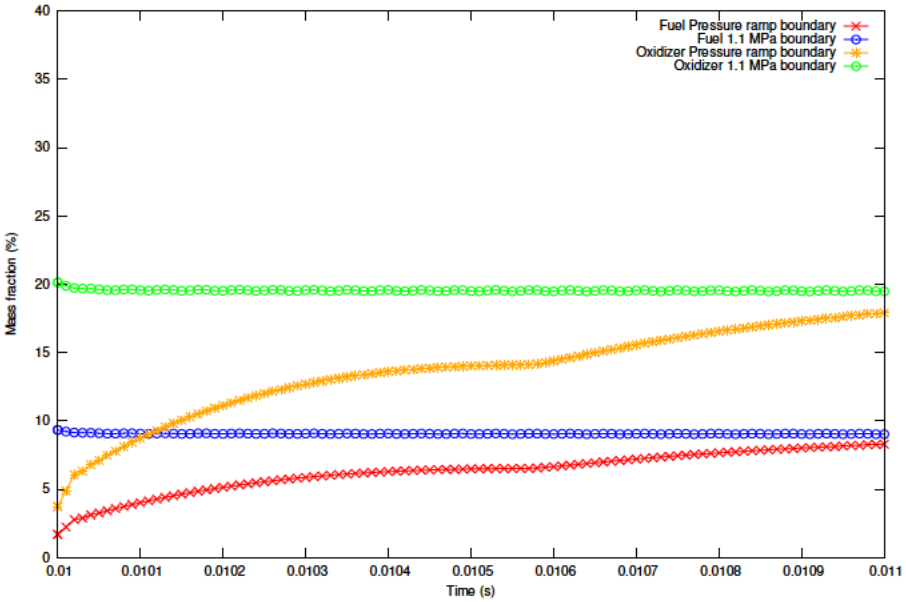

Figure 4.120: Fuel and oxidiser distribution for $P_2 = (750 \cdot 10^{-6}, 85{\cdot}10^{-6}, 85{\cdot}10^{-6})$.

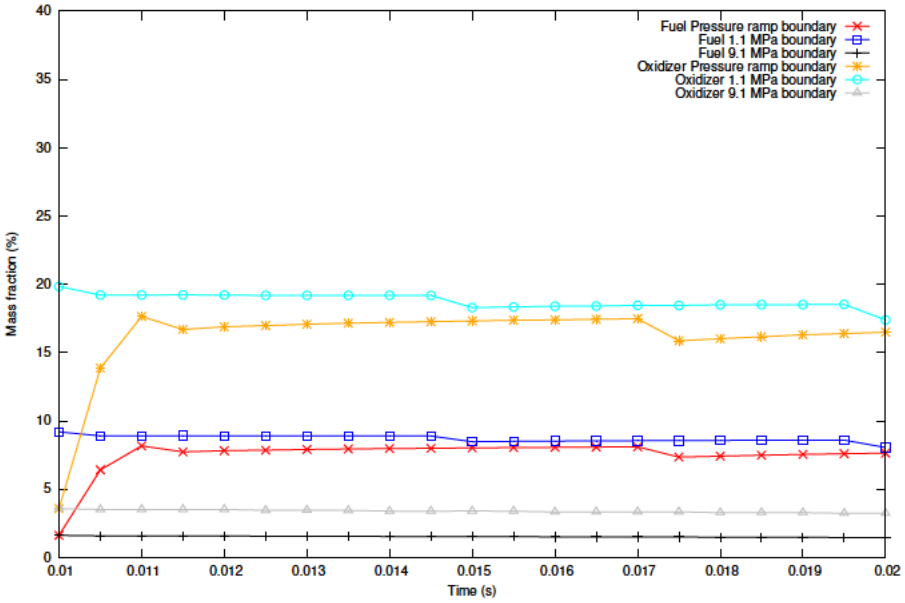

Figure 4.121: Fuel and oxidiser distribution for $P_3 = (950 \cdot 10^{-6}, 85{\cdot}10^{-6}, 85{\cdot}10^{-6})$.

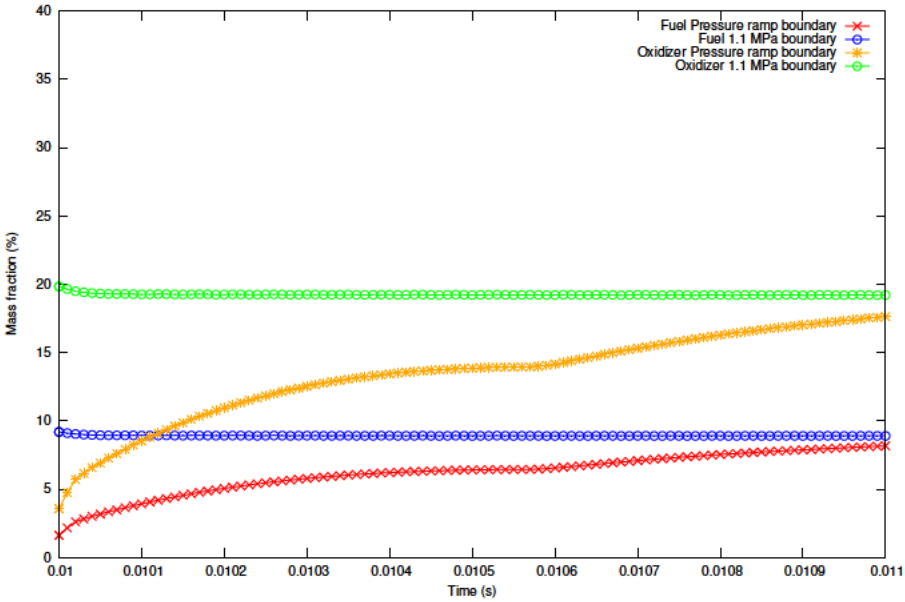

Figure 4.122: Fuel and oxidiser distribution for $P_3 = (950 \cdot 10^{-6}, 85{\cdot}10^{-6}, 85{\cdot}10^{-6})$.

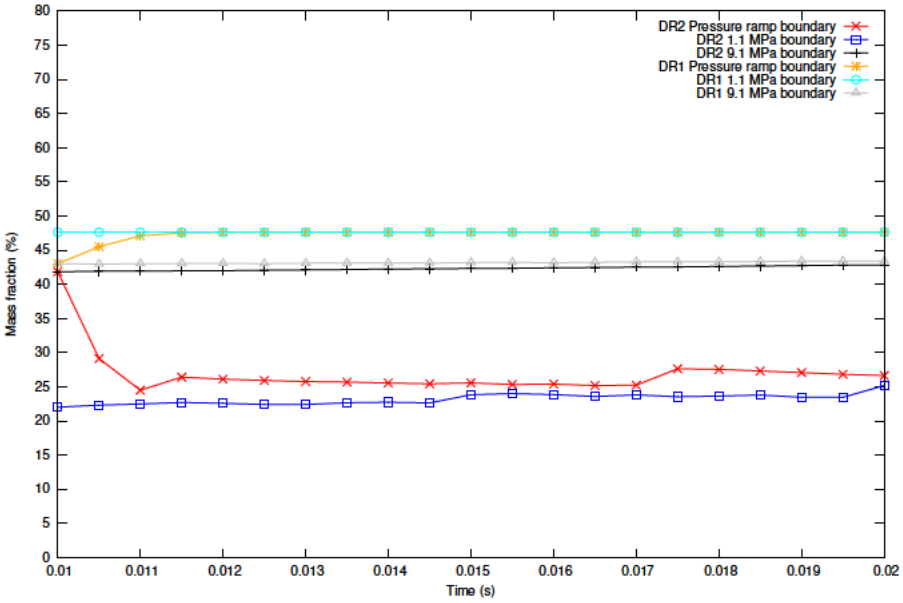

Figure 4.123: DR1 and DR2 distribution for $P_1 = (510 \cdot 10^{-6}, 85{\cdot}10^{-6}, 85{\cdot}10^{-6})$.

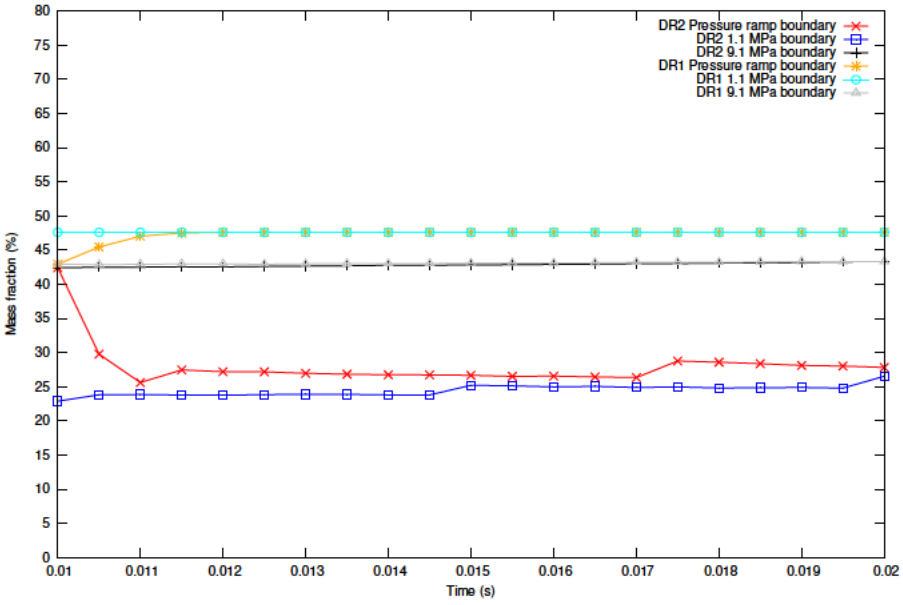

Figure 4.124: DR1 and DR2 distribution for $P_2 = (750 \cdot 10^{-6}, 85{\cdot}10^{-6}, 85{\cdot}10^{-6})$.

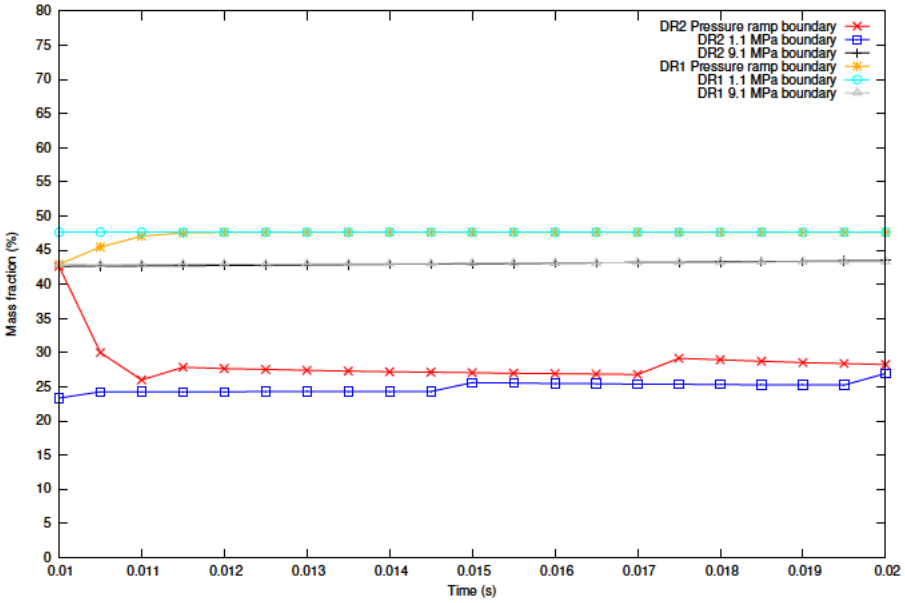

Figure 4.125: DR1 and DR2 distribution for $P_3 = (950 \cdot 10^{-6}, 85{\cdot}10^{-6}, 85{\cdot}10^{-6})$.

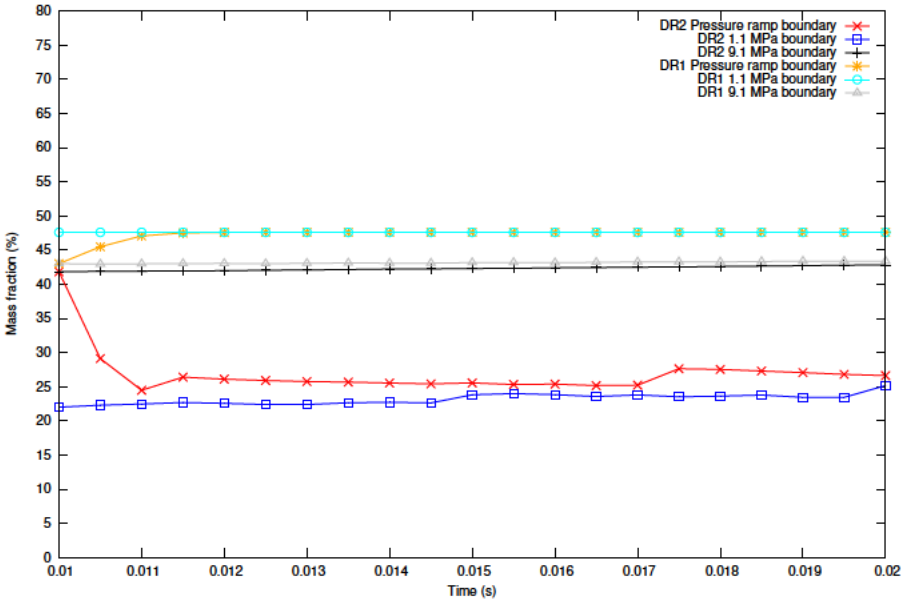

Figure 4.126: DR1 and DR2 distribution for $P_1 = (510 \cdot 10^{-6}, 85{\cdot}10^{-6}, 85{\cdot}10^{-6})$.

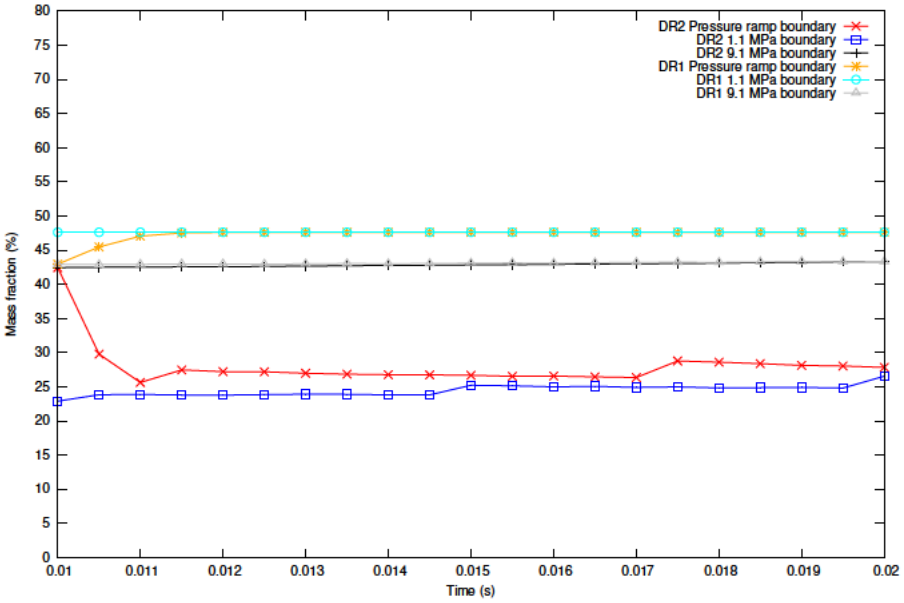

Figure 4.127: DR1 and DR2 distribution for $P_2 = (750 \cdot 10^{-6}, 85{\cdot}10^{-6}, 85{\cdot}10^{-6})$.

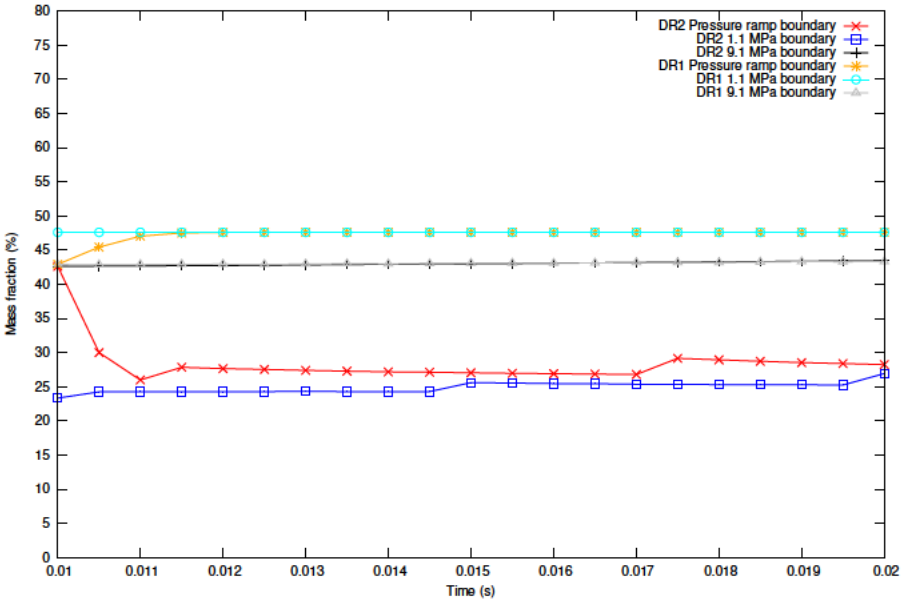

Figure 4.128: DR1 and DR2 distribution for $P_3 = (950 \cdot 10^{-6}, 85{\cdot}10^{-6}, 85{\cdot}10^{-6})$.

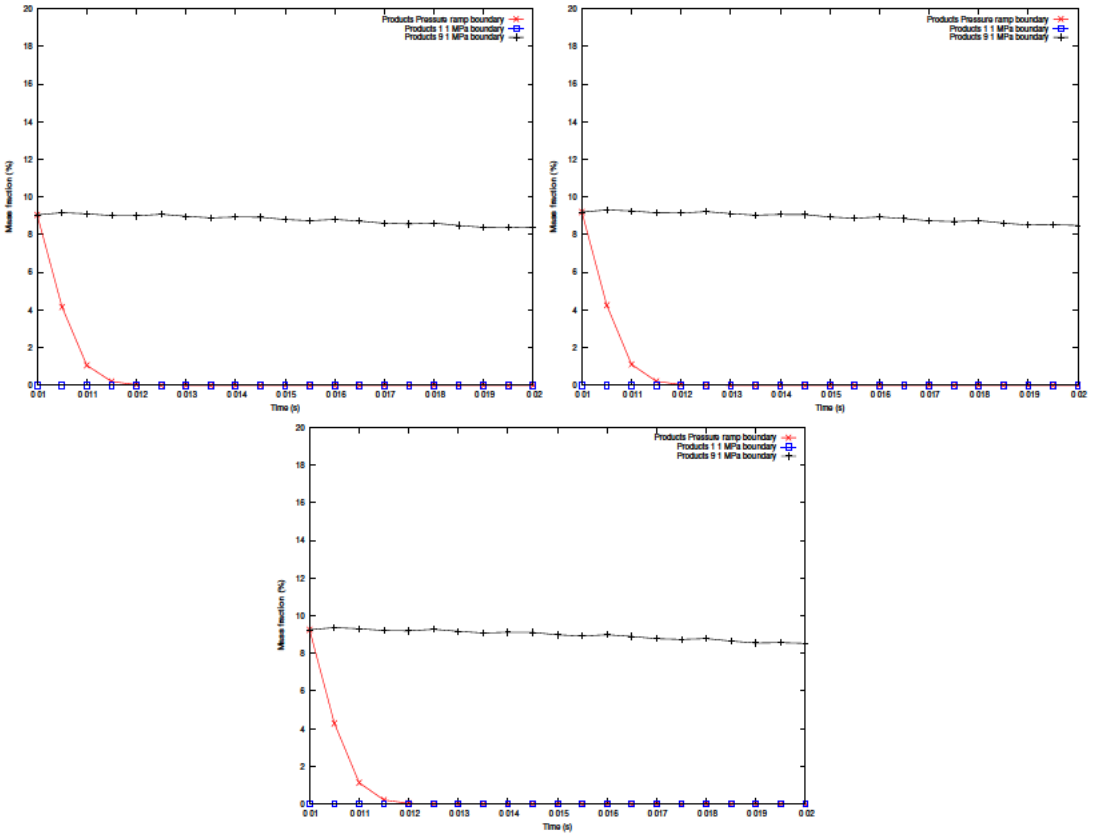

Figure 4.129: Products mass fraction distribution for P_1 (above-left), P_2 (above-right) and P_3 (below).

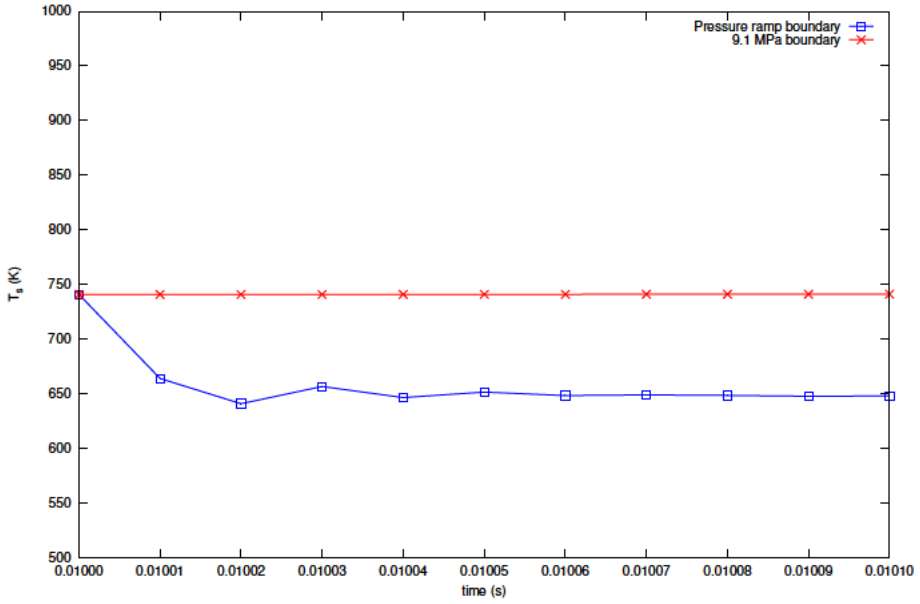

Figure 4.130: Temperature at the burning surface after applying depressurisation.

Finally, global temperature and heat flux variables are analysed. The variable global temperature, represents the temperature from condensed to gas domain and is depicted by using colour diagrams in Figures 4.131, 4.132 and 4.133. The first one of the three figures represents the evolution of the temperature just after the pressure ramp is applied to the right boundary. The other two figures compare the distribution of temperature obtained in each one of the three test considered in this subsection: 1.1 MPa and 9.1 MPa fixed boundary condition and ramp boundary condition. Figure 4.131 shows how the depressurisation provokes immediately a diffusion of the temperature along the condensed phase, phenomenon already seen in the previous subsection from Figure 4.93 to Figure 4.95. This behaviour can be easily seen thanks to Figures 4.132 and 4.133. The higher the pressure, the sharper will be the transition between cold condensed and hot gas temperatures.

Another effect that can be appreciated is the sharp fall of the maximum temperature (around 400 K) immediately after the time in which the pressure ramp is started; afterwards the value decrease smoothly. The differences obtained in the maximum values and the position evolution of the burning surfaces for each test is stated very clear in Figures 4.132 and 4.133. The burning surface for the depressurisation test is located between those of 1.1 MPa and 9.1 MPa fixed boundary condition and the maximum temperature is in between the ones obtained for these two tests too. In order to observe in detail the behaviour of the temperature, as done for pressure and for mass fraction distributions, the evolution of the temperature with the time at the three chosen three points has been represented from Figures 4.134 to Figure 4.139. As happened for the previous variables studied, the temperature for 1.1 MPa fixed boundary condition test measured at the point close to the burning surface present some fluctuations which decrease with the x-coordinate. However, and as was observed when analysing the pressure, this phenomenon does not take place when ramp boundary condition is applied. As has been already explained, the boundary surface for the pressure ramp test when time is equal to 0.01 s is located further from the one of 1.1 MPa fixed boundary condition since before the depressurisation is applied the pressure at the boundary is fixed 9.1 MPa. Figures 4.134, 4.136 and 4.138 show the same conclusion already extracted from Figures 4.132 and 4.133, the temperature suffers a sharp decrease when depressurisation is applied until reaching a value close to the one of 1.1 MPa boundary condition test.

By plotting the temperature from t = 0.01 s to t = 0.01001, the behaviour of the temperature just when depressurisation is applied can be studied in detail (see Figures 4.135, 4.137 and 4.139). As happened for the rest of the variables analysed, the temperature falls abruptly due to the pressure ramp at the end of the tube. After the fall, the temperature will fluctuate until t = 0.01001 from which it will experiment a soft increase until reaching the same value as the one obtained for the 1.1 MPa fixed boundary condition test. The behaviour is exactly the same for the three points but the fluctuations once the stability temperature is reached are more visible in the first point.

The last variable to be studied is the heat flux along the control volume which presents the expected behaviour after studying the rest of the variables. Figures 4.141 and 4.142 show how the maximum value obtained for heat flux when applying the pressure ramp test is in between the ones obtained for 1.1 MPa and 9.1 MPa fixed boundary condition. In addition, the light blue of the condensed phase, which indicates a transfer of heat in the condensed phase due to the progressive warming from the left side of the tube to the burning surface, is more visible for the distribution obtained in the ramp test than the one of 9.1 MPa but less than for 1.1 MPa. The fluctuation of the heat flux just after depressurisation is very well observed in Figure 4.140. The strong fall of pressure at the exit provokes a decrease of the heat flux between 0.01 s and 0.0101 s. After that interval of time, its maximum fluctuates until reaching a magnitude closer to the one obtained for 1.1 MPa fixed boundary condition test.

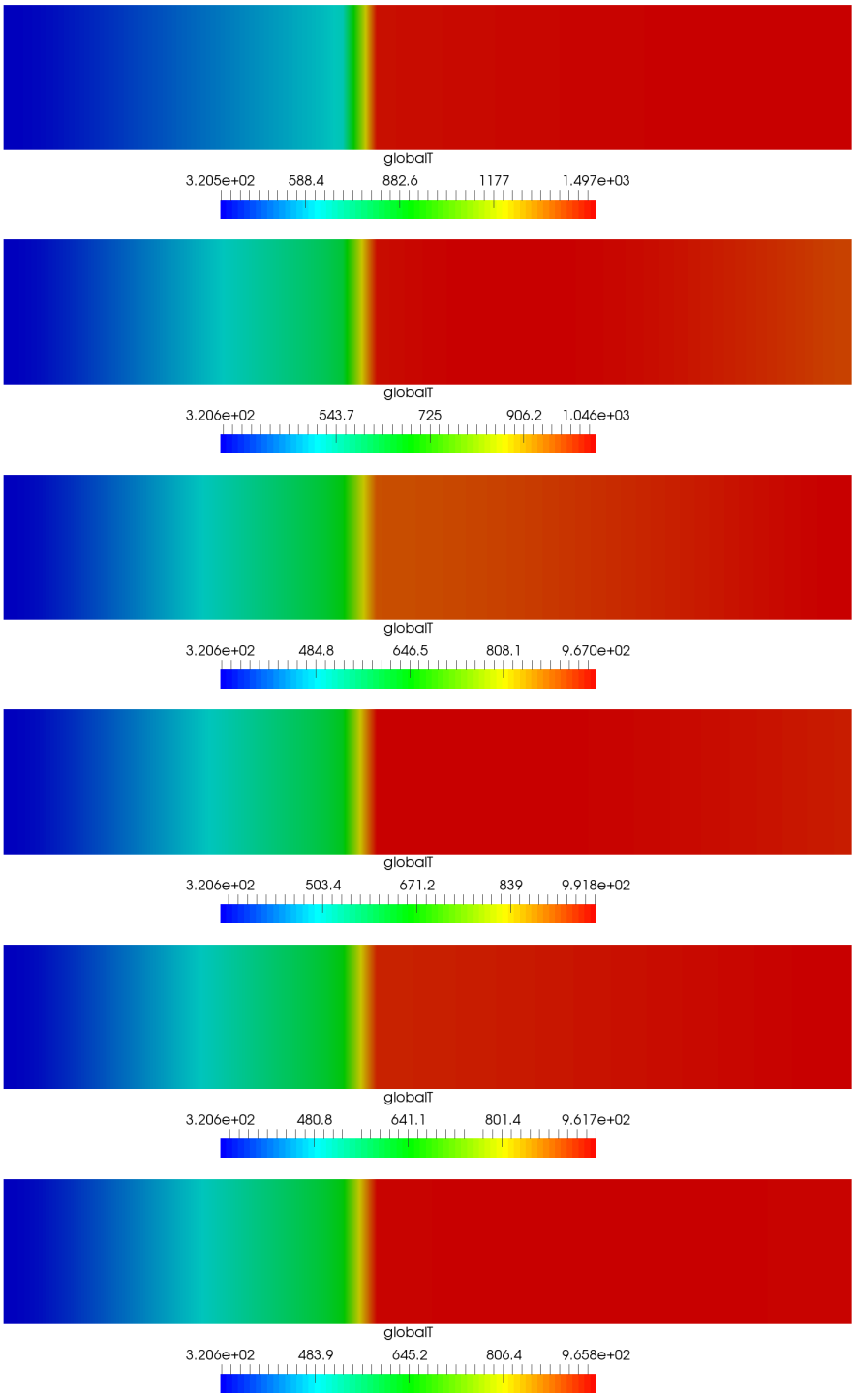

Figure 4.131: Global temperature distribution for t = 0.01000001, t = 0.01001 s, t = 0.01002, t = 0.01003, t = 0.001004 s and t = 0.01005 s (above-below).

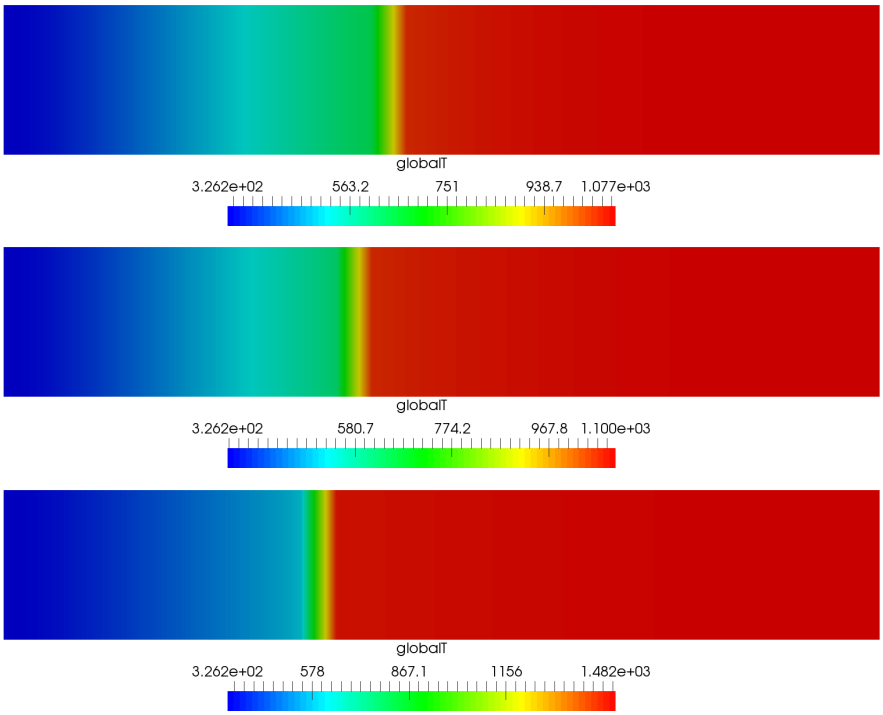

Figure 4.132: Global temperature distribution for fixed 1.1 MPa, ramp and fixed 9.1 MPa boundary conditions at t= 0.015 s (above-below).

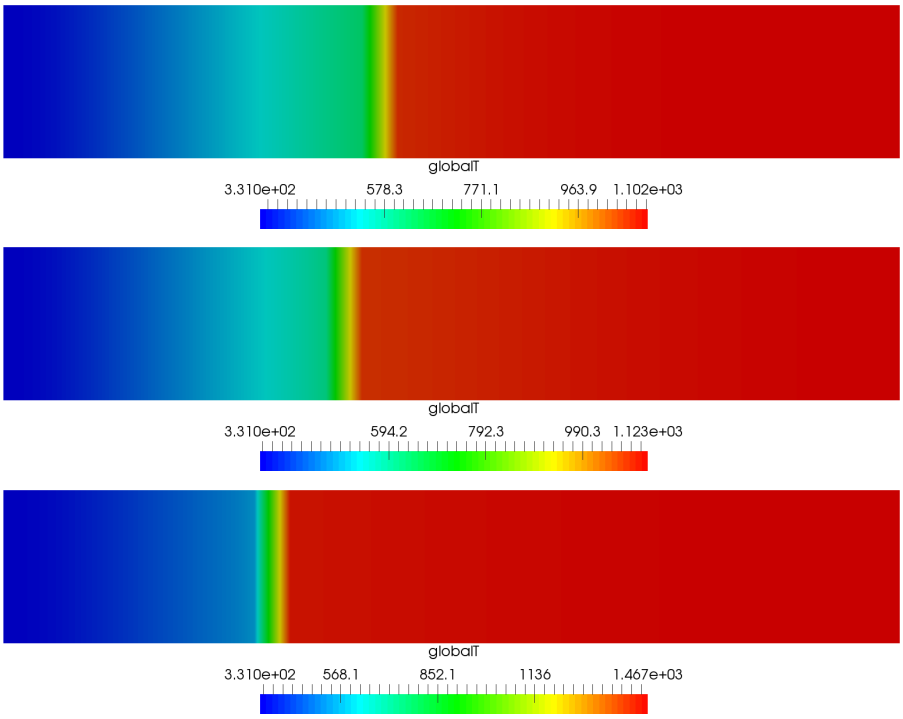

Figure 4.133: Global temperature distribution for fixed 1.1 MPa, ramp and fixed 9.1 MPa boundary conditions at t= 0.02 s (above-below).

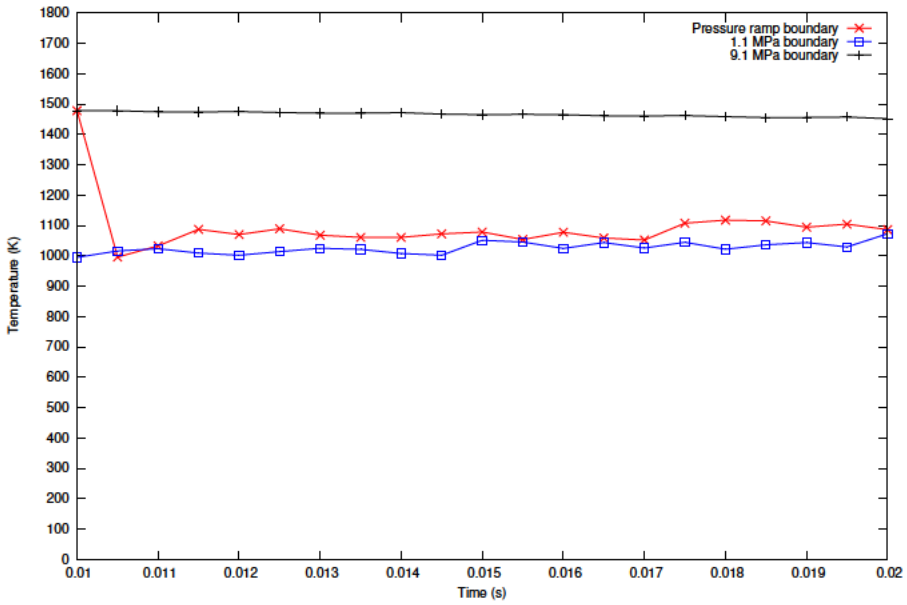

Figure 4.134: Temperature distribution for $P_1 = (510 \cdot 10^{-6}, 85{\cdot}10^{-6}, 85{\cdot}10^{-6})$ from t = 0.01 s to t = 0.02 s.

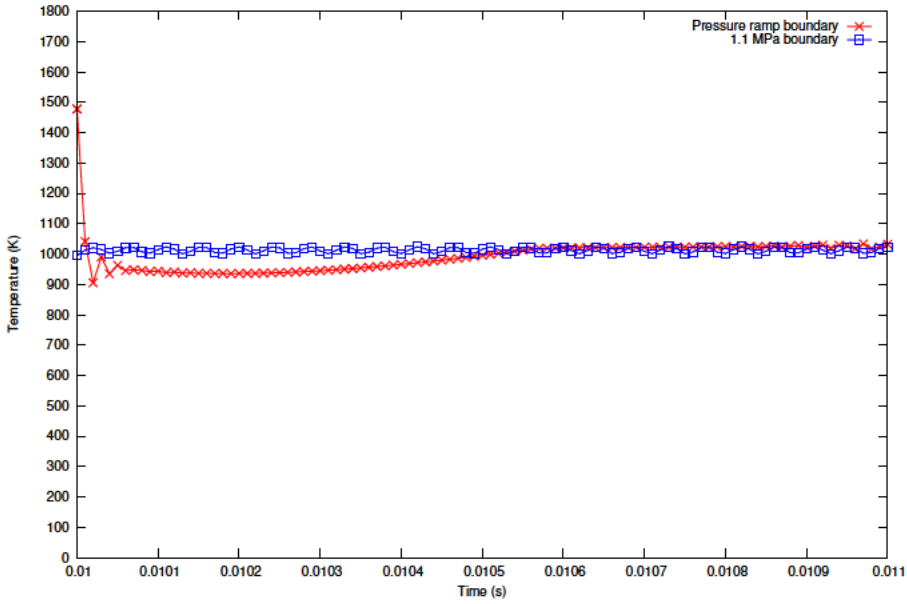

Figure 4.135: Temperature distribution for $P_1 = (510 \cdot 10^{-6}, 85{\cdot}10^{-6}, 85{\cdot}10^{-6})$ from t = 0.01 s to t = 0.01001 s.

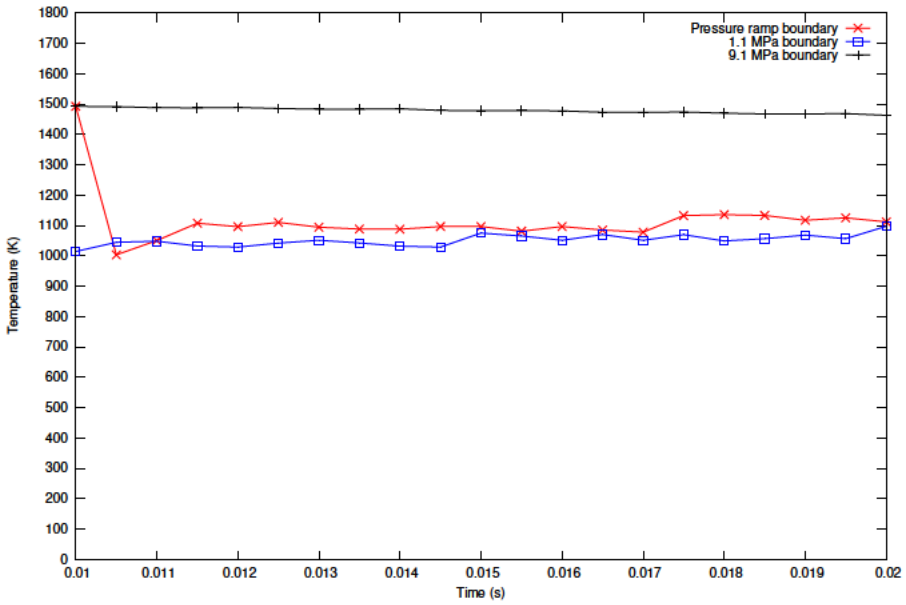

Figure 4.136: Temperature distribution for $P_2 = (750 \cdot 10^{-6}, 85{\cdot}10^{-6}, 85{\cdot}10^{-6})$ from t = 0.01 s to t = 0.02 s.

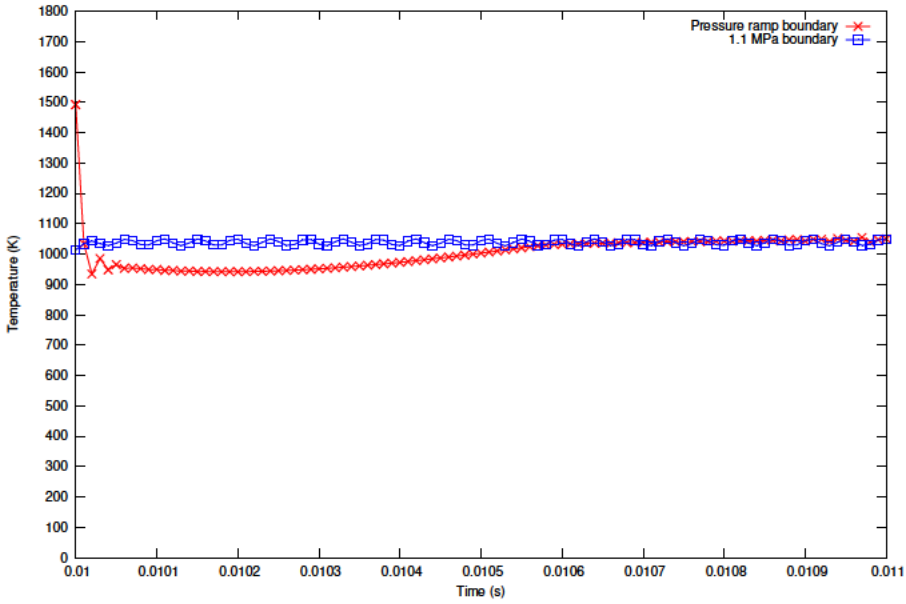

Figure 4.137: Temperature distribution for $P_2 = (750 \cdot 10^{-6}, 85{\cdot}10^{-6}, 85{\cdot}10^{-6})$ from t = 0.01 s to t = 0.01001 s.

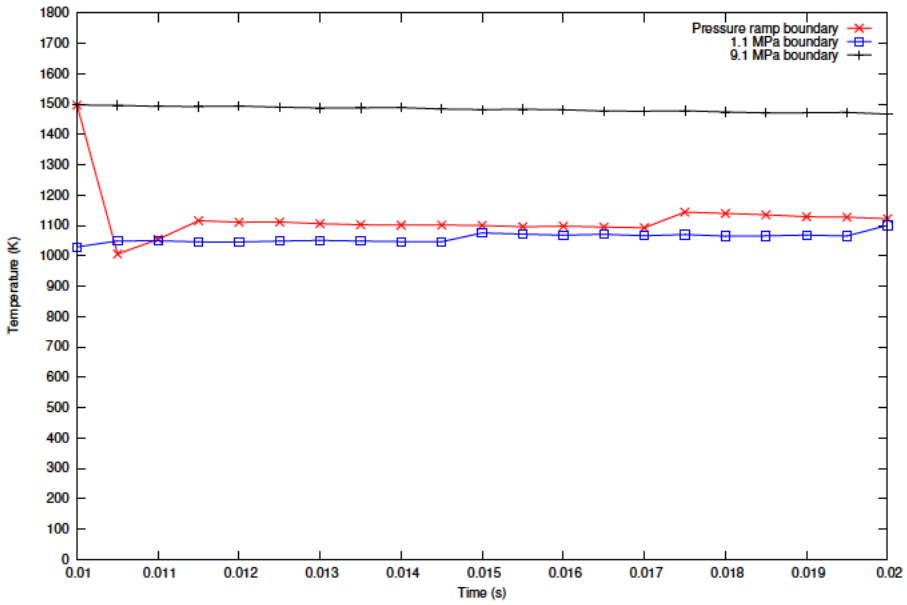

Figure 4.138: Temperature distribution for $P_3 = (950 \cdot 10^{-6}, 85{\cdot}10^{-6}, 85{\cdot}10^{-6})$ from t = 0.01 s to t = 0.02 s.

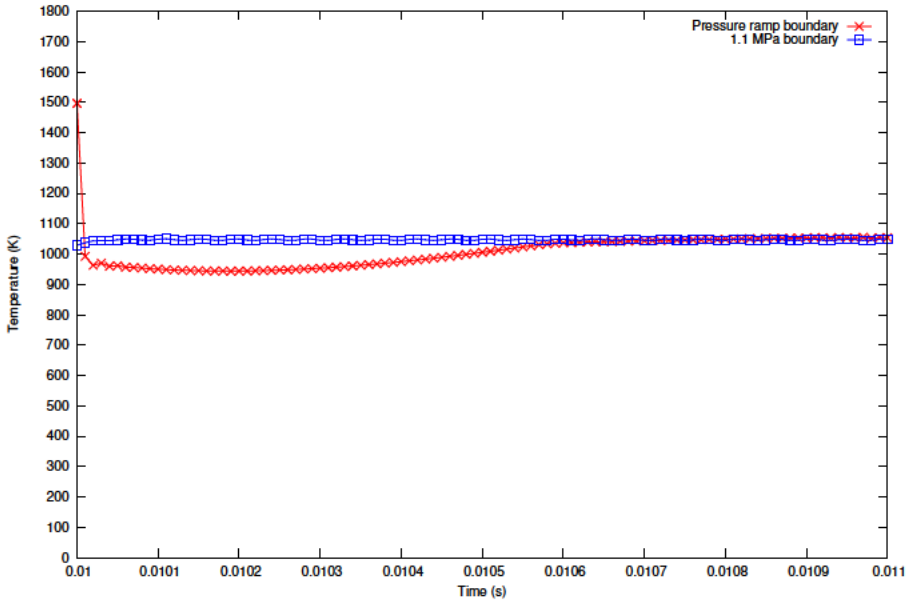

Figure 4.139: Temperature distribution for $P_3 = (950 \cdot 10^{-6}, 85{\cdot}10^{-6}, 85{\cdot}10^{-6})$ from t = 0.01 s to t = 0.01001 s.

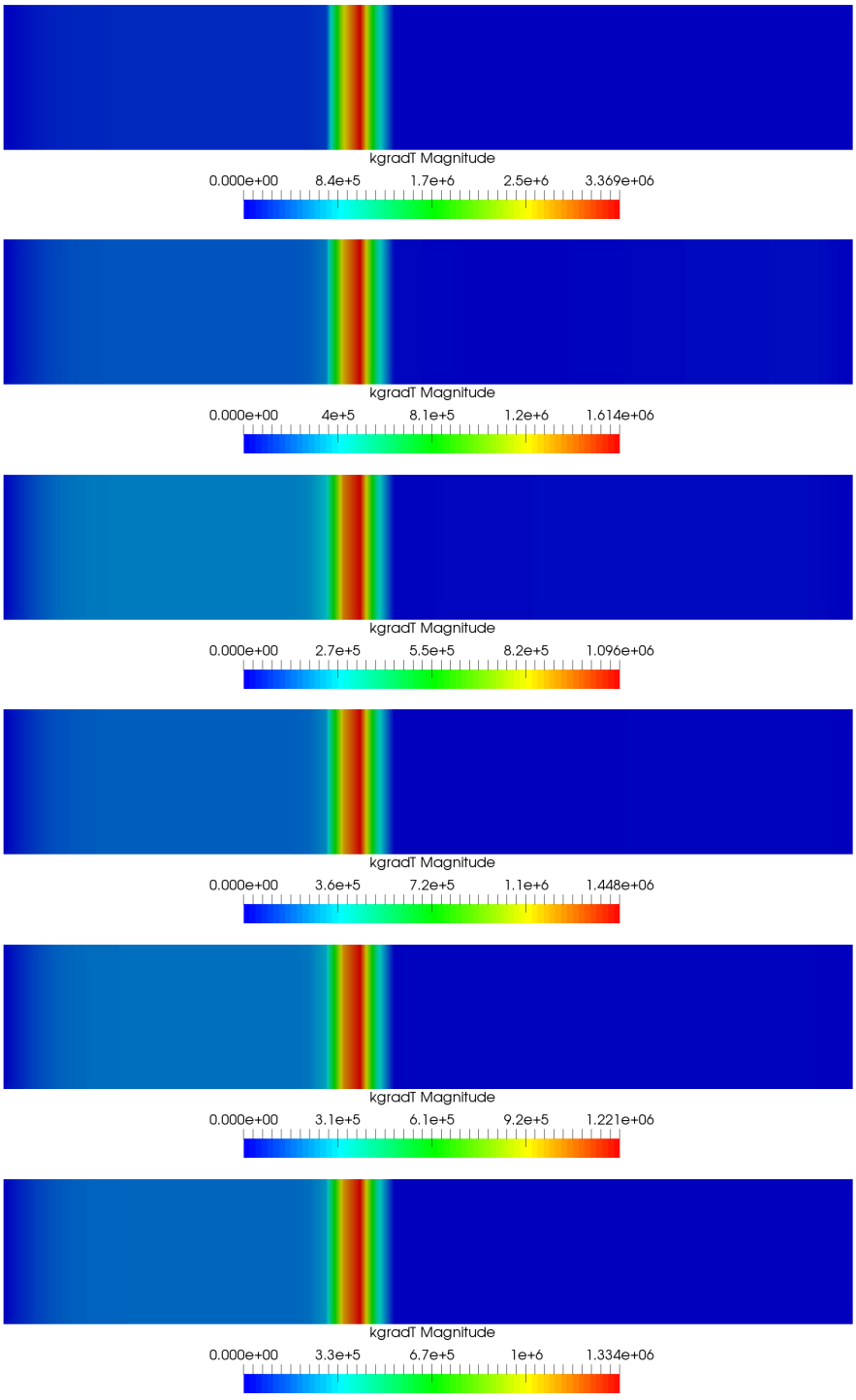

Figure 4.140: Heat flux distribution for t = 0.01000001, t = 0.01001 s, t = 0.01002, t = 0.01003, t = 0.001004 s and t = 0.01005 s (above-below).

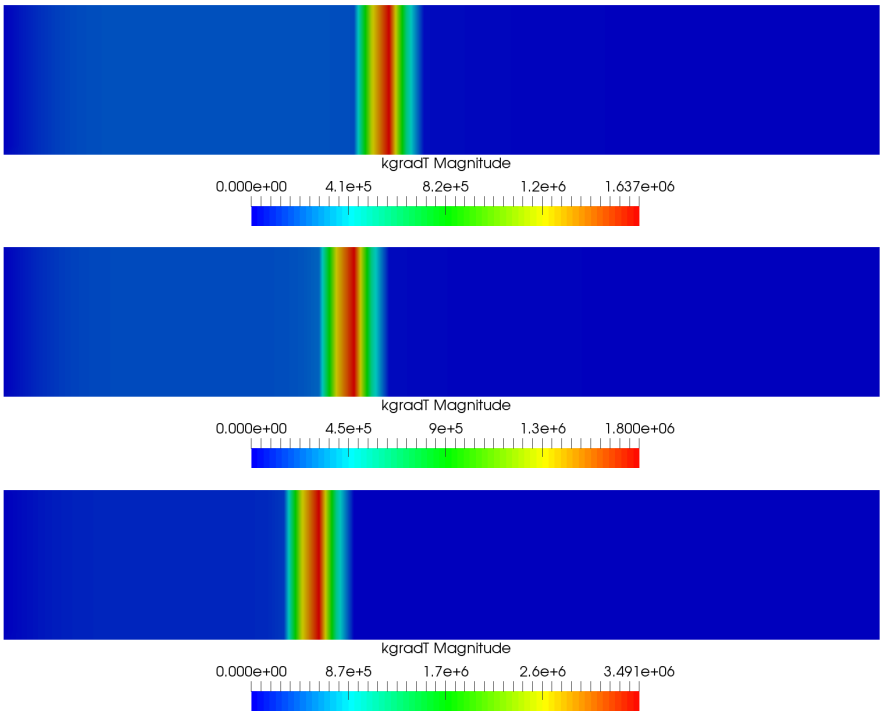

Figure 4.141: Heat flux distribution for fixed 1.1 MPa, ramp and fixed 9.1 MPa boundary conditions at t= 0.015 s (above-below).

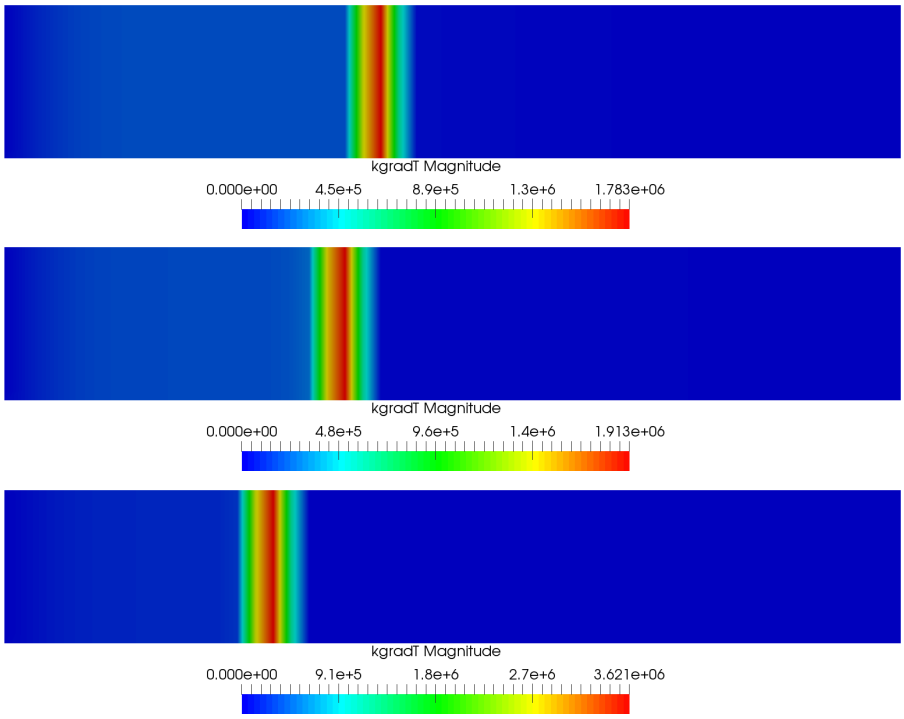

Figure 4.142: Heat flux distribution for fixed 1.1 MPa, ramp and fixed 9.1 MPa boundary conditions at t= 0.02 s (above-below).

4.3.4 Conclusions

The code to study the multidimensional modelling of unsteady combustion of AP/HTPB propellant, which uses Rusanov numerical scheme and first-order Euler method to solve the homogeneous differential equation system and source terms respectively, has been adapted to simulate the combustion of double-base propellants. The kinetics of the model is described by considering firstly, a change of phase of the solid propellant from condensed to gas and secondly, a reduced chemistry scheme which defines simplified chemical reactions to represent the combustion itself. To couple both processes, mass and species conservation, as well as temperature continuity are imposed in the burning surface in which the burning rate will represent a key factor. Moreover, an energy balance is also applied at the burning surface which represents that heat that the gas transfers to the burning surface is invested firstly, in raising the surface temperature to produce the phase change and secondly, in warming the condensed phase by conduction.

Firstly, and in order to validate the code, the problem of a homogeneous double-base strand combustion when pressure at the right boundary is fixed is performed obtaining positive results. The same geometry as that used to validate the code for AP/HTPB composite propellants in sandwich configuration is taken. In this case, the fuel and oxidiser will not be placed in layers, but they will distribute homogeneously along the condensed phase. Once this analysis is performed, the same geometry have been used to check how a depressurisation ramp affect to the combustion of double-base propellants.

For the first part of the analysis, the test has been run for a range of pressures from 1.1 to 9.1 MPa and the results of burning rate has been compared with those found in literature. Afterwards, the main variables o interest have been analysed observing the following conclusions:

1. The burning rate increases with the pressure. In addition, the adjustment between the results obtained with the model and the ones from literature depends on the initial distribution assumed for the temperature. The higher the temperature in the domain, the better adjustment between the calculated and the literature burning rate will be obtained at low and high values of fixed pressure but the worse for intermediate values of pressure range. Finally, temperature of 1100 K is the one chosen to present the results due to its better adjustment with bibliography results.

2. The higher the pressure, the quicker the condensed phase changes sublimates. However, the gas velocity presents its highest value for the lowest fixed pressure boundary condition. This could be due to he increment of the gas density with the pressure which leads to a reduction of the magnitude of the gas velocity field.

3. The evolution of the velocity with the time behaves different depending on pressure considered. For pressures between 3.4 MPa and 9.1 MPa, the maximum value of the velocity field remains almost constant for the time steps considered. However, in case of considering pressures between 3.4 and 1.1 MPa the maximum value of the velocity experiments an increment for the considered time steps. This phenomenon could happen because chemical reactions at low pressures need some time to be able to start and therefore, for the gas velocity to increase its value while at high pressures the reaction mechanism is activated from the very beginning of the combustion process.

4. Since the propellant is homogeneously distributed in the condensed phase, not only fuel but also oxidiser in gas phase are uniformly distributed too, not presenting local concentration of any of them, at happened when analysing AP/HTPB composite propellant combustion. Independently of the considered pressure, the highest amount of fuel and oxidiser is located close to the burning surface decreasing the mass fraction smoothly with x-coordinate. From this behaviour can be concluded that, when the propellant in condensed phase sublimates at the burning surface, it progresses along the control volume until reaching the end of the tube.

5. The maximum value of fuel mass fraction decreases slightly with the time. The increase of the time leads to a fall of the fuel mass fraction at the end of the tube. The same behaviour is

observed for the oxidiser mass fraction. Both, fuel and oxidiser, present an increment of their mass fraction maximum values with the fall of pressure, effect also observed when analysing the combustion of AP/HTPB composite propellant. Reaction rates of chemical kinetics depend on the density of the gas therefore, the higher the pressure, the higher the density and the higher reaction rate will be obtained. A raise of the reaction rate means an increment in the consumption of fuel, oxidiser and intermediate products. Therefore, since at low pressures the combustion of fuel and oxidiser is lower, the mass fraction of both will increase.

6. Final products mass fraction increases with the pressure, which means that, the reaction rates of reaction 2 (R2), reaction 3 (R3) or both increase at high pressures. On the one hand, as expected and explained in the previous conclusion, the mass fraction of DR1 increases with the fall of pressure. That means that the higher the pressure, the higher reaction rate of reaction 2 and therefore, the higher amount of DR1 will react to become final products. On the other hand, DR2 is produced in the reaction of fuel and oxidiser (R1) and consumed when it changes to final products (R3). The overall result is the increase of DR2 mass fraction with the pressure. However, the maximum value of mass fraction at 9.1 MPa experiments a slight decrement. This could be due to the fact that, since reaction rates get stronger with the increase of pressure, at 9.1 MPa, the reaction rate of R3 provokes a consumption of DR2 enough to decrease the content produced in R1.

7. Final products mass fraction increase with the time. However, when pressure is fixed between 9.1 MPa to 5.99 MPa, the mass fraction of final products decreases slightly from 0.01 s to 0.02 s (first slot) and raises between 0.02 s and 0.05 s (second slot). This could be explained by taking into account that final products are the result of R2 and R3 and R3 depends strongly on R1. DR1 mass fraction value is constant in the first slot and decreases in the second one. This means that reaction 2 needs some time to increase their effect. Moreover, two phenomena are observed. On the one hand, at high pressures, the mass fraction of DR2 increases slightly in the first time slot while decreasing in the second one. On the other hand, at low pressures, DR2 mass fraction increases with the time which means that, during the first slot, reaction 1 produces more intermediate species than reaction 3 can consume and therefore, there is an increment of DR2 mass fraction. The same is happening at high pressures for the first time slot. However, between 0.02 s and 0.05 s, the amount of DR2 mass fraction when pressure is high suffers a decrement. Since during the second time slot and the pressure fixed is high there is a strong increment of the final products mass, it can be concluded that, reaction 3 increase its strength with pressure and time.

8. The temperature increases with pressure. Moreover, the lower the pressure, the softer is the transition between minimum and maximum temperature. However, as the time passes, the jump between hot temperature in the gas phase and cold temperature in the condensed phase becomes more abrupt which means that, the transference of heat in the solid increases with the fall of pressure and decreases when the time passes.

9. Temperature increases with time. This effect seems to be more visible at low than at high pressures.

10. The heat flux increases with the pressure and with the time. The greatest amount of heat is transferred in the burning surface between the solid and the gas. Being the expected result to observe since the variable is defined as the thermal conductivity multiplied by the temperature gradient. The value along the rest of the control volume remains very low or even zero.

To conclude, as it was done for AP/HTPB composite propellant, a depressurisation ramp is applied to the right side of the control volume using the same geometry than the one chosen for the previous test. The ramp is designed to decrease the pressure from 9.1 MPa to 1.1 MPa in $1 \cdot 10^{-8}$ s starting at 0.01 s. Besides the render views provided by ParaView software, in order to observe properly how the pressure ramp affect to the behaviour of the variables of interest, three points in the geometry

have been chosen to plot the variables. The first point chosen is located close to the burning surface of the 1.1 MPa fixed boundary case when time is equal to 0.01 seconds, the second one is located at the middle of the initial gas domain and the third one almost in the end of the gas zone. The main conclusions extracted from the simulation are the following:

1. The pressure wave due to depressurisation evolves from the right side of the tube until the burning surface and afterwards, it comes back to the right side. This movement is repeated until reaching the equilibrium pressure of 1.1 MPa.

2. The pressure at $P_1(x = 510{\cdot}10^{-6}\ m)$ when pressure is fixed to 1.1 MPa at the right boundary fluctuates around this value. However, the pressure at the same point for the 9.1 MPa fixed boundary condition test remains stable. This is be explained due to the distance between the first point and the burning surface. When the pressure in the boundary is fixed to 1.1 MPa, the boundary is located close to P_1 while when the pressure fixed at the boundary is 9.1 MPa, the burning surface is located further, closer to the left boundary. Therefore, the further from the burning surface the pressure is measured, the more stable will be the pressure. The cells close to the burning surface are the first to receive the sublimated gas species from the burning surface and, as a result, the fuel, oxidiser and intermediate species combust firstly in these cells. Therefore, the density of cells located close to the burning surface will fluctuate and that will influence to the temperature and pressure distributions.

3. When a pressure ramp is applied to the right boundary the domains suffers a sharp decrease of pressure. Afterwards, the pressure value at $P_1(x = 510{\cdot}10^{-6}\ m)$ oscillates around 1.1 MPa reaching even lower pressure values. Therefore, a strong pressure jump applied at the exit of the chamber leads to an immediate depressurisation in the cells close to the burning surface even lower than the minimum value of the pressure step. Once the pressure reach 1.1 MPa of stable pressure, the fluctuations observed when applying 1.1 MPa fixed boundary condition are less visible. The reason of this phenomenon is attributed again to the position of the burning surfaces for the different tests. Before suffering depressurisation, the pressure of the ramp test was fixed to 9.1 MPa, as a consequence, when time is equal to 0.01 seconds its burning surface is located in the same position far from point one.

4. Depressurisation provokes immediately a diffusion of the temperature along the condensed phase. The higher the pressure, the sharper will be the transition between cold condensed and hot gas temperatures.

5. Just after depressurisation, fuel and oxidiser mass fraction increase their values. DR1, remains almost constant but with a slight increment of concentration while DR2 and final products mass fractions decrease. As has been already explained, the magnitude of the mixture density is smaller for low than for high pressures. Since the reaction rates which represent the chemical kinetics of the combustion process depend on the density, with the fall of pressure, the reaction rates decrease too. As a result, when depressurisation is applied, not only less fuel and oxidiser react to form intermediate product DR2, but also less DR1 and DR2 change to become final products. The sublimation of condensed phase and the decrease of reaction rates are the reason of the increment of fuel, oxidiser and intermediate products DR1. As a result, there creation of new final products will fall down and part of them will be lost by the exit of the tube concluding in a reduction of their mass fraction. The same phenomenon is suffered by intermediate specie DR2 just after depressurisation until time is equal to 0.001004 s. At this time pressure stabilised to 1.1 MPa and therefore, the mass fraction of DR2 remains almost constant too.

6. Fuel and oxidiser mass fraction distributions behave exactly the same. At the beginning the values obtained are the same than those obtained for 9.1 MPa fixed boundary condition. However, when depressurisation is applied, the mass fractions of fuel and oxidiser start to increase until reaching the values obtained when 1.1 MPa fixed boundary condition is applied. This could happen because an increase of pressure leads to a gain in strength of reaction 1 and therefore,

to the fall of fuel and oxidiser mass fraction which react to provide intermediate specie DR2. When depressurisation is applied, reaction 1 loses strength and as a result, the mass fraction of fuel and oxidiser increase.

7. Before depressurisation is applied, the values of fuel and oxidiser mass fractions obtained for the ramp test are the same than those obtained for the 9.1 MPa fixed boundary test. However, when depressurisation is applied, fuel and oxidiser mass fractions start to increase until reaching the values obtained for the 1.1 MPa fixed boundary test. In addition, DR2 and final products increment their concentration while DR1 falls down in order to match the values of the 1.1 MPa fixed boundary test.

8. At the beginning, the temperature at the surface has the same value than that obtained at 9.1 MPa fixed boundary condition. When the depressurisation is applied, the temperature at the surface suffers a sharp decrement fluctuating slightly and afterwards, it remains around 650 K.

9. The maximum temperature of the control volume falls sharply immediately after the pressure ramp at the boundary is applied. Afterwards, it fluctuates until t = 0.01001 s, time from which it will experiment a soft increase until reaching the same value as that obtained for the 1.1 MPa fixed boundary condition test.

10. The temperature for 1.1 MPa fixed boundary condition test measured at the point close to the burning surface presents some fluctuations, phenomenon which does not take place when ramp boundary condition is applied since its boundary surface when time is equal to 0.01 s is located further from the one of 1.1 MPa fixed boundary condition test.

11. The maximum value obtained for heat flux when applying the pressure ramp test is in between those obtained for the 1.1 MPa and the 9.1 MPa fixed boundary tests. The heat flux, as the other variables, presents fluctuations immediately after the applying depressurisation. The strong fall of pressure at the exit provokes a decrease of the heat flux between 0.01 s and 0.0101 s. After that interval of time, its maximum fluctuates until reaching a magnitude closer to the one obtained for 1.1 MPa fixed boundary condition test.

Chapter 5

Conclusions

The improvement on the design and safety in industrial processes which use solid propellants are of major importance in industry of energetic materials. That is the reason why, modelling the combustion of solid propellants is a key problem that has focused the interest of several researchers over the years.

The main objective of this thesis have been the study of the combustion of granulated, composite and double-base solid propellant. In order to reach this target a literature review have been performed for each propellant in the first place and in the second place, numerical codes have been developed to characterise their combustion. Finally, the models developed have been validated, either with the results obtained by other researchers of the existing literature or with experimental data.

Specifically, the objectives of the thesis could be classified in two, depending on the solid propellant. The first one is to improve the understanding and modelling of the deflagration-to-denotation (DDT) phenomenon in granular beds of solid propellants. In order to reach this, a tool which provides the characterisation of the combustion process has been developed. In addition, the results obtained have been compared with those available in the existing literature to assess the effectivity of the model to predict the early stages of transient combustion processes. The second objective is the study of composite and double-base propellants and the characterisation of their unsteady combustion. In this case, a multi-dimensional code which solves the set of differential equations for condensed and gas phases have been programmed in OpenFoam. Finally, the results obtained for the combustion simulation of both propellants have been compared against experimental tests and results from existing literature. As a result, a tool which predicts composite and double propellant combustion behaviour in multidimensional scenarios with transient environmental conditions has been developed.

The main conclusions obtained after the modelling of each propellant are summarised throughout this chapter.

5.1 Granulated propellant

Ignition and subsequent combustion of those propellants are complex mechanisms of high importance in the manufacturing process of many energetic materials. Therefore, and in order to properly understand this problem, a two-phase model for the characterisation of the detonation process of granular solid propellants under shock tube conditions is developed. Conservation equations of mass, momentum and energy for both phases together with the constitutive relations for mass generation, drag force, interface heat transfer and particle-particle form the already mentioned model.

The model has been programmed in C++ and the homogeneous system of differential equations which considered both, gas and solid phase, is solved by using Rusanov and MacCormack-TVD numerical schemes. In addition, first-order Euler method has been used to solve the ordinary differential equations which include the source terms.

Firstly, a sensitivity analysis is performed to determine the effect that Nusselt number, friction coefficient and initiation conditions have in the results. The analysis have been performed using both, Rusanov and MacCormack numerical schemes. Due to the capacity of reproducing very similar results between both numerical schemes and the good behaviour at a wide range of Reynolds number, the Nusselt number and friction coefficient presented by Butler et al. [39] in their work will be adopted afterwards for calculation.

Although the authors consider a small zone of the control volume already initiated, each one applies different values of pressure and temperature as initial conditions of the test. As a result, high differences in the results can be obtained depending on the initial values assumed for the variables. Therefore, and in order to find to validate the model with literature values, the distributions of pressure, porosity and gas and particle temperatures provided by Hoffman and Krier [28] at 20 μs, have been used as initial conditions for the calculations performed afterwards.

Once initial conditions and source terms are defined, two different models have been used to calculate pressure, temperature and porosity distributions. The first model which have been studied considers the modification of the particle momentum governing equation done by Hoffman and Krier [28]. According to the author, this modification prevents the porosity from reaching values below the minimum value of compaction that packed beds of spherical particles can reach. However, a non-realistic value of particle temperature has been obtained as a result of applying this model. The second model which has been studied does not consider the porosity limiter from Hoffman and Krier [28] performing the limitation of the porosity directly in the code. The magnitude of the values which have been obtained for the main variables of interest are similar to those found in literature. Moreover, the results obtained using Rusanov scheme agree well with those resulting of applying MacCormack-TVD numerical scheme. However, the distribution of the variables are displaced in x-direction respect those from literature. These differences could be due on the one hand, to the initial values of the parameters chosen as initial conditions which highly determine the x-location of the peak values for all variables and on the other hand, due to the lack of all necessary input data in a single work from bibliography making necessary the values from different works increasing the difficulty of reproducing the tests available in the bibliography.

Finally, it can be concluded that, despite the difference in the x-location peak values, the last model considered represents accurately the physical behaviour of the propellant combustion for all variables of interest becoming a predictive tool for the characterisation of the early stages of the detonation process of granular solid propellants.

5.2 Composite AP/HTPB propellant

Modelling the combustion of composite and double-base propellants has also been of high interest for researchers not only in terms of safety but also with the ambition of optimising chemical composition to fulfil industrial requirements, to improve propellant design as well as for development and testing activities. Therefore, in this work, a code to study the multidimensional modelling of unsteady combustion of AP/HTPB propellants has been developed in OpenFoam. The code employs Rusanov numerical scheme to solve the homogeneous system of differential equations and afterwards, a first-order Euler methods to solve the ordinary differential equations including the source terms.

The first step which has been done to validate the code is to perform a test which simulates the problem of combustion of a homogeneous AP/HTPB strand in a Crawford bomb strand burner. The simulation assumes that the tube is insulated and there is no transference of mass or energy in any boundary despite the right cross-section which is open to atmosphere. The simulation has been performed twice by fixing the pressure at the right boundary to 4 MPa and 7 MPa. The values obtained for the burning rate have been compared against experimental data from INTA facilities [86] positive results.

Once this analysis has been concluded, the configuration of the binder and the oxidiser is changed from a homogeneous strand to a geometry in which a layer of AP is located in between two layers of HTPB, called sandwich configuration. In this case, the condensed control volume presents two

different regions, one containing AP and other of HTPB, which have different thermophysical properties. As in the Crawford Strand Burner test, the simulation assumes that the tube is insulated and there is no transference of mass or energy in any boundary despite the right one which is open to atmosphere. The pressure at the right side of the tube has been fixed for this test and a range of pressures between 0.5 MPa to 7 MPa have been tested. The main conclusions extracted from the analysis can be summarised in the following lines:

1. The burning rate results obtained with the developed two-dimensional model of this work applied to the combustion of AP/HTPB composite propellant in sandwich configuration agree well with the experimental ones from Kohga [51] for the considered pressure range.

2. The higher the pressure, the lower the gas velocity is obtained. This behaviour may be due to the increase of the gas density with the pressure. However, it has also been observed that an increase of AP mass fraction close to the burning surface leads to a local raise of the gas velocity. This behaviour is attributed to the relationship between burning rate and gas velocity at the burning surface.

3. AP mass fraction presents a local concentration in the cells close to burning surface which has not an uniform distribution along the tube like it happens for HTPB. Since the activation energy that the oxidiser needs to be decomposed is not high, compared with the one from HTPB, it could be deduced that, as soon as condensed AP sublimates to AP in gas phase, the first reaction takes place and most of the AP is decomposed in reaction products. However, binder combustion reaction not only presents a higher activation energy, but also needs the products from the first reaction to take place. This could lead to the conclusion that when HTPB sublimates to gas, it does not burn immediately and therefore, it has enough time to spread along the gas domain making possible for the cells far from the burning surface to accumulate higher concentrations of binder than oxidiser.

4. The content of AP and HTPB in gas phase multiplies with the pressure decrement. This could be assigned to the dependency of reaction rates expressions with the pressure. A large value of reaction rates means that the consumption of both, binder and oxidiser, will be high. Therefore, it has been concluded that high pressures increase the reaction rate leading to a consumption of propellant mass fraction.

5. The diffusivity of AP increases at low pressures. However, it has been observed that at 0.5 MPa, both binder and oxidiser mass fractions present a nonuniform distribution with higher concentrations in the cells of gas adjacent to their condensed phases respectively. This could happen because at low pressures, the degradation of the propellant is less intense and, in addition, R1 and R2 reaction rates of decrease. Therefore, the combustion of AP and HTPB in the cells close to the burning surface is reduced increasing as a result the mass fractions of binder and oxidiser in these cells.

6. The value of constant temperature in gas phase increases slightly with the fall of pressure fixed at the right boundary. The fall of pressure provokes a decrease of reaction rates and therefore, there is a decrement in the combustion of AP and HTPB. As consequence of the loss of strength of AP and HTPB combustion reactions, the concentration of the reaction products (HCl, CO_2, H_2O N_2) decreases mildly too. The slight decrement of the reaction products mass fractions is enough to make the density decrease its value provoking an increment the temperature.

Finally, the combustion simulation of AP/HTPB composite propellant in sandwich configuration has been performed applying a depressurisation ramp from 7 MPa to 0.5 MPa during a short interval of time at the open side of the tube in order to see how it influences in the main variables of interest. The conclusions obtained are the following:

1. The pressure ramp induced at the right boundary leads to a decrease of the pressure value below 0.5 MPa at the cells located in the middle of the tube. Therefore, it has been concluded that when the end of the chamber is put down to a rapid depressurisation the pressure wave evolves from the end to the beginning of the gas control volume and comes back causing a depression under 0.5 MPa.

2. The fall of pressure provoked by the depressurisation at the boundary leads to an increase of both AP mass fraction and its diffusivity.

3. Together with the sharp fall of pressure, comes a raise of HTPB mass fraction. Since the depressurisation at the boundary provokes a fall of pressure close to the burning surface even below 0.5 MPa, the value of HTPB mass fraction increases over the one obtained for the 0.5 MPa fixed boundary test. The mass fraction values obtained for both tests come closer as the pressure for the pressure ramp boundary condition test becomes closer to 0.5 MPa.

4. The immediate effect of the sharp fall of pressure at the end of the tube is the decrease of the temperature at this location as could be expected by taking into account ideal gas law. Afterwards, temperature raises again remaining mostly stable. The highest value of temperature reached at the end of the tube is that obtained when fixing the pressure at the right boundary to 0.5 MPa followed by the depressurisation test and finally, the value obtained for the 7 MPa fixed boundary test. Since the reaction rates depend on the pressure, the lower the pressure, the lower reaction rate. This leads to a decrease of the reaction products mass fractions with the consequent decrease of density and therefore, an increment of temperature. The temperature obtained when pressure is fixed to 0.5 MPa at the right boundary is slightly higher than that of the depressurisation test. This happens because before applying the pressure ramp at the right boundary, the pressure is fixed to 7 MPa and therefore, its density is higher than in 0.5 MPa test.

5. When depressurisation is applied, the burning rate decreases reaching a value even lower than that obtained for the 0.5 MPa fixed boundary test. Sharp depressurisation at the boundary leads to obtaining lower values of pressure closer to the burning surface than the ones obtained by fixing the pressure to 0.5 MPa. Since burning rate is directly related with the pressure, together with a decrease of pressure below 0.5 MPa, a fall of the burning rate below the value obtained for 0.5 MPa fixed pressure test will come.

5.3 Double-base homogeneous propellant

The combustion modelling of composite and double-base propellants has been of high interest for researchers in the latest years. Therefore, in this work, the code to study the multidimensional modelling of unsteady combustion of AP/HTPB propellant, has been adapted to simulate the combustion of double-base propellants.

Firstly, and in order to validate the code, the problem of a homogeneous double-base strand combustion when pressure at the right boundary is fixed is performed obtaining positive results. The same geometry as that used to validate the code for AP/HTPB composite propellants in sandwich configuration is taken. In this case, the fuel and oxidiser will not be placed in layers, but they will be distributed homogeneously along the condensed phase. The main conclusions are the following:

1. The burning rate increases with the pressure.

2. The gas velocity presents its highest value for the lowest fixed pressure boundary condition. This could be due to he increment of the gas density with the pressure which leads to a reduction of the magnitude of the gas velocity field.

3. The evolution of the velocity with the time behaves different depending on pressure considered. For pressures between 3.4 MPa and 9.1 MPa, the maximum value of the velocity field remains almost constant for the time steps considered. However, in case of considering pressures between 3.4 and 1.1 MPa the maximum value of the velocity experiments an increment for the considered time steps. This phenomenon could happen because chemical reactions at low pressures need some time to be able to start and therefore, for the gas velocity to increase its value while at high pressures the reaction mechanism is activated from the very beginning of the combustion process.

4. The maximum value of fuel mass fraction decreases slightly with the time. The increase of the time leads to a fall of the fuel mass fraction at the end of the tube. The same behaviour is observed for the oxidiser mass fraction. Both, fuel and oxidiser, present an increment of their mass fraction maximum values with the fall of pressure, effect also observed when analysing the combustion of AP/HTPB composite propellant. Reaction rates of chemical kinetics depend on the density of the gas therefore, the higher the pressure, the higher the density and the higher reaction rate will be obtained. A raise of the reaction rate means an increment in the consumption of fuel, oxidiser and intermediate products. Therefore, since at low pressures the combustion of fuel and oxidiser is lower, the mass fraction of both will increase.

5. Final products mass fraction increases with the pressure, which means that, the reaction rates of reaction 2 (R2), reaction 3 (R3) or both increase at high pressures. On the one hand, the mass fraction of DR1 increases with the fall of pressure. That means that the higher the pressure, the higher reaction rate of reaction 2 and therefore, the higher amount of DR1 will react to become final products. On the other hand, DR2 is produced in the reaction of fuel and oxidiser (R1) and consumed when it changes to final products (R3). The overall result is the increase of DR2 mass fraction with the pressure. However, the maximum value of mass fraction at at 9.1 MPa experiments a slight decrement. This could be due to the fact that, since reaction rates get stronger with the increase of pressure, at 9.1 MPa, the reaction rate of R3 provokes a consumption of DR2 enough to decrease the content produced in R1.

6. Final products mass fraction increases with the time. However, when pressure is fixed between 9.1 MPa to 5.99 MPa, the mass fraction of final products decreases slightly from 0.01 s to 0.02 s (first slot) and raises between 0.02 s and 0.05 s (second slot). This could be explained by taking into account that final products are the result of R2 and R3 and R3 depends strongly on R1. DR1 mass fraction value is constant in the first time slot and decreases in the second one. This means that reaction 2 needs some time to increase their effect. Moreover, two phenomena are observed. On the one hand, at high pressures, the mass fraction of DR2 increases slightly in the first time slot while decreasing in the second one. On the other hand, at low pressures, DR2 mass fraction increases with the time which means that, during the first slot, reaction 1 produces more intermediate species than reaction 3 can consume and therefore, there is an increment of DR2 mass fraction. The same is happening at high pressures for the first time slot. However, between 0.02 s and 0.05 s, the amount of DR2 mass fraction when pressure is high suffers a decrement. Since during the second time slot and the pressure fixed is high there is a strong increment of the final products mass, it can be concluded that, reaction 3 increase its strength with pressure and time.

7. The temperature increases with pressure. Moreover, the lower the pressure, the softer is the transition between minimum and maximum temperature. However, as the time passes, the jump between hot temperature in the gas phase and cold temperature in the condensed phase becomes more abrupt which means that, the transference of heat in the solid increases with the fall of pressure and decreases when the time passes.

8. The heat flux increases with the pressure and with the time. The greatest amount of heat is transferred in the burning surface between the solid and the gas. Being the expected result to

observe since the variable is defined as the thermal conductivity multiplied by the temperature gradient. The value along the rest of the control volume remains very low or even zero.

To conclude, and as it was done for AP/HTPB composite propellant, a depressurisation ramp is applied to the right side of the control volume using the same geometry than the one chosen for the previous test. The ramp is designed to decrease the pressure from 9.1 MPa to 1.1 MPa in $1 \cdot 10^{-8}$ s starting at 0.01 s. Three points in the geometry have been chosen to plot the variables. The first point chosen is located close to the burning surface of the 1.1 MPa fixed boundary case when time is equal to 0.01 seconds, the second one is located at the middle of the initial gas domain and the third one almost in the end. of the gas zone. The main conclusions extracted from the simulation are the following:

1. The pressure wave due to depressurisation evolves from the right side of the tube until the burning surface and afterwards, it comes back to the right side. This movement is repeated until reaching the equilibrium pressure of 1.1 MPa.

2. The pressure for the 1.1 MPa fixed boundary test measured at $P_1(x = 510{\cdot}10^{-6}\ m)$ fluctuates around 1.1 MPa. The cells close to the burning surface are the first to receive the sublimated gas species from the burning surface and, as a result, the fuel, oxidiser and intermediate species combust firstly in these cells. Therefore, the density of cells located close to the burning surface will fluctuate and that will influence to the temperature and pressure distributions.

3. Depressurisation provokes immediately a diffusion of the temperature along the condensed phase. The higher the pressure, the sharper will be the transition between cold condensed and hot gas temperatures.

4. Since the reaction rates, which represent the chemical kinetics of the combustion process, depend on the density, with the fall of pressure, the reaction rates decrease too. As a result, when depressurisation is applied, not only less fuel and oxidiser react to form intermediate product DR2, but also less DR1 and DR2 change to become final products. The sublimation of condensed phase and the decrease of reaction rates are the reason of the increment of fuel, oxidiser and intermediate products DR1. As a result, there creation of new final products will fall down and part of them will be lost by the exit of the tube concluding in a reduction of their mass fraction. The same phenomenon is suffered by intermediate specie DR2 just after depressurisation until time is equal to 0.001004 s. At this time pressure stabilised to 1.1 MPa and therefore, the mass fraction of DR2 remains almost constant too.

5. The maximum temperature of the control volume falls sharply immediately after the pressure ramp at the boundary is applied. Afterwards, it fluctuates until t = 0.01001 s, time from which it will experiment a soft increase until reaching the same value as that obtained for the 1.1 MPa fixed boundary condition test.

6. The heat flux present fluctuations immediately after the applying depressurisation. The strong fall of pressure at the exit provokes a decrease of the heat flux between 0.01 s and 0.0101 s. After that interval of time, its maximum fluctuates until reaching a magnitude closer to the one obtained for 1.1 MPa fixed boundary condition test.

Future work

Several aspects could be considered as future work of this thesis, not only to complete the understanding of combustion of solid propellants but also to improve the results and decrease the differences obtained between experimental and numerical ones.

The first idea to be considered is the influence of AP size in the burning rate. This effect was taken into account by Kohga [51] who studied the influence of AP size in the burning rate by comparing the results obtained when using particles diameters of 4 μm and 110 μm. In addition, Jeppson and Beckstead [42], studied this effect by choosing AP grains with diameters from 20 μm to 200 μm and plotting the burning rate results for each one of them. Kubota [3] also mentioned the influence that the AP particle size has on the burning rate. The three authors remarked that, considering the same propellant composition, the smaller the particle size, the higher burning rate. Therefore, it is considered of high importance to study the effect of the particle size together with the pressure, not only in the burning rate, but also in the temperature and AP mass fraction distributions. This analysis will be performed by varying the parameters of equations (4.83) and (4.84). By considering a fixed AP composition (α), for each chosen AP particle diameter (d_{AP}), equation (4.84) will provide the height of HTPB (d_{HTPB}). By introducing both values in equation (4.83), the total height of the control volume, (L), can be obtained. Moreover, the burning rate results could be compared with the ones available in the literature, such as the ones from Jeppson and Beckstead [42] and from Kohga [51]. Another aspect considered as future work is the study of the influence of the propellant composition in the burning rate, this could be done, not only for the AP/HTPB in sandwich configuration, but also for the homogeneous strand and the double-base solid propellant. The results could be compared with the ones presented by Kohga [51] who also studied the influence of AP mass fraction in the burning rate.

Finally, and in order to improve the results obtained, it could be interesting to include the release of heat due to radiation and the emissivity of the surfaces which have been assumed negligible when developing the mathematical model. In the present work, only the heat due to conduction has been considered and since the experiments are done in a closed combustion chamber, reflecting walls could be approximated as black body or grey body of high emissivity. This consideration could reduce the error between experimental and numerical results.

Nomenclature

c	Specific heat
c_v	Specific heat at constant volume
c_p	Specific heat at constant pressure
c_g	Speed of sound
d_{AP}	Diameter of AP particles
d_{HTPB}	Diameter of HTPB particles
d	Normal distance between cells centre and considered surface
d_p	Granulated particles diameter
D_j	Reaction rate constants of jth-reaction
Da	Damköhler number
E_c	Activation energy of condensed phase
E_j	Activation energy of jth-reaction
E	Energy
F_D	Drag force
k	Thermal conductivity
M_g	Molecular mass
n_j	Exponential pressure factor of jth-reaction
Nu	Nusselt number
p	Pressure
Pe	Peclet number
Pr	Prandtl number
$\dot{Q}$	Heat transfer
Q_g	Heat of reaction
Q_c	Heat of decomposition of condensed phase
R_j	Reaction rates of jth-reaction
Re	Reynolds number
R_g	Specific constant of gases
R_u	Universal constant of gases
$\dot{r}$	Burning rate
S_p	Granulated particles surface
T	Temperature
t	Time
u	Velocity
V_p	Granulated particles volume
Y	Mass fraction

Greek Symbols

α	Porosity
$\dot{\Gamma}$	Mass transfer
γ	Heat capacity ratio
η_g	Co-volume
μ_g	Gas viscosity
ϕ	rate of production/consumption

Subscripts

c	Condensed
g	Gas
$melt$	Melting
p	Propellant
s	Surface

Appendix I Heat Flux detailed figures

Cell values of the heat flux can bee seen in Figures A I.1and A I.2.

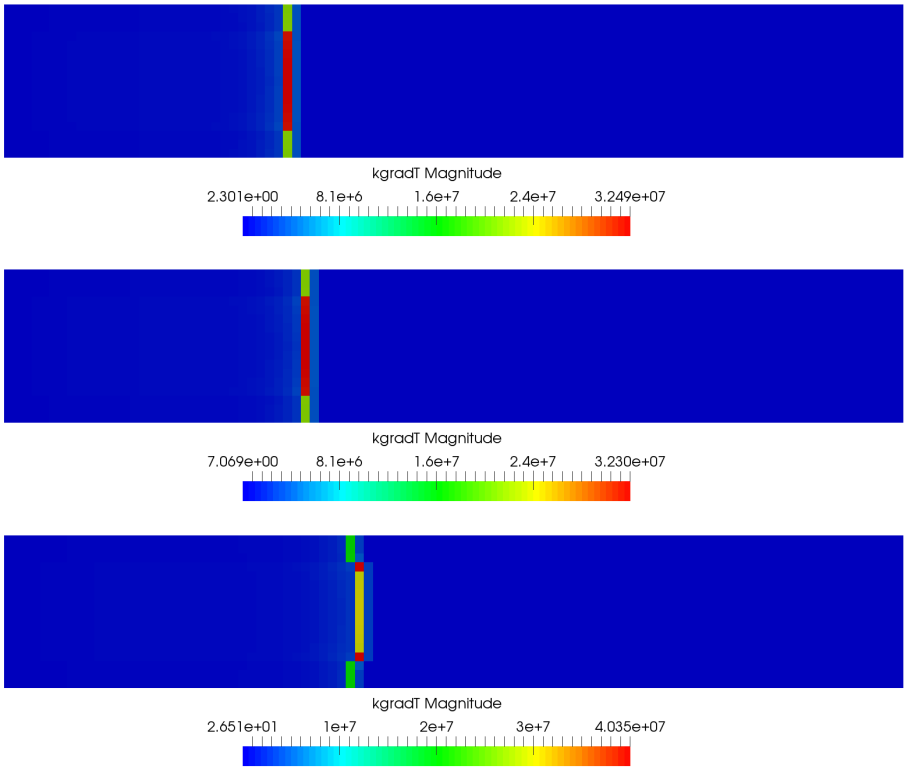

Figure A I.1: Heat flux distribution in t = 0.02 s at 7 MPa, 5 MPa, 3 MPa (above-below).

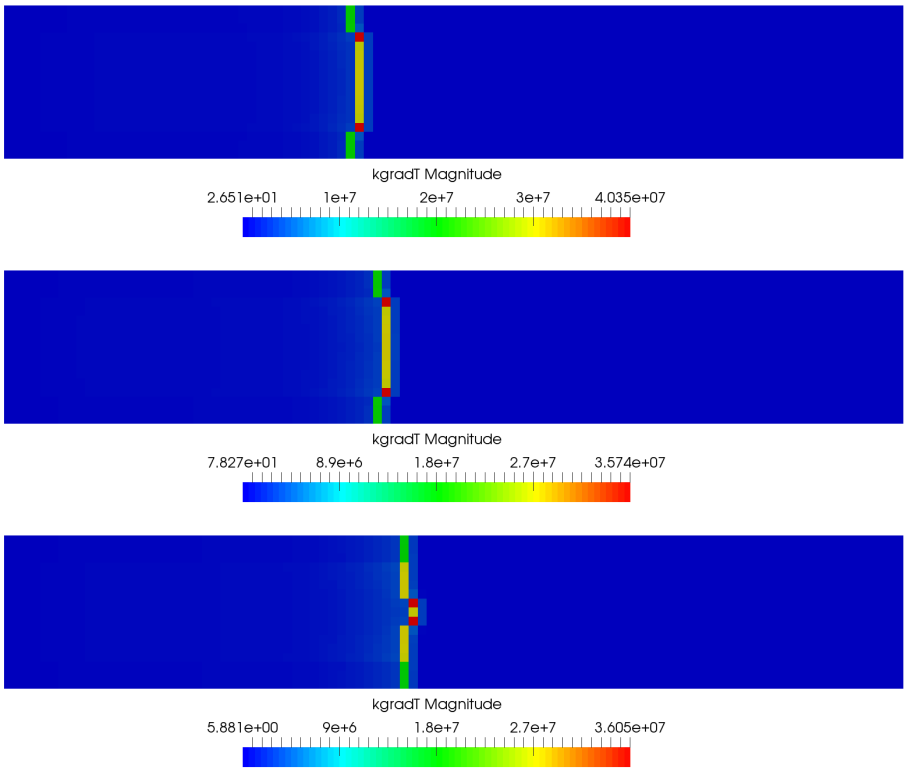

Figure A I.2: Heat flux distribution in t = 0.02 s at 2 MPa, 1 MPa, 0.5 MPa (above-below).

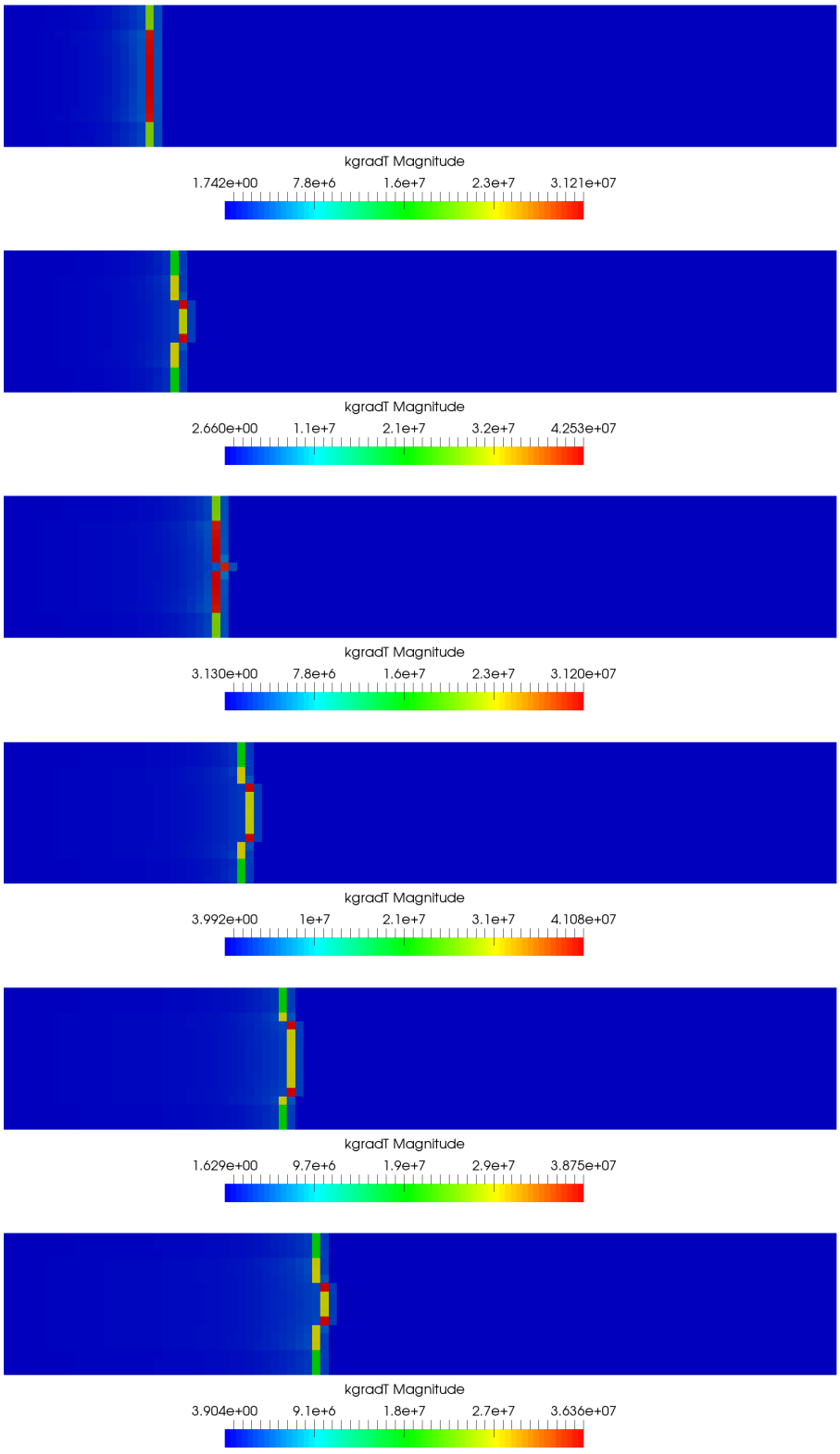

Figure A I.3: Heat flux distribution in t = 0.04 s at 7 MPa, 5 MPa, 3 MPa, 2 MPa, 1 MPa, 0.5 MPa (above-below).

Appendix II Dimensionless numbers

In order to understand and characterise the combustion problem, a nondimensionalisation has been introduced. According to Margolis and Williams [87] the first step should be define a characteristic velocity defined as the speed of propagation $U_c = dx_s/dt$, where x_s is the coordinate of the burning surface. Therefore, the characteristic velocity chosen in this work will be the burning speed which depends on the pressure of the selected test. The remaining expressions [87] for dimensionless variables are,

$$x_a = \frac{\rho_c c_c U_{s,c}}{\lambda_c} L_c,\ t_a = \frac{\rho_c c_c U_c^2}{\lambda_c} t_f,\ T_{a_{g,c}} = \frac{T_{c,g}}{T_0},\ u_{g_a} = \frac{u_g}{U_{s.c}}, \rho_{g_a} = \frac{\rho_g}{\rho_{g,0}},\ p_{g_a} = \frac{p_g}{p_{g,0}} \tag{5.1}$$

where the subindex a stands for dimensionless. T_0, $p_{g,0}$ are the initial unburned temperature and pressure respectively and therefore, $\rho_{g,0}$ is the density at this pressure and temperature conditions. L_c is the characteristic length of the problem which in this case is 170 μm. The characteristic time of the problem (t_f) has been calculated with the following expression,

$$t_f = \frac{\lambda_g}{\rho_g c_{vg} U_c^2} \tag{5.2}$$

Besides the nondimensionalisation of the problem variables, it is also of high interest to calculate the typical non dimensional numbers in order to characterise the properties of the fluid. Characteristic diffusion and combustion time, as well as Reynolds, Peclet and Damköhler number has been calculated and their results are presented afterwards. The expressions of combustion and diffusion times have been taken from Cai et al. [45] as,

$$t_c = \rho/\dot{\omega},\ t_d = L^2/D \tag{5.3}$$

Peclet, Reynolds and Damköhler numbers have the following expressions, .

$$Re = \frac{u_g L_c \rho_g}{\mu},\ Pe = \frac{u_g L_c}{D},\ Da = t_d/t_c \tag{5.4}$$

For AP/HTPB sandwich propellant, the results obtained have been summarised in Table A II.1 and Table A II.2. Dimensionless values of gas and condensed phase temperatures are almost the same independently of the pressure set therefore,

$$T_{a_g} = \frac{T_{c,g}}{T_0} = \frac{2700}{300} = 8,\ T_{a_c} = \frac{T_{c,g}}{T_0} = \frac{370}{300} = 1.233 \tag{5.5}$$

Since the combustion chamber is open, the pressure of the domain is the same as the initial pressure. As a result, the dimensionless pressure is $p_{g_a} = 1$.

Pressure (MPa)	OpenFoam Burning rate (mm/s)	t_f (μs)	t_a	x_a
7	7.52	1.7880	0.0006	7.3800
5	6.61	2.0282	0.0005	6.4870
3	5.53	2.1823	0.0004	5.4271
2	4.82	1.7975	0.0002	4.7303
1	3.89	1.4319	0.0001	3.8176
0.5	3.19	1.0070	0.0001	3.1306

Pressure (MPa)	u_g (m/s)	$u_{g,a}$	ρ_g (kg/m^3)	$\rho_{g,0}$ (kg/m^3)	ρ_g
7	1.8	239.3617	9.2063	80.7614	0.1140
5	2.0	302.5719	6.5740	57.6867	0.1140
3	2.5	452.0796	3.9103	34.6120	0.1130
2	3.4	705.3942	2.5666	23.0747	0.1112
1	5.5	1413.8817	1.2313	11.5373	0.1067
0.5	9.5	2978.0564	0.5868	5.7687	0.1017

Table A II.1: Dimensionless variables for AP/HTPB propellant in sandwich configuration

Pressure (MPa)	$t_{c_1} \cdot 10^{-8}$	$t_{c_2} \cdot 10^{-8}$	$t_d \cdot 10^{-4}$
7	1.3170	4.5967	70.0160
5	1.6911	5.9025	49.9966
3	2.45168	8.5570	29.7389
2	3.2637	11.3914	19.5198
1	5.2446	18.3056	9.3645
0.5	8.3723	29.2221	4.4629

Pressure (MPa)	Re	Da_1	Da_2	Pe
7	41.2	531644.5	152318.7	74.1
5	32.7	295647.4	84704.5	58.8
3	24.3	121302.5	34753.7	43.7
2	21.7	59809.0	17135.6	39.0
1	16.8	17855.4	5115.6	30.3
0.5	13.9	5330.6	1527.2	24.9

Table A II.2: Dimensionless variables for AP/HTPB propellant in sandwich configuration

Appendix III Granulated propellant code structure

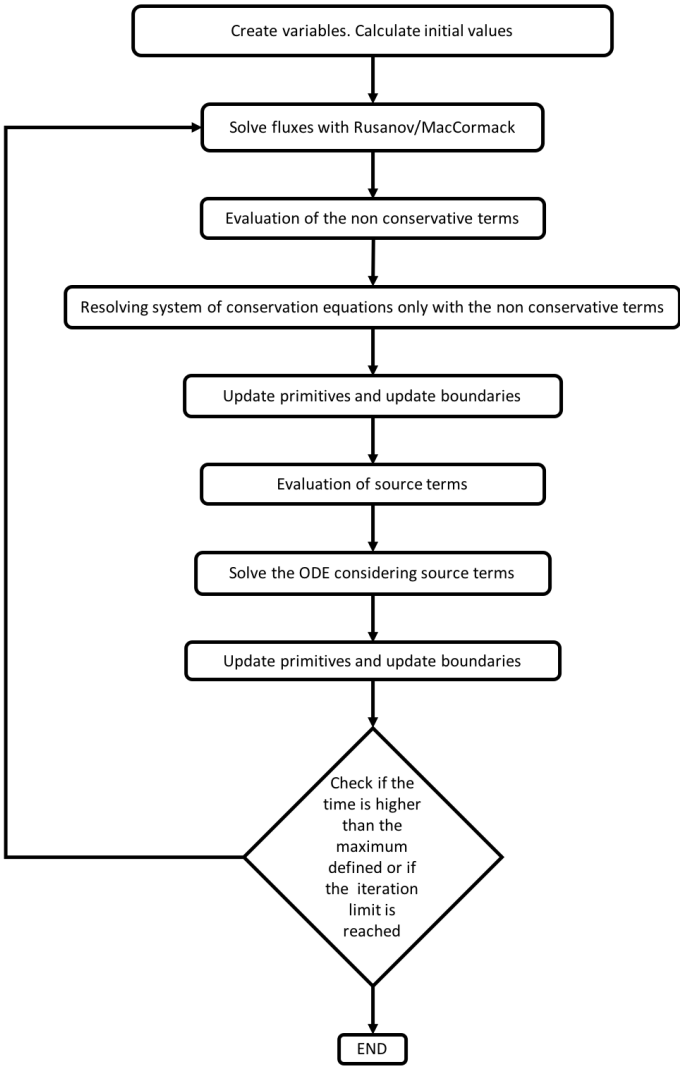

Figure A III.1: Granulated propellant code flowchart

Appendix IV AP/HTPB and double-base propellants code structure

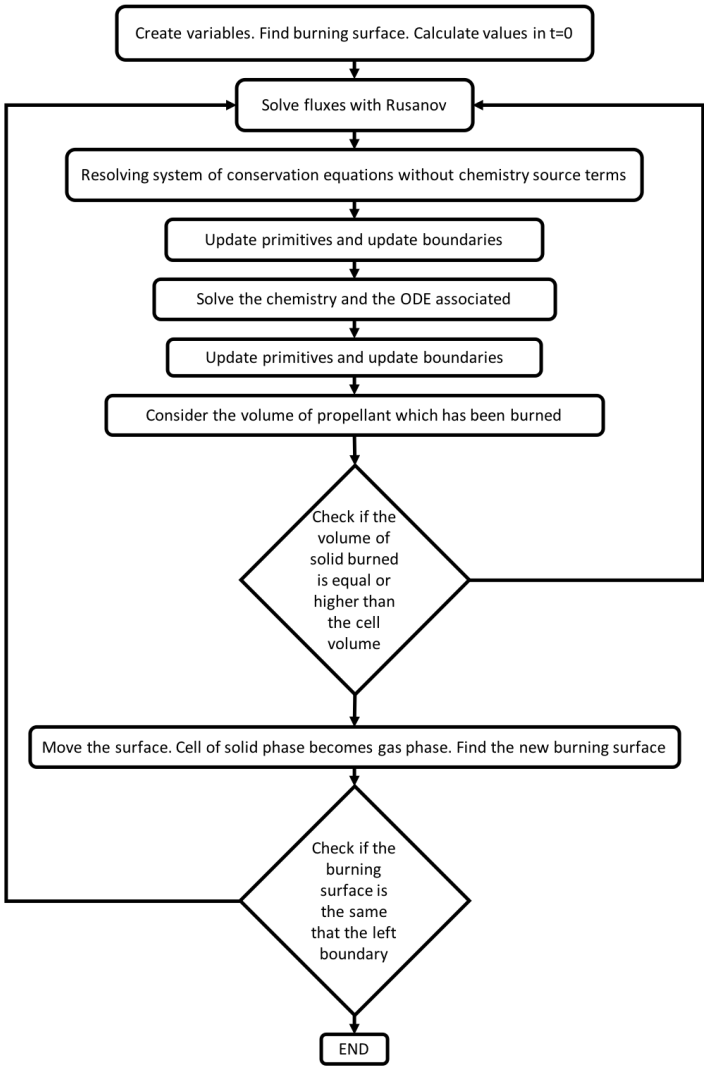

Figure A IV.1: AP/HTPB and double-base propellants code flowchart

Bibliography

[1] Energetic Materials 101. https://www.smsenergetics.com/resources/energetic-materials-101/.

[2] J.P. Agrawal. *High Energy Materials*. Propellants, Explosives and Pyrotechnics. Wiley-VCH, 2010.

[3] N. Kubota. *Propellants and Explosives. Thermochemical Apects of Combustion*. Wiley-VCH, 2002.

[4] M.W. Beckstead, N.L. Peterson, D.T. Pilcher, B.D. Hopkins, and H. Krier. Convective combustion modeling applied to deflagration-to-detonation transition of HMX. *Combustion and Flame*, 30:231–241, 1977.

[5] A. Harrland and I.A. Johnston. Review of Solid Propellant Ignition Models Relative to the Interior Ballistic Modelling of Gun Systems. *Weapons Systems Division Defence Science and Technology Organisation*, 2012.

[6] K.L. Kosanke, B.J. Kosanke, B.T. Sturman, and R.M. Winokur. *Encyclopedic dictionary of pyrotechnics and related subjects*. Pyrotechnic reference series, no. 5. Whitewater, Colo. : Journal of Pyrotechnics, Inc., 2012.

[7] H. Krier and S. Gokhale. Modeling of Convective Mode Combustion through Granulated Propellant to Predict Detonation Transition. *AIAA Journal*, 16(2):177–183, 1978.

[8] M.W. Beckstead, K. Puduppakkam, P. Thakre, and V. Yang. Modeling of combustion and ignition of solid-propellant ingredients. *Progress in Energy and Combustion Science*, 33(6):497–551, 2007.

[9] K.K. Kuo and M. Summerfield. *Fundamentals of Solid-Propellant Combustion*, volume 90 Progress in Astronautics and Aeronautics. American Institute of Aeronautics and Astronautics, Inc., 1984.

[10] H. Krier. Solid Propellant Burning Rate During a Pressure Transient. *Combustion Science and Technology*, 5(1):69–73, 1972.

[11] H. Krier, W.A. Sirignano, M. Summerfield, and J.S. Tien. Nonsteady burning phenomena of solid propellants - Theory and experiments. *AIAA Journal*, 6(2):278–285, 1968.

[12] K.K. Kuo, R. Vichnevetsky, and M. Summerfield. Theory of Flame Front Propagation in Porous Propellant Charges under Confinement. *AIAA Journal*, 11(4):444–451, 1973.

[13] J.H. Koo and K.K. Kuo. Transient Combustion in Granular Propellant Beds. Part I. Theoretical Modeling and Numerical Solution of Transient Combustion Processes in Mobile Granular Propellant Beds. Technical report, Pennsylvania State University Park Dept. of Mechanical Engineering, 1977.

[14] N.C. Markatos. Modelling of two-phase transient flow and combustion of granular propellants. *International Journal of Multiphase Flow*, 12(6):913–933, 1986.

[15] D.B. Spalding. Numerical computation of multi-phase fluid flow and heat transfer. In *Recent Advances in Numerical Methods in Fluids*, pages 139–167. 1980.

[16] P.S. Gough and F.J. Zwarts. Modeling Heterogeneous Two-Phase Reacting Flow. *AIAA Journal*, 17(1):17–25, 1979.

[17] R.A. Oton-Martinez, G. Monreal-Gonzalez, J.R. Garcia-Cascales, F. Vera-Garcia, F.J.S. Velasco, and F.J. Ramirez-Fernandez. An approach formulated in terms of conserved variables for the characterisation of propellant combustion in internal ballistics. *International Journal for Numerical Methods in Fluids*, 79(8):394–415, 2015.

[18] H.W. Sandusky and W.L. Elban. Quasi-static compaction of porous propellant beds. II. Experiments and application of lattice compaction model to cannon propellants. *Powder Technology*, 89(3):219–229, 1996.

[19] D.E. Kooker, S.L. Howard, and L.M. Chang. Convective ignition of a granular solid propellant bed: Influence of propellant composition. *Symposium (International) on Combustion*, 26(2):2033–2040, January 1996.

[20] K.K. Kuo and M. Summerfield. Theory of Steady-State Burning of Gas-Permeable Propellants. *AIAA Journal*, 12(1):49–56, 1974.

[21] W.F. van Tassell and H. Krier. Combustion and flame spreading phenomena in gas-permeable explosive materials. *International Journal of Heat and Mass Transfer*, 18(12):1377–1386, 1975.

[22] H. Krier, S. Rajan, and W.F. Van Tassell. Flame-Spreading and Combustion in Packed Beds of Propellant Grains. *AIAA Journal*, 14(3):301–309, 1976.

[23] K.K. Kuo, J.H. Koo, T.R. Davis, and G.R. Coates. Transient combustion in mobile gas-permeable propellants. *Acta Astronautica*, 3(7):573–591, 1976.

[24] J.M. Lenoir and G. Robillard. A mathematical method to predict the effects of erosive burning in solid-propellant rockets. *Symposium (International) on Combustion*, 6(1):663–667, 1957.

[25] W. Denton. The Heat Transer and Flow Resistance for Fluid Flow Through Randomly Packed Spheres. *American Society of Mechanical Engineers*, 1951.

[26] S. Ergun. Fluid flow through packed columns. *Journal of Chemical Engineering Progress*, 48, No. 2:89–94, 1952.

[27] H. Krier and J.A. Kezerle. A separated two-phase flow analysis to study deflagration-to-detonation transition (DDT) in granulated propellant. *Symposium (International) on Combustion*, 17(1):23–34, 1979.

[28] S.J. Hoffman and H. Krier. *Fluid Mechanical Processes of Deflagration to Detonation Transition in Beds of Porous Reactive Solids.*, volume Technical report AAE -80_2. Aeronautical and Astronautical Engineering Department, University of Illinois at Urbana-Champaign, 1980.

[29] S.J. Hoffman and H. Krier. Fluid Mechanics of Deflagration-to-Detonation Transition in Porous Explosives and Propellants. *AIAA Journal*, 19(12):1571–1579, 1981.

[30] K.K. Kuo and C.C. Nydegger. Cold flow resistance measurement and correlation in a packed bed of WC-870 spherical propellants. *Journal of Ballistics*, 2:1–26, 1978.

[31] S.S. Gokhale and H. Krier. Modeling of unsteady two-phase reactive flow in porous beds of propellant. *Progress in Energy and Combustion Science*, 8(1):1–39, 1982.

[32] P.B. Butler and H. Krier. Analysis of deflagration to detonation transition in high-energy solid propellants. *Combustion and Flame*, 63(1):31–48, 1986.

[33] J.M. Powers. *Theory of detonation structure for two-phase materials*. Thesis. University of Illinois at Urbana-Champaign, 1988.

[34] M.R. Baer and J.W. Nunziato. A two-phase mixture theory for the deflagration-to-detonation transition (ddt) in reactive granular materials. *International Journal of Multiphase Flow*, 12(6):861–889, 1986.

[35] J.M. Powers, D.S. Stewart, and H. Krier. Theory of two-phase detonation Part I Modeling. *Combustion and Flame*, 80(3):264–279, 1990.

[36] J.M. Powers, D.S. Stewart, and H. Krier. Theory of two-phase detonation Part II: Structure. *Combustion and Flame*, 80(3):280–303, 1990.

[37] J. Powers, D.S. Stewart, and H. Krier. Two-phase steady detonation analysis. *NASA STI/Recon Technical Report N*, 1988.

[38] N.I. Gelperin and V.G. Einstein. Heat transfer in fluidized beds. *Fluidization*, Academic Press. New York, 1971.

[39] P.B. Butler, M.F. Lembeck, and H. Krier. Modeling of shock development and transition to detonation initiated by burning in porous propellant beds. *Combustion and Flame*, 46:75–93, 1982.

[40] S.F. Wilcox, D.P. Jones, and H. Krier. Technical Report UILU-ENG 80-0501, 1980.

[41] M.W. Beckstead, R.L. Derr, and C.F. Price. A model of composite solid-propellant combustion based on multiple flames. *AIAA Journal*, 8(12):2200–2207, 1970.

[42] M. Jeppson, M. Beckstead, and Q. Jing. A kinetic model for the premixed combustion of a fine AP/HTPB composite propellant. In *36th AIAA Aerospace Sciences Meeting and Exhibit*, Aerospace Sciences Meetings. American Institute of Aeronautics and Astronautics, 1998.

[43] C. Guirao and F.A. Williams. A model of ammonium perchlorate deflagration between 20 and 100 atm. *AIAA Journal*, 9(7):1345–1356, 1971.

[44] G.M. Knott and M.Q. Brewster. Modeling the combustion of propellant sandwiches. *Combustion Science and Technology*, 174(4):61–90, 2002.

[45] W. Cai and V. Yang. A model of AP/HTPB composite propellant combustion. In *38th Aerospace Sciences Meeting and Exhibit*, Aerospace Sciences Meetings. American Institute of Aeronautics and Astronautics, 2000.

[46] R. Ye, Y.G. Yu, and Y.J. Cao. Analysis of Micro-scale Flame Structure of AP/HTPB Base Bleed Propellant Combustion. *Defence Technology*, 9(4):217–223, 2013.

[47] Y.J. Cao, Y.G. Yu, and R. Ye. Numerical analysis of AP/HTPB composite propellant combustion under rapid depressurization. *Applied Thermal Engineering*, 75:145–153, 2015.

[48] N.D. Vo, M.Y. Jung, D.H. Oh, J.S. Park, I. Moon, and M. Oh. Moving boundary modeling for solid propellant combustion. *Combustion and Flame*, 189:12–23, 2018.

[49] W. Cai, P. Thakre, and V. Yang. A Model of AP/HTPB Composite Propellant Combustion in Rocket-Motor Environments. *Combustion Science and Technology*, 180(12):2143–2169, 2008.

[50] J.A. Moríñigo and J. Hermida-Quesada. Evaluation of reduced-order kinetic models for HTPB-oxygen combustion using LES. *Aerospace Science and Technology*, 58:358–368, 2016.

[51] M. Kohga. Burning Characteristics and Thermochemical Behavior of AP/HTPB Composite Propellant Using Coarse and Fine AP Particles. *Propellants, Explosives, Pyrotechnics*, 36(1):57–64, 2011.

[52] P.A. Ramakrishna, P.J. Paul, and H.S. Mukunda. Sandwich propellant combustion: Modeling and experimental comparison. *Proceedings of the Combustion Institute*, 29(2):2963–2973, 2002.

[53] E.W. Price. Proceedings of the Thirtieth JANNAF Combustion Meeting. *Chemical Propulsion Information Agency*, 2(Publication 606), 1993.

[54] E.W. Price, J.K. Sambamurthi, R.K. Sigman, and R.R. Panyam. Combustion of ammonium perchlorate-polymer sandwiches. *Combustion and Flame*, 63(3):381–413, 1986.

[55] R.P. Fitzgerald and M.Q. Brewster. Infrared imaging of AP/HTPB laminate propellant flames. *Combustion and Flame*, 154(4):660–670, 2008.

[56] F. Miccio. Numerical modeling of composite propellant combustion. *Symposium (International) on Combustion*, 27(2):2387–2395, 1998.

[57] G. Favale and F. Miccio. Modeling unsteady and perturbed combustion of heterogeneous composite propellants. *Aerospace Science and Technology*, 12(4):285–294, 2008.

[58] G.M. Knott and M.Q. Brewster. Two-dimensional combustion modeling of heterogeneous solid propellants with finite Peclet number. *Combustion and Flame*, 121(1):91–106, 2000.

[59] X. Zhou, T.L. Jackson, and J. Buckmaster. A numerical study of periodic sandwich propellants with oxygenated binders. *Combustion Theory and Modelling*, 7(2):435–448, 2003.

[60] T.L. Jackson and J. Buckmaster. Heterogeneous Propellant Combustion. *AIAA Journal*, 40(6):1122–1130, 2002.

[61] W. Cai. *Two-phase flow interactions and combustion of AP/HTPB composite propellant in rocket motors with acoustic oscillations*. PhD thesis, 2001. OCLC: 55721452.

[62] G. Lengelle. Thermal degradation kinetics and surface pyrolysis of vinyl polymers. *AIAA Journal*, 8(11):1989–1996, 1970.

[63] M.M. Ibiricu and F.A. Williams. Influence of externally applied thermal radiation on the burning rates of homogeneous solid propellants. *Combustion and Flame*, 24:185–198, 1975.

[64] G. Lengelle, J. Duterque, C. Verdier, A. Bizot, and J.F. Trubert. Combustion mechanisms of double base solid propellants. *Symposium (International) on Combustion*, 17(1):1443–1451, 1979.

[65] A. Bizot and M.W. Beckstead. A model for double base propellant combustion. *Symposium (International) on Combustion*, 22(1):1827–1834, 1989.

[66] T.S. Roh, S. Apte, and V. Yang. Transient combustion response of homogeneous solid propellant to acoustic oscillations in a rocket motor. *Symposium (International) on Combustion*, 27(2):2335–2341, 1998.

[67] S.Y. Hsieh and V. Yang. A Preconditioned Flux-Differencing Scheme for Chemically Reacting Flows at all Mach Numbers. *International Journal of Computational Fluid Dynamics*, 8(1):31–49, 1997.

[68] M.Q. Brewster, M.J. Ward, and S.F. Son. Simplified Combustion Modeling of Double Base Propellant: Gas Phase Chain Reaction Vs. Thermal Decomposition. *Combustion Science and Technology*, 154(1):2–30, 2000.

[69] S. Apte and V. Yang. Unsteady flow evolution and combustion dynamics of homogeneous solid propellant in a rocket motor. *Combustion and Flame*, 131(1):110–131, 2002.

[70] T.S. Roh, I.S. Tseng, and V. Yang. Effects of acoustic oscillations on flame dynamics of homogeneous propellants in rocket motors. *Journal of Propulsion and Power*, 11(4):640–650, 1995.

[71] X. Wu, M. Kumar, and K.K. Kuo. A comprehensive erosive-burning model for double-base propellants in strong turbulent shear flow. *Combustion and Flame*, 53(1):49–63, 1983.

[72] I. Shih Tseng and Vigor Yang. Combustion of a double-base homogeneous propellant in a rocket motor. *Combustion and Flame*, 96(4):325–342, 1994.

[73] V.A. Arkhipov, V.E. Zarko, I.K. Zharova, A.S. Zhukov, E.A. Kozlov, D.D. Aksenenko, and A.V. Kurbatov. Solid propellant combustion in a high-velocity cross-flow of gases (review). *Combustion, Explosion, and Shock Waves*, 52(5):497–513, 2016.

[74] F.W. Robbins and T. Keys. The Burning Rate Behavior of Pure Nitrocellulose Propellant Samples:. Technical report, Defense Technical Information Center, Fort Belvoir, VA, 1993.

[75] Q.L. Yan, X.J. Li, Y. Wang, W.H. Zhang, and F.Q. Zhao. Combustion mechanism of double-base propellant containing nitrogen heterocyclic nitroamines (I): The effect of heat and mass transfer to the burning characteristics. *Combustion and Flame*, 156(3):633–641, 2009.

[76] Q.L. Yan, Z.W. Song, X.B. Shi, Z.Y. Yang, and X.H. Zhang. Combustion mechanism of double-base propellant containing nitrogen heterocyclic nitroamines (II): The temperature distribution of the flame and its chemical structure. *Acta Astronautica*, 64(5):602–614, 2009.

[77] I. Aoki and N. Kubota. Combustion Wave Structures of High- and Low-Energy Double-Base Propellants. *AIAA Journal*, 20(1):100–105, 1982.

[78] V.N. Marshakov and B.V. Novozhilov. Transient modes of double-base propellant combustion in a semiclosed volume. *Russian Journal of Physical Chemistry B*, 5(1):45–56, 2011.

[79] E. F. Toro. *Riemann Solvers and Numerical Methods for Fluid Dynamics - A Practical Introduction*. Springer, 2009.

[80] V.V. Rusanov. *Calculation of interaction of non-steady shockwaves with obstacles,*. National Research Council of Canada, Ottawa, 1962. OCLC: 12207123.

[81] R.W. MacCormack. The effect of viscosity in hypervelocity impact cratering. In *4th Aerodynamic Testing Conference*, Aerodynamic Testing Conference, Cincinnati,OH,U.S.A., 1969. American Institute of Aeronautics and Astronautics.

[82] J.K. Lee and T.K. Kim. Application of TVD-McCormack Scheme to Analysis of Dam-Break Problems. *Journal of Korea Water Resources Association*, 36(3):365–374, 2003.

[83] P. Lax and B. Wendroff. Systems of conservation laws. *Communications on Pure and Applied Mathematics*, 13(2):217–237, 1960.

[84] D. Liang, R.A. Falconer, and B. Lin. Comparison between TVD-MacCormack and ADI-type solvers of the shallow water equations. *Advances in Water Resources*, 29(12):1833–1845, 2006.

[85] D. Gidaspow. *Multiphase Flow and Fluidization*. Academic Press, 1994.

[86] Ensayos de la velocidad de combustión. Technical report, Ministerio de Defensa, Instituto Nacional de Ténica Aeroespacial (INTA).

[87] S.B. Margolis and F.A. Williams. Structure and Stability of Deflagrations in Porous Energetic Materials. Technical Report SAND99-8458, Sandia National Labs., Albuquerque, NM (US); Sandia National Labs., Livermore, CA (US). US Department of Energy (US), 1999.